CARDIFF
UNIVERSITY
PRIFYSGOL
CAERDYDD

Exploring the use of two-photon lithography and deposition to produce arrays of magnetic elements

By Alaa Khalid Hejazi

A THESIS SUBMITTED TO CARDIFF UNIVERSITY FOR THE
DEGREE OF DOCTOR OF PHILOSOPHY

November 2022

Abstract

The 3D nanostructuring of magnetic materials provides unique opportunities, both in realisation of novel spin textures in 3D geometries as well as perturbing well-known configurations seen in 2D systems. We show a new and simple means to take any planar spin texture and apply 3D defects which can take the form of simple Gaussian bumps or more complex geometries. In this study, the focus is on the much-studied vortex state which is usually encountered in planar ferromagnetic elements. Two-photon lithography is used with a negative resist, to produce arrays of the structures. Two types of samples have been fabricated. In the first case, simple elements are produced with a flat surface. In the second case, the upper planar surface is perturbed with a 3D hemispherical defect. Subsequent evaporation allows $\mathrm{Ni}_{81}\,\mathrm{Fe}_{19}$ (40 nm) to take the geometry of the underlying polymer. Samples were subject to standard physical characterisation including scanning electron microscopy and atomic force microscopy. These showed structures with low edge roughness and an accurate representation of the designed defect. The magnetic reversal of both samples was studied using MFM. For the case of unperturbed samples, a vortex state was observed, with central core. Application of a field yielded vortex core translation, annihilation and re- nucleation as seen in conventional planar systems. Interestingly, for perturbed samples a vortex state was seen but with a significantly different core position at remanence and a modified trajectory during magnetic reversal. The results are discussed in the context of micro-magnetic simulations.

Keywords: Two- photon lithography, defect, MFM, vortex state.

Publications

First-Author

Alaa Hejazi, Matthew Hunt, Arjen van den Berg and Sam Ladak, Engineering three-dimensional nanoscale geometric defects for spin texture control in ferromagnetic elements. In preparation.

Co-Author

Andrew May, Matthew Hunt, Arjen van den Berg, Alaa Hejazi, and Sam Ladak, Realisation of a frustrated 3D magnetic nanowire lattice, Commun. Phys, 2.1, 2019.

Significant Contributions

I would like to start by giving special thanks to the exceptionally talented people who have trained me in numerous techniques during my PhD. Within Ladak Lab, Matthew Hunt and Andrew May taught me two-photon lithography and trained me to conduct MFM measurements, and Arjen van den Berg taught me how to perform finite-element simulations. Joseph askey conducted the voxel size caculation. Outside of our research group, Angela Sobiesierski, Robert Lang, and Tyrone Jones trained me in various experimental techniques in the ICS cleanroom (Thermal evaporation and SEM measurements).

Acknowledgment

Firstly, thank you to God for giving me the perseverance to complete this research. I would like to acknowledge my primary supervisor, Sam Ladak. The door to Dr. Sam office was always open if I had any problems or any questions relating to my research. He consistently directed me in the correct direction when he thought required.

I would also like to acknowledge my secondary supervisors Sean Giblin and Paul Clark for their advice and guidance and special thanks to Matthew, Andrew, Arjen, Joseph, and Edward for their help with the experimental work and the analytical techniques. Without their participation and contribution it would not possible for me to succeed. Also, I must express my very deep gratitude to my parents, my husband, my son and my brothers for their kind support and help over the period of my study and the procedure of writing this thesis. They made this achievement possible for me. Finally, I sincerely thank the Ministry of Education in Saudi Arabia and Saudi Arabia Cultural Bureau in London for their financial support and providing me the opportunity to complete higher education abroad.

This thesis is dedicated to:

My parents, Khalid Hejazi and Thuraya Shegal.
My husband Mazen, My son Abdulrahman Alnami.
My brothers, Uthman, Abdulrahman and Abdulmajeed.
And to everyone who supported me through my journey.

List of Symbols

Symbol	Definition
$\mathbf{a}$	Lattice parameter
$\mathbf{A}$	Area
$\mathbf{H}$	magnetic field
$\mathbf{A_{ex}}$	Exchange stiffness
$\mathbf{B}$, B	Magnetic induction
$\mathbf{d_{ij}}$	Dzyalashinskii Moriya interaction vector between atoms i and j
$\mathrm{d_{vox}}$	Voxel diameter
$\mathrm{E_{ms}}$	Magnetostatic energy density
$\mathbf{e}$	Electron charge
E_{A}	Effective anisotropy energy density
E_{DM}	Dzyalashinskii-Moriya interaction energy density
E_{EDM}	Effective Dzyalashinskii-Moriya interaction energy density
E_{ex}	Exchange energy density
E_{ms}	Magnetostatic energy density
Ea	Magnetocrystalline anisotropy energy density
E_{zeeman}	Zeeman energy density
f_{γ}	Laser repetition frequency
h	Planck constant
H	Magnetic field strength
H_{C}	Coercive field
$\mathbf{H_{d}}$	Demagnetising field
H_{eff}	Effective magnetic field
I	Current
I_{γ}	Photon flux intensity
$I_{\gamma 0}$	Photon flux intensity in the focus plane
J_{ij}	Exchange integral
S_i, S_j	Pauli matrices
k	Spring constant
k_{B}	Boltzmann constant
K_{n}	nth order magnetocrystalline anisotropy constant
l	Length
l_{vox}	Voxel length
$\boldsymbol{m}$	Magnetic moment
$\boldsymbol{M}$	Magnetisation

M_r	Remanent magnetisation
M_S	Saturation magnetisation
n	Refractive index
n_{pulse}	Number of pulses
$\boldsymbol{\mathcal{N}}$	Demagnetising tensor
N_D	Demagnetising factor
ND	Numerical aperture
p	Magnetic pole
P_γ	Laser power
Q, q	Charge
$\boldsymbol{S}$	Electron spin vector
t	Time
t_0	Attempt time
t_m	Measurement time
u_{ij}	Dipolar energy between two spins, i and j
υ_γ	Laser frequency
V	Volume
W	Number of possible states
z_R	Rayleigh length
γ	gyromagnetic ratio
α_D	Damping constant
α_{ij}	Factor to modify the strength of interaction between spins i and j
α_n	Directional cosines of the magnetisation vector
δ_i	Disorder parameter
δ_t	Domain wall thickness
δ_W	Domain wall width
ω	Angular frequency
ε_0	Permittivity of free space
γ_P	Precessional term
γ_S	Electron spin gyromagnetic ratio
$\widehat{H}$	Hamiltonian operator
λ	Wavelength
μ	Permeability
μ_0	Permeability of free space
ρ_{init}	Primary initiator particle density
ρ_{rad}	Density of radicals
σ	Variance of a Gaussian peak
σ_2	Two-photon absorption cross-section
σ^-, σ^+	Left and right handed portions of a circularly polarised optical beam
θ	Angle
τ_γ	Laser pulse width
ω_e	Electron angular velocity
ω_0	Optical beam waist

$\omega(z)$	Optical beam radius at a distance z
χ	Susceptibility
l_{ex}	Exchange length

List of Acronyms

2D	Two-dimensional
3D	Three-dimensional
AFM	Atomic force microscopy
CAD	Computer aided design
DMI	Dzyaloshinskii-Moriya interaction
DW	Domain wall
FD	Finite difference
FE	Finite element
GWL	General writing language
IPA	Isopropyl alcohol
LLG	Landau-Lifshitz-Gilbert
MFM	Magnetic force microscopy
MS	Magnetostatic Sample
PGMEA	Propylene glycol methyl ether acetate
QCM	Quartz crystal monitor
RMS	Root mean square
SEM	Scanning electron microscopy
TPL	Two-photon lithography
TPP	Two-photon polymerisation
UV	Ultra-violet

List of Figures

List of Tables

Table of Contents

1. Chapter 1

Introduction

The scientific field of nanomagnetism, focused on researching magnetic objects on the nanoscale has seen a surge in interest over the last few decades. This increase in activity has been driven by many exciting discoveries, such as the interaction of magnetization with spin currents [1, 2], as well as a broad variety of applications in the real world [3]. For instance, given that both the storing and sensing components of hard disk drives make use of nanomagnetic structures, the development of nanomagnetism has played a crucial role in the enormous recent advances in computer speed and the advent of cloud technology [4]. In general, nanomagnetism has mostly been restricted to two dimensional structures [5], with a few self-assembled systems being the notable exception [6].

The maturity that has now been attained in this sector, together with the requirement for lower energy technologies with novel capabilities [7], and the arrival of sophisticated nanolithography methods capable of generating non-planar nano-objects, make the extension of nanomagnetism into three dimensions viable. As a result, spin configurations and associated functionalities may now extend out of the substrate plane, in the vertical position. It is also possible to create more complicated, hierarchical or topological systems that can produce effects not seen in conventional planar systems.

Recent years have seen a meteoric rise in interest in nanostructures across the board in the scientific and technological communities [8, 9]. Because of the advancements that have been made in technology over the last several years, it is now feasible to design nanostructures with a wide variety of different physical characteristics. Because of this, they are a leading contender for use in upcoming applications in the fields of materials, electronics and medicine [10, 11]. In general, due to their intrinsic non-volatility as well as simplicity in manipulation with fields and currents, magnetic nanostructures are an essential component of a range of technologies spanning across everyday computing, medical diagnosis and therapy to sensors within self-driving cars [12-14].

In a broad sense, the goal of all systems is to reduce the total free energy they possess. In ferromagnetic materials studied in this thesis it is the sum of the exchange energy, Zeeman energy, anisotropy energy, and magnetostatic energy that together to form the free energy in the studied ferromagnetic materials [15]. Finding a minimum value for all energy variables simultaneously is not attainable. This leads to a magnetic arrangement as the system tends toward an energy minimum. In this way, the magnetostatic energy of a ferromagnetic system may be minimized, which results in the formation of magnetic domains. When a magnetic structure is shrunk down to the nanoscale, the energetics of a multi-domain state become unfavourable; as a consequence, nanomagnets only show single-domain behaviour where the exchange energy is the dominant term [16]. A well-studied nanostructured system is that of the ferromagnetic disk which has a well-established phase diagram [17]. This phase diagram demonstrates the dependency of the spin texture upon thickness and radius. A vortex state occurs [18-20] for both disk and square structures for intermediate radii, whilst a single domain state is seen in smaller structures.

The formation of the vortex state is due to magnetic flux closure whereby the magnetization curls around the system edges, reducing the magnetostatic energy. The so-called core of the structure is produced in the very centre of the structure to minimise exchange energy, which favours the parallel alignment of nearby spins. This region's magnetization is oriented perpendicular to the plane of the material; hence, it produces a measurable stray field. The magnetization in the core of the vortex can point either up ($p = 1$) or down ($p = -1$) with respect to the plane of the disk, and the direction of rotation may be clockwise (c = 1) or counter clockwise (c = -1) respectively [21]. As a direct consequence of this, there are four degenerate ground states for a magnetic vortex.

In recent times, magnetic vortex formation has garnered a lot of interest in the realm of basic research due to their unique properties. Particularly, factors that control the static state as well as the magnetization switching of the vortex core have been thoroughly researched [22, 23]. In this respect, it has been demonstrated that core magnetization can switch by various mechanisms, such as core displacement, nucleation of a vortex-antivortex pair, and the annihilation of vortices [24]. In addition, the coupling of vortex structures has been studied, with most of the research focused on Landau patterns and disk structures [19, 25], placed into dense arrays [26, 27]. In this situation, the impact of modifying the interelement spacing on the magnetostatic coupling is of special importance. Magnetic vortices are starting to find uses in a variety of sectors, such as data storage in a vortex-based random-access memory device [28], frequency-controlled magnetic vortex memory [29], as a magnetic field sensor owing to its hysteresis-free component [30], for spintronics [31], ultra-fast circuits [32] and biomedical applications [33].

In addition, nanomagnets that have spin configurations that are both stable and controlled may be used in the production of magnetic logic components. The micromagnetic stability of a nanomagnet, on the other hand, declines as the size of the nanomagnet becomes smaller, which results in a lack of controllability over the spin configurations [34]. Therefore, developing efficient techniques for manipulating micro-magnetic structures in nanomagnets is an essential issue not only for basic physics but primarily for high-tech sectors of the economy, including electronic products, data storage techniques, and sensing technologies. This is because the manipulation of micro-magnetic textures in nanomagnets is one of the most significant aspects of nanomagnetism. Previous work has shown that placing simple 3D perturbations upon the surface of planar ferromagnetic structures can be used to control the spin texture, core switching and chirality [35]. This thesis demonstrates a new means to produce standard spin textures seen in conventional planar geometry but in a way that allows bespoke 3D perturbations to be placed upon the surface by design.

Chapter 2 details, the background theory needed to understand the physics in the following chapters. Ferromagnetism is looked at in detail, with the roles of key energies studied, such as that driven by the exchange interaction, the magnetostatic energy and the Zeeman energy. Magnetic domain theory is outlined, and the physics of different domain walls is described. After this, the physics of two-photon polymerisation and the process of generating a model for feature sizes that may be obtained by employing typical photoresists are discussed. The chapter concludes by discussing the primary characteristics that define magnetic vortex behaviour in nanostructures, as well as outlining key literature in the field of micron-sized magnetic elements.

In chapter 3 the experimental methodology of the fabrication process is discussed. This methodology makes use of two-photon lithography (TPL) and thermal evaporation, as well as scanning electron microscopy (SEM), atomic force microscopy (AFM), magnetic force microscopy (MFM), supporting imaging techniques, and micromagnetic simulations. The process of producing three-dimensional magnetic nanostructures using TPL and thermal evaporation to construct the structures that were the research subject for this thesis, is demonstrated. Both scanning electron microscopy (SEM) and atomic force microscopy (AFM) are explained in detail. The logic behind utilising magnetic force microscopy to determine contrast from the ferromagnetic arrays is described. Finally, micromagnetic simulations are discussed. The theory behind how the packages work and why these packages were chosen for the research is detailed.

In chapter 4, we detail a methodology to produce well-known planar ferromagnetic systems using TPL and evaporation. This is carried out by producing cylindrical geometries and placing a $Ni_{81}Fe_{19}$ layer on the top surface. It was shown that it is possible to create well-known spin textures via this method with MFM contrast matching the literature. Finally, we make a proof-of-principle structure to show that a 3D hemispherical defect can be placed upon the disk surface and the resulting spin texture is measured using MFM. Experimental observations are supported with micromagnetic simulations that show general agreement. A key disadvantage of the circular geometry is that MFM contrast can only be seen in the centre, making the impact of perturbations more difficult to interpret.

In chapter 5, TPL was used to construct 2D arrays of cuboidal structures with side length of 2 μm and height of 5 μm. A 40 nm layer of $\mathrm{Ni}_{81}\,\mathrm{Fe}_{19}$ was deposited on the structures. The result is a 2D array of ferromagnetic squares elevated above the substrate. Square geometries of these dimensions take on a typical Landau configuration with four domain walls that can easily be discerned using MFM. After demonstrating that it was possible to reproduce spin configurations seen in the literature, arrays of squares within the high magnetostatic (MS) coupled array were fabricated with a 3D hemispherical defect on the surface, of diameter 600 nm. The 3D defect was shown to pin the domain wall in one of two ways, depending upon the chirality of the vortex structure.

Chapter 6 presents a preliminary investigation into ferromagnetic pyramid structures in order to pave the way for a future student. Proof-of-principle is shown with respect to the fabrication of pyramid structures with dimensions of 2 μm. We move onto show that the pyramid structure takes on a complex multidomain configuration.

2. Chapter 2

Background theory

2.1 Introduction

This chapter provides a brief description of the essential ideas and basic theory which is necessary to set the stage for the research carried out in the subsequent chapters. The physics of ferromagnetism will be explored, and the phenomenon of two-photon polymerisation will be explained within the context of research within this thesis. In addition, relevant literature is examined including observable spin textures in nanostructured 2D elements, with an emphasis upon geometries that harbour a vortex state. Finally, the new and emerging field of 3D nanomagnetism is outlined and an initial vision for the research in this thesis described.

2.2 Background

2.2.1 Magnetic field

Magnetic fields are produced by moving charges. All atoms have electromagnetic properties at the atomic level due to the electrons that orbit the atom's nucleus producing a magnetic field that is perpendicular to the electron’s orbital plane. In addition, quantum electrodynamics shows that electrons possess an intrinsic angular momentum known as spin (S), also yielding a magnetic moment (See section 2.4.2). In general, it is the sum of the orbital and spin components of angular momentum that dictate the magnetic behaviour of a solid. In section 2.4.1, it will be seen that a simple hydrogen molecule model, within the framework of quantum mechanics can yield ferromagnetic behaviour whereby spins on adjacent atoms have parallel alignment. Taking a single electrical wire of infinite extent, one can start to understand the concept of magnetic field. For an infinite wire carrying a current i, applying Ampere’s law to a closed circular path of radius a gives:

$$\int_{closed\ path} \boldsymbol{H}.dl = 2\pi a\boldsymbol{H} = i \tag{2.1}$$

This yields the magnetic field (**H**), that is generated in free space. The unit of **H** is clearly A/m. A second magnetic vector field is defined and is known as the magnetic induction, also known as the magnetic flux density and is denoted with the symbol **B**. This second vector field can be thought as the response of a medium to a magnetic field, **H**. For the case of free space, **B** and **H** are just scaled versions of one another [36]:

$$\boldsymbol{B} = \mu_0\boldsymbol{H} \tag{2.2}$$

Here, μ_0 represents the permeability of free space, with value $4\pi \times 10^{-7}\ H/m$.

2.2.2 Magnetic moment

The most fundamental building block of magnetism is known as the magnetic moment. To gain an understanding of these entities, it is possible to use two models: a magnetic dipole model and a one-turn current loop. First, we look at the magnetic dipole model which has parallels with electrostatics. In this scenario, a magnetic moment, denoted by the symbol $\boldsymbol{m}$, is envisioned as having two poles, each of which has an equal but opposing pole strength characterised by the symbols $+p$ and $-p$, respectively. The magnetic moment is determined by the pole strength and the distance (l) between the poles (see Fig. 2.1); the magnitude of this variable is as follows:

$$|\boldsymbol{m}| = pl \tag{2.3}$$

Therefore, the pole strength is denoted by the units [Am], while the magnetic moment has units Am^2.

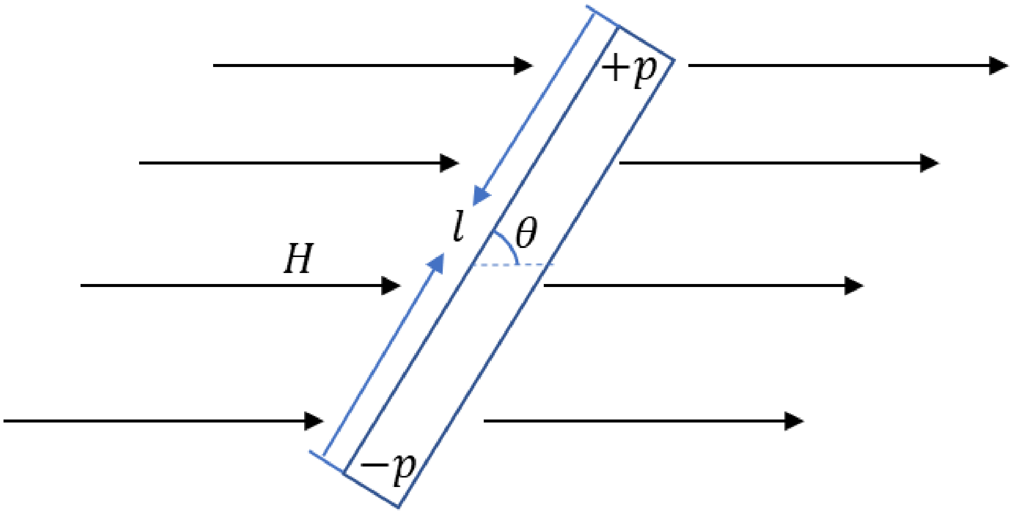

Figure 2.1: Two poles of a magnetic dipole separated by a distance l, in an external magnetic field $\boldsymbol{H}$ with an angle θ to the dipole axis [36].

In a one-turn current loop scenario, a magnetic moment is produced as a result of a current (I) moving around an enclosed region denoted by A (see Fig. 2.2). This magnetic moment is then defined as:

$$|\boldsymbol{m}| = IA \tag{2.4}$$

The moment is oriented in a perpendicular direction to the plane of charge motion and has an orientation that can be characterised using the right-hand rule. Though conceptually different, the two approaches in defining a magnetic moment can be shown to be equivalent [36].

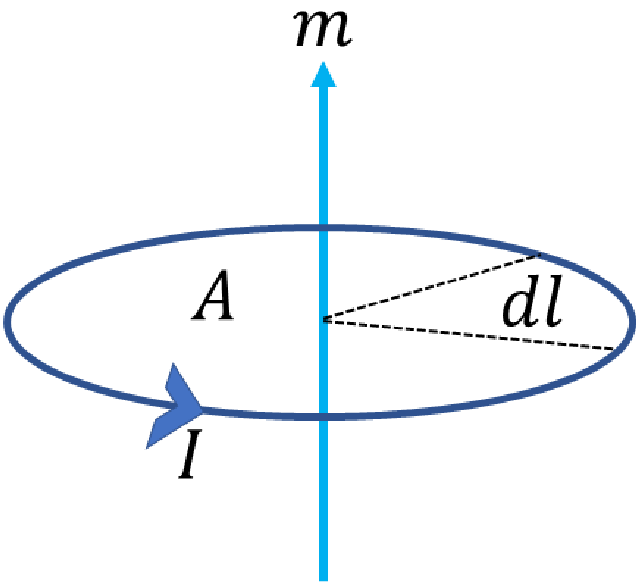

Figure 2.2: One-turn current loop with a magnetic moment generated perpendicular to the current flow.

2.3 Magnetisation

Magnetic moments are often too small when trying to describe the microscopic behaviour of materials. For this reason, it is convenient to define a further vector field known as magnetization as the magnetic moment that occurs per unit volume of material.

$$\boldsymbol{M} = \frac{\sum_i \boldsymbol{m}_i}{V} \tag{2.5}$$

Equation 2.2 can then be written in its most general form:

$$\boldsymbol{B} = \mu_0(\boldsymbol{H} + \boldsymbol{M}) \tag{2.6}$$

Considering that a material can possess a finite magnetisation.

2.4 Types of magnetism

Magnetic materials are classified into five main types which are named diamagnetism, paramagnetism, ferromagnetism, ferrimagnetism and antiferromagnetism [36]. The magnetic susceptibility (χ) is a quantitative means to classify magnetic materials and is defined as:

$$\chi = \frac{|\boldsymbol{M}|}{|\boldsymbol{H}|} \tag{2.7}$$

Where $\boldsymbol{M}$ is the magnetisation and $\boldsymbol{H}$ is the external field. We now explore each type of magnetism.

2.4.1 Diamagnetism

Diamagnetic materials have only a weak response to an applied magnetic field. Diamagnetic behaviour is present in all materials. When an external field is applied, electron orbits undergo a process that causes them to precess about the field direction in a way that causes them to act in opposition to the field. This results in a small negative susceptibility [36].

2.4.2 Spin angular momentum

Electrons also possess an intrinsic angular momentum known as spin. One can define a spin quantum number (s), which for Fermions takes half integer values and for Boson's integer values. For an electron s=1/2. We can then define a wavefunction that is associated with spin, (s) which satisfies:

$$S^2\chi = \hbar^2 s(s+1)\chi \tag{2.8}$$

$$S_z\chi = \hbar m_s\chi \tag{2.9}$$

Where m_s can take values between +s to -s. We therefore see from equation 2.9 that measurement of an electron's spin angular momentum component along the field direction will yield $\hbar m_s = \pm\hbar/2$.

By analogy with conventional angular momentum and from equation 2.8, we can define the total spin angular momentum as followed:

$$S = \sqrt{s(s+1)}\hbar \tag{2.10}$$

The magnitude of an electron spin magnetic moment along the quantisation axis can be written as

$$|m_s| = g_s \frac{e}{2m_e}\sqrt{s(s+1)}\hbar = 2\mu_B\sqrt{s(s+1)}\ \sqrt{3}\mu_B \tag{2.11}$$

Where g_s is a dimensionless factor (or the electron g-factor), m_e is the electron mass and μ_B is the Bohr magneton. The two orientations of spin angular momentum of an electron, +1/2 and -1/2, are commonly denoted as spin-up and spin-down. In most atomic orbitals the electrons are found in pairs, yielding an effective cancellation of the spin magnetic moment, and leaving only an orbital contribution. In instances involving atoms and molecules with an uneven number of electrons, eliminating the spin moment is unattainable, thereby classifying them as paramagnetic.

2.4.3 Paramagnetism

In conventional metals, electronic shells consist of paired electrons each with opposing spin and therefore do not possess a spin magnetic moment. Paramagnetic materials have atomic shells with unpaired electrons, uncompensated spins and hence display an effective spin magnetic moment. However, since dipolar interactions between neighbouring atoms are insignificant when compared to thermal energy, the direction of each atomic magnetic moment is effectively random yielding a net zero magnetisation. The application of a magnetic field causes atomic moments to start aligning into the direction of the field with an increasing number of moments rotating to lie along the field direction as the field increases [36].

2.4.4 Ferromagnetism

A ferromagnet is a material where the magnetic moments of neighbouring atoms have a tendency to align, allowing the development of a spontaneous magnetisation. This vanishes above the Curie temperature T_c.

The extent to which a magnetic field produces a magnetisation can also be quantified using the permeability μ of a material:

$$B = \mu M \tag{2.12}$$

Where the relative permeability is often more convenient to utilise:

$$\mu_r = \frac{\mu}{\mu_0} \tag{2.13}$$

Overall, the susceptibility and relative permeability are just different ways of describing the response of material to an external field. One can relate the two quantities using:

$$\mu_r = \frac{\mu}{\mu_0}(1 + \chi_m) \tag{2.14}$$

Ferromagnetic elements typically have relative permeabilities of order 10^4 or above. In order to explain the ordering within a ferromagnet we now explore the relevant micromagnetic energies.

2.5 Micromagnetic energies

The magnetisation configuration of a magnetic material is governed by micro-magnetic energies. The total magnetic free energy of a material depends on the magnitude of the exchange, magnetostatic, magnetocrystalline anisotropy and Zeeman energies. We now outline these one at a time.

2.5.1 Exchange energy

The exchange energy is a short-range interaction that yields preferential parallel or anti-parallel alignment of atomic spins. In general, the exchange interaction is a complex many-body phenomenon but it can be understood simply by using the H_2^+ hydrogen molecule to represent a model system. The hydrogen molecule is depicted in Fig. 2.3 [37]:

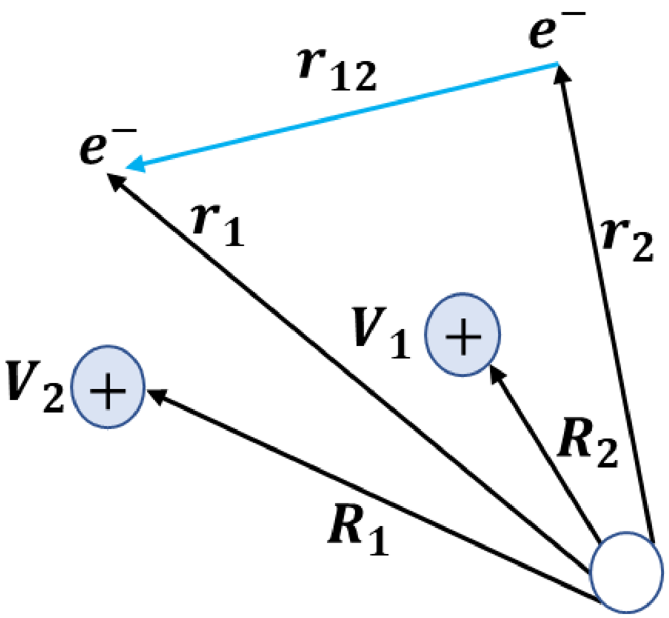

Figure 2.3: Illustration of the hydrogen molecule (1 and 2) which each possess one electron (i and j) [37].

Here, the system’s Hamiltonian is given as [37]:

$$\hat{H} = -\frac{\hbar^2}{2m}\nabla_1^2 + -\frac{\hbar^2}{2m}\nabla_2^2 + V(1) + V(2) + \frac{e^2}{4\pi\varepsilon_0 r_{12}} \qquad (2.15)$$

Where subscripts 1 and 2 denotes the electrons with distinct spatial coordinates; V(N) denotes the Coulomb interaction between electron N and the nuclei at R_1 and R_2. In the absence of an electron-electron interaction (ie. no e^2 term in equation 2.15), we would simply have two Schrodinger equations, one for each electron and this would yield wavefunctions:

$$\Psi^0 = \emptyset_i(1)\emptyset_j(2) \qquad (2.16)$$

Here $\emptyset_i(1)$ means that electron 1 is in state i. The energies can then be written:

$$E^0 = E^{(i)} + E^{(j)} \qquad (2.17)$$

The spatial wavefunction that characterises the two electrons for a pair of atoms may either be symmetric (shown in Figure 2.4a) or antisymmetric (shown in Figure 2.4b) with regard to the exchange of indistinguishable electrons. For symmetric these can be written as:

$$\Psi^{+} = \emptyset_i(1)\emptyset_j(2) + \emptyset_i(2)\emptyset_j(1) \tag{2.18}$$

$$\Psi^{+} = \emptyset_i(1)\emptyset_i(2) \tag{2.19}$$

$$\Psi^{+} = \emptyset_j(1)\emptyset_j(2) \tag{2.20}$$

Forfor antisymmetric it can be written as:

$$\Psi^{-} = \emptyset_i(1)\emptyset_j(2) - \emptyset_i(2)\emptyset_j(1) \tag{2.21}$$

The respective wavefunction for the electron spin may also be either symmetric or antisymmetric similar to the spatial variants. For symmetric they can be written as:

$$\chi = \chi_{+}(1)\chi_{-}(2) + \chi_{+}(2)\chi_{-}(1) \tag{2.22}$$

$$\chi = \chi_{+}(1)\chi_{+}(2) \tag{2.23}$$

$$\chi = \chi_{-}(1)\chi_{-}(2) \tag{2.24}$$

And for antisymmetric can be written as:

$$\chi = \chi_{+}(1)\chi_{-}(2) - \chi_{+}(2)\chi_{-}(1) \tag{2.25}$$

In this scenario, for instance, "electron 2 in a spin-up state" is denoted by the symbol $\chi_{+}(2)$. The spin wavefunctions that correlate to antiparallel spin electrons are called singlet states. This is because they have total spin 0 and the number of states, 2S+1, is equal to 1. Specifically, this is true for Eq. 2.25. Triplet states are the names given to spin wavefunctions with parallel electron spins. This is due to the fact that S = 1 and 2S+1 = 3. Equations 2.22 – 2.24 fall within this category.

The Pauli exclusion principle tells us that the wavefunctions of two fermions that are identical must be antisymmetric with respect to exchange of spatial and spin coordinates. The wavefunction for the electron spin may be either symmetric (with spins parallel to one another) or antisymmetric (with spins opposite to one another). Still, in either case, the space portion of the wavefunction must be the opposite. The total normalised singlet and triplet wavefunctions can then be written as:

$$\Psi_S = \left(\frac{1}{2}\right)^{1/2} \left[\emptyset_i(1)\emptyset_j(2) + \emptyset_i(2)\emptyset_j(1)\right]\chi_S \tag{2.26}$$

$$\Psi_S = \left(\frac{1}{2}\right)^{1/2} \left[\emptyset_i(1)\emptyset_j(2) - \emptyset_i(2)\emptyset_j(1)\right]\chi_T \tag{2.27}$$

The energies of these states can then be written as:

$$E_S = \int \Psi_S^* \, \hat{H} \, \Psi_S dr_1 dr_2 \tag{2.28}$$

$$E_T = \int \Psi_T^* \, \hat{H} \, \Psi_T dr_1 dr_2 \tag{2.29}$$

The exchange energy is defined as being the difference in energy between two electrons being parallel and two electrons being anti-parallel:

$$j = E_S - E_T \tag{2.30}$$

In order to illustrate the manifestation of the exchange interaction, we will use the hydrogen molecule H_2 as a basic example. In this system, each hydrogen atom possesses one electron in its 1s orbital. Upon solving of the Schrodinger equation, two different molecular orbits are found, with wavefunctions shown in Fig. 2.4a. One of these orbits is a bonding orbital that is spatially symmetric and has a high likelihood of having the two electrons located in close proximity to one another. The other orbital is an antibonding state and spatially antisymmetric (Figure 2.4b). The likelihood of finding electrons close together in this orbital is effectively zero.

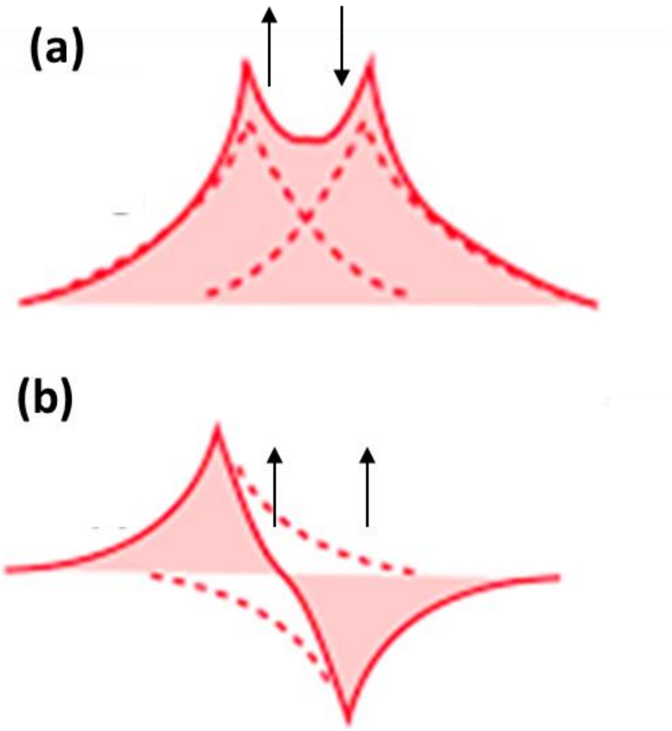

Figure 2.4: (a) Spatially symmetric wavefunction and (b) asymmetric wavefunction for H_2 molecule [36].

Considering the symmetric spatial wavefunction, the Pauli exclusion principle forces the close electrons to exist inside the bonding orbital with antiparallel spins. Similarly, the antisymmetric spatial wavefunction has to be multiplied by the symmetric spin wavefunction, which corresponds to a singlet state with a total spin equal to 1 (S=1). For this reason, anti-bonding orbitals are populated by electrons with parallel spins. This paints a general picture of the exchange interaction. Dirac was the first to obtain an equation for the energy transfer in terms of the underlying spins, and Heisenberg went on to extend this [1]:

$$E_{ex} = -2\sum_{i<j} J_{ij}\, S_i . S_j \tag{2.31}$$

Where J denotes the exchange integral, J > 0 is used for a ferromagnet, and $J < 0$ is used for an antiferromagnet. S_i and S_j, denote the relevant Pauli matrices [1].

Equation 2.31 can be rewritten in a more useful form within a continuum framework:

$$E_{ex} = -2\sum_{i>j} J_{ij} S^2 \cos\theta_{ij} = A\left(\frac{\partial\theta_{ij}}{\partial x_{ij}}\right)^2 \rightarrow A\left(\frac{\nabla M}{M}\right)^2 \qquad (2.32)$$

Where θ_{ij} is the angle between the direction of the spins, and A denotes the exchange stiffness constant (units J/m). The exchange takes the form of a short-range interaction. To contribute to the exchange integral J, it is necessary for the electron wave functions to have sufficient overlap.

2.5.2 Magnetostatic energy

This energy which is referred to as either the dipolar or the magnetostatic energy E_{ms} is a consequence of the mutual Zeeman energy created by all the moments inside a magnetic body through the stray field [37]. The magnetostatic energy is minimised by producing magnetisation configurations yielding flux closure. When a body does not show flux-closure, a divergence of $\boldsymbol{M}$ develops where the magnetization meets a boundary. Applying Maxwell's second equation for the divergence of **B**, and coupling this with eq. (2.6) yields [37]:

$$\boldsymbol{\nabla} . \boldsymbol{H} = -\boldsymbol{\nabla} . \boldsymbol{M} \qquad (2.33)$$

This demonstrates that the divergence of $\boldsymbol{M}$ gives rise to an $\boldsymbol{H}$ field which opposes the magnetization, as illustrated in Fig. 2.5. Inside a magnetic material, this is known as the demagnetising field.

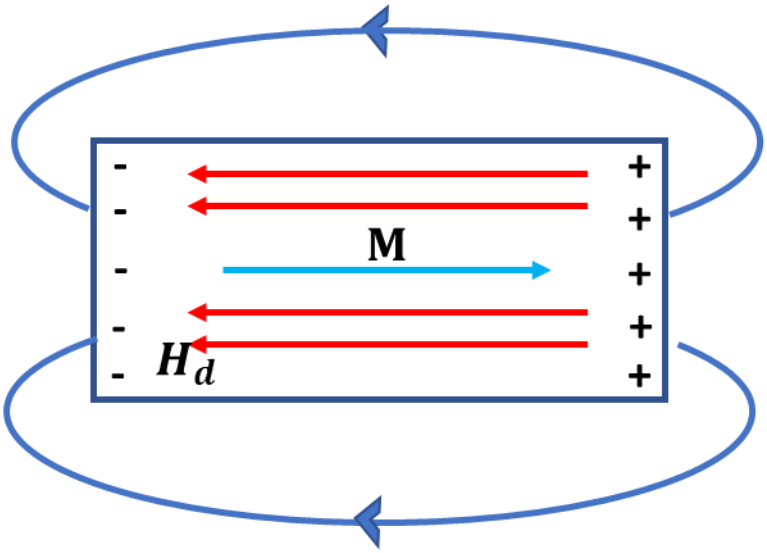

Figure 2.5: Schematic of a ferromagnetic body, with all moments aligned along the long axis. Magnetic poles form at either end of the long axis where the sample magnetisation encounters a boundary, a demagnetising field is generated which opposes the magnetisation. At these boundaries, stray magnetic fields emanate from the body.

This demagnetizing field is very reliant on the number and spacing of these magnetic poles, and as a result, it is highly dependent on the geometry of the sample. For instance, the gap between the positive and negative poles in Fig. 2.5 would be greatly narrowed if the magnetization aligned itself along the short axis. Additionally, the magnetization would cross a much wider region at the borders, resulting in the formation of many additional poles. This greater energy situation would result in a much stronger $\boldsymbol{H}_d$, indicating that the magnetization would normally preferentially align to the long axis. As a result, the demagnetising field is the root of the first anisotropy term discussed in this thesis, shape anisotropy. In its most basic form, anisotropy manifests itself as the presence of preferred axes along which the magnetization of the sample may align. In general, the magnitude of $\boldsymbol{H}_d$ increases proportionally with increasing $\boldsymbol{M}$, hence:

$$\boldsymbol{H}_d \propto -\boldsymbol{M} \tag{2.34}$$

However, here the constant of proportionality strongly depends on the sample geometry. Therefore, to write a generalised expression for $\boldsymbol{H}_d$we include a demagnetising tensor $\mathcal{N}$:

$$\boldsymbol{H_d} = -\mathcal{N}\boldsymbol{M} \tag{2.35}$$

A rudimentary example is an ellipsoid for which the demagnetising field is uniform, as yielding a diagonal tensor:

$$\boldsymbol{\mathcal{N}} = \begin{pmatrix} \mathcal{N}_x & 0 & 0 \\ 0 & \mathcal{N}_y & 0 \\ 0 & 0 & \mathcal{N}_z \end{pmatrix} \tag{2.36}$$

Where the components $\mathcal{N}_x$, $\mathcal{N}_y$ and $\mathcal{N}_z$ each describe one of three principal orthogonal axes. The diagonal components $\mathcal{N}_x$, $\mathcal{N}_y$, and $\mathcal{N}_z$ all add up to a total of 1. Therefore, an infinite sheet along the x and y directions would yield $\mathcal{N}_x = \mathcal{N}_y = 0$ and $\mathcal{N}_z = 1$, depending on whether it was magnetized in-plane or out-of-plane, respectively [37]. For an infinitely extending cylinder with long axis along x, the demagnetising factors are $\mathcal{N}_x = 0$ and $\mathcal{N}_y = \mathcal{N}_z = 0.5$, respectively. The magnetostatic energy density of a sample can now conveniently be written in terms of the demagnetising factor:

$$E_{ms} = \frac{\mu_0}{2}\ \mathcal{N} M_S^2 \tag{2.37}$$

Where M_S is the saturation magnetisation.

2.5.3 Magnetocrystalline anisotropy energy

The spin-orbit interaction relates the electron spin to anisotropic orbitals in a crystalline structure. An electric potential created by the crystal ions couples to the spins [36]. This yields an anisotropy term, whereby the magnetisation has preferential alignment along specific crystallographic axes. The minimum energy axis is known as the easy axis. If a uniaxial magnetic anisotropy is exhibited the anisotropy energy density is expressed as [38]:

$$E_a = k_2 sin^2\theta + k_4 sin^4\theta + \cdots \tag{2.38}$$

Where θ is the angle between the easy axis and the magnetisation, and k_2 and $k_4$are the anisotropy constants. The following refers to the anisotropy energy for cubic materials [4]:

$$E_a = k_1({\alpha^2}_1{\alpha^2}_2 + {\alpha^2}_2{\alpha^2}_3 + {\alpha^2}_3{\alpha^2}_1) + k_2{\alpha^2}_1{\alpha^2}_2{\alpha^2}_3 + \cdots \tag{2.39}$$

Where alpha symbols are the directional cosines of the magnetisation vector. The material systems studied in this thesis, $Ni_{81}Fe_{19}$, have negligible magnetocrystallIne anisotropy.

2.5.4 Zeeman energy

The Zeeman energy refers to the potential energy of a magnetic moment in a magnetic field. Commonly, for a great number of moments, the potential energy per unit volume is as follows [38]:

$$E_{zeeman} = -M.B \tag{2.40}$$

This shows that an energy minimum occurs when the magnetisation is aligned with the applied magnetic field.

2.6 Domains and domain walls

After analysing the essential energy components of ferromagnetism, the next step is to investigate the effects of these interactions competing with one another in ferromagnetic systems. To restate, the current study exclusively considers $Ni_{81}Fe_{19}$ structures which means that the impact of magneto crystalline anisotropy is neglected. Therefore, in the absence of an external field and any strain effects, thought is given to the competition between E_{ms} (which is minimised when the spin texture yields flux-closure) and E_{ex} (which is minimised when nearby spins are aligned). Clearly, a ferromagnetic system with all spins parallel will minimise the exchange energy but come at a high magnetostatic cost. In systems studied within this thesis, which are on the micron scale, the magnetostatic energy cost is important, and this yields the formation of regions whereby the magnetisation points in a fixed direction. These regions are known as domains. Fig. 2.6 illustrates the concept of domains, where the magnetostatic energy becomes a considerable contributor to the total energy of the material if all the spins are aligned in the same direction, as seen in Figure 2.6(a). When domains are now aligned antiparallel to one another, the total magnetostatic energy is lowered (see Fig. 2.6b), and the fields from each mostly cancel. When multiple domains are considered, the material can create complete flux closure, completely minimising the magnetostatic energy (see Fig. 2.6c).

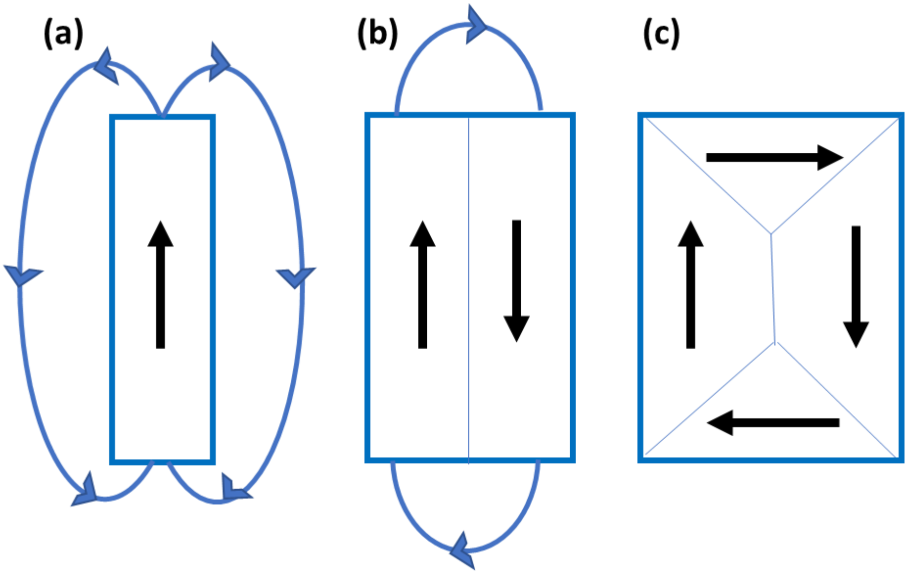

Figure 2.6: Introducing the concept of domains. (a) Single domain, (b) partial closed loop by two anti-parallel domains, (c) complete flux closure from four orthogonal domains, minimising the demagnetisation energy.

In many illustrations such as Figure 2.6, regions between domains, known as domain walls (DWs), are shown as having sharp borders which make a sudden transition between the magnetisation directions. However, if this transformation were to take place in the real world, it would cost significant exchange energy. Instead, this rotation takes place gradually throughout a large number of spins. Figure 2.7 presents two different potential configurations of DWs in thin films. The transition of 180 degrees is facilitated by a Bloch wall (see Fig. 2.7a) where spins gradually rotate out-of-plane, whereas a Néel wall rotates in-plane in the plane (see Fig. 2.7b).

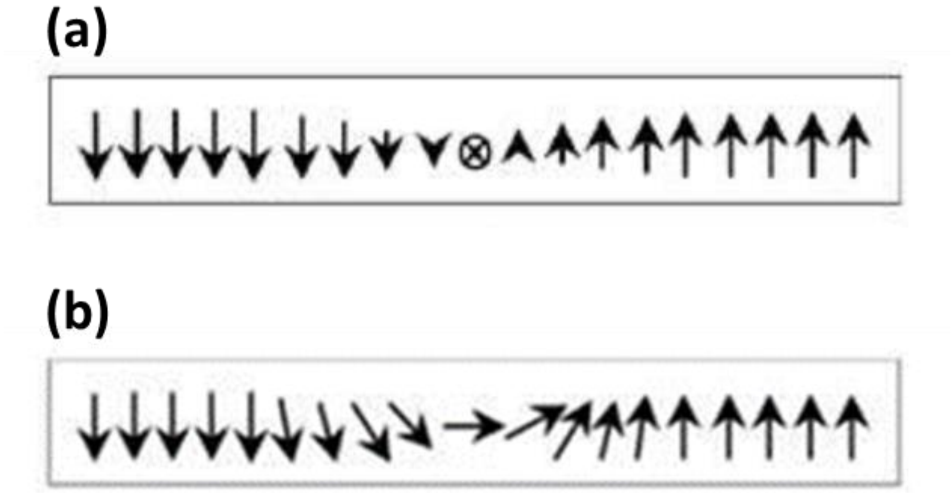

Figure 2.7: Two domain wall spin textures: (a) Bloch wall and (b) Néel wall in a bulk ferromagnet [39].

The two walls are expected to have equivalent exchange energies, but the magnetostatic energy will depend upon sample dimensions. For example, Bloch walls have an advantage from an energy perspective in thick films, whereas Néel walls are the favoured configuration in thin films.

To better grasp this geometric dependence, the case shown in Figure 2.8 is investigated in which DWs are made up of a uniform magnetisation aligned parallel to the transverse components of Bloch walls and Néel walls, respectively. Due to the DW magnetisation, both of these cases result in the formation of magnetic poles on opposing boundaries. In Figure 2.8(a), the number of poles does not change irrespective of what the domain wall thickness (δ_t) is, although the distance between the poles increases as δ_t

becomes higher. Despite the distance between the pole in Néel walls (see Fig.2.8b) being unaffected by δ_t, the number of poles produced at the DW borders increases as δ_t increases, which leads to an increase in E_{ms}. Because of the comparatively high E_{ms} of Bloch walls, thinner films favour Néel walls. However, in films where $\delta_t >> \delta_W$, this E_{ms} approaches zero, so Bloch walls are preferred [36]. Where δ_t and δ_W denote the domain wall thickness and width, respectively.

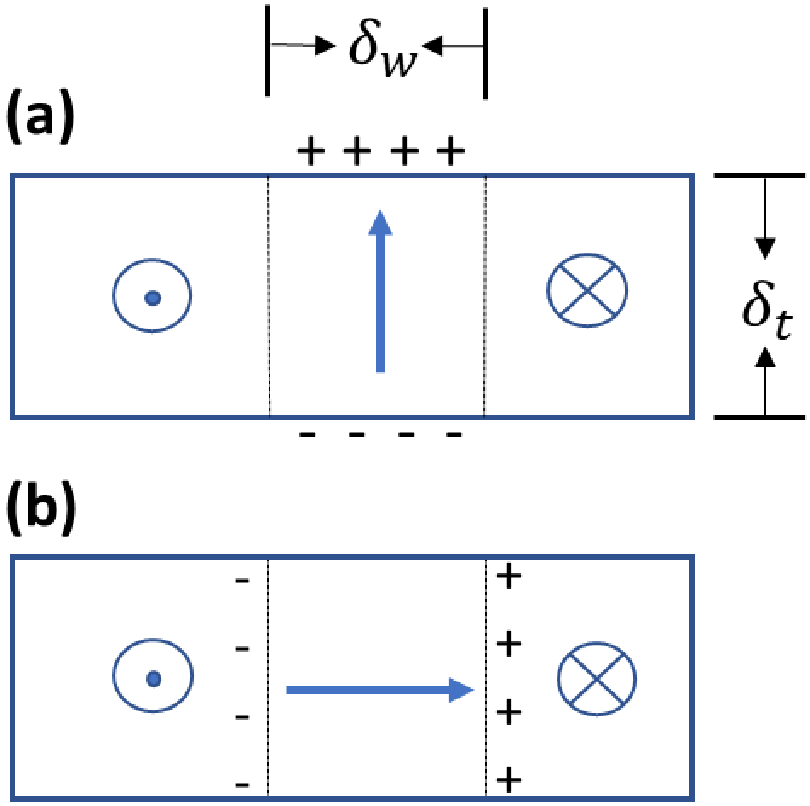

Figure 2.8: Schematic representation of magnetic poles generated by (a) Bloch wall and (b) Néel wall.

2.7 Curvature

Every illustration of DWs presented up to this point has focused on planar nano-element systems. Structures with extra energy terms, such as bent wires in two dimensions, helices in three dimensions, or shells, may give rise to unique exchange-driven behaviour. Around the middle of the 20th century, a phenomenon referred to as the Dzyaloshinskii-Moriya interaction (DMI) was identified as an additional contributor to the exchange of energy [20]. This makes it more likely for canting to occur between neighbouring spins that would otherwise be parallel. Because of this, many people also refer to this phenomenon as an asymmetric exchange interaction. Moriya discovered that this effect occurs in materials that do not show inversion symmetry and have a high spin-orbit coupling. In these cases, the DMI-related energy density E_{DM} is given by [20]:

$$E_{DM} = \sum_{ij} d_{ij} \,.\, (S_i \; x \; S_j) \tag{2.41}$$

The vector representing the DMI between atoms i and j is denoted by d_{ij}in this equation; the direction of this vector changes depending on the kind of system being considered. In curved geometries, we consider an effective-DMI, which originates from the conflict between exchange and demagnetizing energies, yielding a canting of neighbouring spins inside a single domain body. Considering a curved, single domain system, if one were to be too simplistic and examine E_{ms}, one may intuitively anticipate that the spins seen here would align themselves along the arc of curvature in order to reduce the amount of stray magnetic fields. On the other hand, $E_{ex}$is minimized when spins are aligned parallel to one another. Due to these conflicting energy terms, spins will deviate out of the plane by an angle, θ an effect that is not seen in similar planar entities.

Another curvature-induced addition to the exchange energy is an effective anisotropy, acting like a scalar geometrical potential, the exact effect is highly dependent upon the geometry of the system [20]. Due to this, we can update the equation for exchange energy such that it includes the following two additional terms [20]:

$$E_{DM} = E_{ex} + E_{EDM} + E_A \tag{2.42}$$

Where E_{ex} denotes standard isotropic exchange, E_{EDM} denotes the effective DMI and E_A denotes the effective anisotropy. These curvature-induced energy components have several different ramifications in the actual world, ranging from the violation of chiral symmetry to very high DW velocities.

2.8 Hysteresis

Hysteresis is a property displayed by ferromagnetic materials and it is perhaps one of the most well-known features. This phenomenon requires that the magnetic configuration of a substance is dependent not only on the current circumstances (external fields, shape anisotropy, temperature, etc.) but also upon the magnetic history of the body [36]. Figure 2.9 presents a typical example of a hysteresis loop which is often used to illustrate this behaviour. This response provides significant insight into the characteristics of magnetic materials and is a popular approach for measuring their physical behaviour.

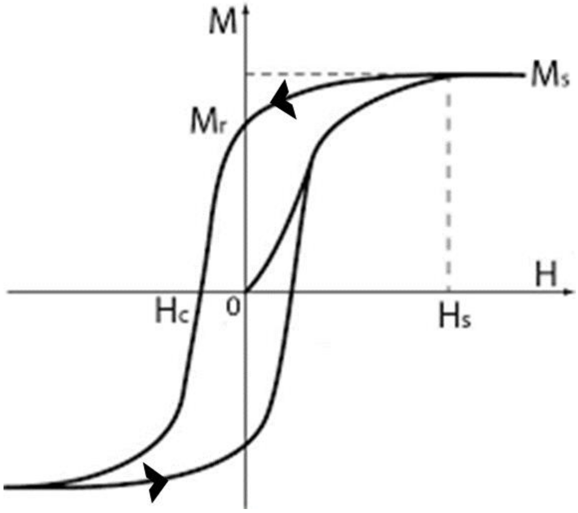

Figure 2.9: Typical example of a ferromagnetic hysteresis loop: magnetisation $\boldsymbol{M}$ vs magnetic field strength $\boldsymbol{H}$ [40].

Typically, a sample magnetisation is zero before being subjected to any significant external fields. This is because the internal domains develop a configuration that inhibits the formation of free magnetic poles and maintains a net zero magnetisation. As soon as an external field is applied, domain walls are displaced in such a way to increase the volume of the domains with the largest components of **M** along **H**. When domain wall motion is no longer possible, due to defects or boundaries, higher energy processes such as rotation continue to increase the magnetisation until saturation is reached. As the field is decreased, the magnetisation first starts to rotate back into their local energy minimum. Since domain wall motion causes energy to be lost and is an irreversible process, it leads to the M-H curve opening, exhibiting hysteresis. This also tends to result in a remanent magnetisation $\mathrm{M_r}$ for the material when the external field is reduced to zero. Thus, a property of ferromagnetic materials is that the magnetic configuration can not only be easily influenced but also be preserved following the removal of an external field. This quality makes ferromagnetic materials appealing for a wide variety of applications involving data storage. After an initial magnetisation has occurred, it is necessary to apply an opposing external field to the sample to bring its magnetisation back to zero. The exact magnitude of this field, known as the coercive field is an inherent property of the material [37]. The coercive field is an essential component to determine how the sample can be magnetised and demagnetised and is one characteristic that distinguishes soft magnets from hard magnets among ferromagnetic materials. In contrast to hard ferromagnets, soft materials often have low hysteresis and H_c, in addition to high, μ and $\boldsymbol{\chi}$, and as a result, they are comparatively easy to magnetise. The only kind of magnetic materials considered in the current study are soft ferromagnets.

2.9 Landau–Lifshitz equation

The Landau-Lifshitz (LL) equation [41] describes the dynamics of the magnetisation that is subject to an effective magnetic field H_{eff}:

$$\frac{dM}{dt} = -\gamma M \times H_{eff} + \left(\frac{\alpha_D}{M_s}\right)\left(M \times M \times H_{eff}\right) \tag{2.43}$$

Where γ is the gyromagnetic ratio and $\alpha_D$is the damping constant. It is possible to obtain the first term using the spin commutator relations and the Ehrenfest theorem [42] corresponding to the precession of the magnetisation around the effective magnetic field. Since the term $M \times H_{eff}$ is conserved, the system energy remains unchanged. The rate of precession, also known as the Larmor frequency, is proportional to the field strength $|H_{eff}|$ with the gyromagnetic ratio γ serving as the proportionality factor.

$$\omega = \gamma \left|H_{eff}\right| \tag{2.44}$$

As shown in Figure 2.10, the second component of the LL equation reflects phenomenologically the energy dissipation that occurs owing to Faucoult currents, spin-phonon scattering and other phenomena [43]. This results in the relaxation of the magnetisation $\boldsymbol{M}$ in the direction of the effective field $\boldsymbol{H_{eff}}$, The amount of damping that occurs is determined by a phenomenological parameter denoted α_D.

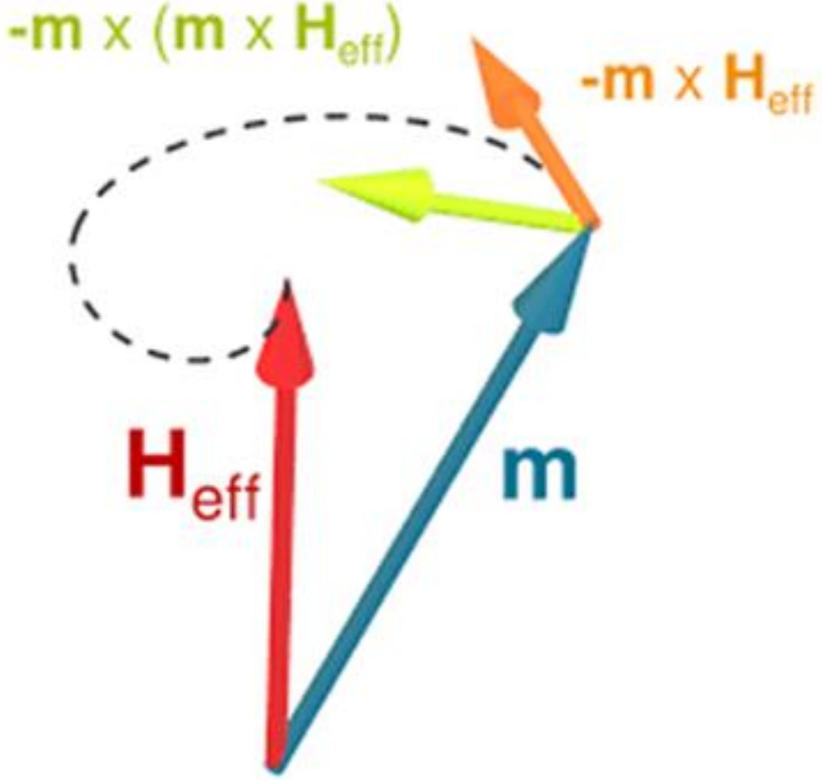

Figure 2.10: The terms in the Landau-Lifshitz-Gilbert equation: orange arrow denotes the precessional component, whilst green indicates damping term [44]

Gilbert proposed a viscose damping term that was somewhat different [45]:

$$\frac{dm}{dt} = -|\gamma_P| M \times H_{eff} + \left(\frac{\alpha_{LLG}}{M_s}\right)\left(M \times \frac{dm}{dt}\right) \tag{2.45}$$

It is possible to convert the implicit Gilbert equation (2.45) into the explicit Landau-Lifshitz-Gilbert (LLG) equation [45]:

$$\frac{dM}{dt} = -\frac{\gamma}{1+\alpha_{LLG}^2} M \times H_{eff} - \left(\frac{\gamma\alpha_{LLG}}{1+\alpha_{LLG}^2}\right)\frac{1}{M_s} M\left(M \times H_{eff}\right) \tag{2.46}$$

With $\gamma' = \gamma/1 + \alpha_{LLG}^2$ and $\alpha = \gamma\alpha_{LLG}/1 + \alpha_{LLG}^2$. It is important to note that the magnitude of magnetisation $|M|$ is preserved because the damping is always perpendicular to $\boldsymbol{M}$ and dm/dt. The LL equation (2.43) and the LLG equation (2.46) are identical from a mathematical standpoint. Still, their behaviour for large damping is somewhat distinct from one another from a physical perspective:

$$\frac{dm}{dt} \to \infty\,, for\ (\alpha_D \to \infty), \quad \frac{dm}{dt} \to 0, for\ (\alpha_{LLG} \to \infty) \tag{2.47}$$

In the case of the LL equation, this results in a divergence of the torque acting on the magnetisation for large values of damping. This demonstrates that the LLG equation provides a more accurate reflection of the actual magnetisation dynamics than the LL equation [43, 46].

2.10 Two photon lithography (TPL)

Two-photon lithography has been established in the last 20 years as a technique suitable for the direct laser writing of 3D microstructures. Interest in this technique has grown primarily because of the recent commercialisation of femtosecond laser systems. Furthermore, the non-linear optical properties of organic materials have increased in popularity because of the spiralling growth of photonics caused by the dramatic increase in optical communication systems [47]. There is a continual need for techniques that are able to fabricate intricate 3D microstructures for applications in 3D nanoelectronics, controlled propagation of light, lab-on-chip devices and ultra-high density data storage.

2.10.1 Theoretical background (TPA)

In single photon absorption a material responds linearly to an applied optical field. The polarisation **P** induced by the applied field is defined as follows [48]:

$$\boldsymbol{P}(\omega) = \varepsilon_0 \chi(\omega) \boldsymbol{E}(\omega) \qquad (2.48)$$

Where ω is the angular frequency, **E** is the electric component of the optical field, ε_0 is the permittivity of free space, and χ is the linear electrical susceptibility of the medium. The absorption coefficient α is proportional to the imaginary part of the susceptibility, as in the following:

$$\alpha(\omega) = \frac{\omega}{cn} \chi_{Im}(\omega) \qquad (2.49)$$

Here, n represents the refractive index of the medium [48]. The total light absorbed by a medium is proportional to the product of the medium absorption coefficient and light intensity. The intensity is proportional to the electric field's magnitude square. Hence, the light absorbed is proportional to $|E|^2 \chi_{Im}(\omega)$. The response of the medium to an applied field is not necessarily linear and, therefore, generally:

$$P = \varepsilon_0 (\chi^{(1)}\, E + \chi^{(2)}\, E.E + \chi^{(3)}\, E.E.E + \cdots) \qquad (2.50)$$

In this case, $\chi^{(n)}$ represents the nth order susceptibility. Evidently, the linear absorption rate of the medium is proportional to $E.P^{(1)}$, which is in turn proportional to light intensity. The two-photon absorption process depends on the square of the intensity. Hence, the rate of this process is proportional to $E.P^{(3)}$, involving four optical fields. Overall, the n-photon absorption rate is proportional to $E.P^{(2n-1)}$. Hence, an n-photon includes only nonlinear susceptibilities of odd order [48].

Overall, the addition of photons of n different frequencies is involved in an n-photon absorption process. Though nondegenerate processes are possible with different frequencies, typically, photons of a single frequency are used in the multiphoton fabrication process. This also simplifies fabrication set-ups since degenerate multiphoton absorption only requires a single laser beam.

The intermediate state is not physical in single photon absorption. As in the Raman transition, the first photon transits into a virtual state consisting of a combination of the far-off-resonance states of the atom or molecule. These states are not close to the resonance. Hence, the duration of the virtual state is very short. Accordingly, within approximately 1fs of the initial transition, the second transition takes place. Both photons need to be at the same place simultaneously for two-photon absorption to occur [48].

For fabrication, the critical element is the multiphoton absorption's nonlinear intensity dependence. If the excitation source is found in a small volume, absorption can be confined to three dimensions. The number of the photo-initiator molecules multiplied by the square of the intensity is proportional to the number of molecules in a transverse plane. Accordingly, the number of excited molecules is proportional to the transverse spatial intensity profile and inversely proportional to the beam area. Hence, excitation can be confined to the beam's focal region under appropriate intensity conditions. Initially, two-photon absorption with ultrafast lasers became popular as a tool for performing 3D fluorescence microscopy [48].

As presented in Figure 2.11, there are two types of TPA mechanism, namely sequential excitation and simultaneous excitation, in which the sequential represents the electronic transition through an intermediary phase to an excited energy phase. Subsequently, the electron which excited to the intermediary phase absorbs the other photon with equal energy and is accordingly pumped to another higher phase. In the next excitation, two photons are absorbed by the electron simultaneously in an instance to get to a higher state. No excited intermediate state is needed. The term TPA is usually used for simultaneous TPA. The virtual intermediary phase of the concurrent excitation lasts for a couple of femtoseconds. For the energy band-gap to be transcended, the absorption of two photons takes place concurrently in such a way that the virtual state decay is preceded by the second photon [49].

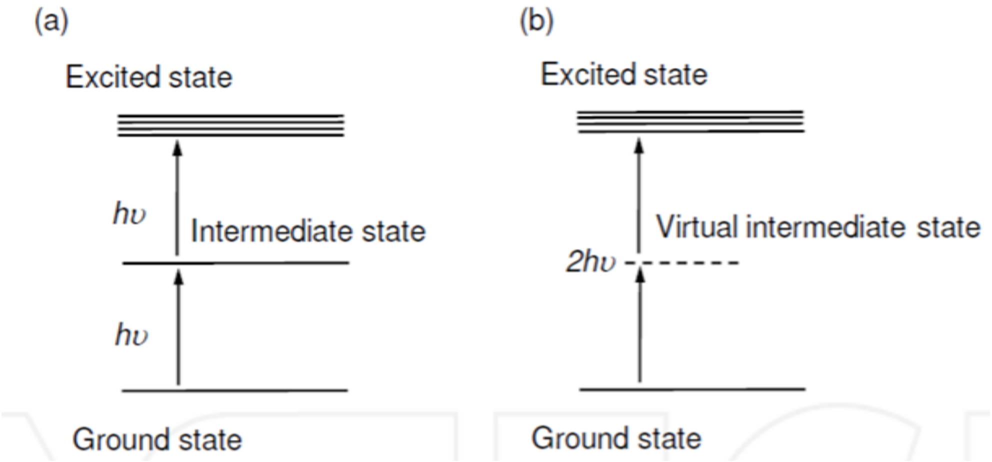

Figure 2.11: Two-photon absorption mechanism: (a) sequential two-photon absorption and (b) simultaneous absorption [49].

2.10.2 Photochemical reactions

The primary molecular components which compose photoresist materials are monomers/oligomers, photo-initiators and inhibitors. They account for 90% of the photoresist material composition. When they are bound in polymeric chains, these molecules can use the energy from a radiation source to polymerise (negative tone resist). When exposed to light, the polymerisation mechanism occurs on the basis of the chain propagation. There are three stages in this mechanism: initiation, propagation and termination. The first stage begins when the excited photoinitiators are generated because of the light generated active species such as cations and free radicals [50, 51]. Subsequently, the monomers interact with radicals, resulting in a new molecule with an active termination. The length of polymeric chains in the propagation stage increases until the active termination gets to a free radical or a terminating monomer reacts with an inhibiting molecule. The confinement of photochemical changes to submicron dimensions within the focal volume (3D voxel) are enabled by the quadratic dependence on laser intensity (see Fig. 2.12). There, the intensity of the laser surpasses a given TPA threshold value [51].

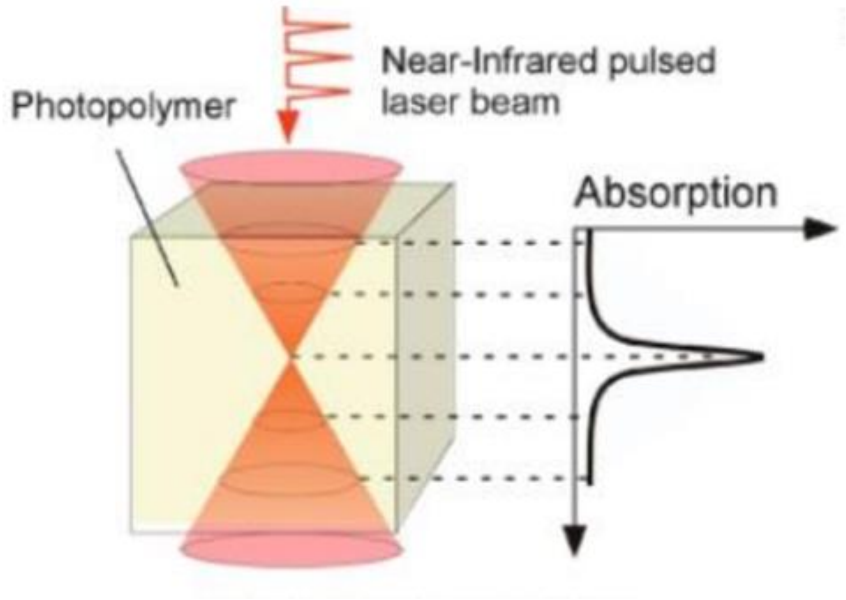

Figure 2.12: Schematic depiction of the optical path of a near-IR pulsed laser beam in a photoresist and the corresponding local absorption [52].

Due to the threshold behaviours of TPA, photochemical reactions begin at a lower volume than the diffraction-limit by regulating the laser and energy. To generate an appropriate starter species concentration through the process of TPA, an exceptionally high laser intensity is needed (see details in Section 4.3.1). An ultra-high femtosecond laser peak intensity created by an innovative pulse-compression system is used to induce two-photon absorption. The femtosecond laser pulse duration typically lasts for 100–200 fs, with 10 ns breaks between pulses. Hence, for the TPA it is possible to achieve a sufficient optical electric field. TPA begins when the laser pulses are focused by a high-NA objective lens.

The density of radicals, denoted by ρ_{rad}, which are produced by laser pulses and the intensity of the photon flux, denoted by $I_{\gamma}(r, z)$, at a location located r distance along the cross-section and z distance along the optical plane can be used to theorise how one might calculate the dimensions of a voxel. To begin, the following is an expression for the rate at which radicals are being produced [53]:

$$\frac{\partial \rho_{rad}}{\partial t} = (\rho_{init} - \rho_{rad})\sigma_2 I_\gamma^2 \tag{2.51}$$

Where ρ_{init} denotes the particle density of the main initiator and σ_2 denotes the two-photon cross-section, respectively. Finding the solution for ρ_{rad} using this equation gives:

$$\rho_{rad} = \rho_{init}\left[1 - \exp(-\sigma_2 I_\gamma^2 t)\right] \tag{2.52}$$

In the event that the laser intensity follows a Gaussian distribution, the variable I_γ may be expressed as:

$$I_\gamma(r, z) = I_{\gamma 0}\left[\frac{\omega_0^2}{\omega(z)^2}\right] exp\left[\frac{-2r^2}{\omega(z)^2}\right] \tag{2.53}$$

$I_{\gamma 0}$ is the intensity of the photon flux at the focus $(r = 0, z = 0), \omega_0$ is the waist of the beam. This determines the beam radius at the focal point and $\omega(z)$ is the beam radius of the laser at a distance of z. Using this method, the beam waist of a laser focused on an oil immersion objective lens can be determined using:

$$\omega_0 = \frac{\lambda}{\pi NA}\sqrt{n_{oil} - NA^2} \tag{2.54}$$

Where λ denotes the wavelength of the laser, NA is the numerical aperture of the objective lens, and n_{oil} represents the refractive index of the immersion oil. An expression for the intensity of the photon flux in the focus plane $(z = 0)$ can be presented as:

$$I_{\gamma focus} = \frac{P_\gamma}{\pi \omega_0^2 \tau_\gamma f_\gamma h v_\gamma} \tag{2.55}$$

Where P_γ is the mean laser power, τ_γ denotes the pulse width, f_γ denotes the repetition frequency, and v_γ denotes the wave frequency. Planck's constant, h, is also included in this equation. $I_{\gamma 0}$ and $I_{\gamma\, focus}$ are connected by:

$$I_{\gamma 0} = \frac{2e^2}{e^2 - 1} I_{\gamma focus} \approx 2.3\, I_{\gamma focus} \tag{2.56}$$

To determine the voxel diameter $(d_{vox}(P,t))$, it is necessary to first look at the I_γ in the focal plane by remembering equation (2.53) and setting $z = 0$. This is done because the focal plane is where the photon flux intensity is at its highest. Therefore, this is the best place to determine the voxel diameter.

$$I_\gamma(r, z = 0) = I_{\gamma 0}\, exp\left[\frac{-2r^2}{\omega_0^2}\right] \tag{2.57}$$

When these equations are combined, an approximation of the voxel diameter can be obtained:

$$d_{vox}(P,t) = \omega_0\left(\ln\frac{\sigma_2 I_{\gamma 0}^2 n_{pulse}\tau_\gamma}{C_p}\right)^{\frac{1}{2}} \tag{2.58}$$

In which the total number of pulses $n_{pulse} = ft$ and C_p is:

$$C_p = \ln\left[\left(\frac{\rho_{init}}{(\rho_{init} - \rho_{th})}\right)\right] \tag{2.59}$$

In a similar manner, by returning to equation (2.53) and put $r = 0$, we can determine the intensity of the axial photon flux.

$$I_\gamma(r = 0, z) = \frac{I_{\gamma 0}\omega_0^2}{\omega(z)^2} \tag{2.60}$$

Using the formula $(l_{vox}(P,t))$, we allow the voxel length to be approximated as:

$$l_{vox}(P,t) = 2z_R\left[\left(\frac{\sigma_2 I_{\gamma 0}^2 n_{pulse}\tau_\gamma}{C_p}\right)^{\frac{1}{2}} - 1\right]^{\frac{1}{2}} \tag{2.61}$$

Conditions under which the Rayleigh length, denoted by (z_R) is

$$z_R = \frac{\pi\omega_0^2}{\lambda} \tag{2.62}$$

2.10.3 Photoresists

Photoresists are split into two types, positive tone resists and negative tone resists. The composition of the two sorts of photoresist differs, resulting in the distinct behaviour of the resist after exposure. Positive tone resists are not soluble in the developer when unexposed. The light catalyses processes that improve the dissolution of the exposed portions by an order of magnitude. When the resist is developed, the exposed parts are removed significantly more quickly than the unexposed areas. In a negative tone photoresist, the light acts as a catalyst for the polymerisation of the resist which causes the exposed areas to become insoluble in the developer and causes them to stay on the wafer after development. This is the reverse of what happens in a positive tone photoresist.

The current study made use of a photoresist manufactured by Nanoscribe GmbH called IP-L 780. It is a liquid negative-tone resin and offers a feature size as small as 150 nm. The IP-L 780 resin comprises a branched acrylic monomer and an α-aminoketone photoinitiator. During the polymerisation process, TPA happens and the C=C of the monomers are consumed to produce carbon-carbon single bonds (C-C) in a strongly cross-linking polymer.

2.11 Magnetisation configurations in ferromagnetic micro- nanostructures

In soft magnetic materials, it is primarily two interactions that compete in order to dictate the ordering. These are the exchange and magnetostatic interactions. Much of the discussion below ignores both magnetocrystalline and magnetoelastic effects since focus is upon $Ni_{81}Fe_{19}$ for which both effects tend to zero.

On a short-length scale, the exchange interaction in ferromagnets favours the parallel alignment of neighbouring atomic moments. However, the magnetostatic interaction tends to favour closed magnetic loops with no net magnetic moment to reduce the stray fields. Even though the magnetostatic interaction is significantly weaker than the exchange interaction because of the longer ranges involved (decaying as $1/r^2$), it is capable of competing with the exchange at sizes that are far greater than what is referred to as the exchange length, $l_{ex} = \sqrt{A/\mu_0 M_s^2}$ where A is the exchange constant [36]. In ferromagnetic nanostructures, the interplay between the exchange interaction and the dipolar interaction may result in a wide variety of potential magnetisation configurations. These configurations are determined by the size, shape and material of the nanostructure [54].

In general, the magnetostatic energy scales with the volume of the element, meaning that for very small structures, of order 100 nm or less, the short-range exchange interaction dominates. This yields a transition to single domain state as shown in Fig. 2.13a at some critical diameter [17]. When the magnetostatic poles at the sample borders are reduced, the amount of magnetostatic energy produced is at its lowest. This indicates that the magnetisation tends to line up in a tangential to the borders of the sample. This effect of the magnetostatic interaction is termed shape anisotropy because the shape of the sample tends to define the easy magnetic axes. Overall, the competition between the exchange energy and magnetostatic energy is crucial in determining the magnetization configuration for a submicron-sized thin film.

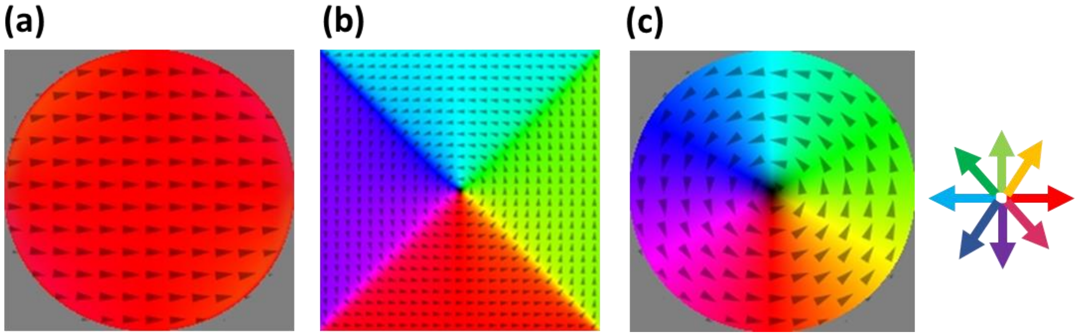

Figure 2.13: Micromagnetic simulations of (a) a single domain in a 100 nm diameter, 20 nm thick nanostructure, (b) a Landau configuration in a 2 × 2 μm^2, 40 nm thick square element and (c) a vortex state in a 40 nm thick disk of 2 μm radius.

The cumulative dipolar interaction in larger structures is large enough to compete with the exchange interaction, favouring flux-closed magnetisation configurations and reducing the majority of stray fields. Examples of flux-closed configurations include the Landau and vortex configurations in which the magnetisation circulates around a single central point (see Figs. 2.13b, c). The magnetisation, however, rotates out of the sample plane at the centre, pointing either up or down. This variable is known as the vortex polarity and an out-of-plane direction is favoured in order to prevent a significant increase in the exchange energy. It was first predicted that the vortex core would be present by Feldkeller and Thomas [43]. However, the small size of the core makes it difficult to observe directly. It has been imaged by magnetic force microscopy (MFM) [55] and by Lorentz microscopy [21]. When using high-resolution spin-polarised scanning tunnelling microscopy, it became possible to resolve the internal spin structure of the vortex core [56]. Following that, the studies described below discuss the static and dynamic behaviour of vortex states in ferromagnetic elements.

2.12 Magnetic vortex behaviour in nanostructure

The term magnetic vortex state in this context refers to the ground states in those ferromagnetic elements which are geometrically confined, typically have length scales of order microns and have little magnetocrystalline anisotropy [57]. It should be noted that magnetic thin films and magnetic microstructures also harbour topological objects, which are referred to as magnetic vortices, but these are typically of order 50–100 nm.

The exploration of magnetic vortices has attracted the attention of scientists because of their use in neuro-inspired and radiofrequency devices [58], non-volatile storage [59], and sensing devices [30]. Many studies have been conducted to determine the static and dynamic properties of magnetic vortices in sub-micron elements. One important aspect is to characterise the degeneracy of such vortex states which is governed by two properties [21], the chirality and the polarity (see Fig. 2.14). Chirality in this context is the phenomenon of circulating magnetisation which can be either clockwise or anticlockwise. Polarity, as discussed above refers to the direction of magnetisation at the vortex core, which can either point in the positive or negative z-direction. Hence, there is the possibility of either clockwise ($c = +1$)

or counter-clockwise (c = −1) chirality and either up (p = +1) or down (p = -1) polarity. The four distinct magnetisation configurations that a vortex is known to comprise are degenerate and can be used for non-volatile data storage devices and other spintronic applications [60]. Interestingly, many studies [26, 61, 62] have looked at the collective behaviour of such vortex arrays. Here, at remanence, the interaction between adjacent elements is minimised and high magnetic stability is induced because the stray fields of these structures with vorticity (curling magnetisation) are relatively small [63, 64].

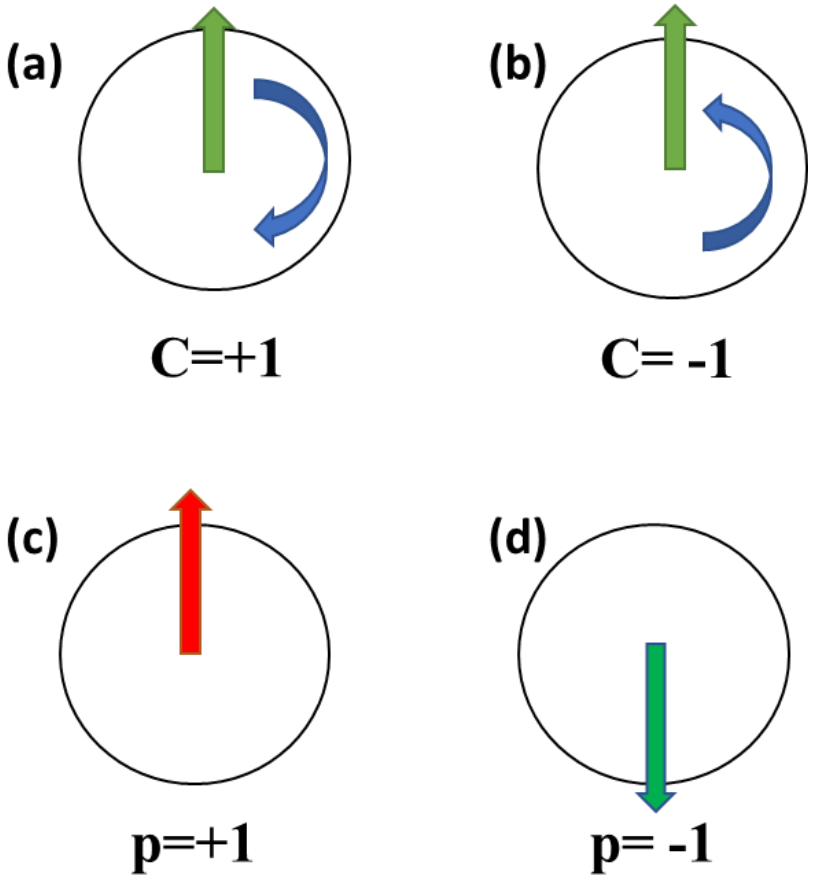

Figure 2.14: The properties that characterise the vortex state: (a, b) the chirality of the in-plane magnetisation, either clockwise or anticlockwise (c = +1 or -1), (c, d) the polarity of the core perpendicular to the disk points up or down (p = +1 or -1).

2.12.1 Static properties

The control of vortex states in microelements involves the switching between polarity and chirality. This state switching process requires vortex annihilation, moving the core out to the boundary of the element and then further re-nucleation of the new vortex by reducing the external magnetic field. This results in a new vortex core that is nucleated, which can be controlled by harnessing an asymmetric geometry of elements or by symmetric breakages created by Dzyaloshinskii-Moriya interactions (DMI). The nucleation process is the production of a new vortex core at the element boundary. These nucleation states are predicted with the help of micromagnetic simulations and which can be compared with the experimentally defined hysteresis loops [65]. Yakata et al. reported that a magnetic vortex can be controlled in a square nanomagnet and they proposed a simple way to change the chirality by changing the in-plane magnetic field direction [66].

Microscopies that are susceptible to magnetisation, such as magnetic force microscopy (MFM) [67], Lorentz transmission electron microscopy [68] as well as x-ray microscopies, are the methods that are most frequently used when attempting to characterise sub-micron elements. MFM is the most extensive method because it can be performed in any laboratory. Nevertheless, caution is required to prevent the field from the tip disturbing the imaged vortex states. Because of this, certain restrictions are imposed which influence the dimensions and magnetisation of the nano-magnets that were seen, as well as the surroundings in which the system was studied.

In introductory studies reported by Okuno et al. [67] and Shinjo et al. [55], it was argued that magnetic force microscopy (MFM) shows first evidence of the vortex state in circular disks of $Ni_{81}Fe_{19}$. In these studies, evidence of a flux closure state with out-of-plane vortex core magnetisation were presented. It was apparent from their results that the vortex core present at the centre is perpendicular to the plane. An additional study conducted by Raabe et al. demonstrated that permalloy disks with a diameter of 0.08–1 µm exhibited a vortex state structure with out-of-plane core magnetisation which supports the findings of the previous studies [21].

MFM was used by Kim [69] to investigate the magnetic configuration of square micron-sized elements. The results depict a Landau-type flux closure domain structure complete with 90 degree domain walls and a central vortex core. Most volume magnetic charges are gathered close to the domain boundaries. Garcıa et al. [70] and Coısson et al. [71] also showed a similar Landau flux closure domain design for the thin square.

Lorentz transmission electron microscopy has also been used in numerous investigations related to magnetic vortex properties. In those studies, circular flux closure at remanence with the vortex core in the centre of the disks was observed in circularly shaped $Ni_{81}Fe_{19}$ systems [68, 72, 73]. A Co vortex magnetic structure was also investigated by Tonomura et al. and the existence of perpendicular magnetisation at the centre of circular element was observed using electron holography [74].

When establishing the magnetisation configuration of patterned permalloy thin films, size and shape are essential factors. Lai et al. [75] studied the phase diagram of ferromagnetic dots and found a number of distinct states as shown in Fig. 2.15 [65, 76]. Both circular and square permalloy elements can be found in a uniform state (sometimes called the flower state in literature), when both squares and circles are very small at 50 nm length or diameter. The uniformity of this state can be attributed to the exchange energy dominating over the magnetostatic energy in this regime. Increasing the length scale of the patterned shape to 100 nm yields an increase in the magnetostatic energy such that it becomes comparable to exchange, leading to the magnetisation at edges starting to cant such that they are tangential with the boundary, but with a uniform magnetisation towards the centre. Overall, this yields a magnetisation configuration which has a C shape, reducing the stray field when compared to the uniform state. A further increase in the feature size to 162 nm yields a transition to a vortex state or S state for which there is metastability. Here, again the increase in magnetostatic energy drives the transition, to produce a magnetisation profile that maximises flux closure for the case of the vortex state. The S state, which has higher energy than the vortex state, has magnetisation that is tangential around the entire boundary, with a small uniform region in the centre. The magnetisation is found to trace an S shape.

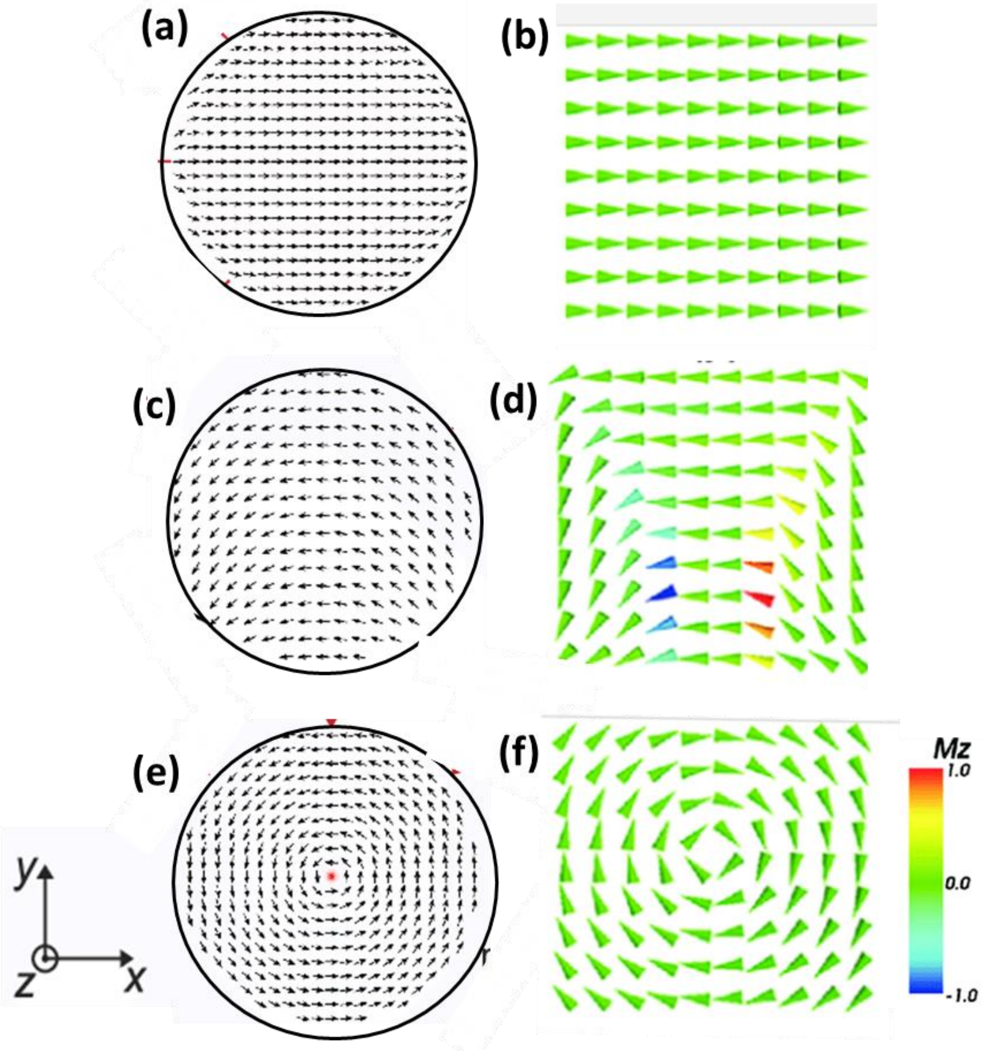

Figure 2.15: Simulated spin configurations of disk and square permalloy elements showing different states: (a, b) the uniform state, (c, d) the C state , (e, f) the vortex state [65, 75, 76].

2.12.2 Magnetic reversal of vortex structures

The in-plane magnetic reversal of two $Ni_{81}Fe_{19}$ disks, 900 nm in diameter and 50 nm thick, were studied using MFM [18]. The results indicated that the vortex core initially displaced perpendicular to the direction of the applied field (see Figs. 2.16a, b). The formation of a wall was observed under the influence of increasing the applying field which shifted to the disk boundary (see Fig. 2.16c). After re-nucleation, any of the four possible vortex configurations can result when reducing the field (see Fig. 2.16d). The field was found to be dependent on the aspect-ratio (diameter/height) of the disks. A higher switching field was required with a decreasing diameter / height ratio as a result of the shape anisotropy.

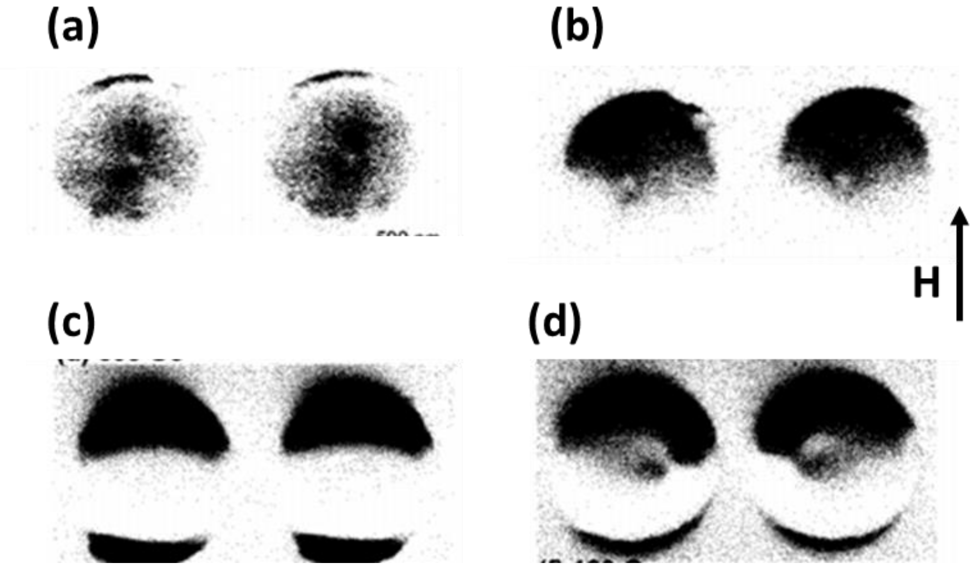

Figure 2.16: MFM images presenting the magnetization process of two $Ni_{81}Fe_{19}$ disks (thickness 50 nm, diameter 900 nm) in an in-plane field H [18].

Recent research has also investigated the application of pulsed magnetic fields to induce vortex core reversal. As demonstrated by several studies [63, 77, 78], the system is excited by a defined duration and amplitude pulse of in-plane magnetic field. This is done to create an anti-vortex / vortex pair within the planar spin texture. The annihilation of the anti-vortex with the old vortex core is observed and this can yield a reversed polarity core. The efficiency and dynamics of vortex core annihilation in $Ni_{81}Fe_{19}$ nanodisks and the influence of pulse parameters on these was explored by Urba`nek et al. [63]. Specifically, a pulse rise-time / pulse amplitude phase diagram was investigated to determine optimal conditions to induce vortex core annihilation.

Several investigations used MFM to study permalloy disks of different parameters. In single permalloy disks of 0.8 μm diameter and of different thicknesses (10, 20, 50 nm) the micromagnetic structures were investigated using MFM under an increasing and subsequently decreasing external magnetic field [64]. This showed that the single vortex spin structure switched to a two-vortex structure when the field reached critical value H_1. However, when reducing the field from saturation to zero, it was observed to switch to the one vortex state at critical field value H_2. The transition field from one to two vortex state was found to increase with increasing disk thickness.

MFM and the magneto-optical Kerr effect (MOKE), supported by micromagnetic simulations was used to investigate the remagnetisation behaviour and vortex properties of systems [77]. The thickness and diameter of the features were 50 nm and 100 nm, and 0.6 μm and 2 μm, respectively. Both experimental and simulation results observed a double vortex to single vortex transition at nucleation in the 100 nm thick disks [77].

By applying a large static magnetic field (0.3–0.4 T), switching of the vortex core polarisation has also been evidenced [18]. There have been progressive efforts to switch the vortex core in magnetic disks. Through micro Hall magnetometry and MFM, Pulwey et al. presented the switching behaviour of single permalloy nano-disks. With a magnetic vortex phase, magnetisation reversal of various thicknesses (5 nm to 60 nm) and diameters (200 nm to 2 μm) was studied with the help of the above mentioned methods. As shown by the studies, the switching of the core polarity in the centre did not affect the chirality of the vortex.

The reversal of magnetisation in a $Ni_{81}Fe_{19}$ square with a dimension of 2 μm and a thickness of 20 nm was studied by Breitenstein et al. [79]. MFM and micromagnetic simulation observed the nucleation, displacement and eventual annihilation of the vortex state that occurs in the presence of an external magnetic field. They were particularly interested in the vortex states discovered in thin squares. Their findings suggest that the Landau pattern (see Fig. 2.17) is the energetically preferred magnetisation configuration at zero external magnetic field for squares of soft magnetic materials with lateral dimensions of several micrometres and thicknesses of some ten nanometres.

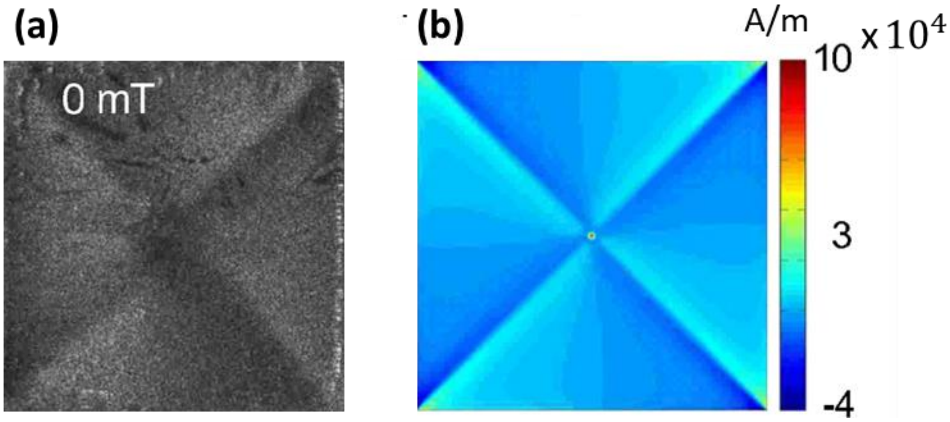

Figure 2.17: (a) MFM image and (b) simulated stray field image of Landau pattern configuration in 2 x 2 μm^2 square with a thickness of 20 nm. The colour bar represents the stray field in units of A/m [79].

Similarly, Coısson et al. [71] defined more detail in the magnetisation process. Some of these aspects include the transition from the saturated state (see Fig. 2.18a) to the nucleation (c-state, Fig. 2.18b), vortex displacement (see Fig. 2.18c) and expulsion of vortices (see Fig. 2.18d). A Ni_{80} Fe_{20} square dot with a lateral dimension of 800 nm was used for this study and the motion of the domain wall in a Landau-like domain configuration was tracked as it evolved in response to an externally applied field.

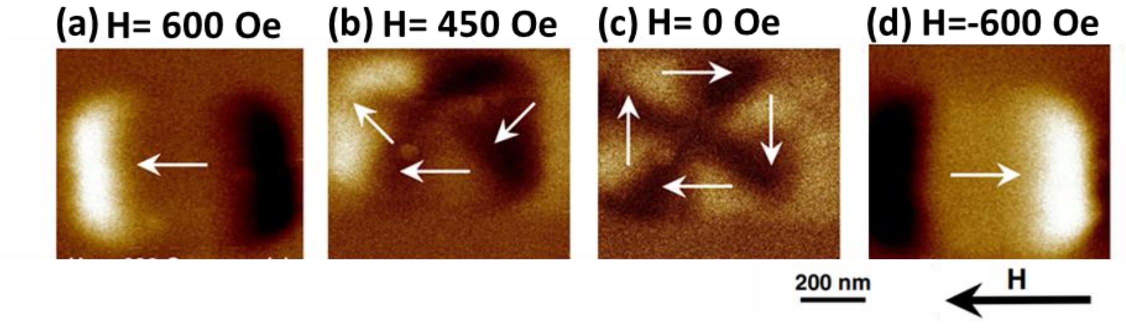

Figure 2.18: MFM images of a Ni_{80} Fe_{20} square with a size of 800 nm at different field values (a) Saturation in positive x-direction (b) Re-nucleation of vortex core. (c) Remanence. (d) Saturation in negative x-direction. White arrows show magnetization [71].

The breakdown of degeneracy in vortex states can often favour practical objectives. To provide one example, the existence of either a single chirality or a polarity state under certain circumstances may be achieved by altering the geometry [80-82]. For instance, Im et al. demonstrated that simultaneous control of chirality and polarity can be achieved by applying an in-plane magnetic field to asymmetrically formed Ni_{80} Fe_{20} disk with two half parts of different thicknesses (see Fig. 2.19) [81].

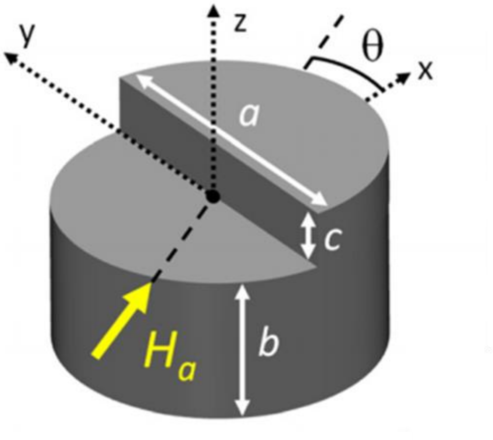

Figure 2.19: Sketch of disk that has a diameter a = 360 nm, a thin half part with a thickness b = 18 nm at x < 0, and a thicker half of thickness b + c = 24 nm at x > 0 separated by a middle edge [81].

Altering the state of a vortex may also be accomplished by manipulating the magnetostatic interaction that occurs between nanoelements. When the components are in sufficiently close proximity to one another, there is a reduction in the vortex nucleation and annihilation fields and an increase in the initial susceptibility [25]. In addition, the nucleation of the vortex states in the orderly dense array goes through a condition in which the flux closure includes more than one single state (multidomain state) , as shown by Konoto et al. for arrays of square structures [19]. In square arrays of circular dots of noninteracting, researchers have not seen any preference in the vortex chirality and appears to be totally random [62, 83].

2.13 The Rigid Vortex Model

The so-called rigid vortex model is a straightforward way to explain a vortex in which the shape of the vortex is not affected by the presence of an external field (RVM). The next section of the chapter will provide a concise analytical explanation of the core profile using the RVM and the magnetization reversal in response to an external field.

2.13.1 Core profile and diameter

In 1993, Usov and co-workers presented a model for the analytical description of the magnetization distribution in a disk structure when no external field is present [84]. A simplified schematic of a magnetic disk is provided here in Figure 2.20. The disk has the following dimensions: thickness L, radius R, and core radius a. The magnetization at a point $r < a$ (inside the core) can be described in polar coordinates:

$$M_x = \frac{2ar}{a^2 + r^2} \sin(\emptyset) \tag{2.57}$$

$$M_y = \frac{2ar}{a^2 + r^2} \cos(\emptyset) \tag{2.58}$$

$$M_z = \sqrt{1 - \frac{2ar}{a^2 + r^2}} \tag{2.59}$$

On the other hand, the magnetization outside the core $(R \geq r > a)$ is given by:

$$M_x = -\sin(\emptyset) \tag{2.60}$$

$$M_y = -cos(\emptyset) \tag{2.61}$$

$$M_z = 0 \tag{2.62}$$

By introducing the exchange length l_{ex}, the ratio $g = L/R$ and the numerical constant κ it is possible to specify an equation for the radius of the core:

$$a = \left(\frac{l_{ex}^2 R}{12\kappa \frac{L}{R}}\right)^{\frac{1}{3}} \tag{2.63}$$

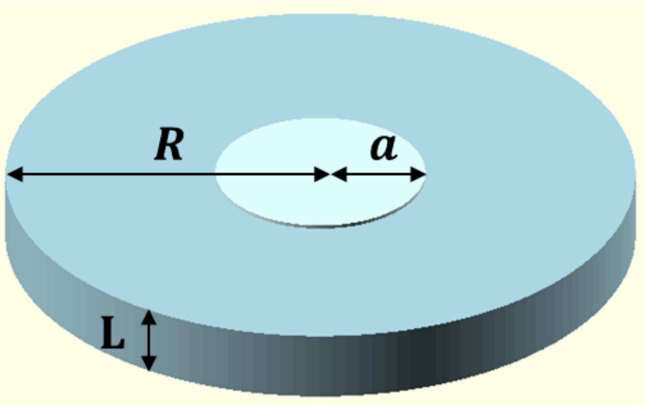

Figure 2.20: Sketch of disk dimensions: the core-radius a, disk radius R and the thicknesses L [84].

2.13.2 Vortex displacement introduced by an external field

As indicated earlier, the RVM can provide a qualitative description of the magnetization variation of a magnetic disk exhibiting a vortex due to the application of an in-plane field, in particular, the location of a magnetic vortex. The vortex is situated in the middle of the structure, just as shown in Figure 2.21(a) at remanence. In contrast, the application of weak magnetic in-plane fields causes the magnetic vortex to displace in a direction that is perpendicular to the direction of the field, as shown in Figure 2.21(b). As the word, rigid suggests, it is important to point out that the vortex magnetization distribution in this model is unaffected by an external field.

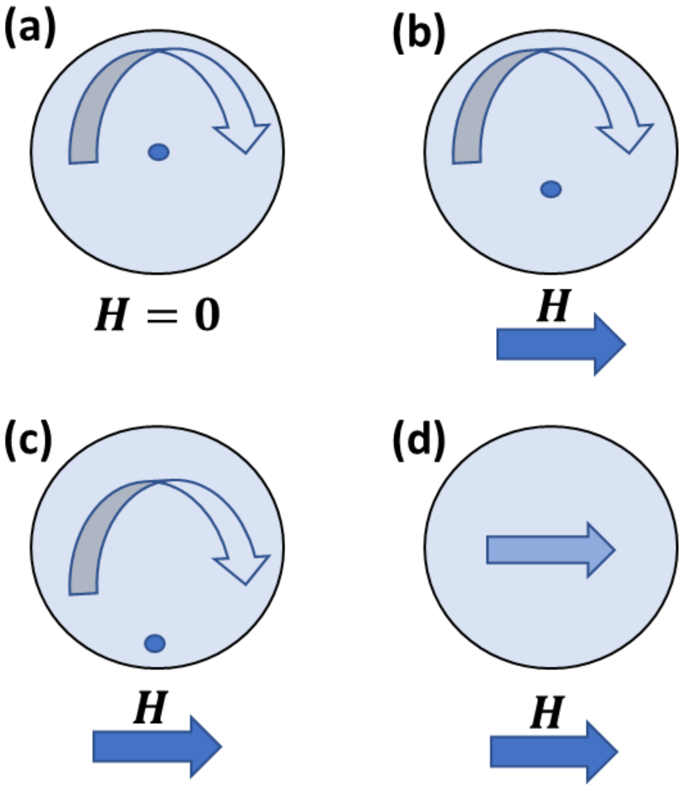

Figure 2.21: Effect of an in-plane field on a magnetic vortex described by the RVM. (a) the centered vortex in remanence, (b) introducing field yielding the displacement of the vortex core perpendicular to the field, (c) further increasing of the field yielding the centre being pushed to the edge of the structure until the magnetization is close to vortex annihilation and (d) the saturated state.

Therefore, the variation in the magnetization results from a shift in the distribution of the magnetization with regard to the disk border, which acts as a limit. On the other hand, when the field strength increases, the vortex's centre moves closer to the border, which continues until the typical annihilation field is obtained, as shown in Figure 2.21(c). The vortex is destroyed due to subsequent increases in the field, and the structure reaches a saturated condition in the in-plane direction. A sketch of such a saturated condition is shown in Figure 2.21(d), and it may be seen as a vortex that is located at an infinite distance. When the external field is made weaker after saturation, a vortex will begin to nucleate, and the process will turn around.

2.14 Perturbing the magnetic vortex state using defects

In the last few years, many research studies have investigated the manipulation of micromagnetic vortex states to either control the state or means of switching. Since a disk has high symmetry, it is difficult to control vortex chirality and polarity. However, one way to do this was by placing geometric defects in the structure. Vortex core dynamics are influenced by defects, as indicated by a number of studies. According to Rahma et al., a point nonmagnetic defect in $\mathrm{Ni}_{81}\mathrm{Fe}_{19}$ disks can be used to pin the vortex core in the remanent state [85]. The defect was achieved by small resist spots of about 50 nm not being removed during the development process. Such processes are difficult to control. Furthermore, it was demonstrated that magnetic switching can be controlled by the artificial point defects and the hysteresis can be significantly altered, impacting both annihilation and re-nucleation fields [59].

Uhlig et al. [86] used conventional lithography to pattern a 300 nm hole in a micron-scale disk and then used Lorentz transmission electron microscopy, to explore the dynamics and energy landscape. It was found that the hole can be used to completely annihilate the core at low field, yielding a simple circulating structure.

Compton et al. utilised time-resolved Kerr microscopy to study fluctuations in the frequency of the gyrotropic mode in nano-disks of permalloy. The movement of the vortex core toward a nanoscale pinning site were found to be responsible for the fluctuations. The authors estimated the average interaction energy of the vortex core with the single defect to be approximately 2 eV [87].

Apolonio et al. investigated the role of nonmagnetic impurities as pinning sites in vortex systems [88]. A model for point like magnetic impurities was developed and dynamic simulations performed. Scatter (repulsive) or pinning (attractive) sites were the two possible impurities. They indicate that the possible origins of the pinning and scattering defects in thin films could be the local reduction or increase in the exchange constant respectively, caused by a local nano-scale structural deformation. A single defect vortex core interaction energy was calculated using known values for $Ni_{81}Fe_{19}$. The interaction range was estimated to be 10 nm. The findings were in accordance with the experimental data. Moreover, the fluctuations that resulted because of the influence of magnetic impurities in the gyrotropic mode were also in accordance with the experimental findings [89].

The drawback of these findings is that they lead to changes in magnetisation reversal because of the breakdown of the structure's magnetostatics. An alternative is to pattern a specific geometric defect on top of the main disk. The magnetisation reversal on the main disk is then significantly influenced by the presence of a geometric defect. Strategic placement of the defect then also allows the direction of the external magnetic field to control the vortex [35, 90]. A Cobalt nanostripe is another means of manipulating the vortex state. Importantly, it was demonstrated that the magnetisation orientation of the single domain nanostripe can be used to control the chirality. The nanostripe magnetisation can of course be switched using an external magnetic field [91]. Also, to study the effect of a ring of magnetic impurities on the vortex core dynamics in nanodisks of permalloy, numerical simulations were used by another research group. With the help of the ring, the vortex core could be confined and the frequency of gyrotropic motion could be modulated. Additionally, it was observed that under specific conditions, vortex core-impurity interactions could help achieve the switching of the vortex core polarity, especially when the ring is present [92].

Circular elements with altered topography were studied by Ding et al. [93], while the majority of the above mentioned research studies are applicable to geometrically flat elements. A geometric confinement effect was provided by a nonmagnetic nanodot inserted under a mesoscale $Ni_{80}Fe_{20}$ dot which caused variations in the vortex translational mode frequency. Depending on the location of the vortex core, two separate resonance frequency ranges were observed which can be controlled if a small magnetic field is applied. By comparison to micromagnetic simulations with experimental data, it can be inferred that as the thickness-diameter ratio of the barrier (the introduced disk-shaped step) is increased, the frequency of the gyrotropic mode also increases. However, a method for experimentally introducing 3D defects in nanostructured disks to manipulate the micromagnetic configuration remains elusive. In this context, conducting a thorough investigation regarding nanodisk 3D structures should be useful and worthwhile.

2.15 3D magnetic nanostructured elements

The majority of micromagnetic research on basic geometries has been conducted on 2D geometries due to limitations of fabrication techniques. More exotic fabrication methods have made preliminary exploration of some 3D geometries. 3D Nanomagnetism is now an emerging field whereby different geometries and topologies are explored to impact remanent state, switching and ultrafast dynamics. Examples of fabricated geometries include tube structures [94], spherical structures [95] , helical structures [9, 96] and 3D artificial spin ice [97] . The approaches for manufacturing were based upon rolling up thin-films, chemical synthesis, focussed electron beam deposition (FEBID) and two-photon lithography (TPL) techniques. In the technique that rolls up thin films, the effect of the differential strain on the films allows the engineering of nanomembranes of nearly any material [94], allowing flexibility in the tuning of material parameters. A severe disadvantage of this technique is that it can only produce systems of circular cross-section. Chemical synthesis methods are a powerful method to fabricate 3D nanoelements and can be exploited to realise very large area samples over 10s of mm, something that would take a long time with direct write technologies. Examples include the chemical synthesis of gyroids unit cells using block copolymer systems [98]. Here these systems have been subject to magnetic imaging, allowing an insight into the frustration in such structures [99]. The main disadvantage of such chemical synthesis is again limitations in the realised geometry. Both the FEBID and TPL techniques are emerging direct-write patterning techniques allowing fabrication of structures on the scale of ~100 nm with times ranging from seconds to a few minutes. The key advantage here is the flexibility with which to choose any geometry. For the case of FEBID, the material choice is limited by the chemical precursor [100] utilised whereas TPL manufactures the 3D structure within a polymer which can then be transferred to relevant magnetic material using evaporation [97], sputtering [101] or electrodeposition [102].

We now focus upon the fabrication of pyramidal elements since these are studied in this thesis. Interestingly, almost all of the work that has been undertaken to investigate the magnetic states that could make observations for pyramids were conducted using micromagnetic modelling which is described in detail below.

Knittel et al. conducted research in 2010 by using a micromagnetic model to investigate how changing the thickness of pyramidally structured core-shell structures affects their magnetic characteristics. They found many distinct forms of single-domain states, most of which take place at more compact system sizes which has an edge length of (35 nm, 120 nm and 300 nm) and thickness of (10–100 nm). These states are referred to as the onion state (Fig. 2.22a), flower state (Fig. 2.22b), C state (Fig. 2.22c), and S state (Fig. 2.22d), because they are analogous to corresponding states in thin square films. When looking at more significant system sizes which has an edge length of (300 nm) and thickness of (10–100 nm), it is apparent that there are two distinct vortex states: a symmetric vortex (Fig. 2.22e) and an asymmetric (Fig. 2.22f) vortex states [103].

In 2011, Nasirpouri et al. examined magnetic hysteresis loops of individual core-shell components and this reversal can be decomposed into sharp steps corresponding to distinct stable magnetic states. The pyramidal structure has six different stable states at zero magnetic field. While they found 10 distinct stable conditions for the more complicated icosahedral-shaped magnetic element in 3D ferromagnets, the metastability of magnetic states is primarily caused by a variety of distinct demagnetisation situations that occur close to the edges of the 3D structure. It is reasonable to anticipate that shells with thinner walls would have more noticeable sharp edges, resulting in increased potential states and greater stability [104].

In 2012, Knittel et al. presented a micromagnetic model used to investigate the effect of 3D magnetic nanostructures (soft-magnetic core-shell pyramids) with rounded corners and edges on the magnetic reversal process which were studied based on two examples. This model was developed to investigate the effect that these nanostructures have on the magnetic reversal process. Taking into consideration the inversion of quasi-homogeneous states in the direction of their easy axis demonstrates that the smoothing out of sharp edges significantly reduces coercivity [105]. According to the findings of research into the magnetic reversal of the asymmetric vortex state, it is possible for this state to also occur when there are rounded corners and edges with curvature radii that are many multiples greater than the exchange length. More recently, an ordered pyramid structures array has been investigated by Irmikimove et al. [106]. Because there are four comparable facet surfaces with four edges, it was discovered that there are three distinct magnetic states: a single domain state, an asymmetric vortex state, and a symmetric vortex state. This was formed due to configurational anisotropy.

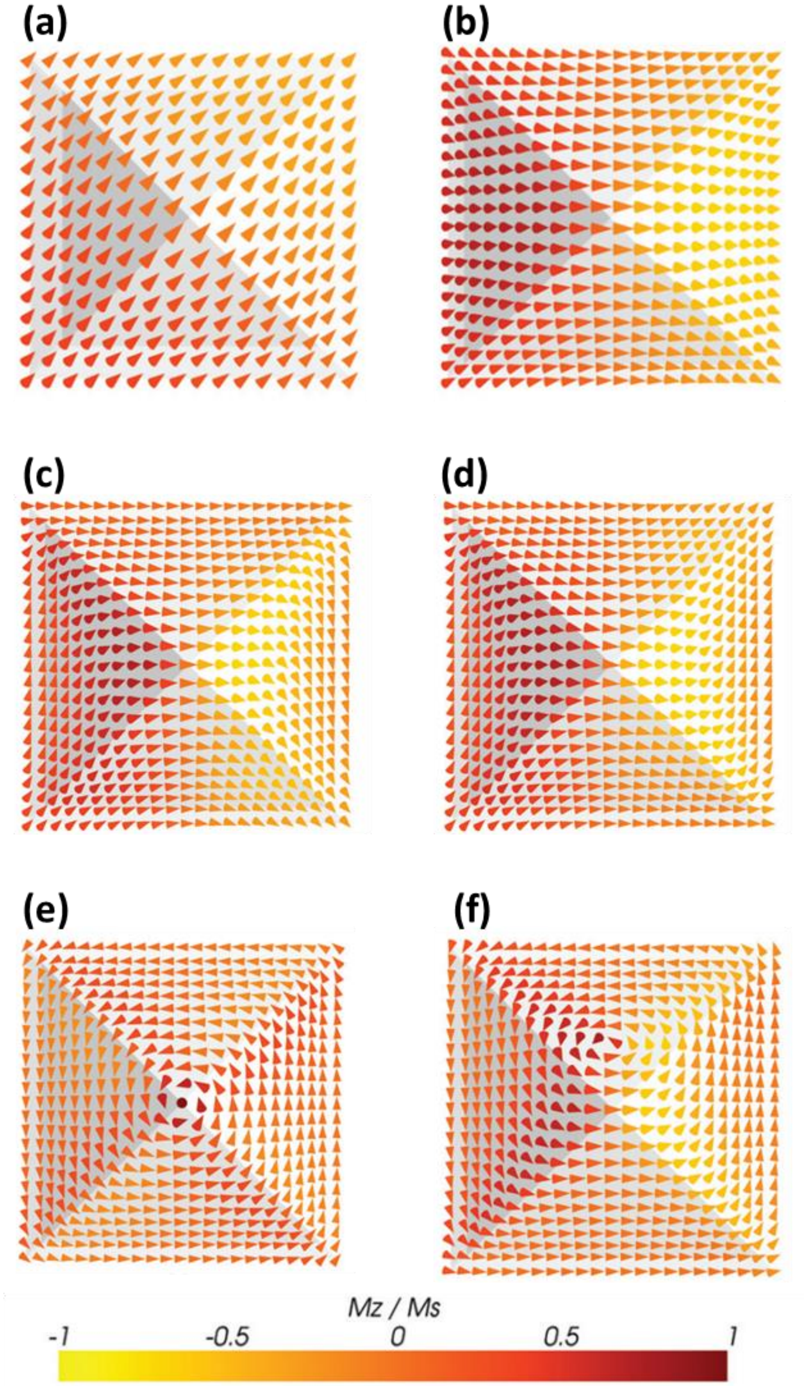

Figure 2.22: Top view of pyramid structures and states determined using micro-magnetic model. (a) An onion state (35 nm length), (b) a flower state (120 nm length), (c) a C state, (d) an S state (250 nm length), (e) a symmetric vortex state and (f) an asymmetric vortex state (300 nm length) [103].

3. Chapter 3

Experimental methods

3.1 Introduction

The fabrication and characterisation of 3D nanostructured magnetic systems is a field that is still in its infancy. In this chapter we detail the physical basis for structure fabrication and characterisation. Specifically, the fabrication of micro-elements using two-photon lithography and thermal evaporation will be introduced. The basis for physical characterisation is explained in terms of the underlying scanning electron microscopy and atomic force microscopy. The physics of magnetic force microscopy will be detailed, with an emphasis upon application to 3D nanostructures. Finally, the basis for finite difference micromagnetic simulations, using the package Mumax3 will be detailed.

3.2 Two photon lithography

Two-photon lithography (TPL) has been established since the early 2000s as a technique suitable for the fabrication of 3D microstructures within a polymer framework. Interest in this technique has recently grown primarily due to the recent commercialisation of femtosecond laser systems and associated TPL systems. The availability of such commercial systems has yielded a rapid acceleration in the exploration of 3D functional materials upon the micro-nano scale, both due to the potential for new physics as well as potential applications in information technology, biotechnology, microfluidic and optical industries.

For decades, scientists have relied on conventional photolithography techniques to conduct their research. This enabled the engineering of nanoscale characteristics into templates for 2D elements. This begins by applying a photoresist to a substrate before exposing the sample to an ultraviolet light (UV) source. A mask is used in the optical path to block certain parts of the sample, resulting in the desired pattern being exposed. For the case of a positive-tone photoresist, subsequent development yields removal of the exposed regions. On the other hand, exposed parts of negative-tone photoresists yield strong cross-linking and hence a retainment of such regions after development. All samples in this thesis are created using a negative-tone photoresist, described in detail below. Once a template has been created, it can be utilised with a wide variety of deposition and processing methods to cast the desired material into the desired 2D geometry.

This conventional 2D photolithography makes use of an UV light source, which with the conventional photoresist, drives single-photon absorption. Due to Beer’s law [107], it is difficult to produce 3D geometries, with characteristics that change along the z-axis, without carrying out multiple steps and even then, finer features in the z-direction are not possible.

TPL is a technique that harnesses the scanning of a femtosecond laser in a conventional photoresist. The wavelength of the laser is typically in the infra-red and hence two photons of half the energy drive the transition within the resist. Since two-photon absorption is a third-order, non-linear optical process, its probability is very low and hence only occurs within the small region of the focal volume of a pulsed laser. This means that only the point of focus yields an exposure and subsequent scanning of the laser can yield 3D templates within the resist.

The 3D nanomagnetism lab in Cardiff hosts a commercial TPL system (Nanoscribe Photonic Professional GT) which was employed for sample production during this PhD. This system is housed in a class 10000 cleanroom with UV filters covering the windows and lighting fixtures. Figure 3.1 depicts a schematic representation of the TPL configuration. A computer is used to digitally control both the laser output and the piezoelectric stage, as shown in Figure 3.1. The laser output allows for quick changes in laser parameters (power, exposure duration, pulse frequency, and so on) during exposure, whilst the piezoelectric stage and galvometers allows precise 3D patterns to be exposed.

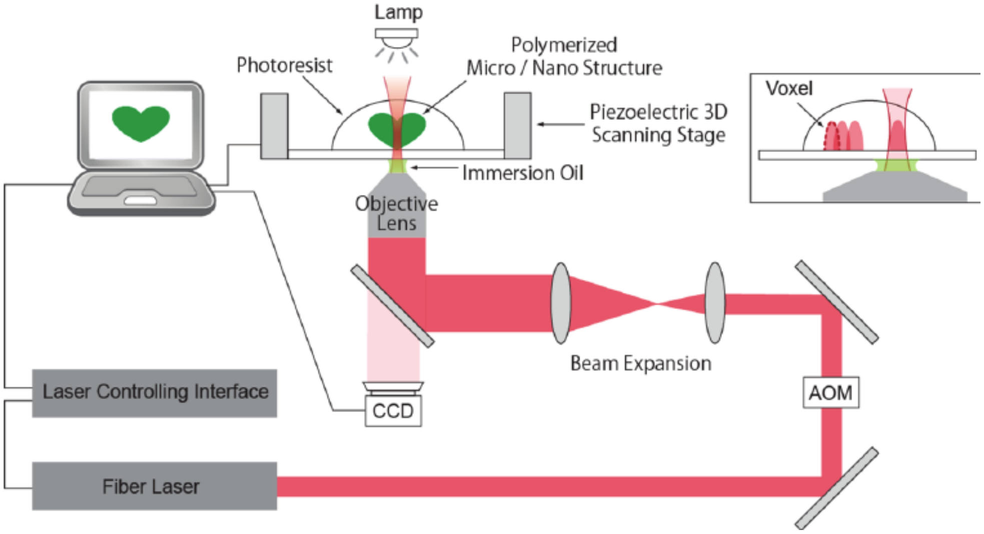

Figure 3.1: Schematic illustration of the two-photon lithography setup [108].

Figure 3.1 depicts the primary optical components of the system. All optics are upon a vibration isolation table. The laser has a wavelength of 780 nm, a pulse duration of ~ 100 fs, a repetition rate of 80 MHz and peak power of 25 kW [109]. The laser beam is first guided into an acousto-optic modulator (AOM) which enables precise modulation of the laser's output power. The beam is then expanded before being guided into an inverted microscope. Here, a high numerical aperture, oil immersion objective lens ($NA = 1.4$) tightly focuses the beam into the photoresist. The beam waist (ω_0) at focus can be calculated using [53, 109]:

$$\omega_0 = \frac{\lambda}{\pi NA}\sqrt{n_{oil}^2 - NA^2} \tag{3.1}$$

Where $\lambda = 780$ nm, $NA = 1.4$, $n_{oil} = 1.518$. The beam waist is calculated to be 104 nm, yielding a spot size diameter of 208 nm at the focal point. Immersion oil is used to match the refractive index of the objective lens and the glass coverslip. Index matching reduces reflections at the glass substrate interface which in turn serves to eliminate any aberrations in the optical beam. The geometry is then defined, and one of two scanning modes needs to be chosen: (piezo or galvo) depending on the writing requirements. The galvo scanning mode is most often utilised primarily because it scans more quickly by 1-2 orders of magnitude higher than a piezo and with scan rates ranging from 1000 to 20,000 μms^{-1} [109]. In addition, high resolution remains possible with a minimum lateral feature size of ~ 200 nm [110]. The mode works using mirrors to steer the beam over a 2D region while the stage remains fixed. The in-plane galvo scan region has a diameter of approximately 200 μm and a height of approximately 300 μm. Following the completion of a layer, the stage uses a piezo to move the z-axis so the next layer can be written, overall resulting in a 3D nanostructure. This mode typically achieves speeds in the tens of centimetres per second (cms^{-1}), with the speed primarily restricted by the mirror actuation. While the galvo mode offers several advantages, its primary disadvantage is that it cannot scan in a direction that contains components in all three axes, and hence as stated above, a piezo is still required to modulate in z.

In piezo scanning mode, the beam is fixed, with the laser remaining focused on a single spot and the stage moves. The scan rates are typically between 25-300 μms^{-1} and the accessible scan area is 300 μm × 300 μm × 300 μm. This scan mode achieves marginally smaller feature sizes than the galvo mode, likely due to reduced aberrations because the laser remains focused on a single point. Even though this approach offers greater flexibility in scanning in 3D and results in slightly smaller feature sizes, the stage reaction time and speed restrict the piezo scan speed to 1-2 orders of magnitude lower than that of a galvo scan. This means that this approach is better suited to smaller structures that may need higher levels of accuracy. Therefore, in this thesis the galvo scan mode was utilised for all fabrication.

Upon writing, a glass coverslip is used as substrate (see Fig. 3.2a) then the femtosecond laser is focused into a negative tone photoresist (IPL-780) and the desired geometry is traced out by moving the point of focus with respect to the substrate (see Figs. 3.2b, c). After writing the unexposed photoresist is developed for 25 minutes in propylene glycol methyl ether acetate (PGMEA), which removes unexposed resist. A cleaning step in isopropyl alcohol is utilised to remove any remaining resist and PGEMA residue, yielding the desired geometry (see Fig. 3.2d). Now that the general apparatus has been described, we move onto describe how the system was used specifically in this thesis.

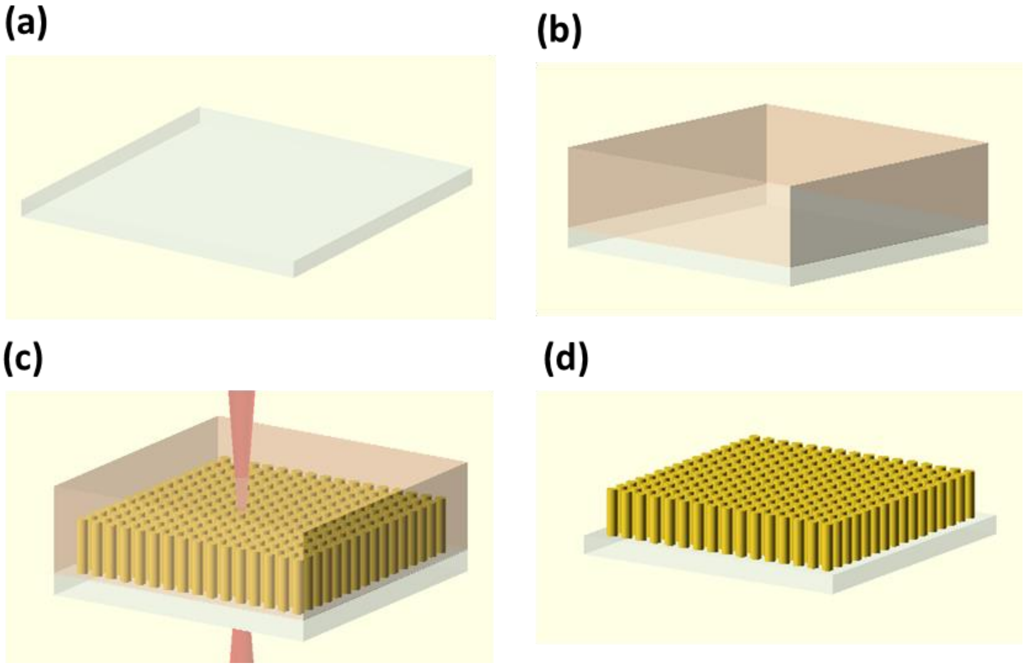

Figure 3.2: TPL fabrication procedure: (a) A glass coverslip, (b) a negative tone photoresist is drop cast on top of a glass substrate, (c) the photoresist is exposed using two-photon lithography, (d) the unexposed volume of the resist is removed by development.

3.2.1 Structure design

To begin fabricating a new structure, the first step is to design the geometry and transform it into a format that can be used. Nanoscribe TPL systems are bundled with a software package called DeScribe which is used to trace out the voxel patterns created by the device itself. The system allows two main means to define a geometry (see Fig. 3.3).

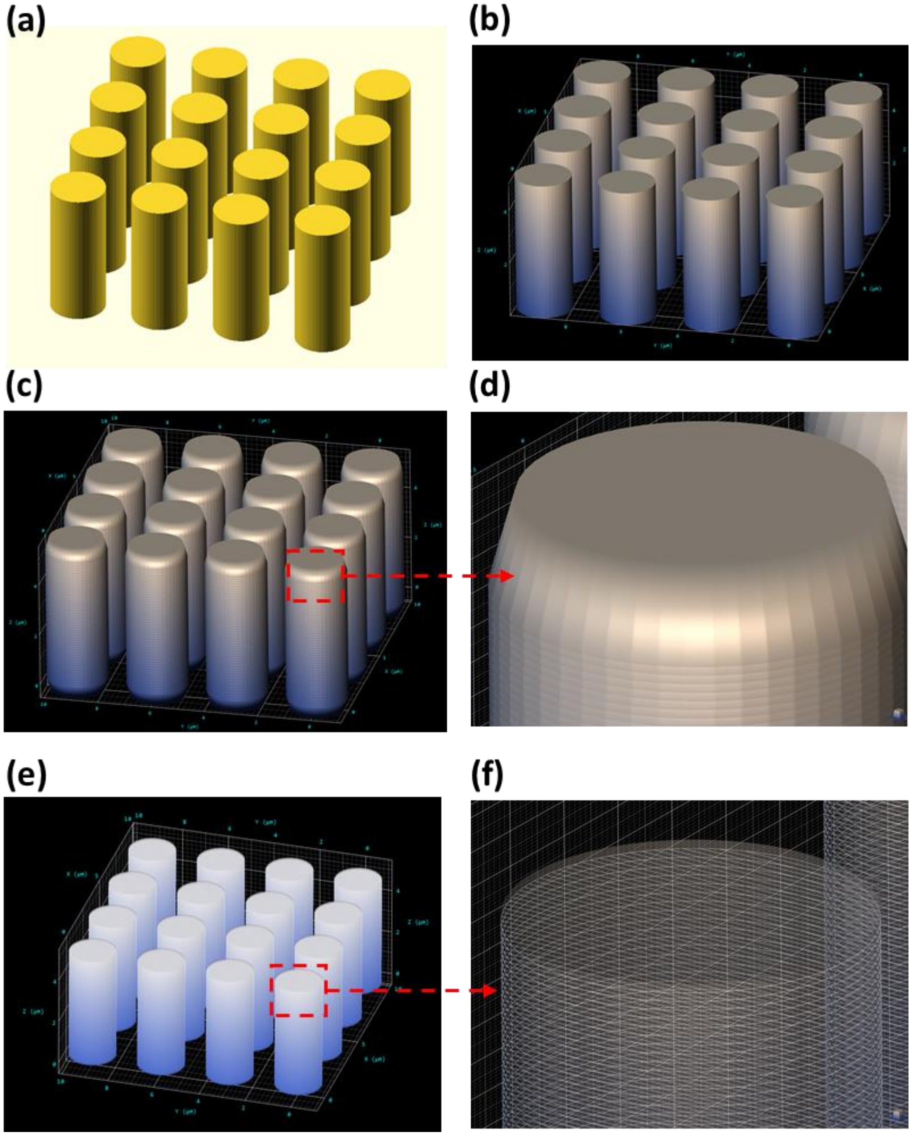

Figure 3.3: Process of designing the desired TPL geometry: (a) A cylindrical array created using CAD software (b) STL file imported into the DeScribe software, (c) A slicing procedure reduces the STL file into a stack of 2D layers of variable thickness, (d) zoomed image of the red dashed squared area in c, which shows the slicing in thin layers and further determines how each layer should be printed, (e) A hatching process separating each layer into a sequence of individual lines and (f) zoomed image of the red dashed squared area in e, which shows the separation between two consecutive laser beams.

Firstly, the software can import a 3D STL file which has been produced in a computer-aided design (CAD) package. Figure 3.3(a) shows an example of identical cylinders that are used to illustrate this point. The geometry is first sliced into 2D layers of a thickness defined by the user (here 50 nm, see Figs. 2.3c, d) and each of these layers is then separated into a sequence of individual lines in a hatching process (Figs. 3.3e, f). It is necessary to carefully select the slicing and hatching distances which define the gap between neighbouring lines to construct a structure resembling the original design. If one wants to build a solid 3D structure, one must set upper bounds for both the slicing and hatching distances equal to or less than the voxel height and width, respectively. Otherwise, one would merely construct a sequence of individual polymer lines. Overall, smaller slicing and hatching distances result in better reproduction of geometries [53], at the expense of longer write times. The second means to write a structure is entering a script directly into the Describe software. The script defines the 3D trajectory of the focus in a point-by-point fashion. This second means is thus more suited to writing structures that have length scales close to the laser spot size, of order 100 nm. All structures presented in this thesis have been fabricated using first method.

3.2.2 Optimising exposure parameters

A dose array is a collection of structures that each have their own set of fabrication parameters (see section 4.3.1 for further details). This is often the first step in engineering a new geometry because the parameters required to obtain a structure that closely resembles the initial design are highly dependent on the desired geometry. This entails using a variety of laser power and scan speed variations along the x-axis and y-axis (see Fig. 3.4a). For this thesis, the laser power varied from 15 to 45 mW in 5 % steps and scan speed varied between 2500 to 5500 μms^{-1} in 500 μms^{-1} steps. When the laser power/scan speeds were too low, the structures were absent as the density of free radicals was below the threshold required for polymerisation (see Fig. 3.4b).

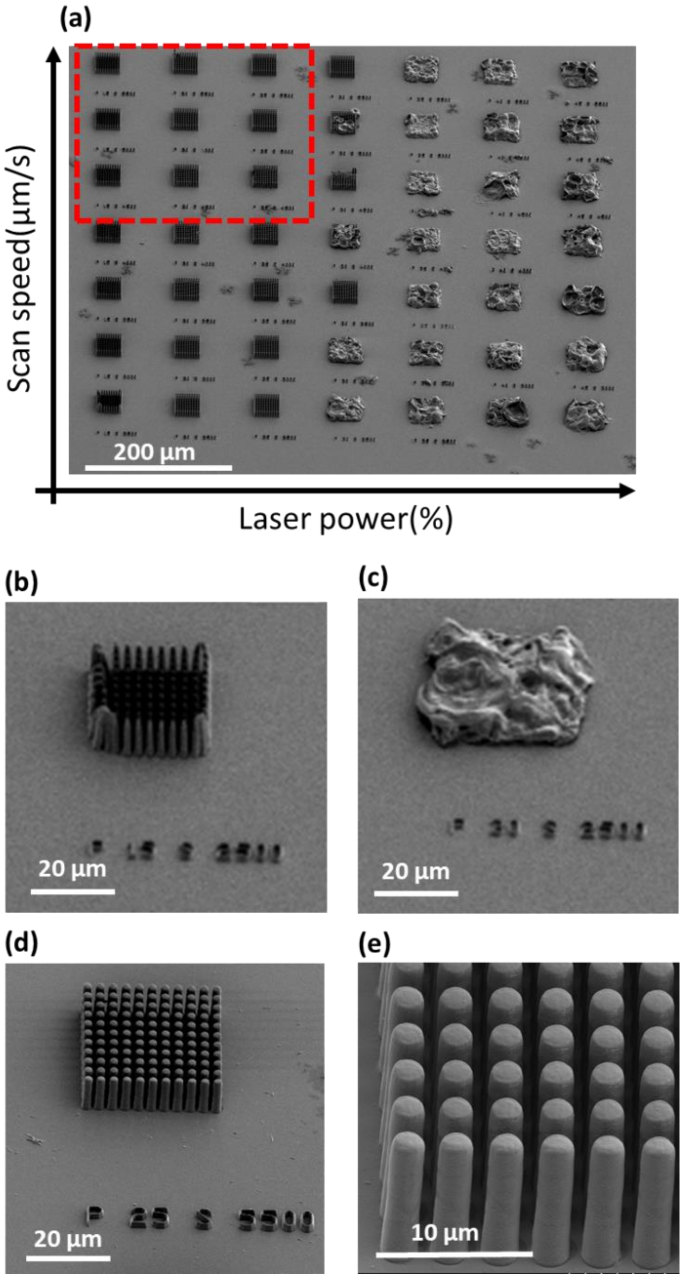

Figure 3.4: Scanning electron microscopy images of (a) disk dose array, laser power increases in step of 5 % (left to right) and scan speed increases in steps of 500 µms^{-1} (bottom to top), red dashed square shows optimal parameters that yields stable structures (b) disk array of 5 mW power and 2500 µm/s scan speed (c) disk array of 20 mW power and 2500 µm/s scan speed ,(d) disk array of 25 mW and 5500 µm/s scan speed and (e) a zoomed image of optimal array shown in d.

At the opposite end of the range, when the laser power/scan speeds were too high, the structures were destroyed as certain regions within the photoresist exhibit micro-explosions, due to rapid expansion of gas trapped within the resist (see Fig. 3.4c). In-between these two extremes an optimal parameter was found, with stable structures formed (see Figs. 3.4d, e).

3.2.3 Process for manufacture of micron-sized polymer cylinders

We now outline the specific TPL process used to fabricate polymer cylinders during this PhD. Further coating of the cylinders, with a $Ni_{81}Fe_{19}$ layer allowed the investigation into magnetism of these structures. All of the samples in this thesis were created using a negative-tone photoresist (IPL-780, Nanoscribe). Glass coverslips (22 mm x 22 mm x 0.2 mm) are utilised as substrates in this experiment; silicon wafers were not used because they are opaque and, hence, would prevent the laser from reaching the photoresist layer. Submersion in acetone is used to clean the glass coverslips and they are then put into an ultrasonic bath for 25 minutes before being treated with isopropyl alcohol (IPA) for approximately 10 minutes. The substrates are dried using a compressed air gun before fixing them to a holder using adhesive tape. There are ten positions on the holder which means an automated program can explore parameter space upon separate samples. Next, immersion oil (Immersol 518F), which has a refractive index of 1.518, is applied in the centre of the lower substrate surface while the negative-tone photoresist is placed on the upper substrate surface. A Nanoscribe photoresist (IPL-780) is employed throughout this investigation because it offers the greatest possible resolution and mechanical stability when compared to other photoresists. The sample holder is now placed into the TPL system in such a way that the oil faces the objective. The objective lens is elevated until it comes into contact with the immersion oil. The geometry file of choice is then placed on the computer, and the exposure routine is initiated.

As soon as the program is completed, the objective lens is lowered to prevent damage to the sample mount. The samples are gently separated from the mount before being immersed in propylene glycol methyl ether (PGMEA) for 25 minutes in a beaker. Using this development procedure, all excess unexposed photoresist and oil are removed from the substrate. However, because PGMEA leaves a residue, the substrates are put into a beaker of IPA for a further 2 minutes. During this time, any PGMEA residue on the coverslips is considerably diluted. The final step is to dry the samples gently using an air gun. The samples are now ready for next stage (metal deposition).

3.3 Thermal evaporation

There are numerous ways to in which metallic coatings can be deposited. Examples includes sputtering, electron beam / thermal evaporation and atomic layer deposition. One of the goals of this thesis is to explore well-defined 2D spin textures and then place 3D perturbations to determine the impact upon the remanent state and switching. Evaporation matches the aims of the project since it is a line of sight deposition that has a very high evaporative flux, normal to source. In fact, the flux Vs angle shows a delta function-like dependence [111]. In contrast, sputtering produces a deposition flux that is distributed across a wider range of angles. Whilst this may be useful for some structures that require sidewall coverage, it would be detrimental to the present study.

Thermal evaporation is a well-known process for depositing a thin layer. The source material evaporates in a vacuum, allowing the deposition of clean, low defect films. The rate at which the background gases impact the substrate must be lower than the rate at which the evaporating species impinge on the substrate. This is done so that the background gases do not react with the deposition, which would result in the production of oxides and nitrides. This means that evaporation must take place in an atmosphere consisting of a very high level of vacuum, usually less than 10^{-5} mbar. In order to avoid collisions with the molecules of the background gas while in transit, the mean free path has to be much longer than the distance from the source to the substrate, which is also referred to as the throw distance. The equation that describes the collision-free fraction N of a particle stream that is made up of N_o particles and moves in a gas x-direction is as follows [112]:

$$N = N_o e^{-x/\lambda} \text{ ,} with \;\; \lambda = (n\sigma)^{-1} \tag{3.2}$$

Where λ denotes the mean free path, n represents the particle density and σ represents the interaction cross-section. In a more rigorous procedure [113]:

$$\lambda = \frac{k_B T}{\sqrt{2}\pi d^2 p} \tag{3.3}$$

Where k_B is Boltzmann's constant, T represents the temperature in Kelvin, p represents the pressure of the gas, and d represents the diameter of the gas.

A large, bell jar thermal evaporator (see Fig. 3.5) is located in a class 1000 cleanroom, permitting the application of a uniform metallic film. The process entails weighing a solid piece of the metal $Ni_{81}Fe_{19}$ to be deposited and then placing it in a beaker filled with IPA before placing it in an ultrasonic bath for five minutes. After that, the metal is dried thoroughly using an air gun. The cleaned metal is inserted into the centre of an alumina boat and firmly secured between two electrodes. The samples are then placed on the holder which is installed at the very top of the chamber (source-substrate distance equal approximately 30 cm). Subsequently, the glass bell jar is installed and firmly pushed downwards. A roughing pump evacuates the chamber to a pressure of approximately 2×10^{-2} mbar, over several minutes. It is necessary to use a second pumping technique to produce a significantly lower pressure than this. As part of the roughing step, a liquid nitrogen trap beneath the chamber is filled with nitrogen. Once a sufficiently low pressure has been achieved, the valve is opened. The diffusion pump is then functional and brings the pressure down to suitable values. In order to produce $< 3 \times 10^{-6}$ mbar, the second pumping phase typically takes one to two hours, depending on the conditions. This pressure is generally considered sufficient to evaporate films in this thesis.

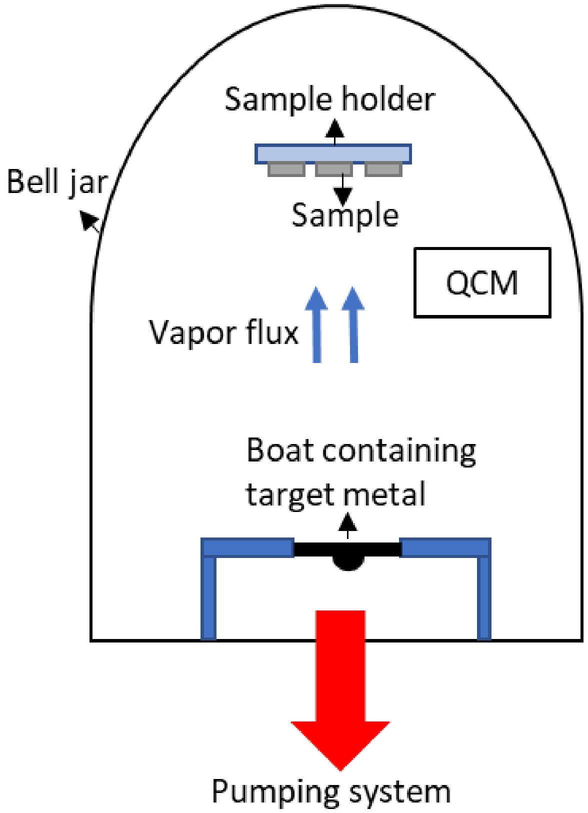

Figure 3.5: A schematic of the thermal evaporation system. The evaporation boat containing the metal is connected between two electrodes, the sample holder is placed at the top of the bell jar, and the quartz crystal monitor (QCM) is placed at the edge of the bell jar. The pumping systems (valve, N_2 trap, roughing and diffusion pump) are below the chamber.

A current of 80 A is applied across the boat to achieve the evaporating temperatures of $Ni_{81}Fe_{19}$. It is necessary to gradually increase this current to prevent a substantial rapid temperature change, which might cause the boat to break. The onset of evaporation becomes apparent when the quartz crystal monitor (QCM) registers a continuous deposition rate, at which point the shutter is opened. The QCM is based upon a quartz crystal that resonates at a specific frequency. As material is deposited, the resonant frequency of the crystal is slightly modified, allowing a quantitative measure of thickness.

To function, the density of the evaporated material, acoustic impedance, and chamber tooling factor (a calibration parameter) are required before one can measure the deposition rate and resulting film thickness. The tooling factor is a scaling parameter that takes into account the geometric separation between substrate and crystal monitor. A 40 nm deposition would take approximately 10 minutes on average because the films are generally produced at a rate of 0.1 − 0.2 nms^{-1}. Once deposition is complete, the shutter is closed, and the current is lowered to zero at a steady rate in a similar manner to how it was first increased. A minimum of one hour must elapse before the chamber can be vented, and the samples can be withdrawn from their holder.

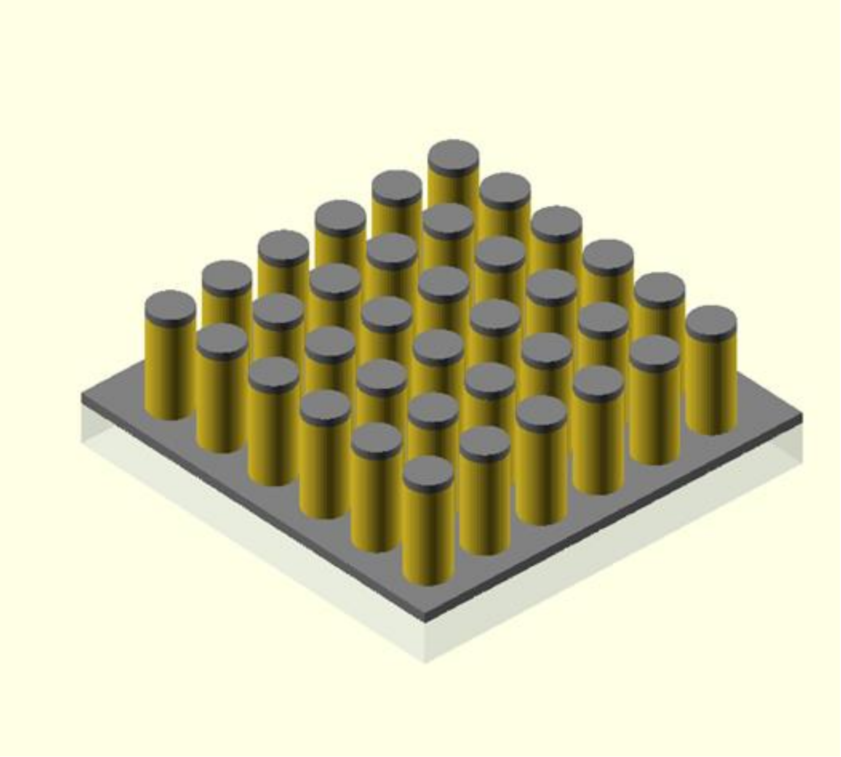

Figure 3.6: Idealised schematic of a cylindrical array after thermal evaporation was used to deposit $Ni_{81}Fe_{19}$. Yellow depicts the photoresist and grey depicts the $Ni_{81}Fe_{19}$.

Figure 3.6 illustrates shows an idealised schematic, of the sample after evaporation. It also shows that any metal deposited upon the cylinder scaffold is disconnected from the surrounding sheet film (5 microns below) which is essential when attempting to study the magnetic configuration.

3.4 Scanning electron microscopy (SEM)

The diffraction limit of optical microscopy with visible light wavelengths ranges from 400 to 700 nm, which is a significant factor that restricts low-dimensional study. Due to this, different approaches with better spatial resolution are required to analyse the physical characterisation of the materials on a nanoscale level. The use of scanning electron microscopy (SEM) has facilitated considerable improvements in microstructure characterization. The scanning electron microscope was developed during the 1930s and 1940s. The first commercialised scanning electron microscope was created in 1965 by the Cambridge Equipment Company following several instrument modifications [114]. A SEM is a surface inspection device that employs incident electrons and an electronic detector to obtain very high resolution and depth of focus on a surface under investigation.

Two SEMs were employed in this work: a Hitachi SU8230 and a Zeiss Sigma HD. Both systems use a field emission gun as the electron source. Specimens were placed on an SEM stub before being introduced into the chamber. The chamber was evacuated to a pressure below 1×10^{-4} mbar before imaging. Both systems were capable of tilting samples more than 45 degrees.

The basic layout of an SEM comprises of four main components: an electron optical system, a specimen chamber, a detecting system, and a presentation system. Electrons are created by an electron gun, whether a field emission gun (FEG), a thermionic gun, or a Schottky gun [2]. The electrons that comprise the beam are then accelerated by the positively charged anode which is located adjacent to the emitter and allows them to flow through the column and down to the specimen. In the arrangement depicted in Figure 3.7, the beam of electrons travels into the condensing lens along the axis of the column. These lenses have the function of focusing the beam into a tiny beam with a diameter of down to 10 nm. The object's surface is scanned using suitable placement of coils. Throughout this process, the electrons from the beam impact the specimen surface, scattering and generating secondary electrons which are then detected and used to create the image shown on the screen.

When the incoming electron beam interacts with the specimen, backscattered electrons and x-rays are also produced. A positive charged Faraday cage detector is used to gather secondary electrons in the typical mode of operation of the device. In addition, x-ray detectors can be used to determine sample composition.

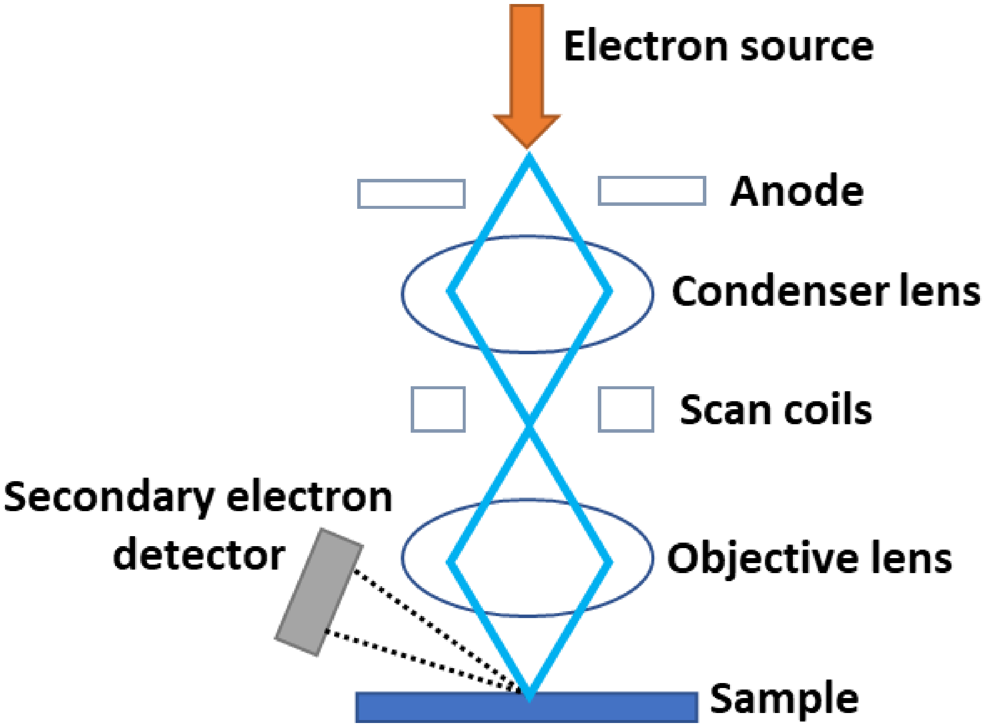

Figure 3.7: Schematic representation of the basic components of scanning electron microscopy.

3.5 Atomic force microscopy (AFM)

Binning, Quate and Gerber developed AFM in 1986 to address the challenges associated with measuring non-conductive materials using scanning tunnelling microscopy (STM) and other techniques [115]. It is quickly becoming the preferred tool for scientists studying surfaces in the fields of physics, chemistry, and biological research. The atomic force microscope (AFM) represents one type of scanning probe microscope (SPM). It is designed to measure with a probe, a local property such as topography, electrostatic field, or magnetic field. AFM measures forces between the sample and a sharp probe over a short distance to obtain a 3D profile of the surface on the nanoscale. The probe is supported by a flexible cantilever. The force between the probe and the surface is influenced by the distance between the sample surface and the probe (x), as well as the spring constant of the cantilever (k). Depending upon the specific mode, AFM can measure both long- and short-range interactions [116].

AFM can be operated in various modes, depending on the requirements, including non-contact mode, contact mode and tapping mode. Contact mode is a scanning mode where the tip of the AFM remains in contact with a surface while scanning at a very low force (see Fig. 3.8a). The deflection of the tip is measured as it scans over the surface. This procedure produces topographical maps of the specimen’s surface with resolution < 1nm [117]. However, because the cantilever tip is in constant contact with the sample, soft surfaces can be perturbed, which could affect both the resultant image and the quality of the material.

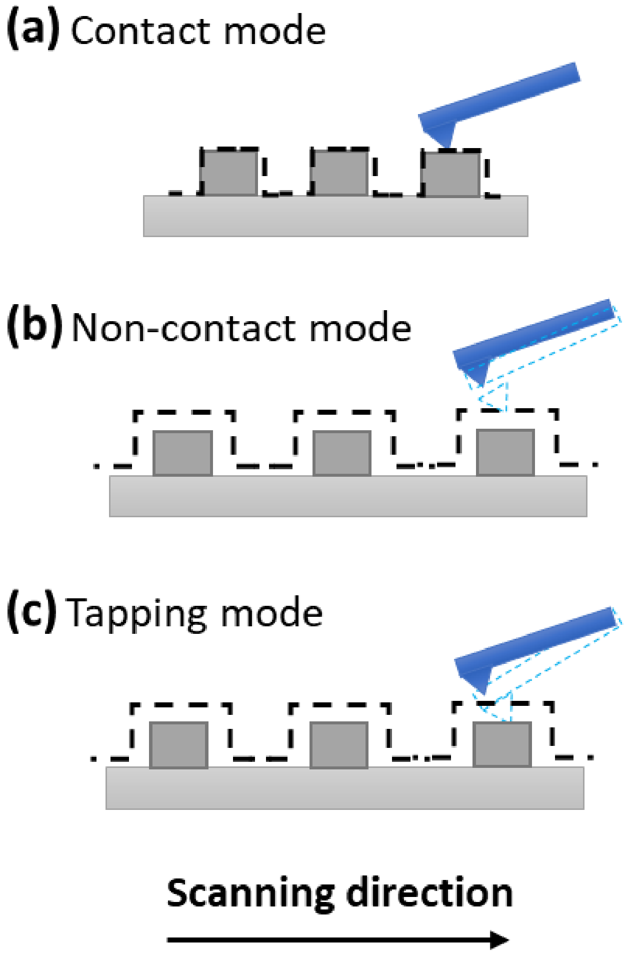

Figure 3.8: Schematics for different modes of AFM, including (a) contact mode, (b) non-contact mode and (c) tapping mode. The dashed black lines indicate the scanning profile.

A non-contact mode is possible and is illustrated in Figure 3.8(b). In this mode, the tip vibrates close to the surface at above its resonant frequency. The amplitude of the oscillations produced by these vibrations is often relatively small, falling below 10 nm [118]. With each oscillation upwards, the attraction of Van der Waals forces reduces the amplitude and frequency of the oscillations as the cantilever retracts from the surface. An extension of non-contact mode, so called tapping mode, excites the cantilever to vibrate at its resonant frequency while scanning the surface (see Fig. 3.8c). When the tip of the cantilever starts to contact the surface gently, a sensor reverses the cantilever, allowing the oscillation to continue. A feedback loop is used during the scanning process to monitor the oscillations and maintain a consistent amplitude. This is accomplished by moving the probe in the z-direction whenever a deflection is identified. This probe shift's magnitude is recorded, making it possible to map out the surface topography. During the course of this thesis, AFM was performed in a tapping mode in order to achieve high resolution scanning with minimal sample damage. Working in a tapping mode also allows magnetic contrast to be obtained upon a second pass.

The forces experienced by an AFM tip can be modelled in its simplest form by the Lenard-Jones potential which take the form

$$V_{Lennard-Jones}(z) = \epsilon \left[\left(\frac{\sigma}{z}\right)^{12} - 2\left(\frac{\sigma}{z}\right)^{6}\right] \tag{3.4}$$

This is often a suitable estimate for the short-range interactions. The well depth ϵ denotes the depth of the attractive well and the zero-potential distance σ denotes the interparticle distance where the potential changes sign. During the course of this thesis, AFM was operated whereby the tip is oscillated at its resonant frequency, operating in the attractive regime of the Lennard-Joners potential.

In Tapping mode, the cantilever is operated close to its resonance frequency f_0. The intrinsic spring constant k_0 and the mass m are used to calculate the cantilever's resonance frequency, which can be approximated as follows:

$$f_0 = \sqrt{\frac{k_0}{m}} \tag{3.5}$$

As the cantilever moves progressively closer to the sample's surface, the resonant frequency will change. The cantilever spring constant has been changed from its inherent value to an effective spring constant, resulting in this change [119]:

$$k_{eff} = k_0 - \frac{\partial F}{\partial z} \tag{3.6}$$

At greater tip-sample distances, when attractive forces predominate, the force gradient $\partial F \,/\, \partial Z$ is positive, and k_{eff} becomes less than k_0. Therefore, given a repulsive tip-sample interaction close to the surface, k_{eff}will become greater than k_0 as it approaches the surface. In Tapping mode, the variation in the effective spring constant and, therefore, the transition in resonant frequency is recognized as a shift in the oscillation amplitude. The identification of variations in the amplitude is more sensitive to adjustments in the tip-sample distance than variations in the static cantilever deflection.

The AFM Dimension 3100 is used for these measurements which was positioned on an air-cushioned table. The Dimension 3100 identifies nanoscale differences in topography by detecting small changes in laser reflection off the cantilever. A laser beam is projected down through the piezo tube and aligned manually by the user, the beam reflects off the top cantilever surface and onto a quadrant photodiode (see Fig. 3.9). Following the alignment, an automatic tuning operation is undertaken. This method uses a voltage to drive cantilever oscillations, scanning over a frequency range until the resonant frequency is determined. The AFM probe itself is a tiny (approx. 3 × 1 × 1 mm^3) rectangular silicon device from which an extruded microscale cantilever (approx. 200 × 30 × 3 µm^3) protrudes from one of the short edges. A sharp point emerges from the bottom surface. First, it is necessary to place a probe on a cantilever holder (about 2 × 2 × 0.5 cm^3), which is then held by a spring-loaded clip before mounting it on the AFM. Using this cantilever holder, the piezo tube can be securely fastened to the bottom of the piezo tube to start the measurements.

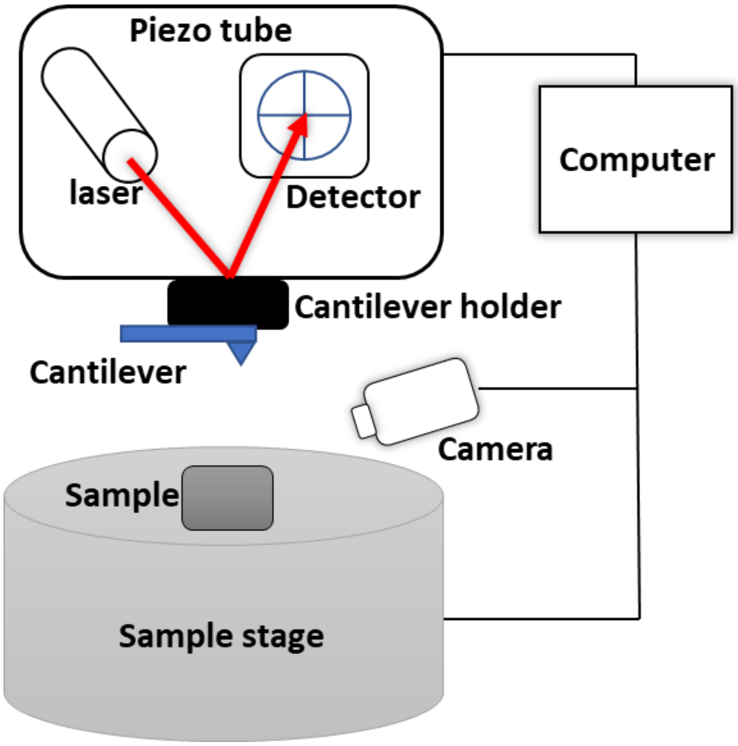

Figure 3.9: Schematic diagram of a setup for AFM Dimension 3100.

Many parameters can be tailored to improve the quality of the acquired image but the variables that are most typically investigated here are the amplitude setpoint, drive amplitude, number of lines, and scan speed. The amplitude setpoint maintains the oscillation amplitude via a feedback loop, as previously described.

The drive amplitude is a measure of the voltage used to drive cantilever oscillation. Increasing the drive amplitude yields an improvement in signal to noise at the expense of potential tip strike. By increasing the number of lines, the slow-scan axis line spacing is reduced and image resolution is increased. Scanning speed refers to the rate at which the probe travels down the fast-scan axis. While higher scan speeds save image collection time, they may also adversely affect image quality. Both the proportional gain and the integral gain feedback control affect the image quality [120]. To optimise these values, you should first increase the integral gain until oscillations are observed in the measured data, then reduce this value by several increments until no oscillations are observed and repeat this process for the proportional gain until no oscillations are observed [121].

The procedure starts by positioning a sample on the stage immediately underneath the piezo tube. The probe is lowered until it is within one millimetre of the substrate. The probe location with respect to the substrate is monitored by a camera linked to a computer. Once the substrate has been brought into focus, the user starts an engage procedure. The piezo tube now lowers the oscillating cantilever until it detects Van der Waal forces from the sample, at which point the oscillation amplitude reduces. When a user defined set-point is reached, the piezo starts scanning in the plane of the sample. AFM images are created by scanning along individual lines (fast-scan axis), with each line being scanned twice (trace and retrace) so that the probe returns to its initial position before shifting a predefined distance perpendicular to the fast scan-axis (slow scan-axis) and starting another line.

It is necessary to optimise AFM parameters, considering the image quality, measurement duration and any harm to the probe or sample. For instance, one may mistakenly believe that using a very low amplitude setpoint with a very high drive amplitude and scan speed might produce excellent quality data. However, in many cases, this combination would result in the tip contacting the sample, referred to as a tip strike. A bright line appears across the image instead of line topography and this has the potential to harm both the probe and the sample in this situation. AFM tip strikes are greatly influenced by the topography being measured; more prominent features along the z-axis enhance the likelihood of this happening, which is why AFM is often employed to investigate the properties of 2D materials. Another effect can be caused by tall features, whereby the probe encounters an edge and feedback does not allow the tip to respond within the time scale of line scan. The tall, micron-sized 3D structures used in this study may have the same issue to some extent.

However, careful optimisation of feedback settings has minimised this effect as confirmed by comparison to SEM images. Many studies have shown that AFM remains a powerful method, primarily when used in conjunction with an in situ secondary technique such as electric force microscopy or magnetic force microscopy, which is addressed in more detail below.

3.6 Magnetic force microscopy (MFM)

MFM is a complementary technique to atomic force microscopy (AFM), which employs a method comparable to imaging the magnetic configuration. The initial setup for MFM measurements is similar to described in Section 3.5 for AFM measurements. The MFM probes utilised in this thesis are from Nanosensors with a 40 nm CoCr coating and low magnetic moment ($0.5 \times 10^{-13}\mathrm{emu}$) which is comparable in size and shape to the AFM probes used in the previous section. Prior to installing the cantilever holder on the piezo tube, it is necessary to magnetise the probe parallel to the tip-axis; a 1 T permanent magnet is employed for this purpose. The MFM tips are magnetic along the z-axis of the tip, which is typically magnetized in a perpendicular direction to the sample surface. MFM typically only measures the component of the sample magnetization that is perpendicular to the sample surface.

MFM determines the magnetic configuration of a sample by analysing tiny differences in the cantilever oscillations that occur throughout the measurement. Deflections are created by interactions between stray magnetic fields coming from the sample and the probe tip, which can be approximated as a magnetic dipole. In the first step, the morphology of the sample is reconstructed as in the standard AFM tapping mode. After the profile of each line has been acquired, it is used to perform a second scan of the surface at a fixed tip-sample distance (lift mode), also referred to as the lift height Δz (see Fig. 3.10). At such values of Δz, only the long-range tip-sample interaction forces (i.e., electrostatic and magnetic) affect the cantilever motion. In the second step, the cantilever is set into oscillation at (or near) its first free resonance frequency f_0. Due to its magnetic coating, in the presence of magnetised samples the tip experiences a force, normal to the sample surface. Such a force produces variation in the amplitude A and a shift in the phase φ of the oscillation of the cantilever as well as in its first resonance frequency f_0 given by [122]:

$$\Delta A = \frac{A_0 Q_c}{2k_c^2}\left(\frac{\partial F_z}{\partial z}\right)^2 \tag{3.7}$$

$$\Delta\varphi = \frac{Q_c}{k_c}\frac{\partial F_z}{\partial z} \tag{3.8}$$

$$\Delta f_0 = -\frac{f_0}{2k_c}\frac{\partial F_z}{\partial z} \tag{3.9}$$

$$\Delta\varphi = \frac{\mu_0}{4\pi}\frac{12\pi Q_c}{k_c} m_s m_{ct} \frac{180}{\pi}\frac{1}{(\Delta z + h_{ts})^5} \tag{3.10}$$

where μ_0 is the vacuum magnetic permeability; k_c and Q_c are the spring constant and the quality factor of the cantilever, respectively; m_s and m_{ct} are the magnetic moments of the nanoparticle and the coated tip, respectively; $\Delta z + h_{ts}$ is the distance between the magnetic centres of the tip and the sample during the second pass.

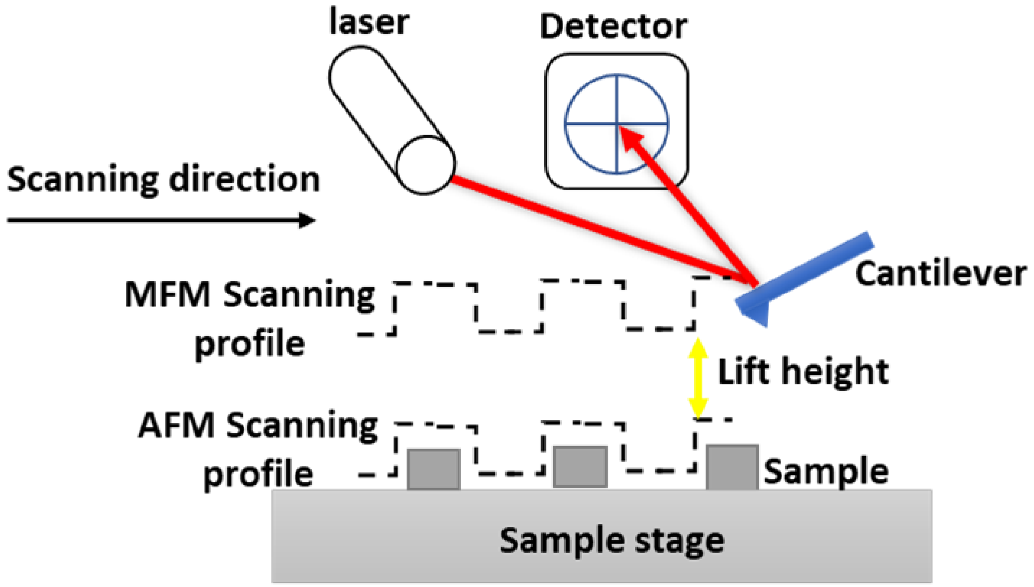

Figure 3.10: Schematic for the two-pass technique of the MFM. The AFM path is scanned first, before the probe lifts by a set height and performs a second scan.

If we assume that the sample produces a magnetic stray field H_{sample} to which the tip magnetization M_{tip} is subjected, the tip–sample magnetic potential can be written [123]:

$$U_{inter} = -\mu_0 \int_{V_{tip}} M_{tip} \, . \, H_{sample} dV \tag{3.11}$$

$$= -\mu_0 \int_{V_{sample}} M_{sample} \, . \, H_{tip} dV$$

Where M_{tip} and M_{sample} are the tip and sample magnetisation, H_{tip} and H_{sample} are the stray magnetic field associated with the tip and sample, V_{tip} and V_{sample} are the tip and sample volume. During MFM scanning, the probe resonant characteristics, such as the frequency and phase of the vibration, are continuously monitored through the detected laser signal discussed earlier. To simplify, assuming that the force and the direction of the cantilever are aligned in the z direction, i.e., the tip's magnetic dipole moment is along the z-axis and magnetization of x and y components of the tip are zero; and also, the magnetostatic forces arise purely from the magnetic dipoles in the tip interacting with dipoles in the sample. In this case, the magnetic force on the tip is the gradient of the magnetostatic interaction energy, and the force gradient depends only on the second derivative of the z-component of the sample stray field as shown in following equation [124]:

$$\frac{\partial}{\partial z}F_z = \mu_0\left(m_z\frac{\partial^2 H_z}{\partial z^2}\right) \tag{3.12}$$

Considering a magnetic sample that is saturated in-plane, a stray field will emerge at the sample extremities. The z-component of this stray field is shown in Fig. 3.11b. Taking the first derivative with respect to z, yields distinct positive/negative values of extremities. Consequently, MFM is sensitive to any where there is a changing stray field, such as around edges or areas in the sample where there is a finite divergence of magnetisation.

In the event of the probe experiencing an attractive force, k would soften, causing a reduction in the resonant frequency, detected as alterations in the aforementioned resonant characteristics. The majority of MFM images are provided as phase shift colour maps. The magnetic transitions are either dark or bright in MFM images, with dark representing an attractive force gradient and bright representing a repulsive force gradient. The resonant frequency of the cantilever shifts in response to a force gradient. Because of the attractive force and the negative force gradient, the cantilever essentially becomes softer, reducing the cantilever's resonance frequency which is indicated by a dark signal. On the other hand, the action of repulsive forces effectively makes the cantilever stiffer, raising the resonance frequency of the cantilever and resulting in a bright signal being observed (see Fig. 3.11).

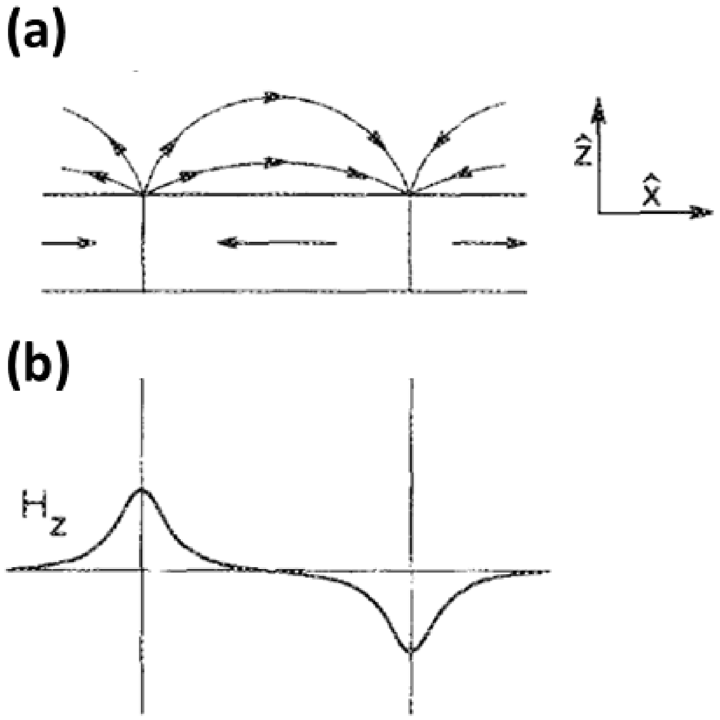

Figure 3.11: Sketch of (a) the magnetic stray field above an in-plane magnetised sample (b) typical variation of the H_z components above the sample [125].

The MFM image of a $Ni_{81}Fe_{19}$ micron-sized disks array developed in this thesis, under the application of a saturating field can be seen in Figure 3.12. Since the disks are magnetised, the z-component of stray field is only present at the sample extremities. Since MFM produces a signal that is proportional to derivatives in H_z, this yields lobes of different sign on either side of disks.

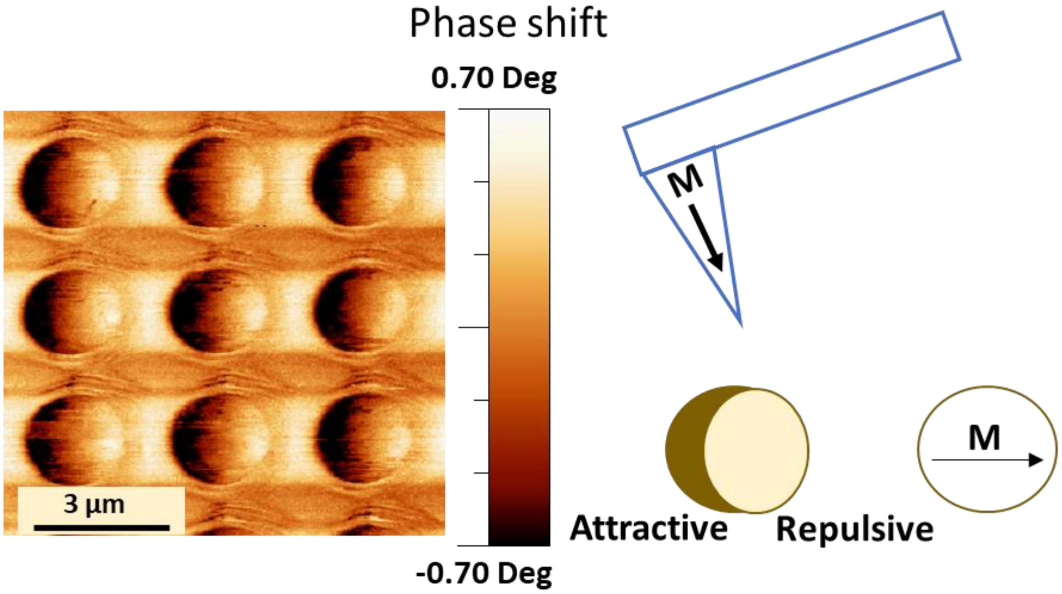

Figure 3.12: Magnetic image of $Ni_{81}Fe_{19}$ disk array (left) and schematic drawing (right) illustrating the contrast of MFM in phase shift mode. The magnetisation of the disks points from dark to bright under a saturating in-plane magnetic field.

Standard MFM systems are often not well suited to the investigation of magnetic switching and the magnetisation process. As a result, this thesis employs a custom-made electromagnet (see Fig. 3.13) installed on the sample stage. This enables the application of an in-plane magnetic field to a sample. The electromagnet is attached to a power source that can be manually adjusted to change the current being provided which changes the applied magnetic field that is being produced along the A-C axis. Although the magnet is a quadropole configuration, a current was only applied to a single pair of poles at a time.

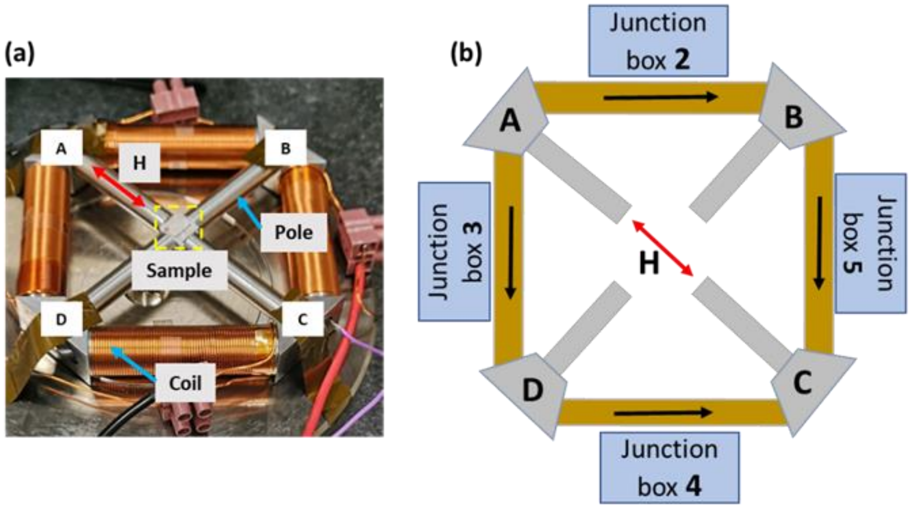

Figure 3.13: (a) Annotated photograph of the electromagnet seated on the AFM stage and a sample (7 mm × 7 mm) is mounted on an SEM stub between the magnet poles, (b) A diagram showing how the coils are connected to a power supply in parallel so the field is produced between the A-C direction (as indicated by red arrow).

It was critical to calibrate the electromagnet before testing with a sample. A Hall probe was suspended directly between the two active poles while the current provided to the electromagnet was varied. This field-current dependence is shown in Figure 3.14 for the positive and negative field directions, with a residual field of ≃ ± 1.2 mT. A linear relationship was found after the first data point in both directions. Hence the I = 0 data points have been ignored when computing the gradient of either dataset. The positive and negative slopes provide gradients of (10.36 ± 0.04) mT/A and (9.87 ± 0.04) mT/A, respectively, indicating that this electromagnet has a current-field relationship of ≃ 10 mT/A. Magnetisation processes were investigated in this work using magnetic fields applied during MFM scanning.

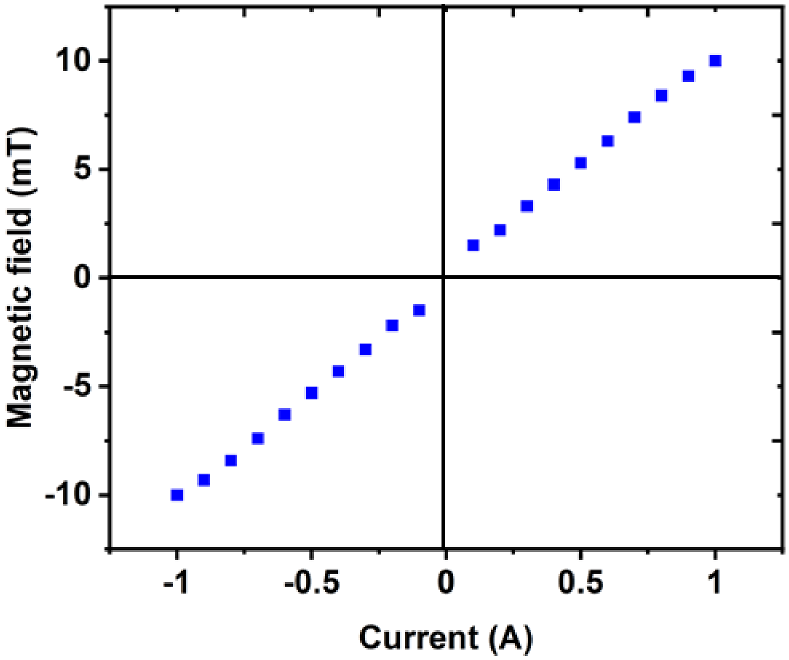

Figure 3.14: Relationship between the applied current and the magnetic field produced by the electromagnet along the A-C axis. A residual remanent field of ≃ ± 1.2 mT is present in the absence of current.

After capturing MFM images, the data often requires processing to assist with visual observations and this is typically performed using WSxM. Firstly, lines generated due to tip strike were removed, particularly when measuring a topography with significant features along the z-axis. This involves selecting the line/lines that need to be removed. These are then replaced by an average of the data that is directly above and below the removed lines. Secondly, the precise magnitude of the measured phase can vary from image to image, so a manual adjustment of the contrast/brightness is typically performed in order to aid comparisons between images.

3.7 Micromagnetic simulations

In order to understand the magnetic behaviour of fabricated systems, micromagnetic simulations were utilised. Various software packages are now available, some of which are commercial, some available as freeware, and others are privately produced. Simulations are useful, both for trying to understand the behaviour of established experimental systems but also for guiding fabrication of new structures. For example, magnetic disk samples have a number of separate phases, including single domain, vortex and multidomain. Simulations can help to ensure the target phase is achieved experimentally.

The two approaches for running micromagnetic simulations are finite element (FE) and finite difference (FD) simulations (FD) [126]. Figure 3.15(a) illustrates how a tetrahedral mesh is used to map the structure in a finite element simulation. The model of the system is tessellated into several triangular regions. In contrast, the finite difference method utilises cubic means to discretise the geometry (fee Fig. 3.15b).

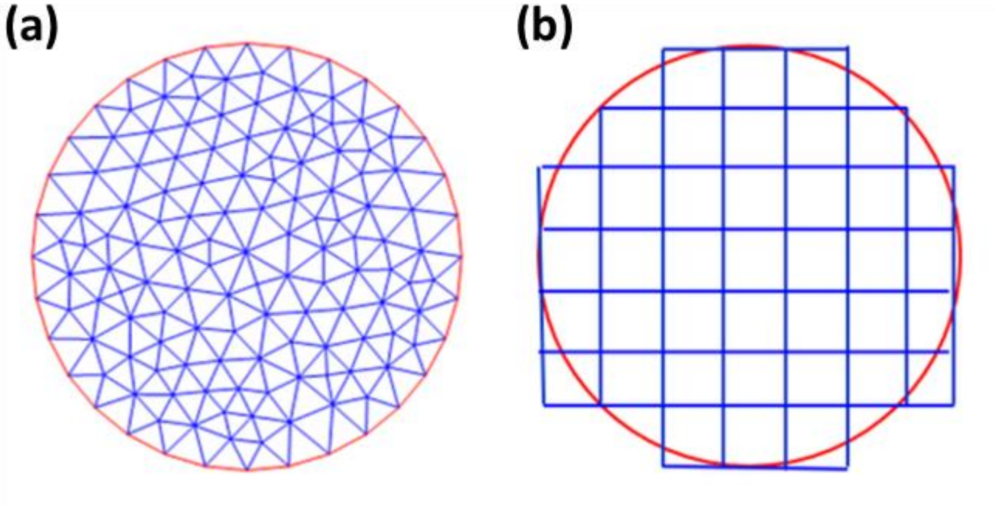

Figure 3.15: Approximation of the disk mesh using (a) finite element (b) finite difference approaches [127].

Micromagnetic simulations were performed here using the MuMax3 code [128]. Using a finite-difference (FD) discretisation technique, it is possible to simulate spatial and time-dependent magnetisation dynamics using this software. The simulation space is discretised into a grid of orthorhombic cells parallel to one another. The process of defining the simulation mesh entails determining the simulation size (the number of discretisation components or cells and the dimensions of the unit cell) depending on the size of the magnetic system under consideration. Following that, the geometry of a magnetic element is defined, and a material area and an initial magnetisation are assigned to each of the magnetic elements in the system under consideration. The number of cells required for effective and rapid computation must be a number stated as a power of two.

The size of the cells is another significant factor to consider when configuring the geometry. The cell edge length must be lower than the exchange length l_{ex}= $\sqrt{A/\mu_0 M_S^2}$ [36] to ensure an accurate simulation of the system. In this approach the magnetisation that travels from one cell to another is not subjected to abrupt shifts. To start, it is advised to test any magnetic scalar entity such as a remanence magnetisation or a coercive field and observe how it changes with cell size before proceeding with a full set of simulations. It is expected that this magnetic entity will converge to a specific value when the cell size decreases in an ideal situation. It is recommended that this number be treated as a critical value or as the maximum allowable size of the cell and utilised for the simulations [126].

Periodic boundary conditions ($PBC(x, y\ , z)$), involves mirroring the geometry along specific axes, in order to approximate the magnetostatic interactions within an array. The use of PBC facilitates the running of simulations on large magnetic systems in a shorter amount of time due to the reduction in calculation time [128]. Mumax3 solves the Landau–Lifshitz–Gilbert equation [129], to evolve the magnetisation with time:

$$\frac{dm}{dt} = -|\gamma_P| m \times H_{eff} + \left(\frac{\alpha_D}{m_s}\right)\left(m \times \frac{dm}{dt}\right) \qquad (3.13)$$

Where γ_P is the gyromagnetic ratio, defined as the ratio of magnetic moment to angular momentum and has units of rad/s/T or Hz/T, α_D is a dimensionless

Gilbert damping coefficient and $\mathrm{H_{eff}}$ is an effective magnetic field (T). For systems in this thesis, H_{eff} is defined a

$$H_{eff} = H_{zeeman} + H_{exchange} + H_{dipolar} \qquad (3.14)$$

The equation of motion, as seen in 3.13 has two terms. The first term, $m \times H_{eff}$ describes the precessional motion of the magnetisation whilst the second term $\left(m \times \frac{dm}{dt}\right)$ describes an effective damping. Figure 3.16 shows the trajectory of the magnetization (dashed line) drawn under the assumption that the effective field H_{eff} is constant. One can see that the first term on its own would simply yield infinite precession of the magnetisation. The second term, which can also be written as $-m \times (m \times H_{eff})$, tries to align the magnetisation with the field. The resultant motion is precession that decays into the field direction.

During field application protocols, at every increment each moment will attempt to align with H_{eff}, such that θ exhibits the time-dependent response $d\theta/dt$. Each step is only completed when the system is settled, which occurs as $d\theta/dt$ tends towards zero, eventually falling below a user-defined threshold value. Time-dependent simulations allow users to observe the spin dynamics which occur during this settling process.

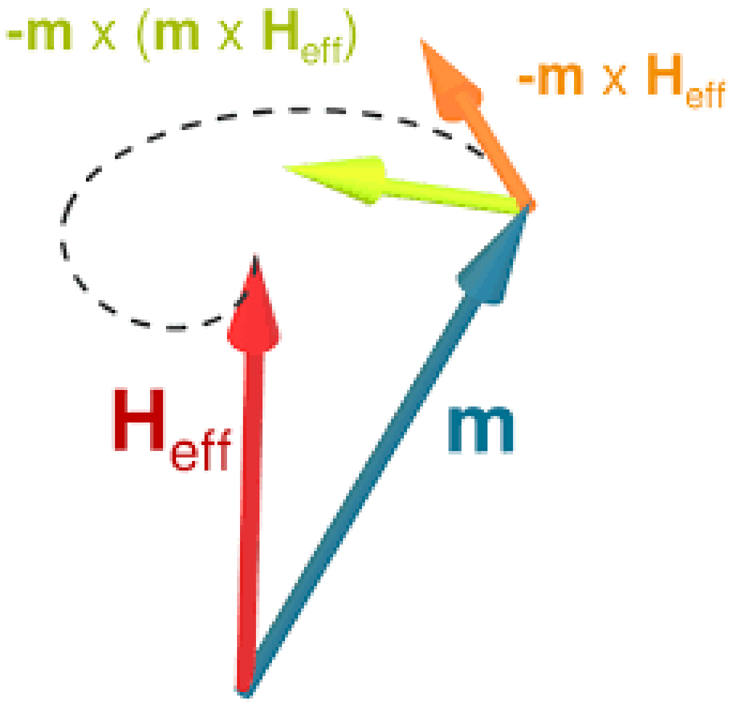

Figure 3.16: The terms in the Landau-Lifshitz-Gilbert equation: orange arrow denotes the precessional component, whilst the green indicates the damping term [130].

Two functions (relax and minimize) can be used to assess the ground state of a system in order to determine its stability. The former seeks to determine the system's energy minimum. It makes the precession term in (Eq. 3.13) ineffective, i.e., α = 0, so that the effective field is directed towards minimizing the total energy of the system. When the ground state is approached from the random magnetisation state or when the shift in the system's energy is highly substantial, the relax function is more appropriate than the other functions.

With the minimize function, an attempt is made to reach the lowest possible energy state by employing the conjugate gradient method. This function is most appropriate when the change in energy is minimal. The minimize function can be employed to evaluate a sudden energy shift. The system ends up in some local minima but not in the true energy state. As a result, the minimize function is well suited for the computation of magnetisation loops.

Typical parameters for $\mathrm{Ni_{81}Fe_{19}}$ (the saturation magnetization $Ms = 8.6\,x\,10^{5}\,A/m$, the exchange constant $A = 1.3\,x\,10^{-13}\ \mathrm{J/m}$, the gyromagnetic ratio γ = 2.954 GHz/T, the damping factor 0.01, negligible magnetocrystalline anisotropy) and a 4 × 4 × 4 nm^3 cell size was used in all of the simulations here. This cell size is still below the exchange length of $\mathrm{Ni_{81}Fe_{19}}$, which is $\sqrt{A/\mu_0 M_s^2} \simeq$ 5.7 nm [131] when considering the parameter values given above. All simulations were also conducted without the consideration of thermal effects (T = 0 K). When comparing these simulations to experimental measurements at room temperature, one can expect an increase in coercive field of approximately a factor of 5, in the modelled result [132]. Despite this difference in H_c, the spin texture itself is believed to show a strong agreement between simulations and the experimental equivalent [44].

4. Chapter 4

Paving the way to 3D nanostructured magnetic elements

4.1 Introduction

This chapter outlines a novel fabrication procedure to realise 3D nanostructured magnetic elements. The emphasis in this preliminary study is to initially realise well known spin textures, after which 3D defects are used to perturb the remanent state and switching. This is accomplished by harnessing a negative resist with two-photon lithography (TPL) to produce 3D structures with the projection of well-studied geometries, well above the substrate surface. Use of simple evaporation then allows the magnetic coating to take the underlying geometry of the patterned structures. Two-dimensional (2D) arrays of cylindrical structures with target diameter 2 µm and height 5 µm were fabricated using TPL and a 40 nm thickness of $Ni_{81}Fe_{19}$ deposited on top, yielding an effective 2D array of ferromagnetic disks raised above the substrate. Scanning electron microscopy (SEM) was used to image the disk arrays and the distribution of feature sizes within arrays were investigated. The average diameter was found to be 1.96 ± 0.06 µm, close to the design. Atomic force microscopy (AFM) was used to image the surface topography of the nanostructured array. The root mean square (RMS) roughness of elements was found to be 4.5 ± 0.3 nm for the plain arrays and 8.0 ± 0.7 nm for the arrays with 3D defects. After initial proof-of-principle, samples were fabricated in regimes of high magnetostatic (MS) coupling, with lattice spacing of 3 µm and low magnetostatic (MS) coupling, with lattice spacing of 4 µm. Magnetic force microscopy (MFM) was employed to image the spin texture. Both samples, measured at remanence, showed sharp contrast in the disk centre consistent with a vortex state configuration. Applying an in-plane magnetic field also yielded typical vortex reversal characteristics, with translation of the vortex core in a direction transverse to the field, annihilation of the core, re-nucleation and relaxation back to the centre. With this milestone in place, a detailed comparison was carried out between the high MS array and low MS array. The high MS array showed a remanent state consisting of almost a single chirality whilst the low MS array showed equal chirality distributions. The investigation shows that the magnetostatic interaction plays an important role in the magnetization process for ferromagnetic micron disk arrays with small interdisk distances. Furthermore, the increased magnetostatic interaction is found to increase the vortex annihilation and re-nucleation fields.

With this feasibility of producing well-known spin textures being shown, arrays of disks within the high MS regime were produced with a 3D hemispherical defect upon the surface. This perturbation was found to significantly alter the remanent state and magnetisation reversal. In disks with the defect, the vortex annihilation and re-nucleation occurred at lower fields than the plain disks in high MS array. Furthermore, it is found that upon relaxation, a specific chirality preference is shown.

To realise initial feasibility of the fabrication approach, a test sample was first produced which contained a number of 3D nanostructured polymer geometries with a $Ni_{81}Fe_{19}$ deposition (40 nm) at normal incidence. As shown in Figs. 4.1(a, b), the polymer structures are 1.5 μm in height and have a variety of aspect ratios. Dark lines between the consecutive lines of polymerised material are caused by slight undulations between adjacent lines of polymerised material [133]. To understand this, it is necessary to recall that TPL generates 3D geometries by tracing an ellipsoidal voxel along individual lines to build sample.

It is possible to reduce the appearance of undulations by further optimising the hatching parameter, which determines the distance between individual lines in the substrate plane (discussed in chapter 3). Despite this, the preliminary sample serves to show initial proof-of-principle in realising well-defined states seen in two-dimensional systems.

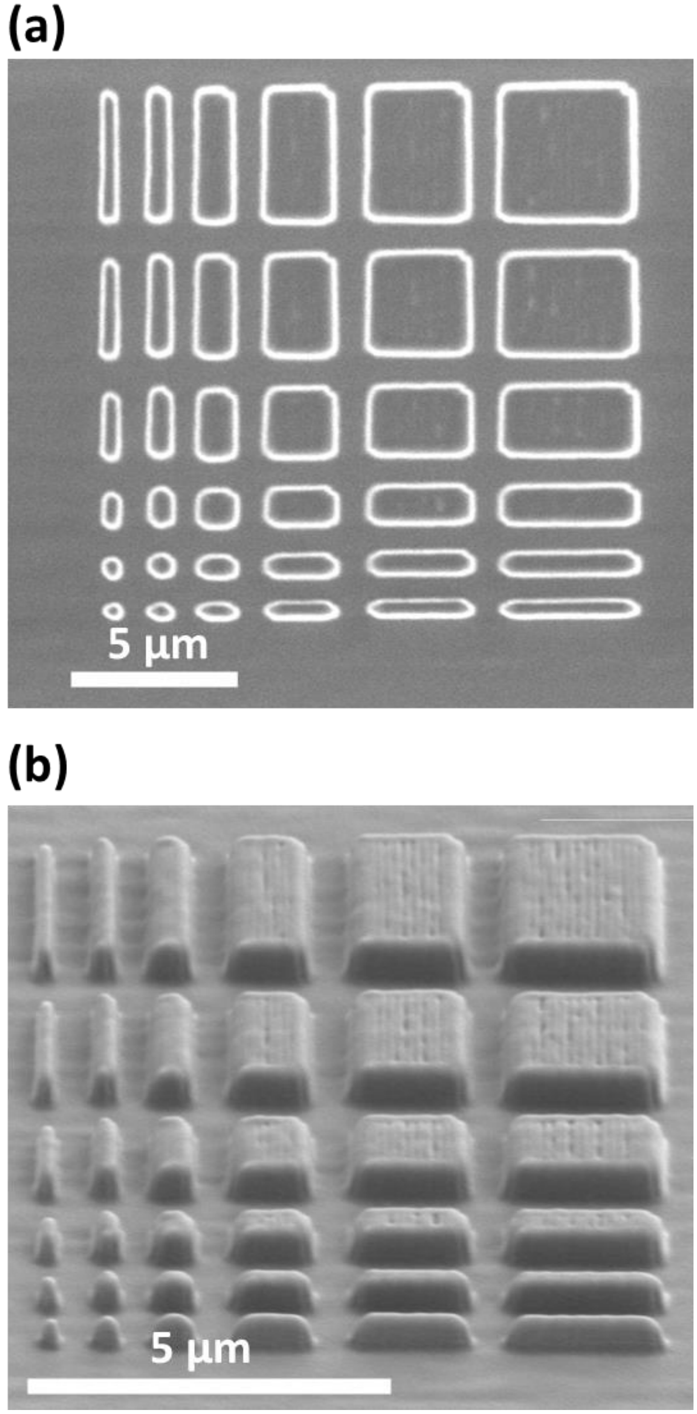

Figure 4.1: SEM images for $Ni_{81}Fe_{19}$ islands from (a) a top-down view as well as at (b) a 45° tilt with respect to the substrate plane.

Figure 4.2 shows the AFM and MFM data obtained upon the test sample using a low-moment MFM probe. First and foremost, it is essential to ensure that the topography in the AFM data is meticulously followed, enabling this to be compensated for during the second pass so as to acquire reliable MFM data. The AFM image in Fig. 4.2(a) demonstrates good agreement with the SEM image in Fig. 4.1(b), indicating that the AFM probe closely monitors the 3D topography. It can be seen in Figure 4.2(a) that the borders of the nano and microstructures are sharp and clearly defined, which is evidence that the feedback parameters have been appropriately optimised. This helps to develop confidence in the MFM data shown in Figure 4.2(b).

Each magnetic island shown in Fig. 4.2(b) was discovered to have a distinct domain structure, depending upon their aspect ratio and consistent with literature [134]. Islands surrounded by the yellow dashed lines have an aspect ratio of 1:1, are found to be in a multi-domain state with a Landau pattern consisting of four domains. These domains are depicted by two dark lines extending from the centre to the lower left and from the centre to the upper right. Also, two bright lines extend from the centre to the upper left and from the centre to the lower right [135]. Since a 1:1 aspect ratio result in each boundary creating a demagnetisation field that is equal in magnitude, this configuration is anticipated. Four domains are produced, each of which is divided by DWs with a rotation angle of 90° to accomplish flux closure and a minimum in the magnetostatic energy. As discussed in chapter 3, conventional MFM is sensitive to d^2H_z/dz^2 and as a result is sensitive to domain walls and edges, for in-plane magnetised systems [136]. An aspect ratio of 4:3 (blue dashed lines), results in a domain structure that is comparable to that of previous islands; however, the increased length results in asymmetric demagnetisation fields at both the long and short boundaries. The magnetisation along the long axis is not constrained since this asymmetry is not significant enough.

Increasing the aspect ratio (red dashed lines) results in a flux-closure domain pattern once again, but with an increased number of domains, to compensate for the greater demagnetisation field, along the short axis. In particular a pattern that resembles a single crosstie state is seen due to the increased shape anisotropy [137]. The specific configuration of the islands bordered by green dashed squares in Figure 4.2(b) shows an increased number of domains. However, it is difficult to characterise these islands' exact configuration due to limited image resolution. It is anticipated that these islands will have a double-cross-tie state or a double-diamond structure [138].

Above an aspect ratio of 4:1, several single domain islands are evident. These islands are recognised easily since they have opposing contrast at wire extremities and in Fig 4.2(b) have a purple dashed border. Compared to other islands, this configuration results in significantly greater stray fields and, therefore, magnetostatic energy; nevertheless, the amount of exchange energy produced is reduced since there is only a single domain present. The presence of this configuration suggests complex 3D magnetic nanowires will also be possible, but this is not studied in this thesis. Finally, an artefact can be seen in the MFM data which consists of stripes with bright and dark contrast, located just above each row of nanostructures. There is a consequence of an abrupt change in topography, corresponding to island edges.

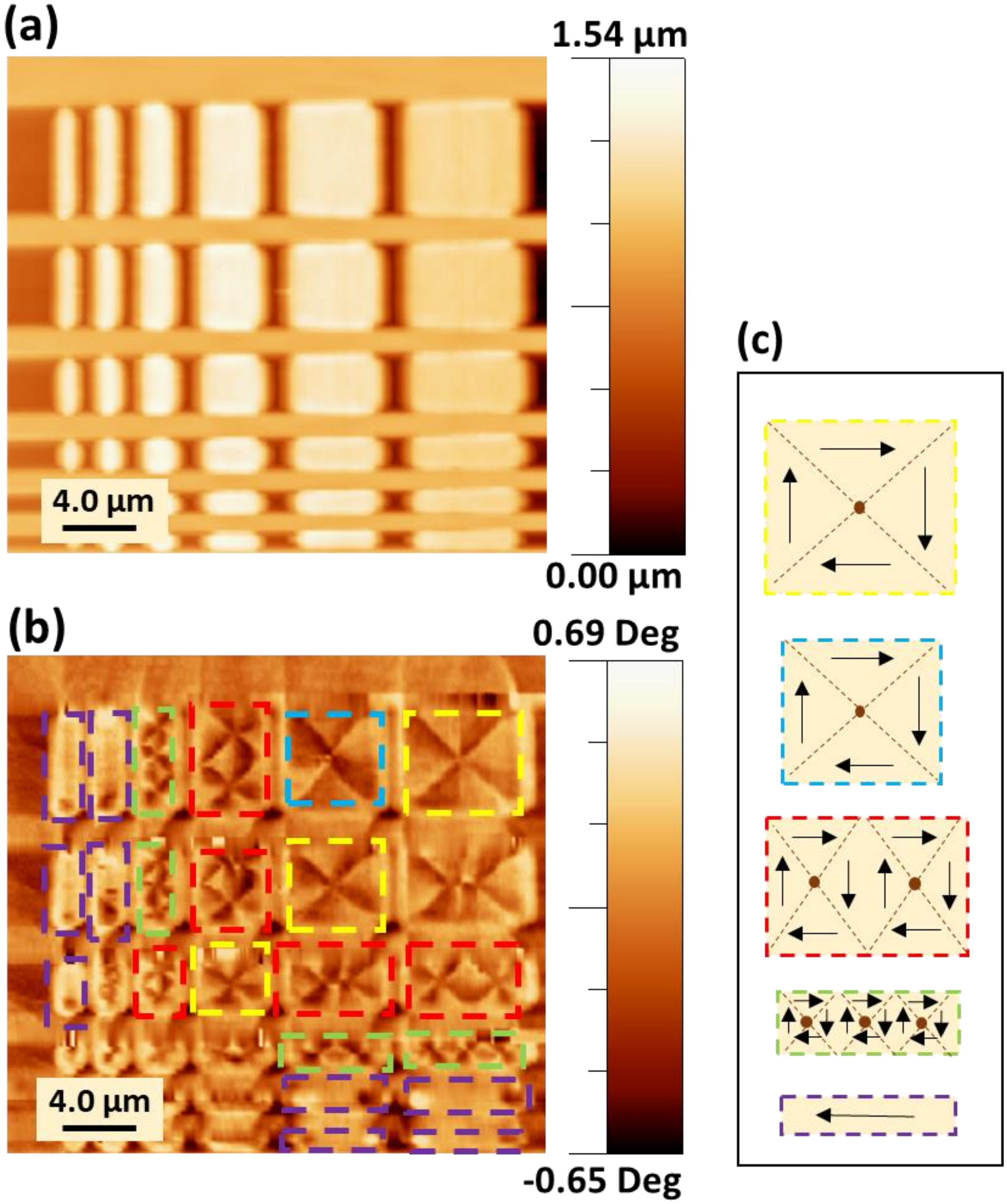

.

Figure 4.2: (a) AFM and (b) MFM images of an array of $Ni_{81}Fe_{19}$ islands at remanence. Yellow dashed lines have an aspect ratio of 1:1, blue dashed lines have an aspect ratio of 4:3, red dashed lines depict an aspect ratio of greater than 4:3, green dashed lines have an aspect ratio of 4:1 and purple dashed lines depict an aspect ratio of greater than 4:1. (c) Schematic showing magnetisation of each of coloured lines in b.

This section has shown that combining TPL and thermal evaporation to deposit a thin layer of $Ni_{81}Fe_{19}$ onto a 3D polymer scaffold may result in the formation of complex magnetic states, comparable to those seen in conventional 2D structures. Furthermore, MFM can directly image the magnetic configuration of such structures, which provides a foundation for constructing and probing 2.5D magnetic systems (systems that are restricted to a two-dimensional (2D) plane with limited access to a third dimension).

4.2 Magnetic Vortices in Py disk Structures

In a single magnetic disk, the magnetic state is governed by geometrical parameters such as the diameter and thickness. In two or more magnetic disks the separation distance and lattice arrangement also becomes important due to the magnetostatic interaction [26]. Since magnetic vortex states have complete flux closure, in the remanent state magnetostatic interactions are negligible. However, application of an in-plane magnetic field breaks the symmetry of the flux-closure, resulting in magnetic charge formation at the disk edges. The overall magnetic properties are hence altered when the separation distance is considerably less than the diameter [27, 139]. This implies that the separation distance can be modified to tune the global magnetic ordering of the array, and potentially the switching in individual disks.

An investigation of how disk diameter (25-3000 nm) and thickness (20-40 nm) affect the magnetic configuration was performed in this work but is not shown here using micromagnetic simulations. This was performed to confirm the previous work conducted in the literature and was shown to be consistent with what has been observed [17, 140]. Simple consideration of micro-magnetic energies suggests exchange dominated systems for low thicknesses and diameter, yielding a single domain system. For larger diameters and thicknesses the magnetostatic energy, which scales with volume, eventually dominates, yielding a vortex state. Figure 4.3 shows results of simulations demonstrating the single domain and vortex regime. Figure 4.3(a) is the result of a simulation with diameter of 50 nm and 25 nm thickness yielding a single domain state, with uniform magnetisation throughout the centre and some canting at the edges. Figure 4.3(b) shows the result of a simulation with diameter of 2 μm and thickness of 40 nm, which shows a vortex state with the magnetisation vectors remaining parallel to the edges, minimising the magnetostatic energy and a core at the centre where the magnetisation is out-of-plane.

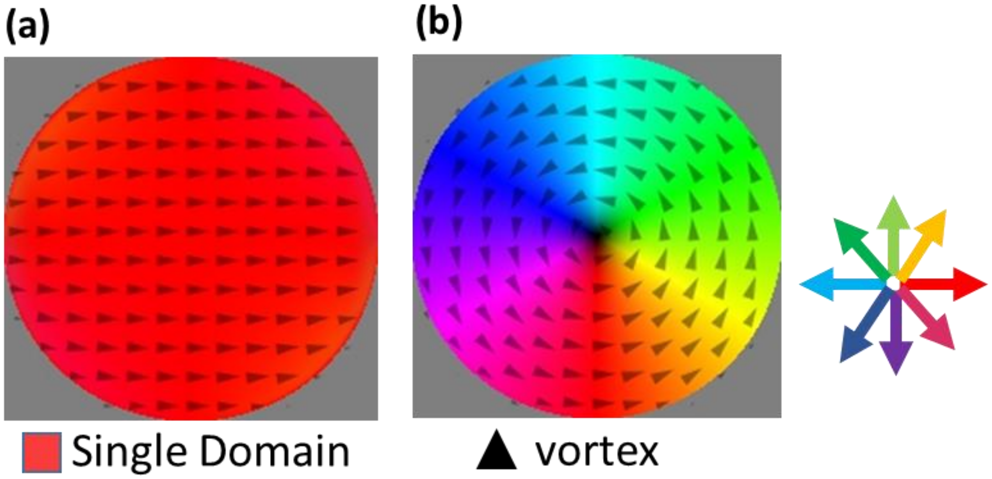

Figure 4.3: Micromagnetic simulation for (a) disk of 50 nm diameter and 25 nm thickness, showing a single domain state [17]. and (b) disk of 2 μm diameter and 40 nm thickness, showing a vortex state [140]. Colours represent the direction of magnetisation as depicted in the colour wheel. In both cases, the magnetisation was aligned along the positive x-axis prior to relaxation.

4.3 Experimental details

Based on previous simulations carried out as part of this thesis, fabricated samples consisted of cylinders with a diameter of 2 μm, height of 5 μm and with $Ni_{81}Fe_{19}$ thickness of 40 nm. These samples were fabricated in a high magnetostatic coupled regime (high MS array), with simple square lattice spacing (a, distance from centre to centre) of 3 μm as depicted in Fig. 4.4(a) and a low magnetostatically coupled regime (low MS array), where a was equal to 4 μm, as depicted in Fig. 4.4(b). Since the resolution of the TPL system is about 200 nm, any attempt to fabricate disks of ~200nm in diameter, commonly seen in the literature today would yield a curved ellipsoidal system due to the point spread function geometry. Therefore, the focus here is on larger systems of order microns, which can be reproduced with adequate resolution.

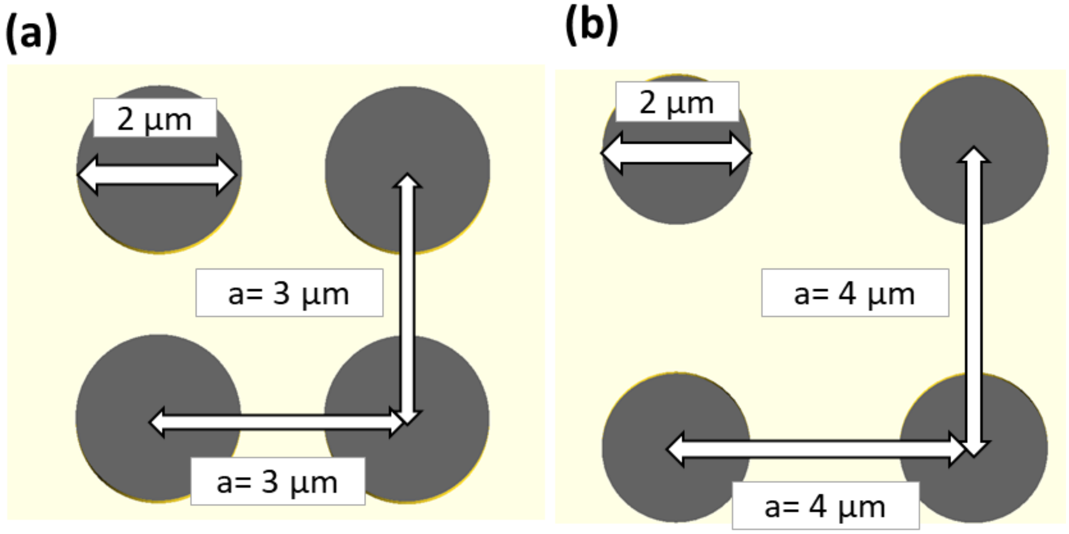

Figure 4.4: A schematic of the realised cylinders with a diameter of 2 µm and (a) high MS array with simple square lattice spacing, a, of 3 µm and (b) low MS array with lattice spacing of 4 µm. Note that a is measured from centre to centre.

4.3.1 Optimisation of process parameters

It is well known that the magnetic configuration of sub-micron elements is heavily dependent upon the intrinsic roughness of the substrate. Such samples have traditionally been fabricated upon Si which has roughness of <1 nm [67, 140]. Since the magnetic structures in this study are grown upon a polymer, it is important to investigate how roughness varies with TPL process parameters such as laser power and scan speed. Cylindrical structures, of the relevant dimensions were fabricated using TPL in a negative resist. The laser power and scan speed were varied, resulting in a dose array as shown in Figure 4.5 whereby the laser power varied from 15 to 45 mW in 5 % steps and scan speed that varied between 2500 to 5500 µm/s in 500 µm/s steps. When the laser power or scan speeds were too low, the structures were absent as the density of free radicals generated within the resist was below the threshold required for polymerisation. At the opposite end of the range, when the laser power/scan speeds were too high, the structures were destroyed as certain regions within the photoresist exhibit micro-explosions, due to rapid expansion of gas trapped within the resist. Between these two extremes, a range of optimal parameters were found, with stable structures formed.

4.3.2 Morphological characterisation of plain disk arrays

The optimal range (red solid square), with laser power varying between 15 – 25 mW and scan speed varying between 4000 – 5000 μm/s were then subject to a 40 nm $Ni_{81}Fe_{19}$ deposition using thermal evaporation and measurement using AFM and SEM.

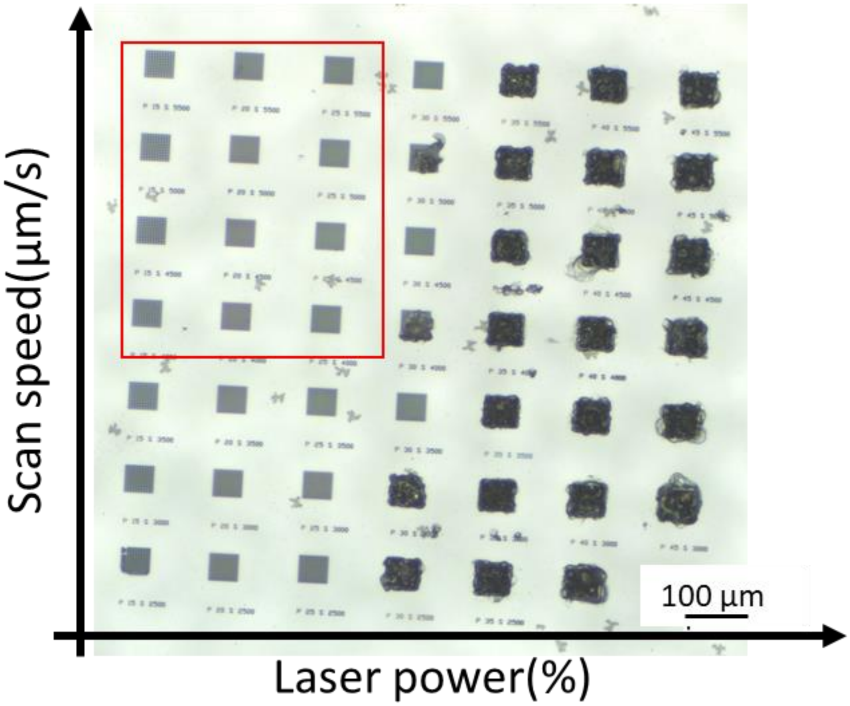

Figure 4.5: Optical microscopy image of disks dose array. The laser power increases in 5 % steps (left to right), while the scan speed increases in 500 μm/s steps (bottom to top). Red solid squares represent the optimal laser power and scan speed range which is between 15 – 25 mW and between 4000 – 5000 μm/s , respectively.

Surface roughness is an important indicator to consider since it can significantly impact the spin texture of magnetic elements. AFM was performed upon the dose array and the surface roughness was calculated using the WSxM software. This is accomplished by analysing the height distribution within a region that has been specified within an image. The function assumes that the heights have a Gaussian distribution and calculates the root mean square width of the curve by using following equation [141]:

$$RMS = \sqrt{\sum_{m=1}^{N} \frac{X_m^2}{N}} \tag{4.1}$$

Where x_m is the measured heights and N is the total number of data points. Figure 4.6 shows a summary plot for surface roughness as a function of laser power and scan speed. When the laser power is 15 mW, the RMS is highest with values ranging between 5 to 8 nm. Further increase of power decreases the roughness until saturation occurs at 2 – 3 nm. A general trend can also be identified with respect to scan speed, with lower values yielding lower roughness values. Based on the above investigation, it can be concluded that the RMS roughness is drastically influenced by the applied laser power/scan speed. As described in section 3.2.2, the laser writing process gives rise to polymerized volumes (voxels), which overlap to create the geometrical shapes that constitute the microstructure. In order to produce microstructures with smooth surfaces, the exposure and laser scanning parameters must be adjusted to ensure that the voxels are overlapping sufficiently, i.e., the surface roughness associated with the individual characteristics of the voxels becomes insignificant. For arrays of the size described in this chapter, the optimal parameters were determined to be a laser power of 25 mW and a scanning speed of 5500 μm/s.

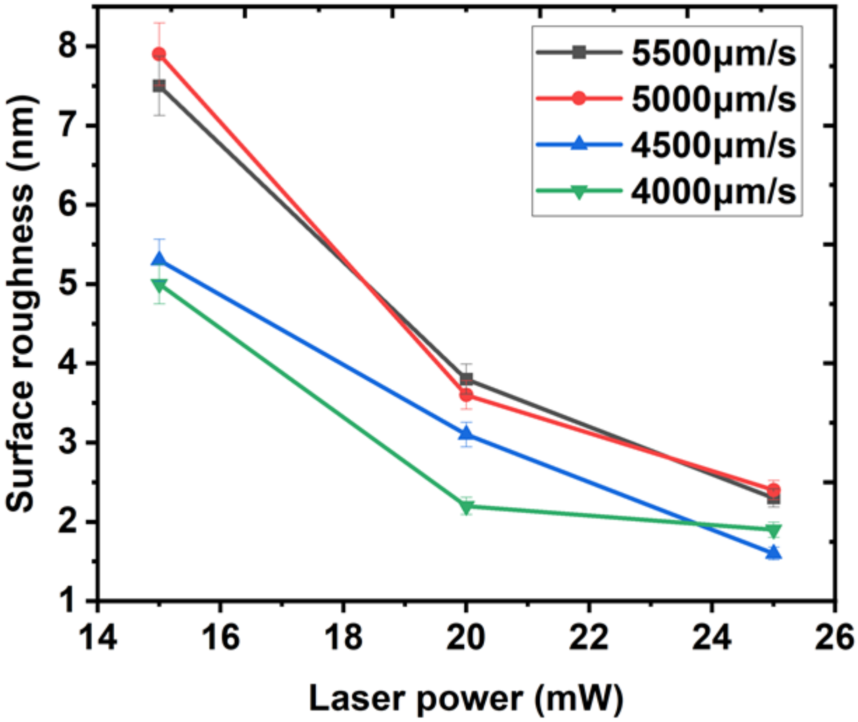

Figure 4.6: Surface roughness of the disk dose array as a function of laser power and scan speed in the optimal range (a laser power of 25 mW and a scanning speed of 5500 μm/s).

Disk arrays with optimal process parameters were fabricated in the high MS and low MS regime, then followed by characterisation. Scanning electron microscopy (SEM, Hitachi High-Tech) and AFM using a tapping mode with a commercial low-moment tip, were applied to perform a morphological assessment of the disk's arrays. In Figure 4.7(a), a top-view SEM image of the 30 x 30 disks array is shown, indicating an ordered lattice. The SEM micrograph taken at a 30° angle is shown in Fig. 4.7(b). These closely follow the design parameters with a diameter of 2 μm. A 45° tilted SEM image, Fig. 4.7(c), was also obtained showing the 3D geometry of the array and illustrates that the magnetic material on the cylinder surface is greater than 5 μm above the substrate. Consequently, any stray field from the substrate layer film is negligible and should not influence the disk spin texture [97].

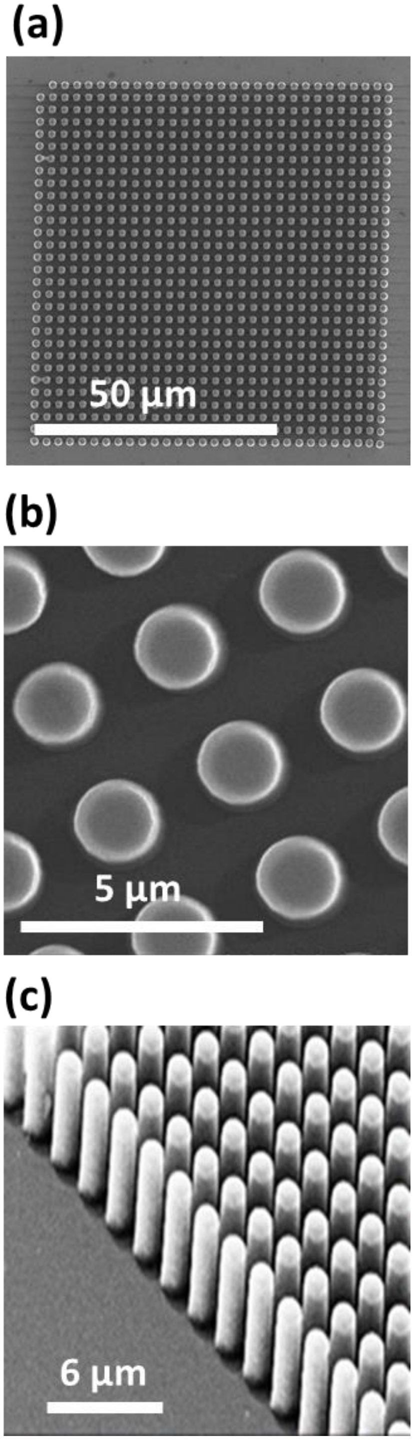

Figure 4.7: SEM images for a plain disk array from (a) a top-down view as well as at (b) a 30° (c) a 45° tilt with respect to the substrate plane.

A key benefit of the system geometry is the presence of a virtual plane for scanning probe microscopy studies. In principle, this should allow both atomic force microscopy and magnetic force microscopy studies. Atomic force microscopy images of the plain disk array in high and low magnetostatic coupling regimes are shown in Figures 4.8 and 4.9 respectively. An AFM image in Fig. 4.8(a) is showing the topography of high MS array. The AFM line profile is exhibited in Fig. 4.8(b). The AFM derivative image (error image) is displayed in Figure 4.8(c). Figure 4.8(d) illustrates a 3D rendering of high MS array.

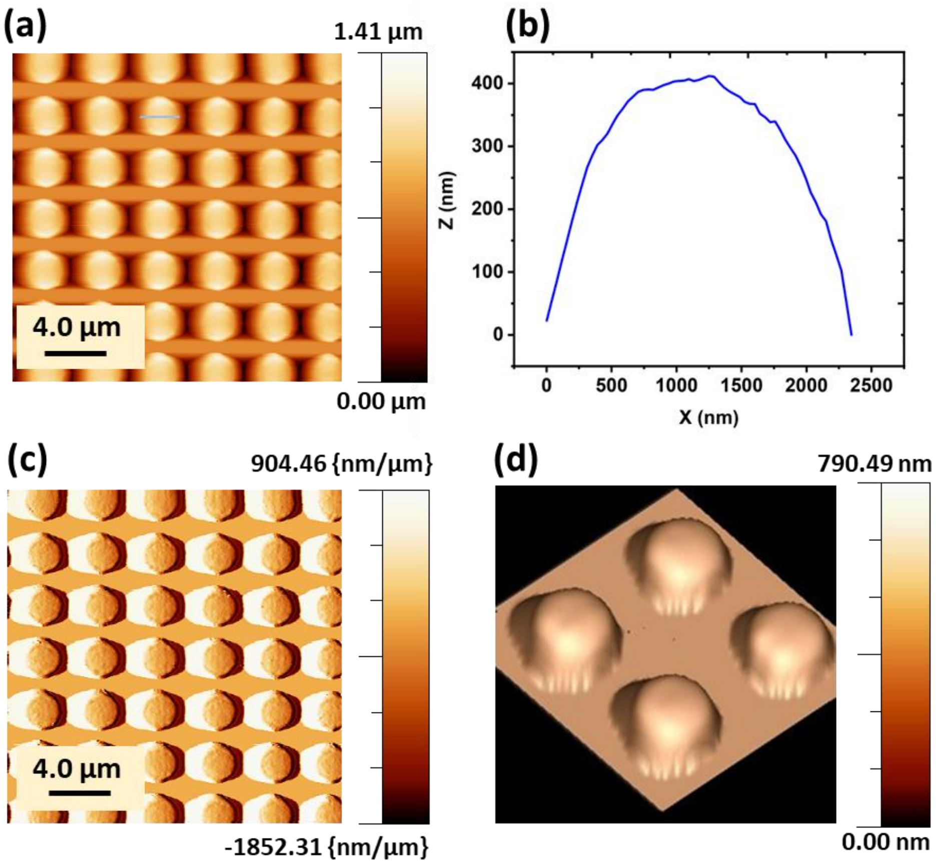

Figure 4.8: (a) AFM image of the high MS array (b) Line profile of a single disk in the array (c) error image and (d) 3D view of array portion.

Figure 4.9(a) shows the topography of the low MS array, and the AFM line profile is exhibited in Fig. 4.9(b). The AFM derivative (error images) image is displayed in Figure 4.9(c). Figure 4.9(d) illustrate a 3D rendering of low MS array. For both arrays, we note that the measured AFM shows a maximum height change of 1.2 μm, which is less than the vertical distance between the cylinder top and substrate plane as demonstrated by previous SEM. The discrepancy is due to the AFM feedback. Although, the maximal z-range of the piezo is ~ 5 μm, the high scan speed (~1 Hz) and active feedback means that the tip encounters and reacts to the next cylinder before encountering the substrate.

Overall, the topography reveals a relatively flat surface with low roughness of approximately 4.3 ± 0.3 nm for the high MS array and 4.7 ± 0.2 nm for the low MS array. This is higher than the surface roughness of $Ni_{81}Fe_{19}$ micron size-disks fabricated using Si substrate [4, 5], which has values less than 1 nm. This is an important point which will need to be considered when analysing the magnetic properties later in the chapter.

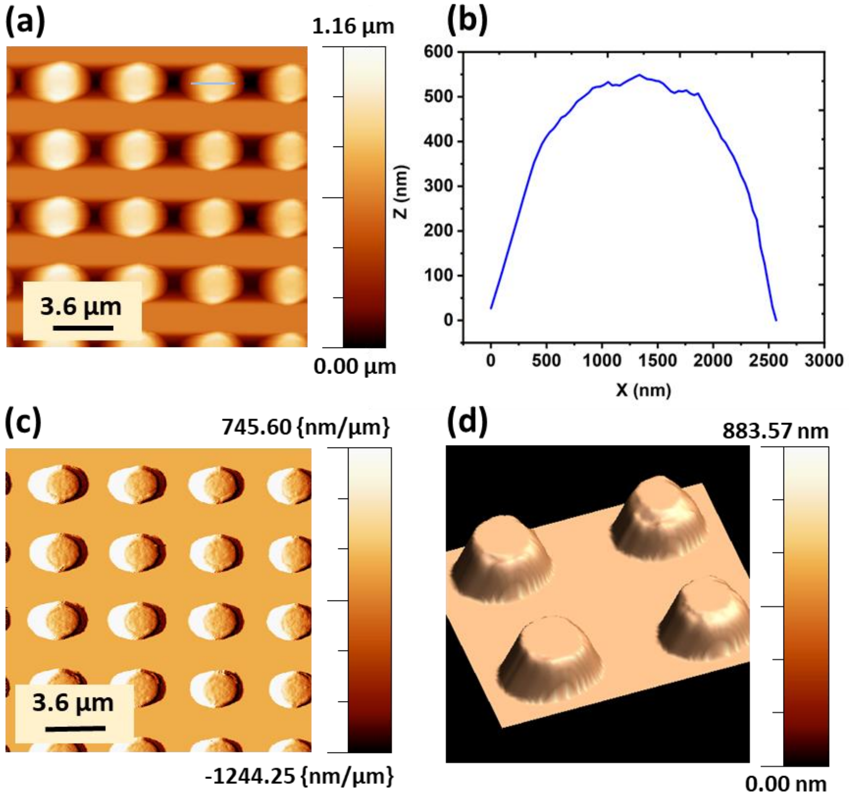

Figure 4.9: (a) AFM image of low MS array. (b) Plot of line profile of one disk. (c) Error image and (d) 3D view of array portion.

4.3.3 Magnetic characterisation of plain disk arrays

A Digital Instruments Dimension 3100 AFM was utilised in lift mode in order to carry out MFM experiments at ambient conditions. MFM tips from Nanosensors with a 40 nm CoCr coating and low magnetic moment ($0.5 \times 10^{-13}\text{emu}$) were utilised. Prior to conducting the measurements, the tips were magnetised upwards, along the tip axis (z), using a permanent magnet and field of approximately 1 T. A number of preliminary investigations were carried out in order to determine the optimal imaging parameters for these novel samples. This is particularly important, since MFM is not usually used to image 3D nanostructures. As detailed in section 3.6, a reduced lift height increases the MFM resolution at the expense of potential tip strike. Therefore, to determine the optimum lift height, a preliminary investigation was carried out whereby it was varied between 85 – 200 nm, as shown in Figs 4.10.

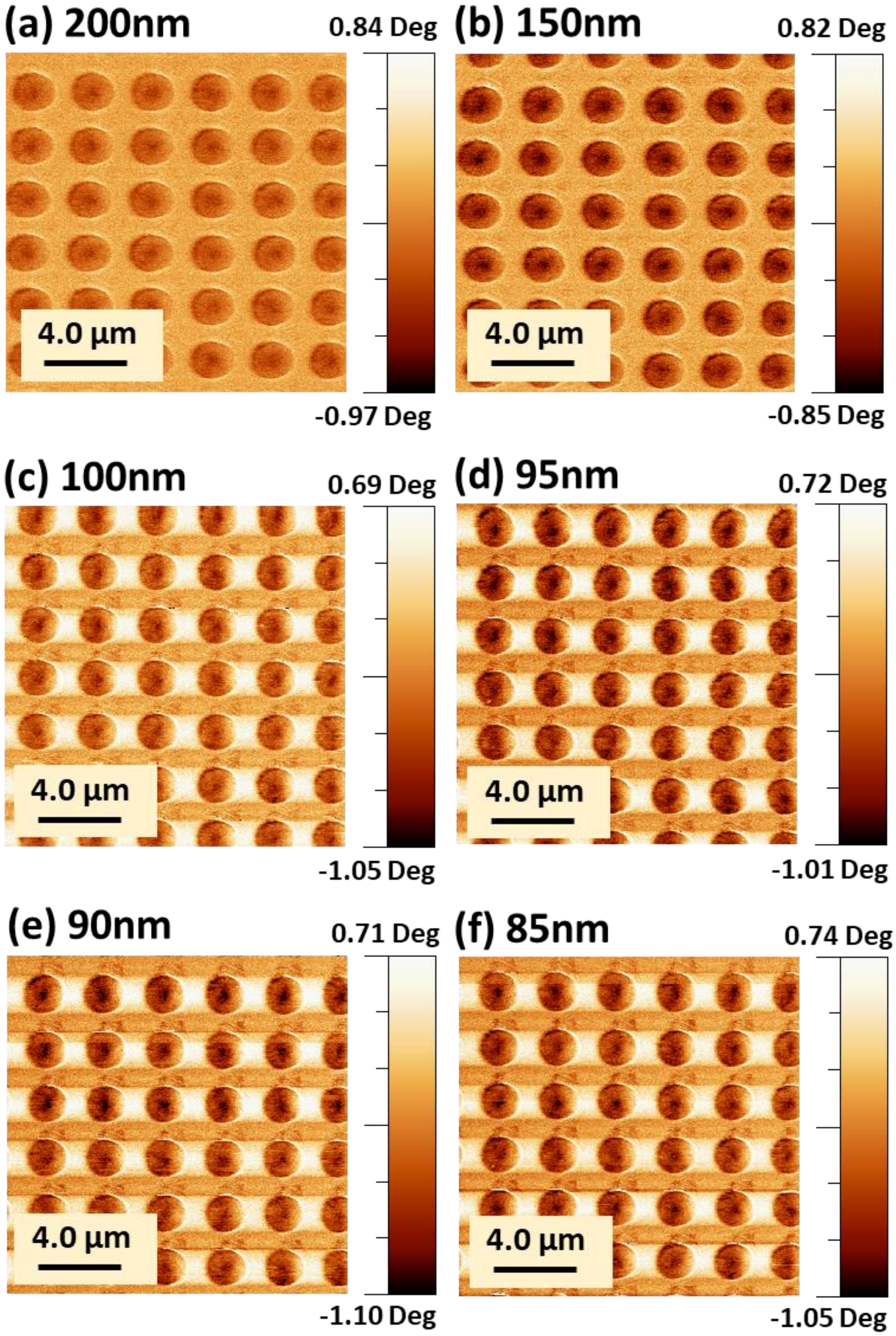

Figure 4.10: MFM images of high MS array for different lift heights (a) 200 nm, (b) 150 nm, (c) 100 nm, (d) 95 nm, (f) 90 nm and (f) 85 nm. In conjunction with the width of the core as a function of lift height (Fig. 4.12) an optimal lift height of 85 nm was chosen.

At a high lift height of 200 nm, the vortex core can only just be seen above the noise floor. Reducing the lift height, (Figs. 4.10b-f), is found to both improve the signal to noise and lateral resolution as shown in summary plot Fig 4.11.

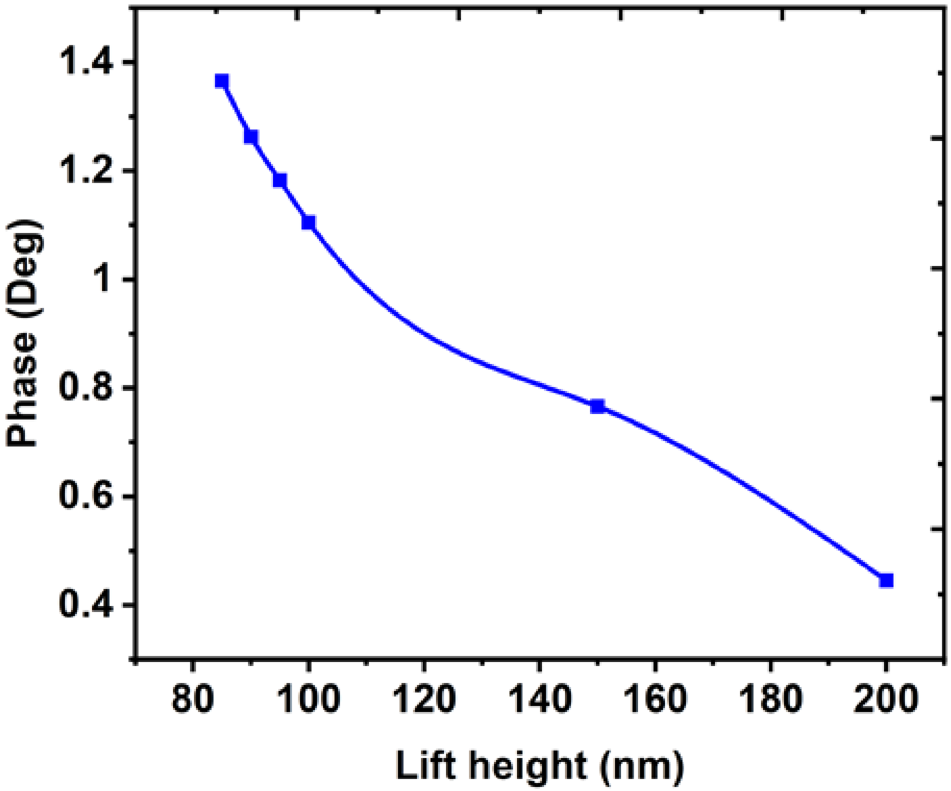

Figure 4.11: A summary plot of MFM phase shift from the disk core as a function of lift height (85 nm to 200 nm).

At each lift height, several images were collected to see if there was any influence of tip upon magnetic texture. No differences were found between images and hence we conclude that the tip–sample interaction does not significantly perturb the magnetisation of the disks. In Figure 4.12, a further investigation has been carried on the vortex core width as a function of the lift height. The core width of the vortex was deduced from Full Width Half Maximum (FWHM) of the phase trace, and it was correlated to the six values of lift height between 85 nm to 200 nm. The lift height of 85 nm gave the narrowest core width while the lift height of 200 nm gave the widest vortex core, as expected from literature [142].

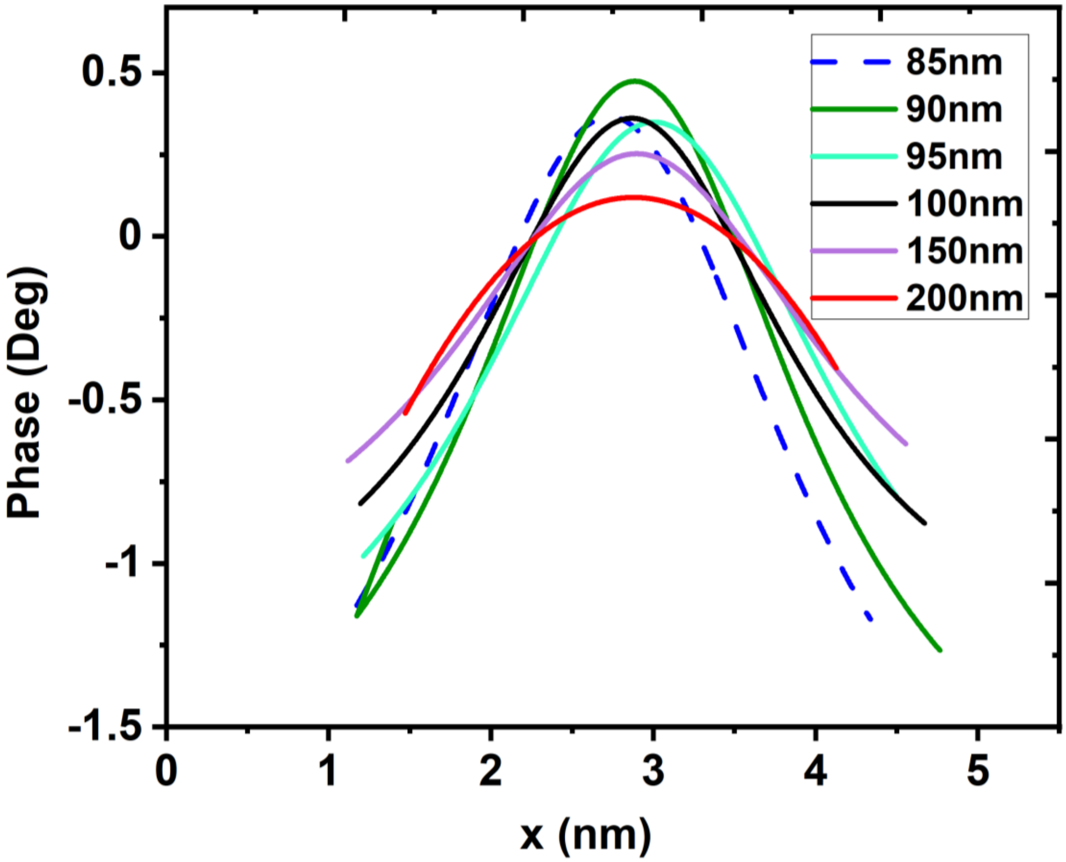

Figure 4.12: Full width at half maximum (FWHM) of vortex core as a function of lift height (85 nm to 200 nm).

A summary plot shown in Figure 4.13, also depicts the increase in core vortex width as the function of lift height increases. Hence to achieve the narrowest vortex core having minimum lift height is important.

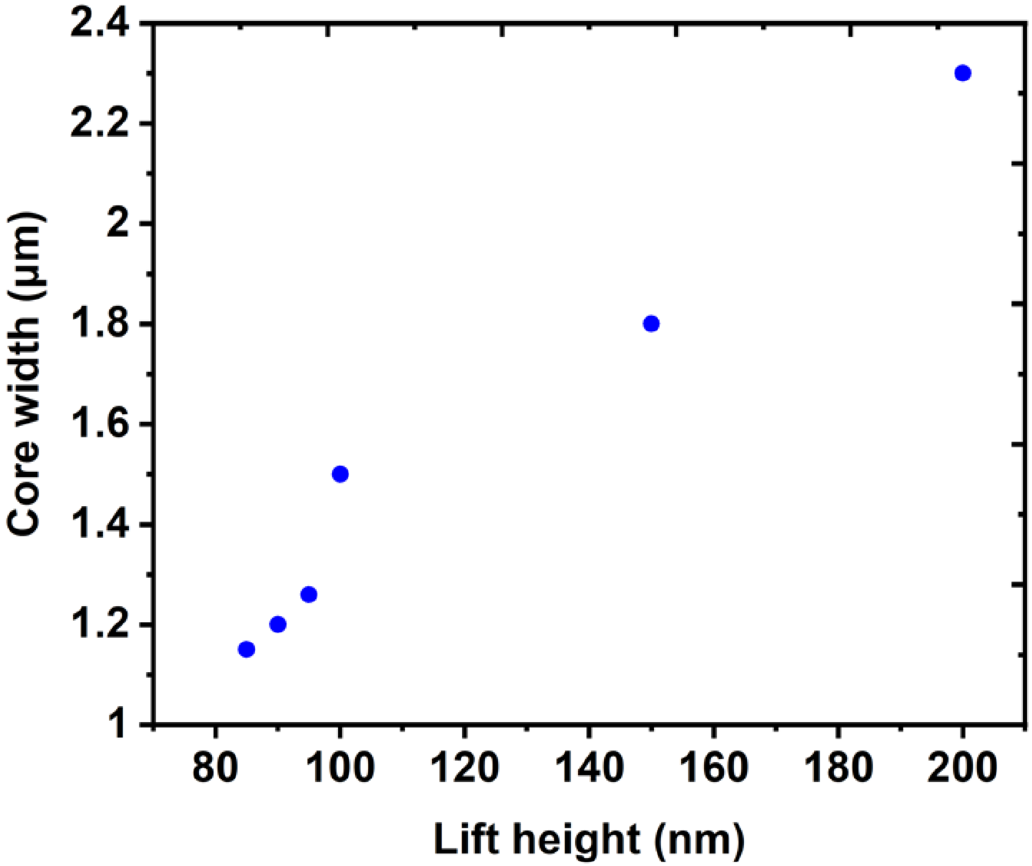

Figure 4.13: A summary plot of the measured vortex core width variation as a function of lift height (85 nm to 200 nm).

Figure 4.14 shows an examination of how the signal-to-noise ratio improves when the MFM driving amplitude is increased. Here, the drive amplitude was increased until the first signs of the tip strike were seen (as can be noticed by the white and black dots in the image), after which the amplitude was reduced slightly. The image with tip strike is not seen here as the amplitude was reduced back immediately after tip strike appeared.

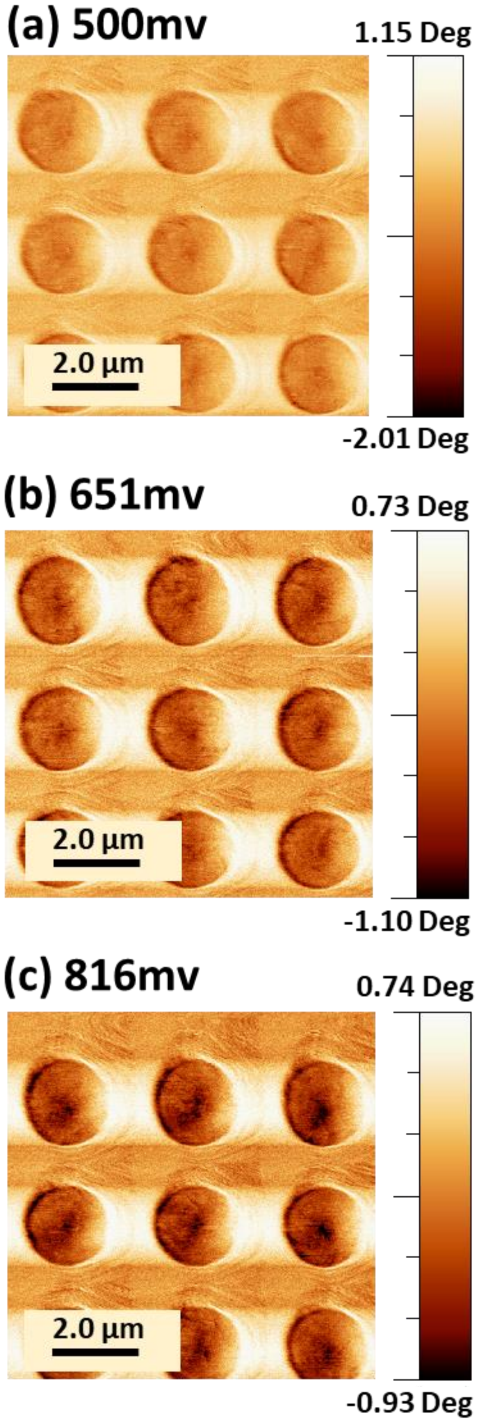

Figure 4.14: MFM images for plain disk array of different drive amplitudes (a) 500mV, (b) 651mV and (c) 816 mV. The vortex core is visible in all three images but note the signal to noise is found to increase with drive amplitude.

In Fig. 4.15 a summary plot shows how the signal to noise increases as drive amplitude increases. As discussed in section 3.6, the drive amplitude dictates the voltage applied to drive cantilever oscillations.

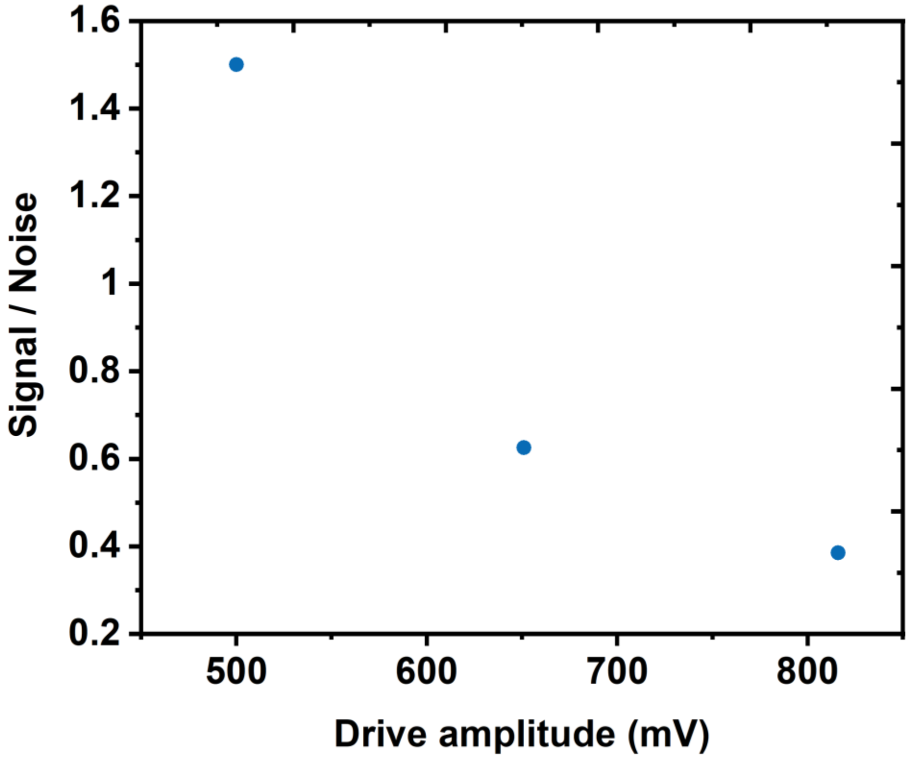

Figure 4.15: A summary plot of MFM signal to noise as a function of drive amplitude (500, 651 and 816 mV).

4.3.4 Initial ordering of the disk arrays

In the absence of an external magnetic field, MFM images of the disk arrays for both high MS and low MS samples are shown in Fig. 4.16. The MFM contrast is only evident in the centre of the disk (black contrast) at the remanent state, which is compatible with the vortex spin texture [67, 77].The presence of a vortex state suggests a low stray field and reduced magnetic interaction between the disks.

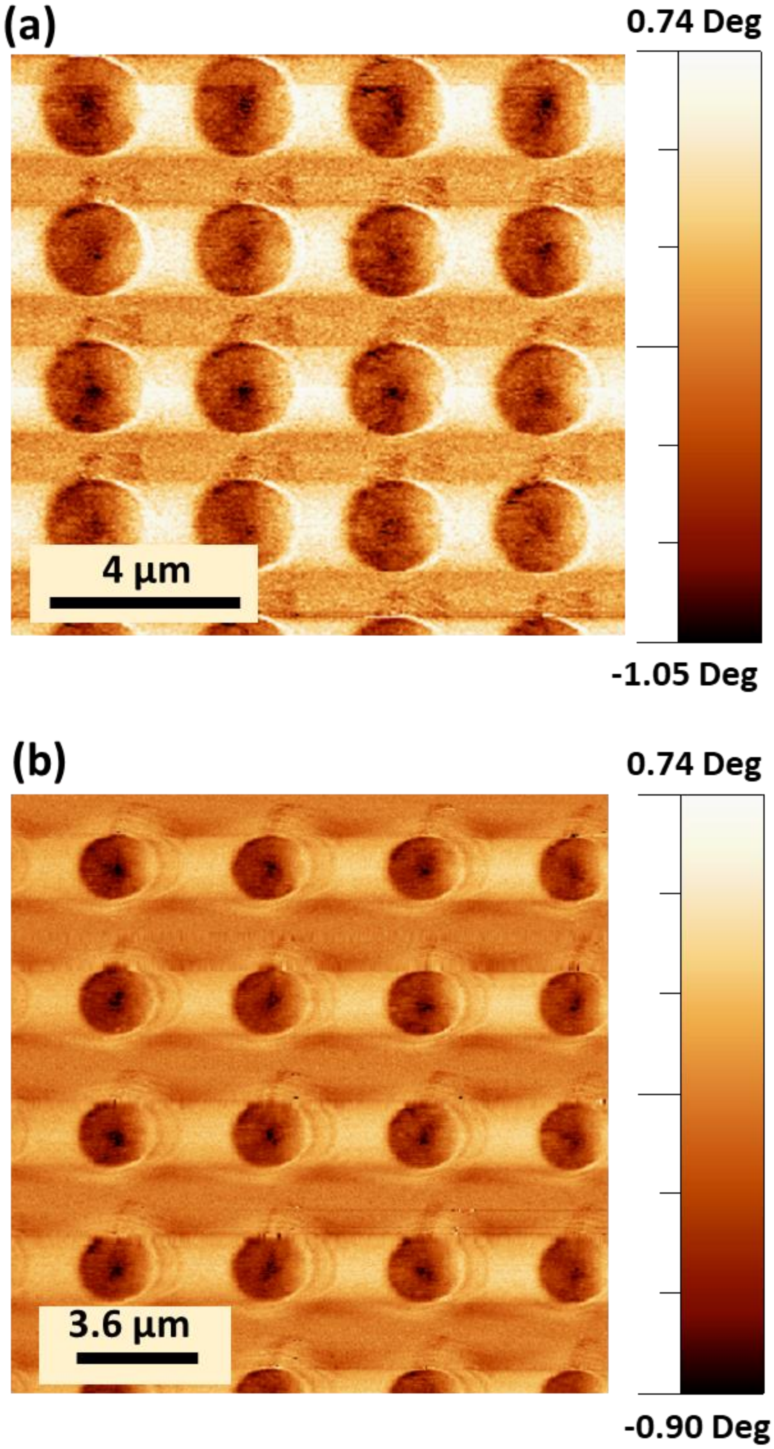

Figure 4.16: MFM images of 4 x 4 plain disks for (a) high MS array and (b) low MS array for the as-deposited state and in the absence of an applied field. The colour bar represents phase shift.

Literature suggests that even for arrays of very low lattice spacing, there is negligible interaction at remanence [18, 143]. However, application of a field, yields an interdisk magnetostatic interaction that is more significant due to the appearance of magnetic charges upon edges and, as expected such an interaction increases with reducing disk lattice constant [25, 144]. Interestingly, each of the disks exhibit the same vortex polarity in the remnant state. After finishing the evaporation process and taking the sample out, the sample holder was subjected to additional testing using a gauss meter. A very small (<1 mT) magnetic field was measured, which may explain the preference in vortex polarity.

It is interesting to note that at remanence, the chirality of disks cannot be determined but application of a small perturbation field, will result in the vortex core in each disk displacing up or down, allowing complete determination of the magnetic state. It is recognised that the vortex core moves perpendicular to the field and that the direction of the displacement depends on the vortex chirality [11, 12], where the core moves upwards for counter-clockwise (CCW) and downwards for clockwise (CW) chirality for a positive field. Consequently, the region with magnetisation along the field direction increases, whilst the region with magnetisation antiparallel to the applied field reduces. Figure 4.17 illustrates this and shows the distribution of CW and CCW chirality for both high MS and low MS samples when applying a 3 mT field, along the positive x-direction. Figure 4.17(a) reveals an MFM image obtained of the high MS array in the presence of a field. The image signifies that a strong preference occurs in the chiral state of the vortices**.** The ratio observed in this image was 16:0 between the CW against CCW vortex chirality. In an external magnetic field, the centres of the vortices are shifted, resulting in a nonzero dipolar moment M and appearance of interdisk magnetostatic coupling. Interestingly, a nonzero quadrupolar and high-order multipole moments of the in-disk magnetization distribution in square arrays leads to an induced magnetic fourfold anisotropy for a square disk array [145]. This may be relevant in the next chapter.

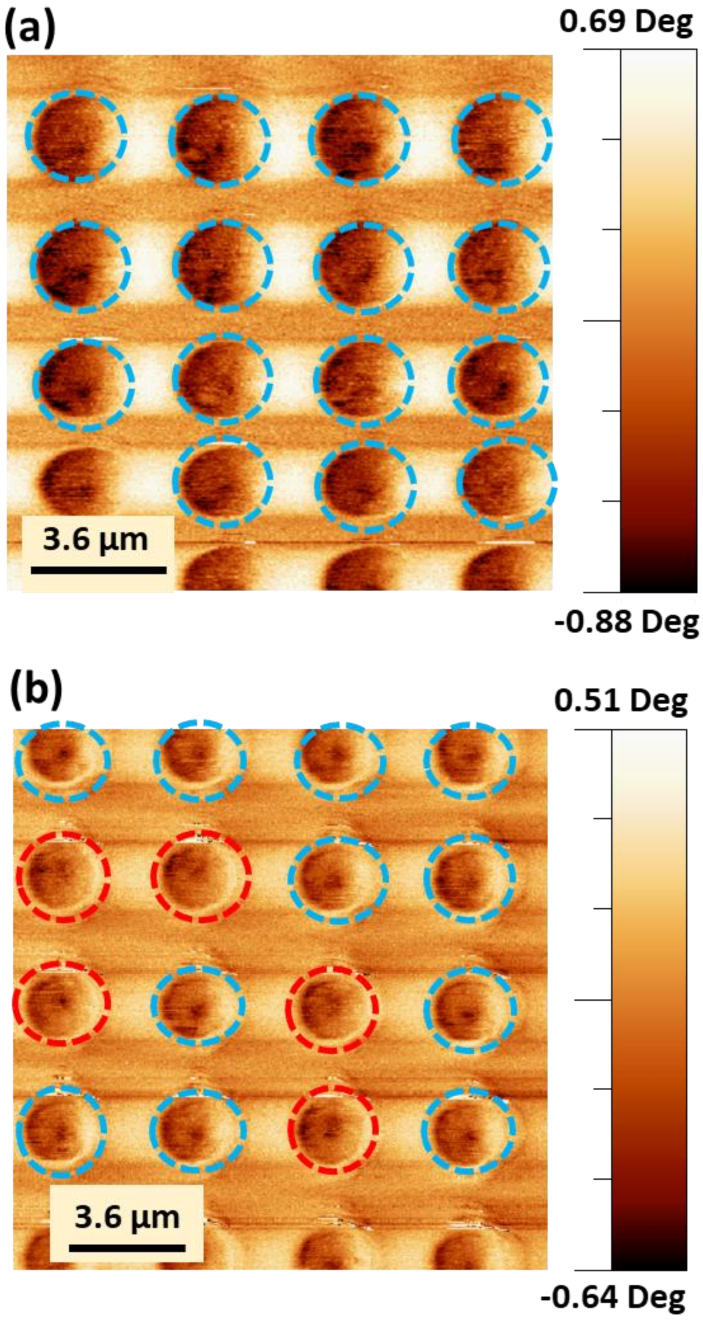

Figure 4.17: MFM images of 4 x 4 plain disks for (a) high MS array (b) low MS array at 3 mT. Circles with red and blue outlines represent CCW and CW, respectively. The legend represents the MFM phase shift.

The same measurement was performed on the low MS array and yields a 11:5 vortex chirality ratios Fig. 4.17(b). Overall, this suggests that early in the growth process, before a definitive spin texture is determined, local magnetostatic interactions between disks, prime the system into a given chirality for the high MS interaction sample. It is possible that any having an opposing chirality have minor structural defects which make the local energetics non-degenerate.

4.4 Plain disks in high MS regime

4.4.1 Field driven motion

With an external electromagnet placed on the AFM stage, it was possible to apply an in-plane field up to values of 7 mT (discussed in detail in section 3.6). MFM images were taken at 2 mT field steps in order to investigate the magnetisation processes. MFM investigations without switching the tip magnetisation were possible at least up to 7 mT. It should be noted that field application was applied and maintained constant during scan. Initially, an area showing 3 x 3 disks were chosen randomly in the sample and are presented. However, for a much closer examination, we subsequently chose a representative disk in the array to explore more closely the magnetisation process in the system.

Representative MFM images for the high MS array under application of an in-plane field in the ± x direction is shown in Figure 4.18 and Figure 4.19. As an in-plane field is introduced along the positive x-axis, the vortex core moves upwards or downwards (see Figs. 4.18b-d)**.** The chirality preference ratio after a 3 mT field application is 7:2 for CW and CCW, respectively. An additional field increment as shown in Fig. 4.18(e), results in core annihilation at approximately 7 mT and contrast of opposing sign emerging at disk extremities, suggesting that saturation is approaching*.* A non-negligible stray magnetic field is then present around the disks due to the magnetic charges produced on opposing sides. For this lattice spacing, the coupling between the disks is consistent with previous studies of a similar size, thickness and spacing, taking into account the difference in the arrangement of the disks. Coupling is evidenced at the re-nucleation field of 5 mT (see Fig. 4.18f) where the CW chirality is found to be dominant with a distribution ratio of 7:2 (CW: CCW). This is a novel investigation for the chirality distribution arranged in a square lattice array which has not previously been conducted in the literature concerning re-nucleation.

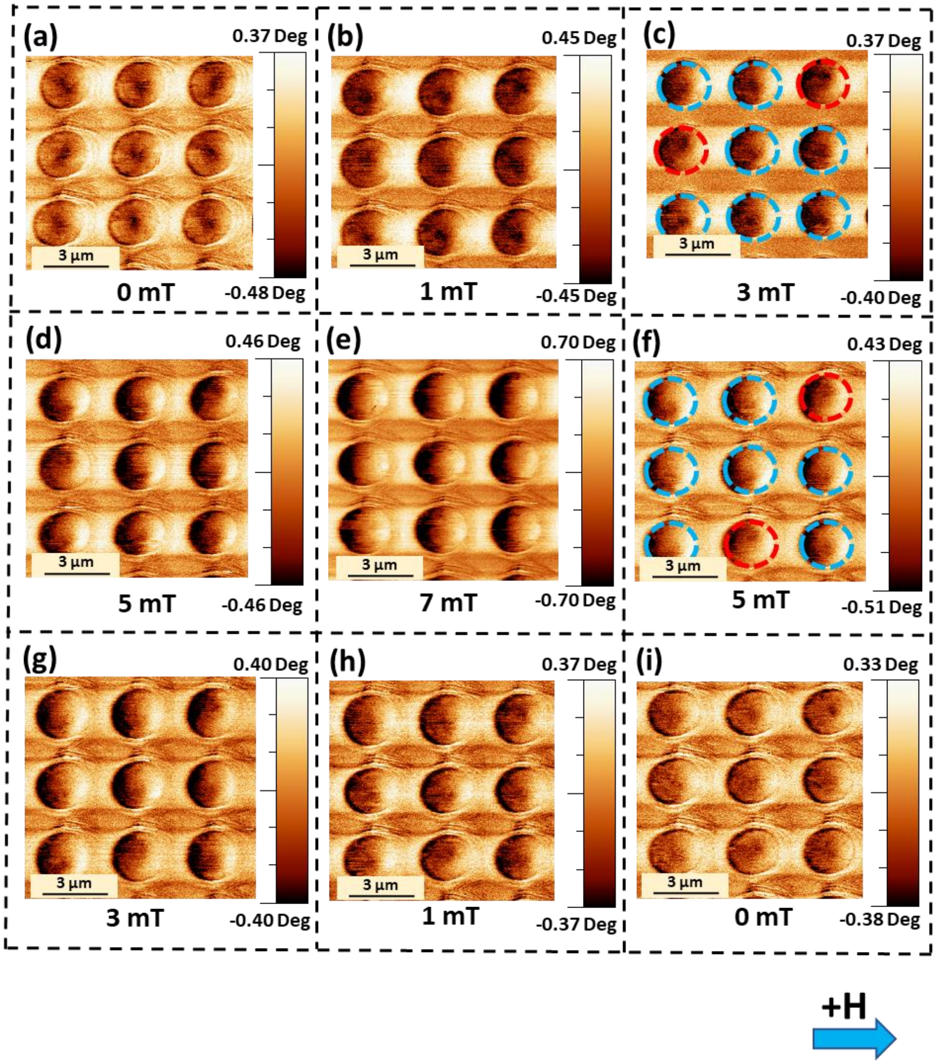

Figure 4.18: MFM images of 3 x 3 disks for the high MS array at (a) zero field and (b-h) under the application of an in-plane field H in the +x direction and (i) once returned to remanence, obtained at 2 mT steps up to +7 mT. Circles with red and blue outlines represent CCW and CW, respectively. The colour bar represents phase shift. Note that for the 0 mT case, a maximum residual field of 1.2 mT is present due to remanence in the magnet poles.

Following the re-nucleation, the vortex core maintains a significant distance from the centre of the disk as shown in Figs. 4.18(g, h), due to the imbalance between the magnetostatic and Zeeman energies. As the field is reduced further, the vortex core translates towards the disk centre as shown in Fig. 4.18(i). We note that in this simple square lattice array, it is straightforward for the array to reach a minimum energy configuration by maximising the number of disks with specific chirality. Other array geometries, for example disks arranged in a hexagonal array or as recently recorded for a chain of disks, yields frustration and the areas where the circulations rotate in opposite directions [146, 147].

When a field is applied in the negative x-direction, a symmetric behaviour is observed, the vortex core moves upwards or downwards depending upon chirality (see Figs. 4.19b-d). The chirality distribution ratio is equal to 8:1 for CCW against CW.

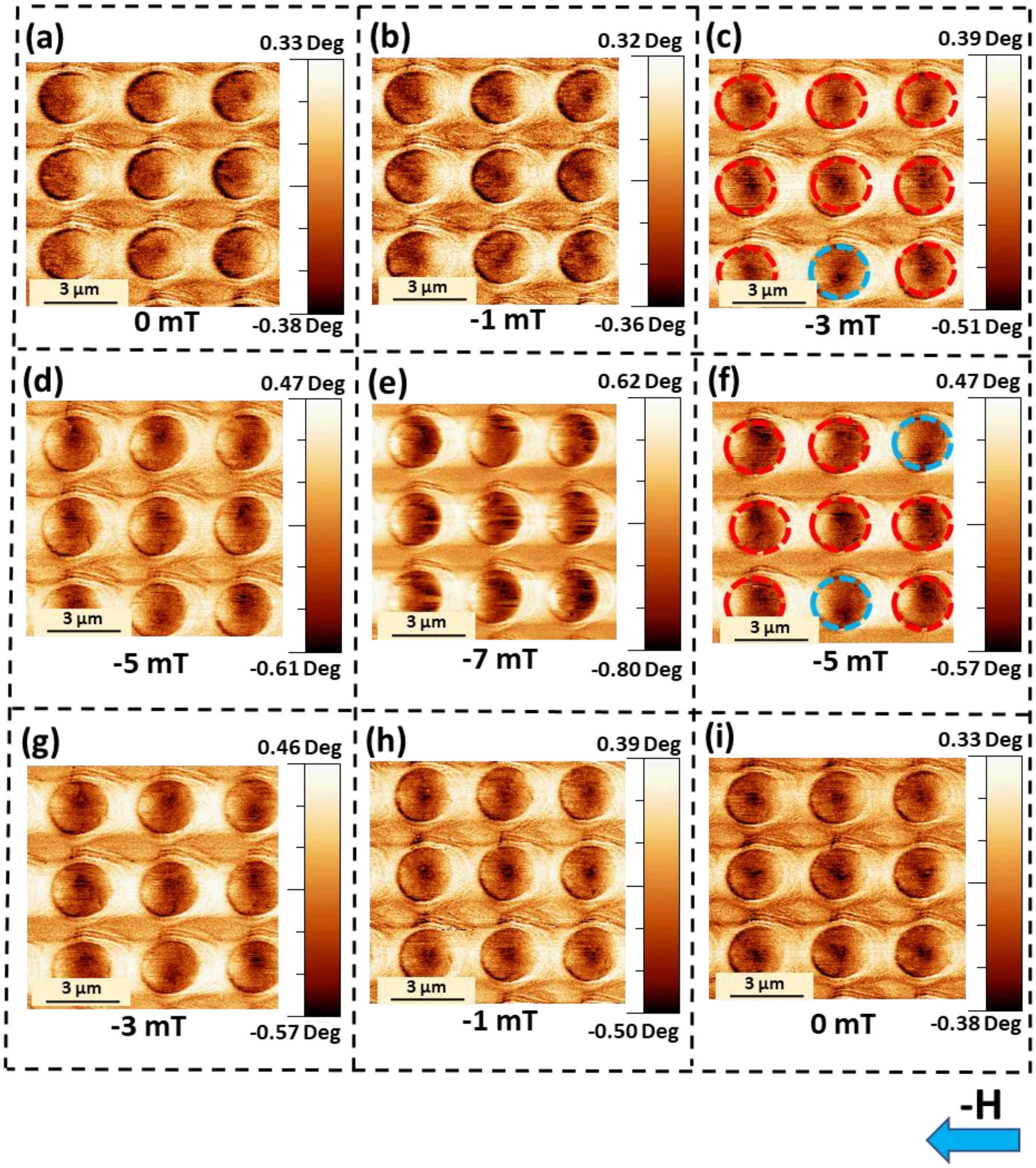

Figure 4.19: MFM images of 3 x 3 disks for high MS array at (a) zero field and (b-h) under the application of an in-plane field H in the -x direction and (i) once returned to remanence, obtained at 2 mT steps up to -7 mT. Circles with red and blue outlines represent CCW and CW, respectively. The colour bar represents phase shift. Note that for the 0 mT case, a maximum residual field of magnitude 1.2 mT is present due to remanence in the magnet poles.

We now closely examine the magnetisation process in a representative disk in the array as shown in Fig. 4.20. When applying a field equal to H= ± 1 mT (b, j), the core displaces downward and upward in the positive and negative sweep, respectively. The disk at field values equal to H= ± 5 mT, illustrate the core re-nucleates from the lower edge after the positive saturation (f) and from the upper edge after evolving from negative saturation (n). As can be clearly noticed, in this field a single magnetic vortex is formed inside each disk.

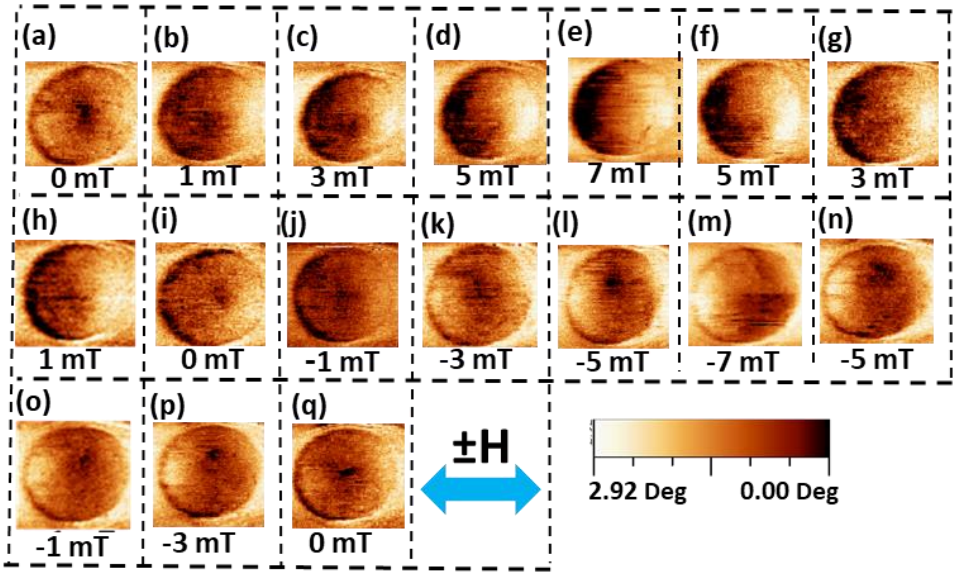

Figure 4.20: MFM images of a single disk in a high MS array under the application of an in-plane field H in the ± x direction. Note that for the 0 mT case, a maximum residual field of magnitude 1.2 mT is present due to remanence in the magnet poles.

A further investigation was performed on a 3 x 3 image of a high MS array to investigate the core displacement dependence on the field direction. In Figure 4.21, it can be seen that when the field is applied in the positive y-direction, the vortex core displaces in the x-direction (see Figs. 4.21b, d). Further field increments in Fig. 4.21(e) result in core annihilation at around 7 mT. Figure 4.21(f, g) reveals that a further field reduction, yields core re-nucleation at around 5-3 mT and core displacement returns to the centre of the disk (see Fig. 4.21i).

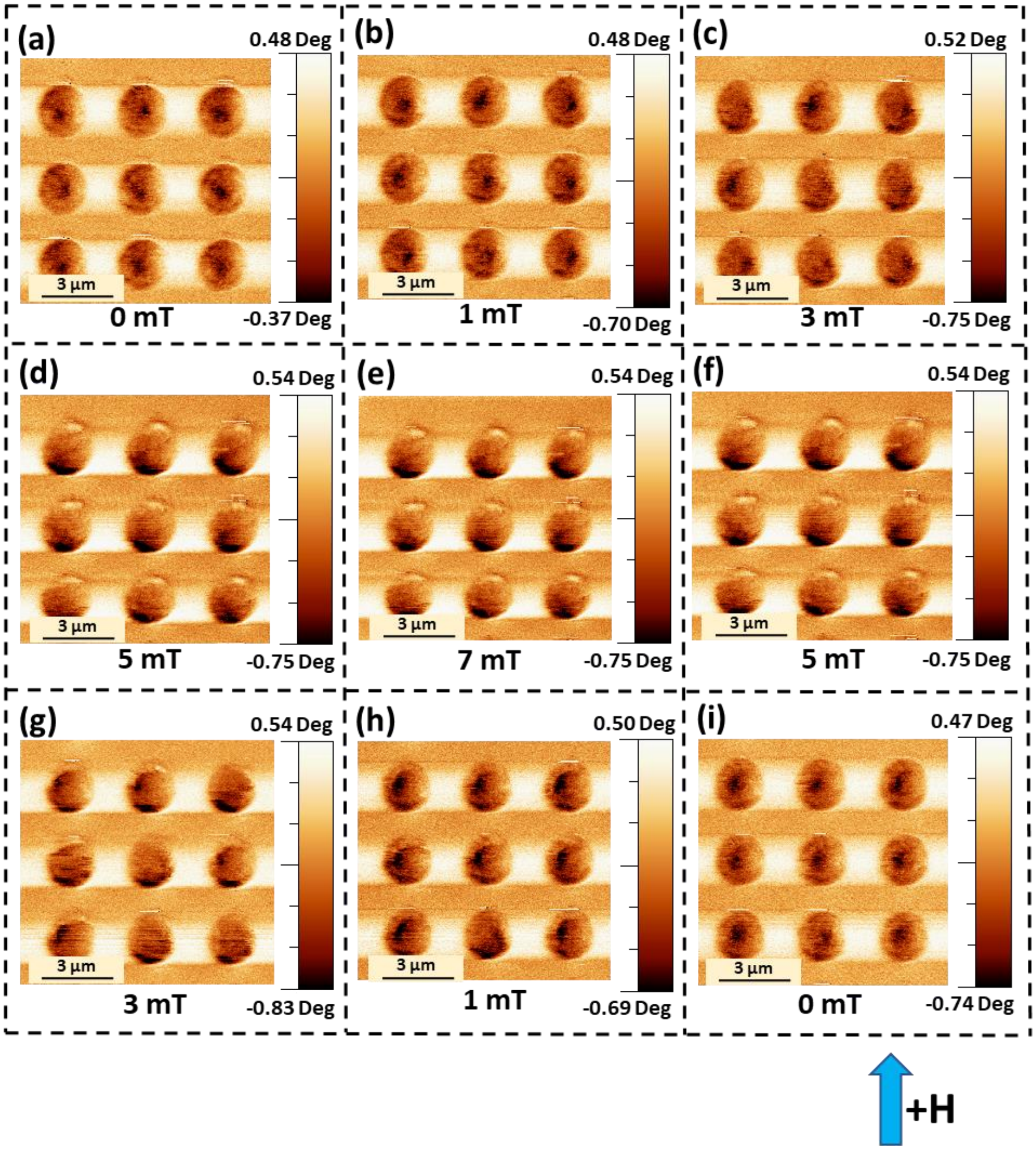

Figure 4.21: MFM images of 3 x 3 disks for high MS array at (a) zero field and (b-h) under the application of an in-plane field H in the +y direction and (i) after return to remanence, obtained at 2 mT steps up to +7 mT. The colour bar represents the phase shift. Note that for the 0 mT case, a maximum residual field of magnitude 1.2 mT is present due to remanence in the magnet poles.

Figures 4.22(b,d) illustrates that when a field is applied in the negative y-direction, symmetric behaviour occurs with the core shifting to the right or left, respectively. Saturation is approaching at Fig. 4.22e. Overall, these simple additional experiments make it completely clear that a vortex state is present and demonstrate that the systems have the expected symmetry with respect to magnetisation behaviour.

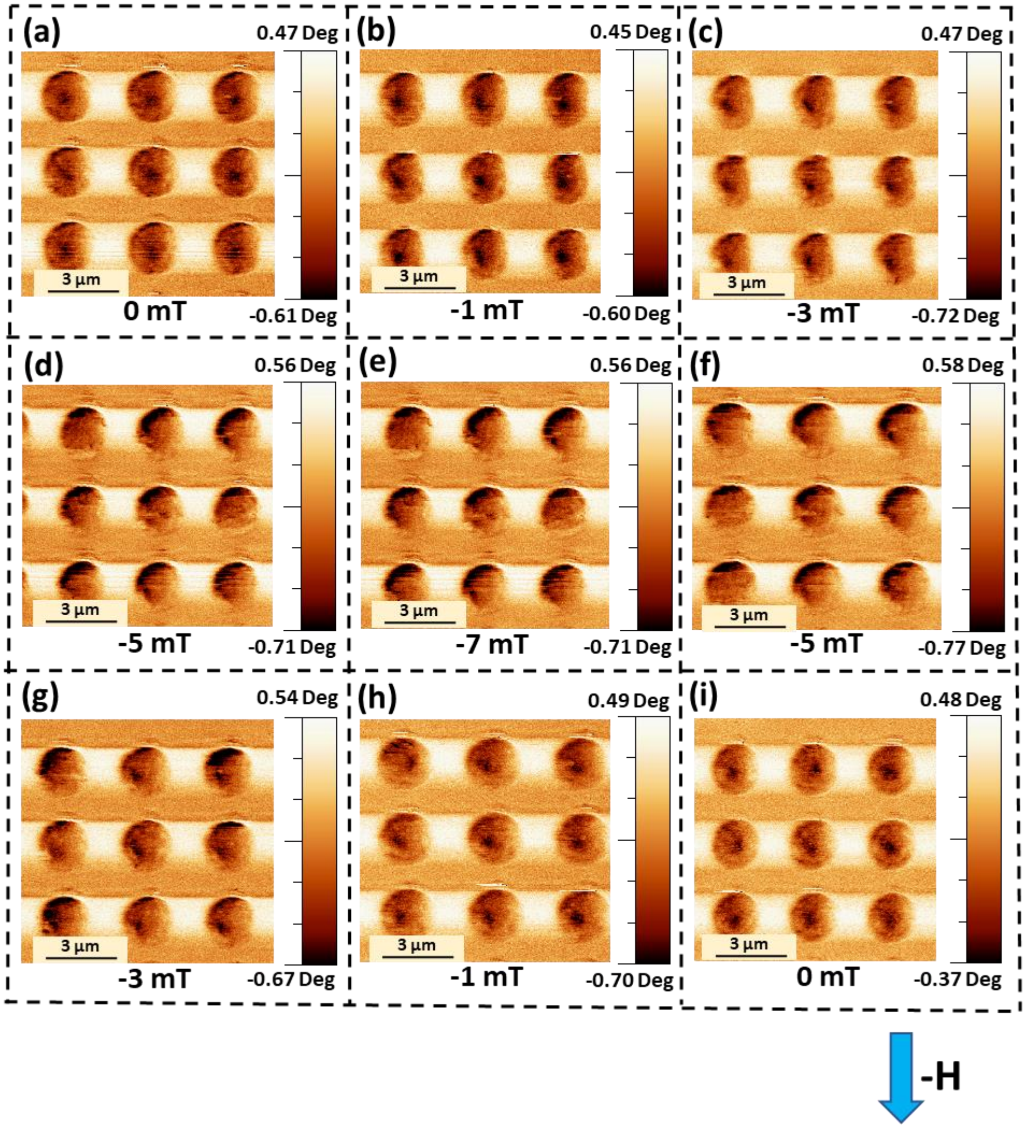

Figure 4.22: MFM images of 3 x 3 disks for high MS array at (a, i) zero field and (b-h) under the application of an in-plane field H in the -y direction and (i) after return to remanence, obtained at 2 mT steps up to -7 mT. The colour bar represents phase shift. Note that for the 0 mT case, a maximum residual field of magnitude 1.2 mT is present due to remanence in the magnet poles.

4.4.2 Micromagnetic simulations of high MS array

In this section, micromagnetic simulations of permalloy $Ni_{81}Fe_{19}$ plain disks of the coupling array is presented to understand the magnetisation process in experimental samples. The simulations were performed with open source software known as Mumax3 code [128], using typical $Ni_{81}Fe_{19}$ parameters: saturation magnetisation $\mu_0 M_s = 1\ \mathrm{T}$, exchange constant $A = 1.3 \times 10^{-13}$ J/ m the damping factor 0.01 and zero magnetocrystalline anisotropy. The simulations were performed with a cell size of 4 nm, below the exchange length of the $Ni_{81}Fe_{19}$, which is $\sqrt{A/\mu_0 M_s^2} \simeq 5.7\mathrm{nm}$ [148]. A magnetic disk of identical dimensions to experimental system was arranged into a square array of 3 × 3 disks, allowing a realistic depiction of the lattice and accurate magnetostatic interactions to be considered in the simulation. The system was relaxed into its minimum energy configuration at zero magnetic field and at a temperature of zero Kelvin. It should be noted that micromagnetic simulations do not take into account temperature or thermal fluctuations. Therefore, these zero Kelvin simulations will yield a systematic difference that results in higher field values when compared to experimental results. This effect is well-documented and can be found in the literature [132]. The resulting magnetisation configuration and simulated MFM images are shown in Figure 4.23.

In Figure 4.23, results are presented for the middle disk that is expected to experience a magnetostatic field similar to the experiments, when only considering nearest neighbour interactions. Overall, the simulations are consistent with the literature, revealing the translation, annihilation and re-nucleation of the vortex core [77, 149]. The magnetic field was applied in-plane, along the x–direction (indicated by arrow), from 0 to 70 mT in 20 mT steps. At remanence the vortex core is observed in the middle of the disks as expected for this spin texture (see Fig 4.23a). When introducing a field, the core starts to displace upwards (see Figs. 4.23b-d). The disks then saturate into a single domain state at a field of 70 mT (see Fig. 4.23e). Subsequently, the field was gradually reduced until vortex re-nucleation was observed, which occurred via a double vortex state as depicted in Fig. 4.23(f, g).

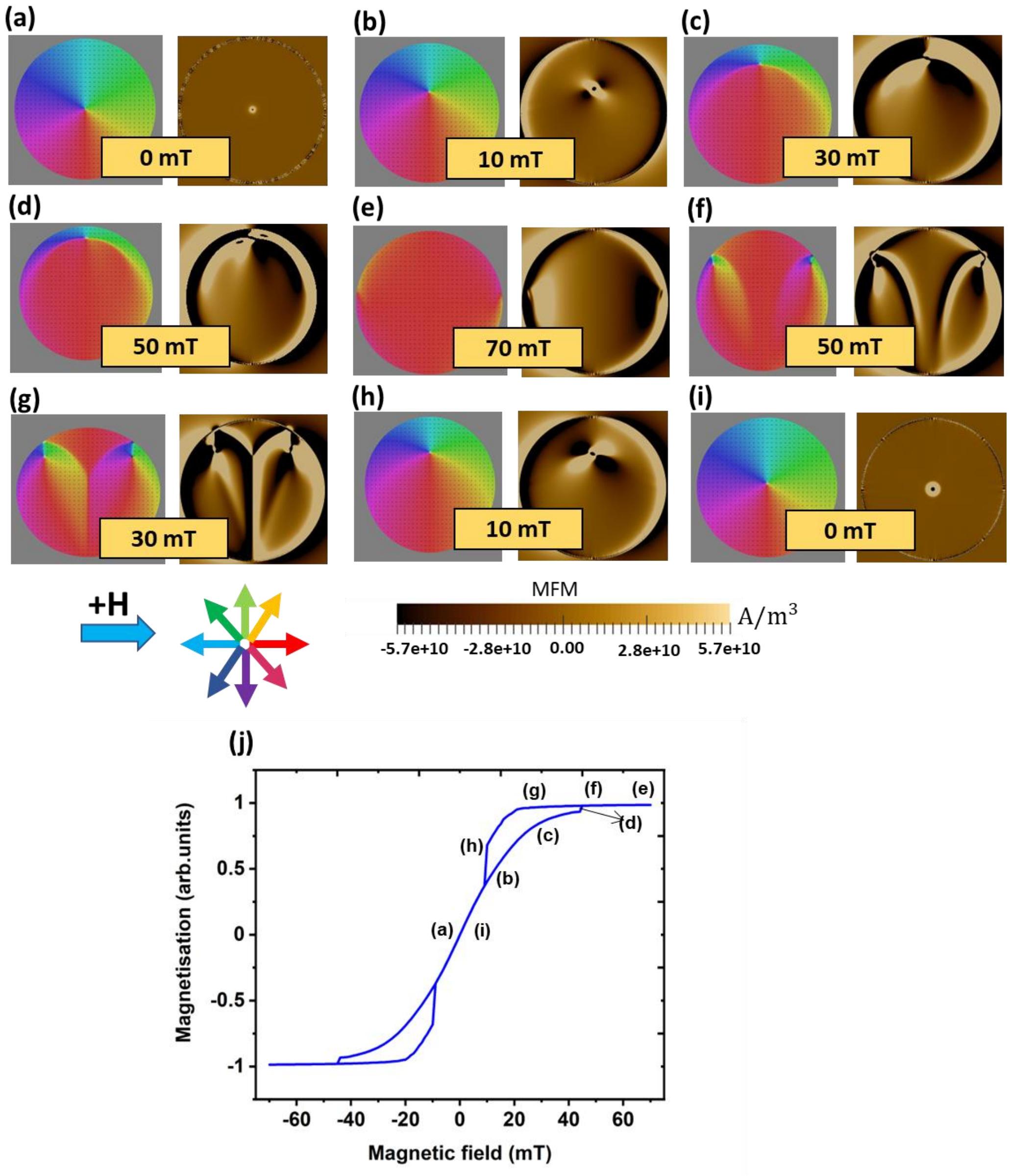

Figure 4.23: Simulated spin configuration and the corresponding MFM for the high MS array at (a) zero field and (b-h) under the application of an in-plane field H in the +x direction (see arrow) and (i) return to remanence. Different colours represent the direction of magnetisation with respect to the applied field, as depicted in the colour wheel. (j) Simulated hysteresis loop, with labels corresponding to the configurations (a-i).

However, the double vortex state was not observed in the experimental images. This difference between the re-nucleation in our experimental observations and this simulation strongly suggests that extrinsic factors, such as edge defects, roughness and geometric variations of individual disks might also have an impact on the experimentally observed results in real systems which not been account in the simulation here. By reducing the applied field further, the two cores move towards each other until they combine to form a single vortex core (see Fig. 4.23h). A displaced, re-nucleated single core was observed in the experiments at a field of 5 mT and as shown in Fig. 4.18(f).

The hysteresis loop in Fig. 4.23(j), summarises the overall magnetisation process. An initial increase in field yields core displacement (Figs. 4.23.a-c) at low field, corresponding to a linear regime in the loop. A change in the loop gradient is then noted, due to the increased magnetostatic energy, which competes with the field. The core then annihilates (see Fig. 4.23d), and the magnetisation distribution becomes quasi-uniform at point (e). Vortex annihilation is accompanied by a characteristic step in the hysteresis loop, due to an abrupt increase in the magnetisation in field direction. The quasi-uniform state remains stable as the applied magnetic field reduces before point (f), when the double vortex state emerges. The magnetisation pattern of the double vortex state is observed in Figure 4.23(f, upper panel), where the magnetisation in the field direction is still relatively large. Subsequent reduction in field shows an abrupt drop in magnetisation due to the two cores annihilating and displacement of the single core downwards.

Overall, there is a reasonable agreement between the experimental and simulation results for the high MS array. Both exhibit common vortex magnetisation mechanisms, such as vortex core translation, annihilation and re-nucleation, with characteristics fields shown in table 4.1. We note that the experimental MFM does not show any evidence of a double vortex, despite its distinctive MFM signature. This may be due to fields steps being too large, such that the two vortices already annihilate before observation or may be due to edge roughness since this may provide preferential nucleation for a single vortex state. This could be addressed by decreasing the field steps or by refining the mesh geometry.

	Annihilation field (mT)	Re-nucleation field (mT)
Experiment	7	5
Simulation	70	50

Table 4.1: A summary of experimental and simulated annihilation and re-nucleation fields for high MS array.

4.5 Plain disks in low MS regime

4.5.1 Field driven motion

A second sample set, whereby the lattice spacing was increased to the non-interacting regime (low MS), was subject to MFM experiments. Figure 4.24(a) depicts the remanent state in which all disks are in the vortex state, with the core in the centre. Overall, similar characteristics are seen as in the previous sample set, with characteristic core displacement as shown in Figs. 4.24(b-d), but with chirality distribution ratio approximately 5:4. The core annihilates by 7 mT (see Fig. 4.24e) and the core re-nucleates at 3 mT (see Fig. 4.24g). Interestingly, all chiralities observed for the re-nucleation field have the same orientation and this could be attributed to a systematic asymmetry of the disk shape [150] with respect to the applied field direction, leading to re-nucleation of vortices with a given chirality upon reducing the applied field.

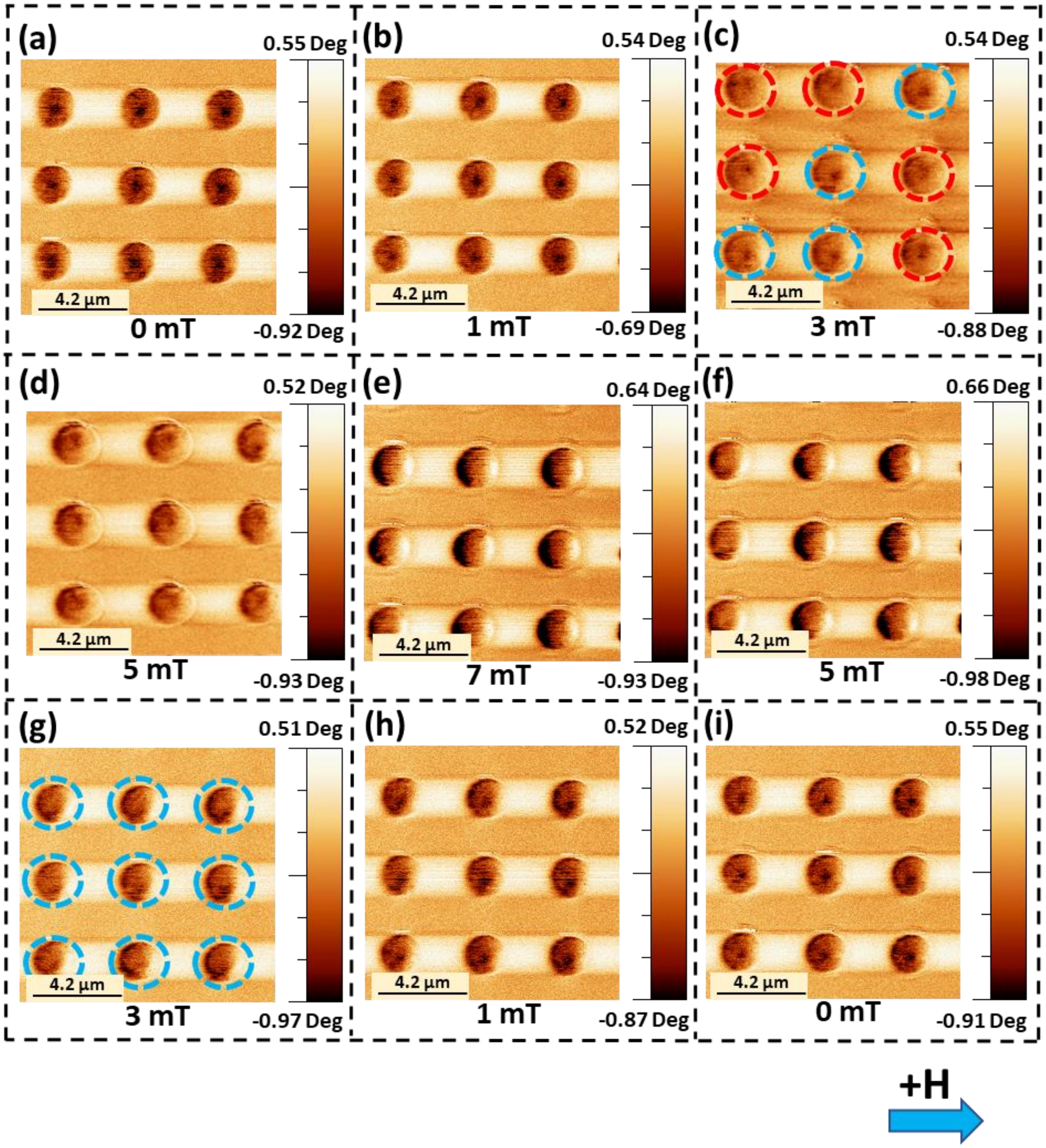

Figure 4.24: MFM images of 3 x 3 disks for low MS array at (a) zero field and (b-h) under the application of an in-plane field H in the +x direction and (i) return to remanence, obtained at 2 mT steps up to +7 mT. Circles with red and blue outlines represent CCW and CW, respectively. Note that for the 0 mT case, a maximum residual field of magnitude 1.2 mT is present due to remanence in the magnet poles.

Comparison between experiments for the high MS and low MS regime show a lower re-nucleation field for the low MS array (see table 4.2).

	Annihilatin field (mT)	Re-nucleation field (mT)
High MS array	7	5
Low MS array	7	3

Table 4.2: A summary of experimental annihilation and re-nucleation fields for both the high MS and low MS array.

The field-driven displacement of the vortices results in a non-negligible stray field around the disk, which defines the strength of interdisk magnetostatic coupling. The magnetic properties of identical interacting disks can be modelled on the basis of a “rigid vortex” model [25]. This model assumes that the vortex moves in in-plane applied magnetic fields while keeping its shape. The reduced equilibrium core displacement $s = l/R$ is determined by minimizing the total magnetic energy as a function of the disk sizes and interdisk distances. In an external magnetic field, the disk energy consists of exchange W_{ex}, Zeeman W_H, and magnetostatic W_m contributions. The exchange and Zeeman terms are not affected by interdisk magnetostatic coupling and hence are the same as those for an array of isolated disks. The energy of magnetostatic coupling in two-dimensional arrays of identical disk arrays can be calculated starting from the general expression for the magnetostatic energy density of an in-plane magnetized patterned films. The following expression for the annihilation field can be deduced [151]:

$$H_{an}(\beta,\delta,R,\varphi_H) = 2\Gamma(\beta,\delta,R,\varphi_H)M_s, \tag{4.1}$$

$$\Gamma\,(\beta,\delta,R,\varphi_H) = \frac{4\pi}{T_xT_y}\sum_k f(\beta kR)\frac{J_1^2(kR)}{k^2}cos^2(\varphi_k - \varphi_H) - \frac{1}{2}\left(\frac{R_0}{R}\right)^2$$

Where $f(x) = 1 - (1\exp(-x))/x$, $\beta = L/R$ is the disk aspect-ratio, $J_1(x)$ is the Bessel function, and φ_k and φ_H are respectively the polar angles for the reciprocal lattice vector k and applied field H, $T_{x,y} = 2R + d_{x,y}$ are the disk lattice periods, R_0 is the exchange length. The function $\Gamma\,(\beta,\delta,R,\varphi_H)$ defines angular variation of magnetostatically induced anisotropy. As shown by [151], when interdisk distance is smaller than disk radius arrays, the magnetostatic interaction decreases the vortex nucleation and annihilation fields which is reverse to our result. We note that there are several possible reasons for the discrepancy between our work and that of Shima et al. Firstly, the geometry of the array is fundamentally different with a rectangular lattice geometry being explored. Since the authors utilised the dipolar approximation in the above mentioned derivation, the energy of interaction between two elements can be written as:

$$E_D = \frac{\mu_0}{4\pi}\left[\frac{\boldsymbol{\mu_1}.\boldsymbol{\mu_2}}{r^3} - \frac{3(\boldsymbol{\mu_1}.\boldsymbol{r})(\boldsymbol{\mu_2}.\boldsymbol{r})}{r^5}\right] \tag{4.2}$$

Where the 1/r^5 term was discarded by the authors, within the approximation. The energy of interaction between two adjacent disks is then seen to be critically dependent upon the distance. For the rectangular lattice case, studied by Shima et al. this yields a dominant magnetostatic interaction along one-dimension, between adjacent elements. In this regime, the closer the elements, the larger the stray field experienced from the neighbour and the symmetry of the field promotes magnetisation in the field direction, lowering the annihilation field. For our square lattice samples, the situation is much more complex. There is now an additional stray field contribution that comes from elements in the row above and this opposes both the external field and stray field from elements within the row. We note that though these two field contributions would cancel exactly in an ideal 2D sample, disorder within the array and its three-dimensional nature may yield a preference for one over the other. In this case, it appears to be the inter-row interaction that dominates.

4.5.2 Micromagnetic simulation of low MS regime

Figure 4.25 depicts simulations for a non-interacting array. A 3 x 3 disk array was used in a similar way to previous simulations, and the central disk chosen for symmetry reasons. Overall, a similar behaviour is seen apart from the annihilation and re-nucleation fields which have lower values of 50 mT (see Fig. 4.25d) and 30 mT (see Fig. 4.25e), respectively and consistent with experiments.

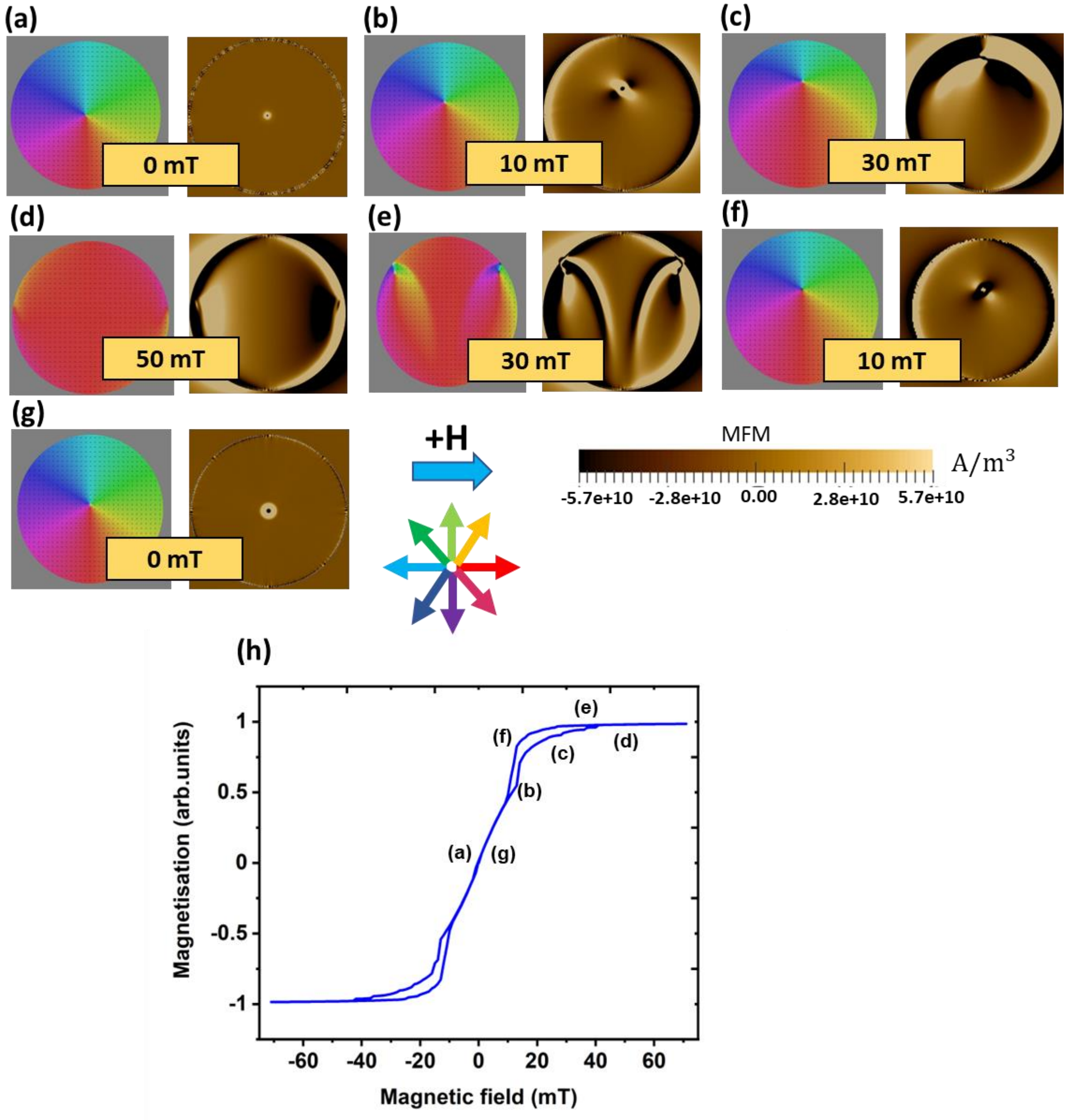

Figure 4.25: Simulated spin configuration and the corresponding MFM for the low MS array at (a) zero field, (b-f) under the application of an in-plane field H in the +x direction and (g) return to remanence. Different colours represent the direction of magnetisation with respect to the applied field, as depicted in the colour wheel. (h) Simulated hysteresis loop, with labels corresponding to the configurations (a-g).

The simulated hysteresis loop is shown in Fig. 4.25(g). The loop is qualitatively similar, but there are some important quantitative differences between this system and the high MS system. Comparing the simulated hysteresis loops for high MS and low MS arrays reveals that the characteristic field for vortex annihilation at point (d) in Fig. 4.25 is slightly lower in the low MS array. Likewise, as the applied magnetic field is reduced, the double vortex state emerges at point (e) and the vortex core in the low MS array re-nucleates by 3 mT at a lower field value. The increased field for the interacting array is thought to be due to the fact that the stray field contribution that comes from elements in the row above and this opposes both the external field and stray field from elements within the row. This is consistent with literature since the annihilation field and re-nucleation in soft magnetic elements was previously found to be influenced by the symmetry of the stray field due to neighbouring elements [25, 144]. Figure 4.26 shows that in the saturated state a stronger stray field (H_s) interaction, is expected in high MS array. It is not simple to determine, via inspection, how the stray field distribution will impact the characteristic fields due to the anisotropic nature of the MS interaction. Disks that interact upon the same horizontal line will have a component of stray field parallel to the magnetisation, adding a small perturbation to the external field seen by a disk. At the same time, the stray field from disks above and below the central element will be opposing the magnetisation, reducing the stray field. Micromagnetic simulations indicate that this latter interaction is dominant since they show an increase in the annihilation and re-nucleation field for the high MS array.

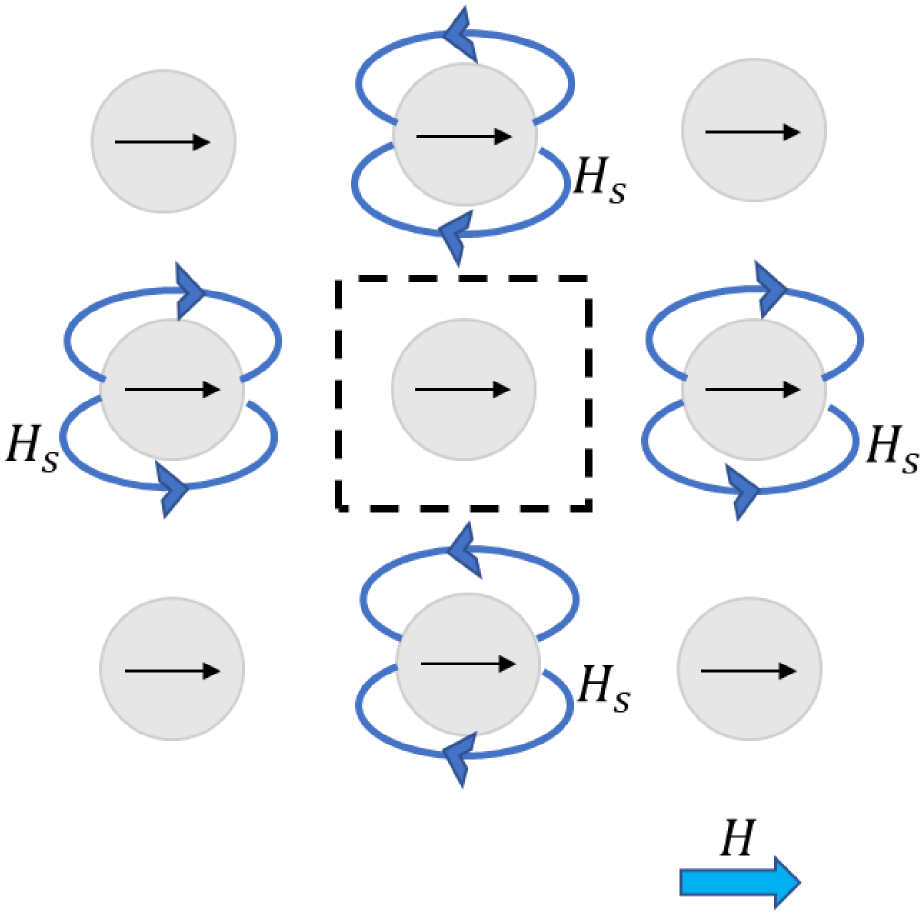

Figure 4.26: Illustration of stray field lines in high MS sample at saturation state.

4.6 High MS disks array with 3D defect.

4.6.1 Morphological characterisation

Having now clearly demonstrated that the new methodology can yield spin textures seen in conventional planar systems, we now exploit TPL in order to produce an array with a hemispherical defect. In the first instance, we attempt to explore the smallest perturbation possible with TPL and investigate how such a defect can actually impact the spin texture of the system. The investigation focuses on a $Ni_{81}Fe_{19}$ disk with a diameter of 2 μm and a height of 40 nm in the high MS array. Here we chose to look at the coupled regime for the defect sample in order to investigate if collective interactions, driven by magnetostatics can be controlled via small 3D perturbations. The disk has one hemispherical defect which has a diameter of 400 nm while its height is just 50 nm. The design places a spacing of 250 nm between the defect and the disk centres (see Figure 4.27).

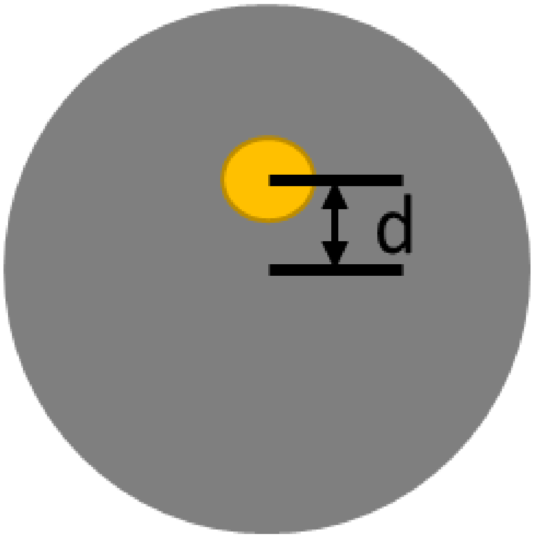

Figure 4.27: Design of a $Ni_{81}Fe_{19}$ disk with a hemispherical defect. The distance (d) between the disk and hemispherical defect centre is defined to be 250nm.

The fabrication of such a subtle defect requires careful consideration of both TPL point-spread function, its position with respect to the disk surface and then the impact of this upon the film deposition. The focus of this investigation was to design a defect that is integrated with the disk, with no discontinuity in the $Ni_{81}Fe_{19}$ film. Clearly, producing a defect with steep sidewalls, coupled with line-of-sight deposition, would result in such a gap. Therefore, the focus is upon a hemispherical structure with low z component, yielding a subtle perturbation on the surface. TPL yields an ellipsoidal point spread function (see Fig. 4.28) and a voxel that follows this symmetry. In order to yield a subtle hemispherical perturbation, the position of the PSF needs to only slightly protrude the surface as demonstrated in Fig. 4.28.

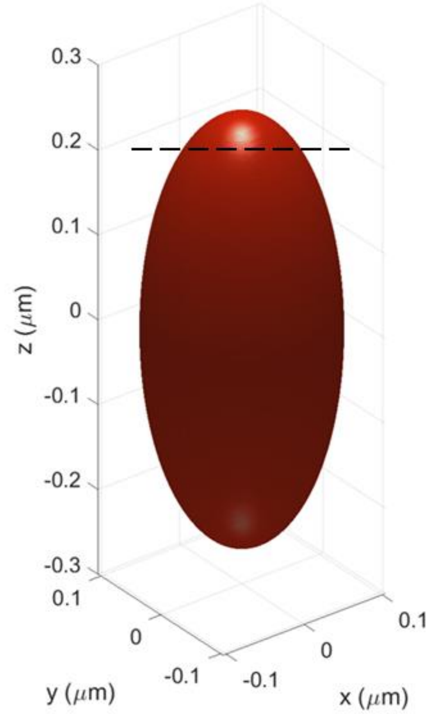

Figure 4.28: Schematic showing the TPL point spread function. Calculation was performed via solving the diffraction equations, courtesy of Joseph Askey. Dashed line indicates a small protrusion of the PSF above the disk surface.

A dose array was created for a disk geometry and a single exposure of the PSF offset from the surface as shown in Fig 4.28. The laser power and the scan speed were adjusted to determine the ideal parameters required to yield an observable defect. In Figure 4.29(a), the top-view SEM image of the defect array is shown. The structures appear to follow the design parameters with a diameter of 2 µm and a lattice spacing of 3 µm (centre - centre). A 20° tilted SEM image (see Fig. 4.29b) was also obtained allowing a better idea of the 3D geometry and an initial view of the defect. A closer view of the 400 nm hemispherical defect upon a single disk is shown in Fig 4.29(c). It is also clear from this image, that there is finite edge roughness, where the $Ni_{81}Fe_{19}$ film, meets the polymer circumference.

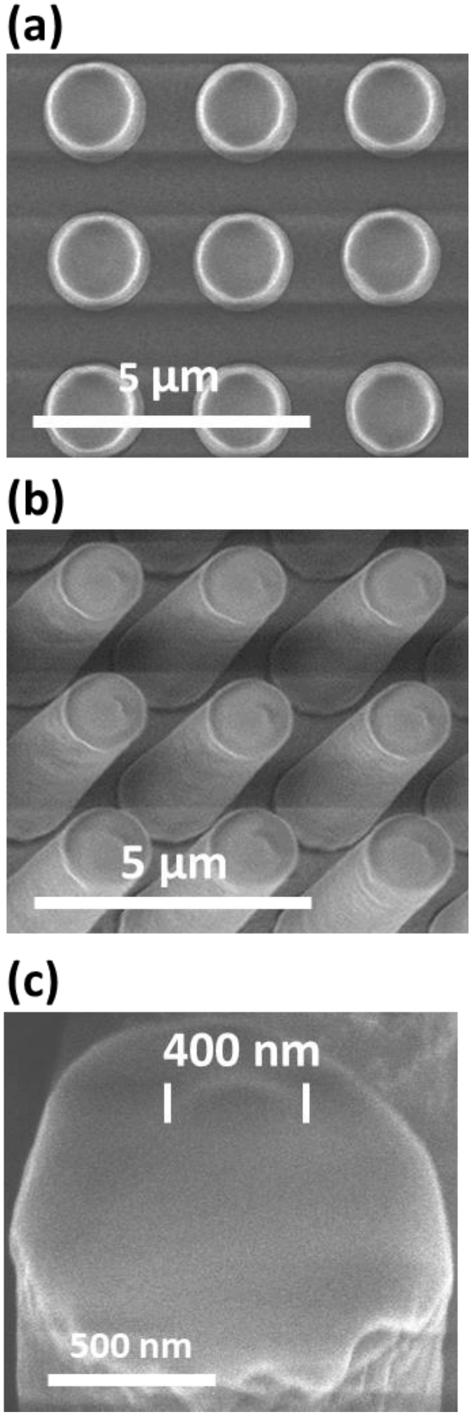

Figure 4.29: SEM images of disk array with hemispherical defect from (a) a top-down view as well as at (b, c) a 20° and 60° tilt with respect to the substrate plane respectively.

AFM images of the defect disks array are shown in Figure 4.30. Fig. 4.30(a) shows the topography of array, with a line profile shown in Fig 4.30(b). Analysis of areas away from the defect shows that the disks have a flat surface together with low roughness of approximately 8 ± 0.7 nm. The profile shown in Fig 4.30(b) clearly shows a small increase (50 nm) in height, close to the centre of the disk (circle with red dashes). However, the defect can be more clearly seen in the derivative image shown in Figure 4.30(c). Fig. 4.30(d) shows a close-up AFM image of the defect revealing the 3D topography more clearly and allowing the geometry of the defect to be determined.

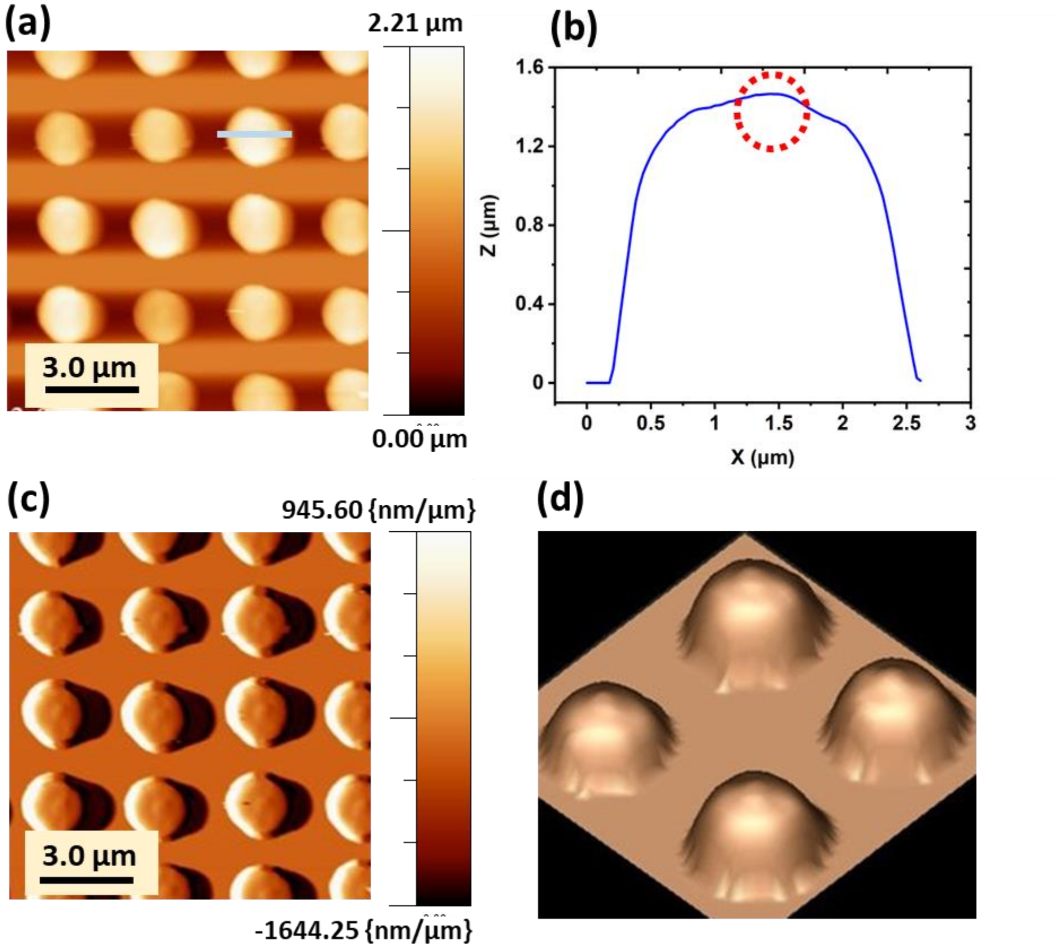

Figure 4.30: (a) AFM image of disks array with hemispherical defect in high MS regime (b) Line profile across disk showing the defect (c) error image and (d) 3d view.

Figure 4.31(a) depicts an MFM image of the as-deposited state for a 4 x 4 defect array. Two distinct states are observed (b, c). Figure 4.31(a) shows that in some disks the contrast is spread about the centre of the disk (denoted by a solid black square). We label this the centred state. The second state is characterised by contrast above the centre of the defect (denoted by dotted black squares) and is labelled the offset state. Zoomed images of the contrast for each state is shown in Figs, 4.31b and 4.31c. The centred state is observed greatest in the array with statistics 9:3.

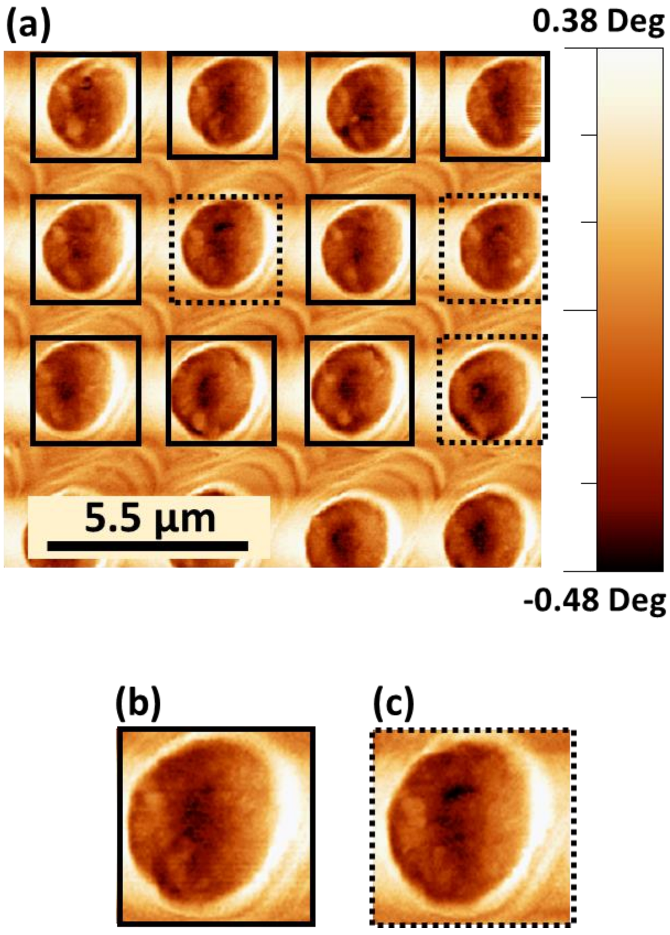

Figure 4.31: (a) MFM images of 4 x 4 defect disks array in the as-deposited state showing two different core states, (b) the centred state with contrast at the middle of the disk and (c) the offset state with core shifted upwards on defect upper edge. The colour bar represents phase shift.

4.6.2 Field driven motion

MFM images of a 3 x 3 array of disks with defects for the high MS regime under the application of an in-plane field are illustrated in Figure 4.32. At remanence, most of the core contrast is spread around the centre. When a magnetic field is introduced, the vortex core displaces onto the lower or upper edge of the disk, depending on the chirality as can been seen in Figs. 4.32(b, c). The chirality distribution ratio is 6:3 (CCW: CW) indicating a chirality preference as expected for high MS. Interestingly, the chirality preference is opposite to that's seen in the plain disks in for same field direction (CW: CCW). Interestingly, the chirality preference is opposite to that seen in the plain disks in for same field direction (CW: CCW). Previous methods to control chirality include the use of slightly elliptical geometries [152] and edge notch defects [153], with the latter study being most similar to the situation studies in this thesis. Therein, it was noted that a simple break in symmetry of the disk, with respect to the field axis can be used to control chirality. In our system, we note that the complex shape of the 3D defect, also breaks the symmetry. In particular, any subtle differences in height upon the right and left side of the defect will yield different magnetic pole distribution upon the defect sidewalls producing a non-uniform demagnetisation field, which may account for a preferential chirality. This is a novel method for manipulating the micromagnetic configuration of the magnetic structures by realizing a 3D defect which allows one to control vortex chirality without deformation of the 2D shape [81]. Further micromagnetic studies will be performed in Dr Ladak's laboratory in order to understand the origin of this phenomenon.

Characteristic opposing contrast appears as the field increases high enough to saturate the structures at 5 mT (see Fig. 4.32d). It is worth noting that when the applied field value is reduced, the vortex core appears to re-nucleate in a double vortex state (see Figs. 4.32e, f). Importantly, the contrast associated with the double vortex state is located on the lower half of the disk, indicating re-nucleation takes place on the lower edge. Back to zero field, Fig. 4.32(g) shows that all disks are in the same state with contrast offset at upper edge.

Figure 4.33 and Figure 4.34 illustrates an example of the two different states shown in Figs. 4.31, which provides a better examination of the vortex transition.

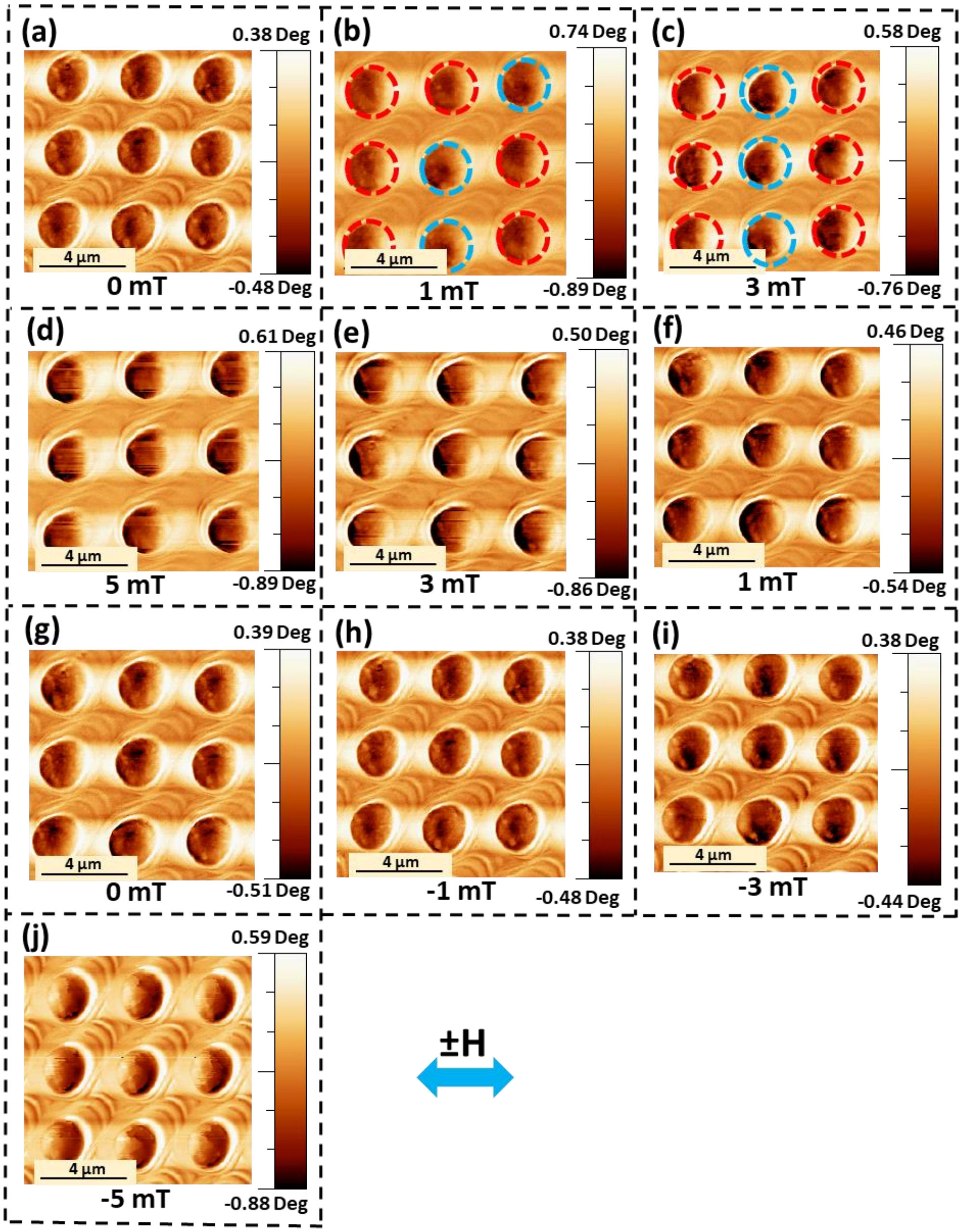

Figure 4.32: MFM images of 3 x 3 defect disks for high MS array at (a) zero field and (b-j) under the application of an in-plane field H in the ± x direction, obtained at 2 mT steps. Circles with red and blue outlines represent CCW, CW states, respectively. The colour bar represents phase shift. Note that for the 0 mT case, a maximum residual field of magnitude 1.2 mT is present due to remanence in the magnet poles.

Figure 4.33 displays the MFM images for the switching mechanism for one disk in the defect array, having core located at the disks centre in remanence and previously shown in Fig. 4.31(b). As a small positive in-plane field is applied, the central contrast broadens and offsets upwards, Figs. 4.33(b, c), compatible with CCW chirality. Further field increments result in abrupt core annihilation at 5 mT, a lower field than in the plain array and saturation being approached as shown in Fig. 4.33(d). At 3 mT and 1 mT, the core re-nucleates by double vortex state (see Fig. 4.33e, f). This state emerged previously during the re-nucleation phase, in circular disks thicker than 30 nm [56, 65]. Concerning the negative field increments, the core moved downwards, as predicted for this chirality (CCW) Fig. 4.33(i) until it is annihilated at 5 mT Fig. 4.33(j).

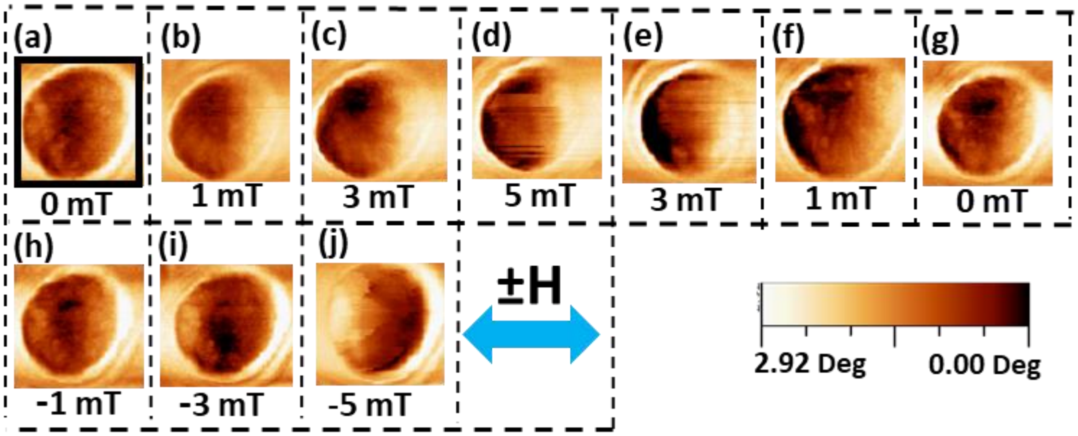

Figure 4.33: MFM images of single defect disk for the core located at the middle at (a, g) zero field and (b-j) under the application of an in-plane field H in the ±x direction (see arrow). Note that for the 0 mT case, a maximum residual field of magnitude 1.2 mT is present due to remanence in the magnet poles.

In the offset state, (see Fig. 4.31c) the core is shifted upwards from the disk centre at remanence. MFM images for the magnetisation process for this state is shown in Figure 4.34. In this state, when a positive field is applied in the x-direction the core is displaced downward indicating CW chirality as shown in Figs. 4.34(b, c). Increasing the field results in core annihilation by 5 mT (see Fig. 4.34d) and the re-nucleation of the core observed via a double vortex when the field reduced back to 3-1 mT (see Figs. 4.34e, f). Introducing a negative field result in core displace downward associated with CCW chirality. It is noticeable that the vortex core remains displaced upwards in its remanent state. This is due to the remanent field from the electromagnet poles which yields a small ~1 mT field. Hence, application of a negative field, 1 mT (see Fig. 4.34f), yields the zero field scenario.

The defect appears to yield two different behaviours, yielding two vortex core positions with respect to the defect. Previous studies, with simpler defects placed upon disk surfaces, via conventional lithography has yielded some similar results. In that study the disk upon the surface was approximately 200 nm in size and MFM showed a remanent state with core contrast spread throughout the centre [154] and a second state was not observed. However, we note that a distinct difference between our work and that in ref [154] is the geometry of the defect. Our perturbation has a smooth transition from the main disk to the upper surface, whereas in [154] the lithography process will yield a steep sidewall, perhaps make it less favourable for the core to reside upon the perturbation edge (high exchange energy). Despite an extensive review of the literature, no studies with true 3D defects, made by design, could be found. This is likely to be due to 3D lithography techniques being relatively new. However, the introduction of such defects is interesting from a number of perspectives. For example, vortex systems have been studied a great deal in spin-torque oscillators [155-157]. The addition of 3D defects may provide an additional degree of freedom in controlling the frequency of oscillation.

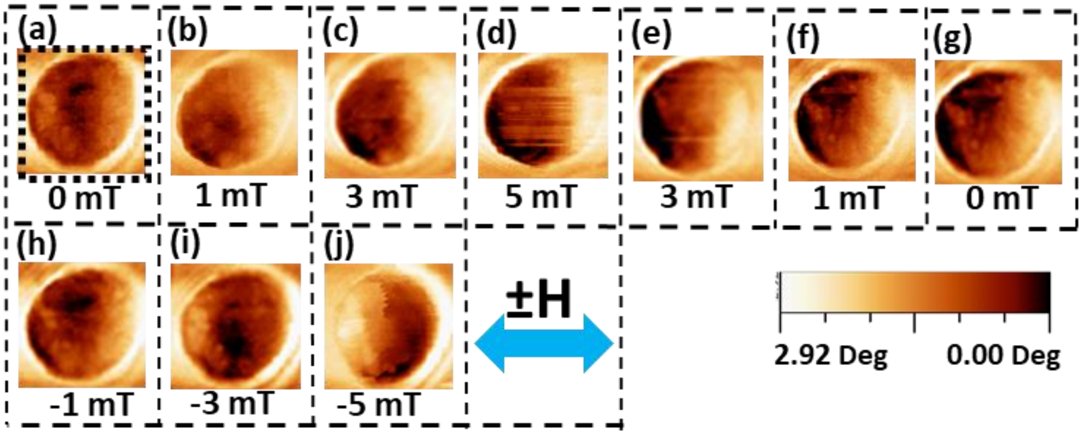

Figure 4.34: MFM images of single defect disk for the core shift upward at (a, g) zero field and (b-j) under the application of an in-plane field H in the ±x direction (see arrow). Note that for the 0 mT case, a maximum residual field of magnitude 1.2 mT is present due to remanence in the magnet poles.

4.6.3 Micromagnetic simulation

In order to shed light upon the expected behaviour from the array with defects, idealised simulations were performed. The defect was assumed to be of hemispherical geometry with diameter 400 nm and height 50 nm, as shown in Fig. 4.35 where it is clear that it is a shell geometry.

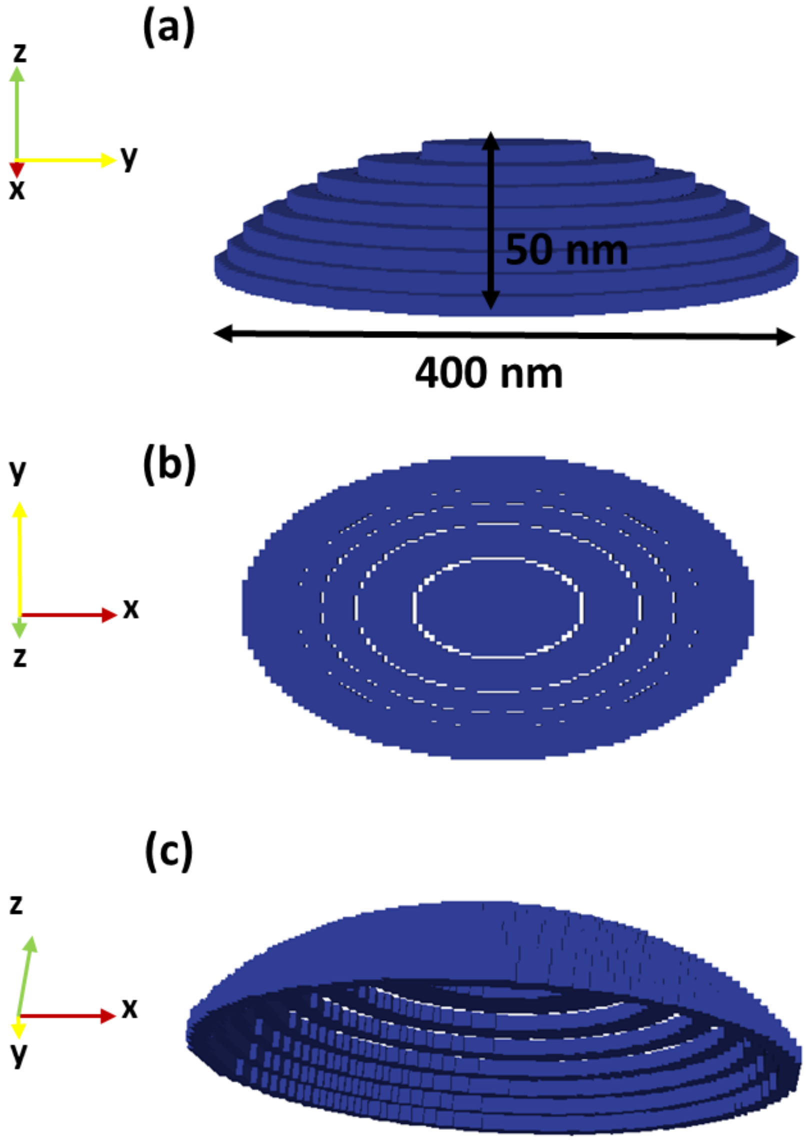

Figure 4.35: Simulated thin hemispherical shell defect geometry of 400 nm diameter and 50 nm height. The three panels show the defect from different angles (a) side view, (b) top view and (c) tilted down view.

Simulations were run with a 3 x 3 array as previously. The behaviour of the central disk was then analysed in positive and negative field directions as depicted in Fig. 4.36. At remanence, a vortex state can be seen but with a core slightly offset from the disk centre (see Fig. 4.36a). The simulated MFM image shows strong dark contrast at the core as well as a bright and dark contrast on the opposite sides due to the defect's hemispherical geometry and the change in $\mathrm{M_z}$ sign through its geometry. This remanent simulation agrees qualitatively with some of the experimental results in Fig. 4.32(a), which exhibit a dark contrast across the defect area, implying that the core is located there. When applying a field in the positive x-direction the core displaces upwards (see Figs. 4.36b, c) until it annihilates by 50 mT Fig. 4.36(d) at field value close to the experimental field Fig. 4.32(d). Two vortex cores re-nucleate from the top on either side of the defect as the field is reduced to 30 mT (see Fig. 4.36e). This sort of a double core nucleation has been seen previously in similar disks [35]. Further field reduction causes both vortex cores to shift upward until they are above the defect, and this occurs when a third core nucleates near the defect edge. The creation of an antivortex immediately above the defect is driven by the constraints imposed by these three vortex cores. The complex spin texture, which consisted of two vortices and an antivortex, has vanished at 10 mT, leaving only a single core inside the defect (see Fig. 4.36f).

The magnetic field in the opposite direction (negative x-direction), the core must move farther in the opposite direction since the defect is not centred. In Figure 4.36(h, i), the core displaces downwards till it annihilates by 50 mT, as shown in Figs. 4.36(j), at field value similar to the experimental field (see Fig. 4.32j). As the field strength is decreased to 30 mT, the start of two vortex cores can be seen forming on each downside of the defect (see Fig. 4.36k). The complex spin texture, comprised of two vortices and an antivortex, has disappeared at 10 mT. There is now just a single core present inside the defect (see Fig. 4.36l and 4.36m).

Figure 4.36(n) reveals the simulated hysteresis loop for the defect array. The linear part on the hysteresis loop at low field, represents the movement of the vortex core. The core appears to pin to the outer edge of the defect. The pinning is magnetostatic in nature, since the defect becomes uniformly saturated in the positive x-direction, an attractive magnetostatic interaction exists between the defect and the upper portion of the core, which has a large -ve x component of magnetisation. A sharp jump in magnetisation at point b, indicates the point at which the core detaches from the defect, as it translates upwards. A change in slope then occurs (between b and c) as the core is pushed against the boundary of the main disk, after which saturation is seen, with the core annihilating at approximately 50 mT (d). Coming down from positive saturation, the renucleation of a double vortex is not easily seen in the loop (e) since a complex domain patten maintains a very large component of magnetisation along the field direction. An abrupt drop is seen at (f), at which the core abruptly relocates to inside the defect. When the magnetic field is decreased back to zero, the vortex core is shifted to the centre of the defect (g). Application of a field in the opposite direction yields similar behaviour but with the core displacing vertically downwards. Again, a sharp jump is seen (at h) whereby the core detaches from the defect. The remainder of the loop is similar to positive branch, with annihilation at (j), re-nucleation of a double vortex at (k) and an abrupt drop at (l) as the core starts to interact with the defect.

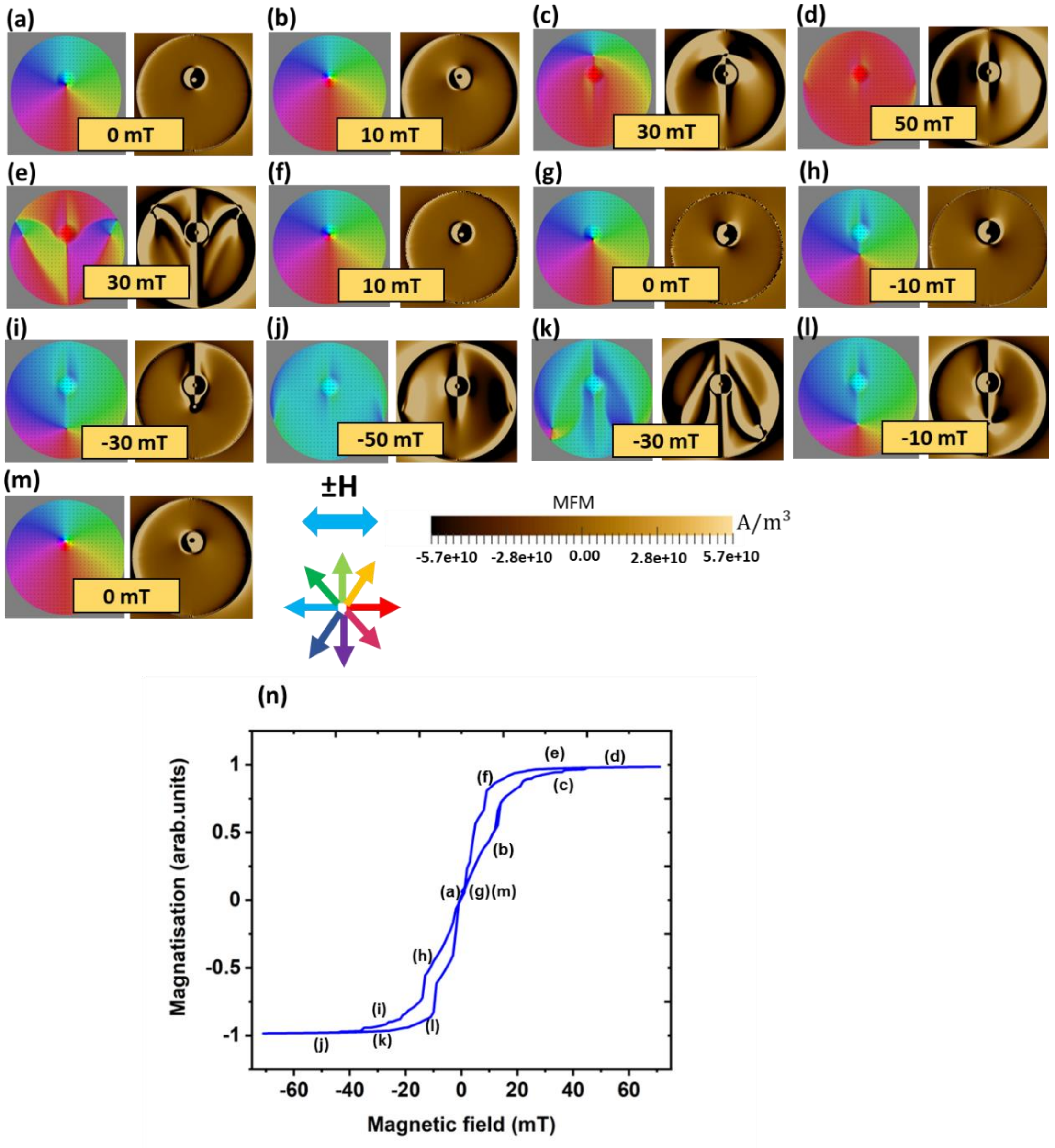

Figure 4.36: Simulated spin configuration and the corresponding MFM for high MS defect array at (a) zero field and (b-l) under the application of an in-plane field H in the ±x direction and (g,m) return to remanence. Different colours represent the direction of magnetisation with respect to the applied field, as depicted in the colour wheel. (n) Simulated hysteresis loop, with labels corresponding to the configurations (a-m).

Prior to the formation of the final vortex state, small submicron disks typically proceed through the so-called single state (C-state) while the larger micron-sized disks proceed through the more complicated vortex-pair state. In this study, we also observed a double vortex state in our 2 μm defect disk, as also mentioned in the literature [65, 147]. Three Bloch domain walls with in-plane magnetisation curling around them are typical features of the double vortex state (see Figs. 4.36e, k). Different configurations of out-of-plane magnetisation directions can be observed on the three walls. The three-domain walls shift into each other as the applied field is reduced, forming a vortex state.

The previous observation from both experimental and simulation results demonstrated that the presence of a 3D defect impacted both the remanent state and magnetic reversal of the disks and yielded significant changes to the vortex re-nucleation and annihilation fields (see table 4.3). The vortex core in the plain disks begins to re-nucleate at a field value equal to 5 mT but in the case of the defect disks, the core starts to re-nucleate at a field value equal to 3 mT (see Figs. 4.28e, f and Fig. 4.31e).

	Annihilation field (mT)	Re-nucleation field (mT)
Plain high MS	7	5
Defect high MS	5	3

Table 4.3: A summary of experimental annihilation and re-nucleation fields for plain and defect high MS array.

Moreover, the vortex chirality can be controlled by the direction of the external magnetic field when breaking the symmetry. The majority of methods of chirality manipulation are based on an application of magnetic asymmetry in disks through cutting of a part of the disk, forming of a hole or producing a magnetization gradient [158, 159]. However, the modified shape or magnetization asymmetry of a disk results in significant changes in the values of vortex nucleation and annihilation fields as shown in this thesis. We also highlight here that the core seems to be much wider at the remnant state for the defect array, taking up a large area of the defect.

Discussion

In this chapter it has been demonstrated that two-photon lithography (TPL) can be used to realise magnetic disks upon the micon-range and with defects of order ~100 nm, placed upon the surface. We note that previous attempts to study the impact of defects upon spin texture and magnetic reversal in vortex systems have utilised multi-step optical lithography and electron beam lithography.

Of the numerous laser-based techniques that are available, two-photon lithography (TPL) is considered to be the optimal option for the development of distinct 3D micro/nanostructures on the grounds that it facilitates the building of arbitrary structures with high spatial resolution [48]. Furthermore, local polymerisation and feature sizes below the diffraction limit can be achieved by utilising laser beams with intensities slightly surpassing the polymerisation threshold, as has been extensively discussed in Chapter 2. The technology is distinct due to its capacity to facilitate the construction of true 3D freestanding structures.

The resolution of multi-step optical lithographic processes is constrained by the wavelength of the light employed for photoresist exposure. These processes are primarily designed to produce patterns ranging from a few micrometres to a few hundred microns in size [160]. The obvious disadvantage of such multi-step optical lithography in attempting to realise true 3D structures, is the additional processing time for multiple exposures. In addition, any 3D geometry has to be built from a number of planarized layers, only providing a coarse approximation of a complex 3D geometry.

In self-assembly, achieving precise control over the density and shape of nanostructures presents challenges and it is also susceptible to defects. Furthermore, the attainment of perfect periodicity in self-assembled structures composed of nanoscale components is typically limited to areas of micrometre scale [161].

Electron-beam lithography is a powerful technique that can generate structures with a resolution of tens of nanometres. However, the technique is usually utilised to realise only 2D structures [162], unless complex cryogenic systems are utilised [163]. Focused electron beam-induced deposition (FEBID) is a highly adaptable method for fabricating nanoscale structures in 2D and 3D. This process achieves a remarkable level of precision regarding positional accuracy, all within a single processing step. However, the technique is usually only suited to writing small structures, rather than large arrays and in addition the technique suffers from carbon contamination which can be detrimental to the magnetic properties [100]. Hence, of the other techniques investigated it seems TPL remains optimal for realising complex 3D magnetic structures, with high purity and fidelity.

Concerning the influence of defects on switching behaviour in micron-scale disks, previous studies have demonstrated that the presence of a hole in a disk structure leads to a change in the displacement of the vortex core. In one study [86], a disk with a diameter of 3 μm and incorporating a centrally located hole measuring 300 nm in diameter was fabricated. The position of the vortex core was plotted against the applied field using Lorentz transmission electron microscopy. Upon applying an external field, the vortex core experienced displacement from the central region of the disk towards the edge of the hole. Furthermore, based on their observations, it can be inferred that as the core approached the hole edge, it underwent a complete transition into the hole, signifying the annihilation. This behaviour resulted in a reduction in the overall energy of the system. This highlights the advantage of using 3D perturbations as in this thesis. Here, the spin-texture of the vortex is maintained but controlled using the perturbation. Simply placing holes in the centre, yields an annihilation of the core, completely changing the underlying spin-texture.

Another research group [35, 154] conducted an experiment involving the manipulation of the magnetic vortex state in a disk measuring 600 nm in diameter. This was achieved by employing conventional lithography techniques to position a smaller disk measuring 200 nm in diameter on top of the larger disk. The researchers employed magnetic force microscopy (MFM) to measure the magnetic vortex chirality and track the vortex core's trajectory within the disk-on-disk structure. The observation revealed that at remanence, the core contrast is spread within the central region. At the same time, the small disk exhibits a single-domain structure. There are crude similarities between this study and what has been observed in this thesis. Notably, in our work the core appears to exhibit a significantly greater diameter in the remanent state, occupying a substantial portion of the defect area. Our study previously discussed that two distinct positions of the vortex core were observed in relation to the defect. This has not been observed in this study. Presumably, the planar disk defect does not yield a significant energy barrier when the core approaches close to remanence. In contrast, the 3D nature of the defect in our study has an out-of-plane sidewall which will yield an energy barrier (both magnetostatic and exchange), for the core to surpass. Stochasticity in the reversal process is expected to yield subtly different paths of the core, and when approaching remanence will yield slightly different energy barriers. This may explain why distinct states have been observed at remanence. We also note that differences in the 3D geometry of the defect yields distinct magnetic reversal behaviour. Whereas, in the literature [2,10] re-nucleation was found to occur close to the defect, in the system studied in this thesis, this would be energetically unfavourable and in particular yield a high exchange energy close to the defect centre, forcing re-nucleation at edges.

An alternative method for manipulating the vortex state involves the utilisation of a Cobalt nanostripe positioned on top of a disk, as described by [164]. A Cu spacer was deposited between the disk and the nanowire. The utilisation of MFM revealed that the chirality direction of disk is dependent upon the orientation of the single domain nanowire. The nanowire magnetisation direction can be manipulated through the application of an external magnetic field and hence one has a means to control chirality. Field driven studies demonstrated that vortex core re-nucleation and trajectory do not change when compared to conventional disks and at remanence, the vortex core was observed at the centre of the disk. Here it is interesting to note the difference between a nanowire defect, planar disk defect and hemispherical defect. Clearly, the single domain nature of the nanowire, simply allows it to take a simple magnetisation texture, aligned with the local easy axis as forced by shape anisotropy. The Cu layer is of sufficient thickness to ensure no direct exchange or RKKY coupling, and hence it is purely the stray field from the nanowire that controls the underlying vortex chirality. In contrast, in our structures and in planar disk structures there is continuity between the defect and the disk layers, forcing a perturbed spin texture of the vortex.

Conclusion

The results reported in this chapter demonstrate that TPL can be used to realise standard 2D spin textures observed previously, but with the powerful ability to place 3D defects upon the surface. The magnetic characteristics of circular systems, in a vortex state were investigated. Three main systems were studied, plains disks with low MS array, plain disks with high MS array and disks with hemispherical defects also in the high MS array. For each case, MFM at remanence and in the presence of an external field was used to measure the spin texture.

In the case of the plain arrays (high and low MS arrays), there is a reasonable agreement between the experimental and simulation results. Both exhibit common vortex reversal magnesium, such as vortex core translation, annihilation and re-nucleation, although the process of how the core re-nucleates is not discernible from our MFM observations. At remanence, the high MS array showed a preference in chirality distribution whilst the low MS array showed equal chirality distribution. Moreover, low MS array show a lower re-nucleation and annihilation field than the high MS array due to the role of the magnetostatic interaction in the magnetization process for small interdisk distances.

For the case of the defect array, where the core of the vortex can be shown to be offset due to the defect position, there is some consensus between the experimental findings and simulations at remanence. Furthermore, the experimental findings indicate that the perturbed geometry induces core re-nucleation on the edge of the disk by means of double vortex state which is also displayed by the simulations. Several factors must be considered: the defect geometry in the simulation is only an approximation of the experimental situation. Similarly, the core field-driven dynamics and its re-nucleation would be affected by local roughness inside the defect and across the disk, possibly illustrating the more complicated behaviour exhibited at low fields Fig. 4.32(i). We anticipate further TPL method parameter optimisation and the use of seed layers to minimise the underlying roughness, could remedy this situation.

Moreover, the difference in the vortex re-nucleation and annihilation fields between the plain disks and disks with defects in high MS arrays can still been seen, which indicates the strength of the magnetostatic interaction due to the adjacent defect. The re-nucleation and annihilation fields of the vortex state differ when comparing both the plain disks and disks with defects in high MS arrays, when applying the in-plane field. The plain disks magnetisation process behaves akin to that reported in the literature, with characteristic field values also agreeing [154]. However, in the defect disk, the vortex nucleates and annihilates at lower applied fields than in the plain disks. Moreover, in the defect array, the nucleation process occurs in a two-step transition state. The switching from double vortex state to one vortex state is associated with a reduction in total stray field from the entire ferromagnet disk.

5. Chapter 5

Magnetic behaviour of micron-sized squares with three-dimensional defects

5.1 Introduction

In the previous chapter, a proof of principle showed that 3D defects upon surfaces impact the spin texture in well-studied 2D systems. A significant disadvantage of this first system was that contrast is only seen at the core when using readily available magnetic force microscopy (MFM). Ultimately, this limits the extent to which the perturbed spin texture can be interpreted. This chapter aims to investigate the magnetic behaviour of a micron-sized ferromagnetic square system which provides contrast that can be interpreted more easily. With the pristine samples understood, we move on to investigate how significant defects can perturb the remanent state and switching of these square systems.

TPL was used to construct 2D arrays of square structures with optimum side length of 2 µm and heights of 5 µm. Additionally, a 40 nm layer of $Ni_{81}Fe_{19}$ was deposited on the structures. The result is 2D array of ferromagnetic squares elevated above the substrate.

The square arrays were imaged using scanning electron microscopy (SEM) and the distribution of feature sizes within the arrays was analysed. It was determined that the average length was 2.1 ± 0.03 µm, close to the design. Atomic force microscope (AFM) was used to understand the underlying topography of the square samples. The root mean square (RMS) roughness of the non-perturbed arrays is 4.4 ± 0.3 nm and for the array with hemispherical defects was 6.20 ± 0.08 nm. Samples were constructed in regimes of high magnetostatic (MS) coupling with a lattice spacing of 3 µm and regimes of low magnetostatic (MS) coupling with a lattice spacing of 4 µm. The spin texture was imaged using magnetic force microscopy (MFM). At remanence, contrast was observed for both samples with a closed magnetic flux configuration consisting of four domains that are separated by 90˚ walls and a vortex core in the centre. Applying a magnetic field in-plane yielded the usual vortex translation via wall movement and annihilation. Upon field reduction, the core re-nucleated and could be readily tracked back to the centre via observation of domain wall movement. Overall, this initial work is consistent with previous literature upon micron-sized magnetic squares.

Following this proof-of-principle, an in-depth comparison between the high MS array and the low MS array was carried out. Both the high MS array and low MS array in the as-deposited state demonstrated a remanent state with an equal chirality distribution. Application of a saturating field and subsequent imaging showed a preference in chirality in the high MS array whilst the low MS array showed equal chirality distribution. These findings suggest, during the growth process, a flux closure state is quickly formed in both cases, meaning the magnetisation in adjacent squares cannot interact, yielding equal chirality distributions. Application of a saturating field, in the sample after growth yields single domain states in the field direction and for high MS regime, yields a relaxation that minimises the MS energy via single chirality formation. Furthermore, an increase in the magnetostatic interaction was found to increase the vortex annihilation and re-nucleation fields, consistent with literature and previous results upon disks.

After demonstrating that it was possible to reproduce spin configurations seen in the literature, arrays of squares within the high MS array were fabricated with a 3D hemispherical defect on the surface, of diameter 600 nm. It was discovered that this perturbation had a considerable impact on both the remanent state and the magnetisation process. The domain walls within the remanent state were found to be offset, with the core apparently pinned to the defect. Subsequent application of a field showed the familiar vortex annihilation and re-nucleation processes but observed for lower fields than the pristine sample. The lower field values than the high MS plain array are attributed to the asymmetric spin texture formed due to the defect which leads to a reduced distance for vortex displacement for a single field direction.

5.2 Magnetic vortices in Py square structures

In the case of square elements, the vortex structure typically seen in squares, arranges into a Landau vortex state [165], due to the straight edges. In this arrangement, four domain walls which are positioned along the square diagonals divide the system into four triangular domains, yielding flux closure (see Fig. 5.1). At the centre, exchange energy is minimised by forming an out-of-plane core.

Initially, micromagnetic simulations were used to study how the thickness (10-50 nm) and square diameter (500-2000 nm) impacts the magnetic configuration. All investigated simulations across the range showed a Landau vortex state, with typical structure shown in Figure 5.1(a). The magnetisation is seen to break up into four domains with 90˚ walls along diagonals and an out-of-plane core in the centre. The presence of walls and their associated volume charge (Divergence in magnetisation) yields MFM contrast, making the configuration simpler to interpret as shown in Figs. 5.1(b, c). This yields MFM contrast along the square diagonals (indicated by the black contrast). At the square centre, at the intersection of diagonal, there is strong contrast from the vortex core, as seen in circular elements [166, 167].

Since all simulations in the range showed this behaviour, dimensions were chosen that could be accurately reproduced with TPL, whilst also attempting to minimise the write time. For this reason, all structures discussed in this chapter have dimensions of 2 x 2 $\mu\mathrm{m}^2$. A review of the literature [27, 168] suggest that when the interelement distance is less than the lateral size of one element the magnetostatic interaction between single elements has to be considered. This has enabled us to again define two sample types for this study, those that have high MS coupling (separation 1 μm) and those that have low coupling (separation 2 μm).

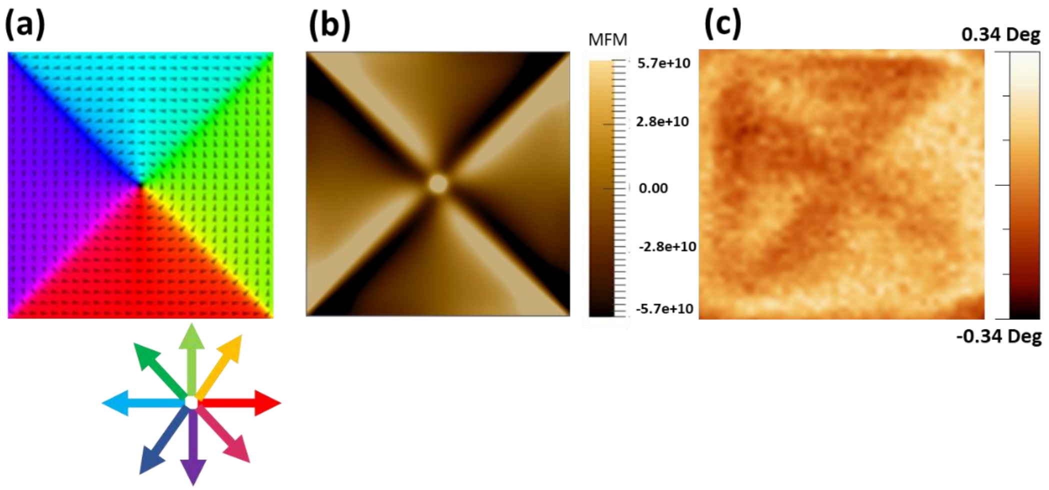

Figure 5.1: (a) Micromagnetic spin configuration, (b) simulated MFM and (c) MFM images of 2 x 2 μm^2 Ni$_{81}$Fe$_{19}$ element of 40 nm thickness at remanence. Different colours in (a) represent the direction of magnetisation with respect to the applied field, as depicted in the colour wheel. The colour bar represents phase shift.

5.3 Morphological characterisation of plain square arrays

Structures were fabricated with varying process parameters and the optimal writing conditions chosen (see section 4.3.1). Top-view SEM images of an array sub-section are displayed in Figure 5.2(a) which demonstrates that they follow specific design specifications with a square side length of 2 μm. A tilted SEM image at 45° (see Fig. 5.2b) was also produced showing the 3D geometry of the array and a height of 5 μm above the substrate. The geometry of the measured structures is expected to differ slightly from planar structures at the edges, due to the ellipsoidal voxel used during the TPL stage of fabrication. This voxel geometry results in curved out-of-plane edges and rounded corners, which is then translated into magnetic material during evaporation. This can be clearly seen in the SEM images in Fig. 5.2.

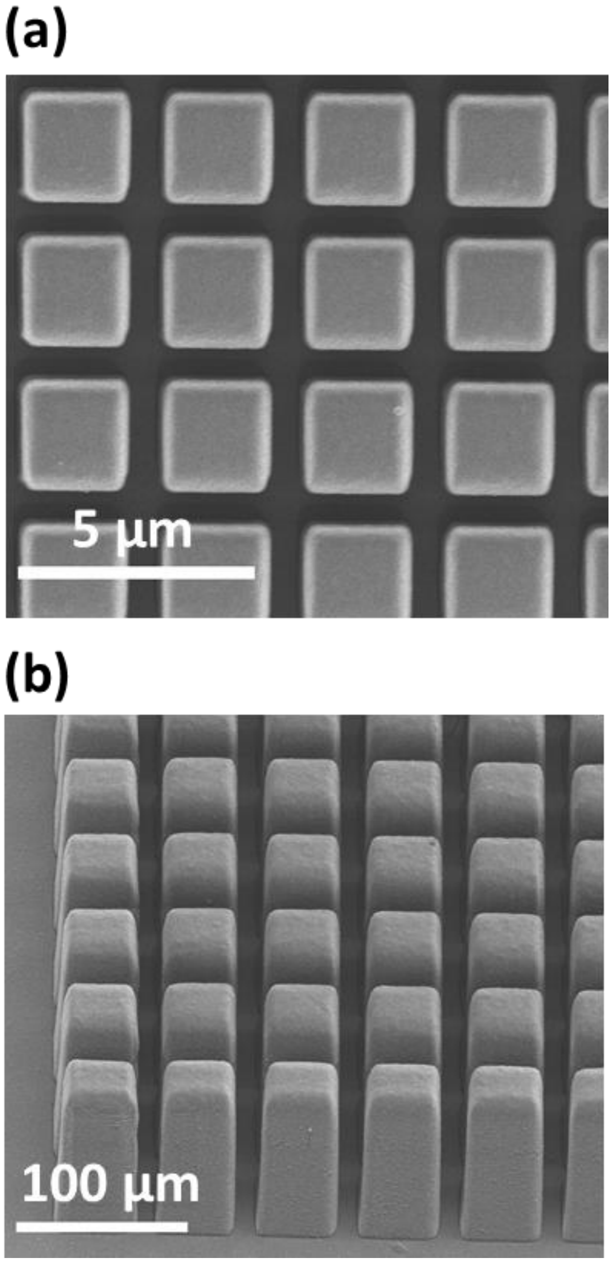

Figure 5.2: SEM images for a pristine squares array from (a) a top-down view as well as (b) a 45° tilt with respect to the substrate plane.

Figures 5.3 show atomic force microscopy images of the squares array in a high and low magnetostatic coupling regime. Figure 5.3(a) is an AFM image demonstrating high MS array topography. Figure 5.3(b) illustrates the topography of the low MS array. The topography reveals a flat and smooth surface with a low roughness of approximately 3.8 ± 0.2 nm for the high MS array and 5.0 ± 0.4 nm for the low MS array. This is slightly higher than the surface roughness of $Ni_{81}Fe_{19}$ micron size-squares fabricated using Si substrate [169], which has values less than 1 nm.

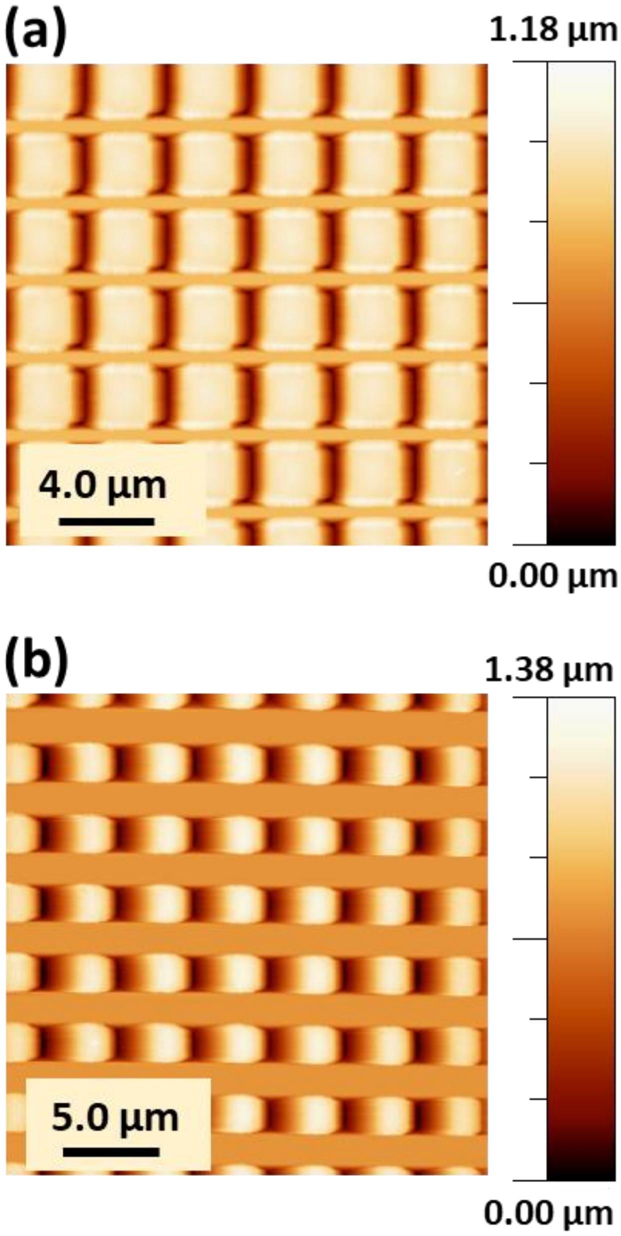

Figure 5.3: AFM images of (a) high MS square array (separation 1 µm) (b) the low MS square array (separation 2 µm).

5.4 Initial ordering of square arrays

Figure 5.4 illustrates MFM images of a squares array taken without the application of an external magnetic field (as-deposited state) and displaying both high MS and low MS arrays. MFM contrast is evident with a flux closure state consisting of four domains separated by 90˚ walls. At the square centre (at the intersection of diagonals), there is a vortex core as at the centre of circular elements. The two vortex chirality's appear in both arrays: counter-clockwise CCW (represented by the red dashed square) and clockwise CW (represented by the dashed blue square) as shown in Figure 5.4. Here we can determine chirality in absence of an applied field, unlike the circular case. As seen from the simulated MFM contrast and micromagnetic sims (see Fig. 5.1a, b), 90˚ domain walls develop, and the associated contrast allows the magnetisation in each domain to be determined.

As can be seen, for both high and low MS arrays both states are generated at approximately equal probability 8:8 (CCW: CW) due to the twofold energy degeneracy, as also observed in the literature [19]. The flux closure state yields a low stray field and a reduced magnetic interaction between the squares. In contrast to our examination of the disk structure in the preceding chapter even for arrays within the high MS regime, there is equal chirality distributions, again consistent with the literature [15, 16]. However, when a field is applied and each element develops a magnetisation, an interelement magnetostatic interaction is produced, owing to the development of magnetic charges upon edges. As predicted, the magnitude of this interaction grows as the element's lattice constant is reduced [17, 18]. It should be noted that the remanent state within a circular vortex, has the majority of its exchange and magnetostatic energy stored in the vortex core. In squares, there are some additional magnetostatic and exchange energy contributions owing to the noncircular element shape [170]. For example, a vortex spin distribution in square systems will result in spin alignment along the square edges, but misalignment at corners.

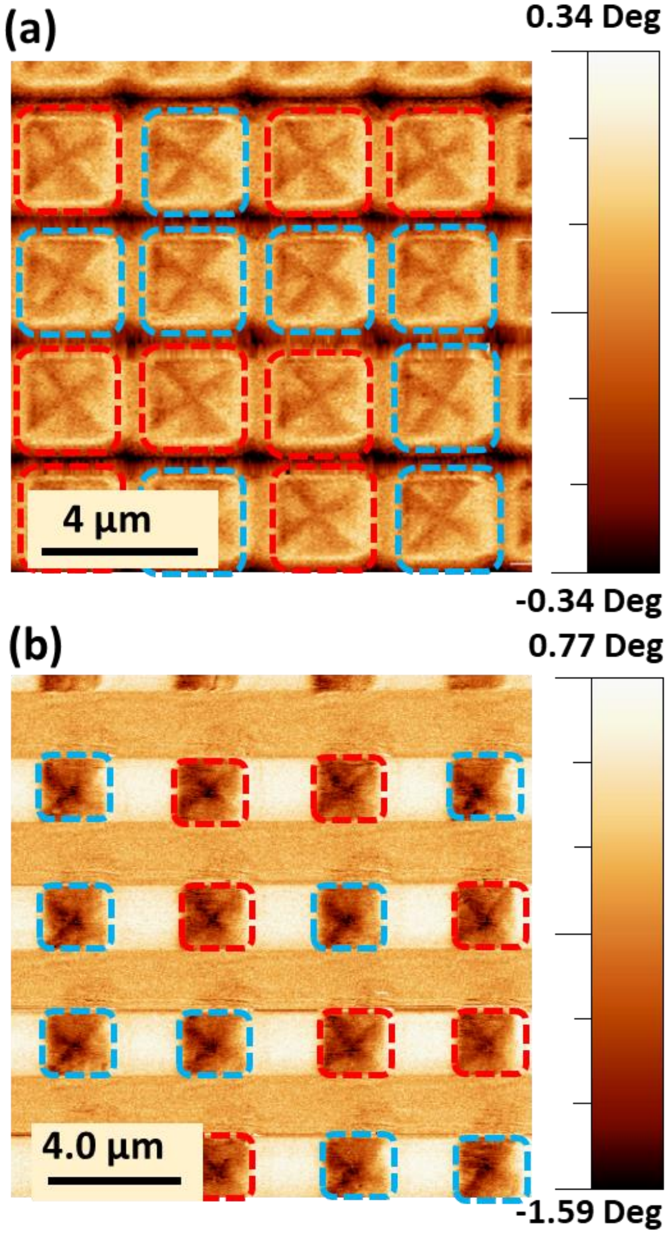

Figure 5.4: MFM images of a 4 x 4 portion of the (a) high MS array and (b) low MS array in the as-deposited state and in the absence of an applied field. Squares with red and blue dashes represent CCW and CW, chiralities respectively. The colour bar represents phase shift.

Figures 5.5(a) and 5.5(b) show MFM images of the high MS and low MS array, respectively, in the presence of a 3 mT field along the positive x-direction. As in circular structures, the core moves upwards for counter-clockwise (CCW) chirality and downwards for clockwise (CW) chirality for a positive field. The high MS array (Fig. 5.5a) shows both upward and downward chiralities. Interestingly, a double vortex state also appears here (represented by the purple dashed square) which has also been observed in the empirical literature [19, 128]. A double vortex state is a complex magnetic domain state. The structure of such a state can be described as a sequence of magnetic vortices and anti-vortices arranged along the domain wall segmented by 90˚ walls of opposite chirality where a 90˚ wall is significantly lower than that of a 180˚ wall. The complicated 90˚ domain wall network of the double vortex state reduces the energy when compared with a regular 180˚ domain wall.

The ratio of the double vortex state to the CW and CCW chirality single vortex states was measured to be 10:4:2 in this image. The same experiment was carried out on the low MS array and the results showed that the ratio of CW to CCW vortex chirality was 9:8 (see Fig. 5.5b), with no observation of a double vortex state. Overall, these datasets indicate that during growth in both high and low MS samples, a flux closure state forms immediately, as soon as the film is continuous on the structure. This results in both sample sets having almost equal chirality distributions, as-deposited. Subsequent application of a field then allows the magnetostatic interaction within the high MS array to dictate the chiral ordering within the array. The high MS array also promotes the formation of double vortex states, which helps to reduce the magnetostatic energy of the array by reducing the domain size, total length of 90˚ walls and improving flux closure at corners. This observation has also been confirmed in previous work [134] demonstrating that for these parameters a double vortex state is the lowest energy state that replaces single vortex state.

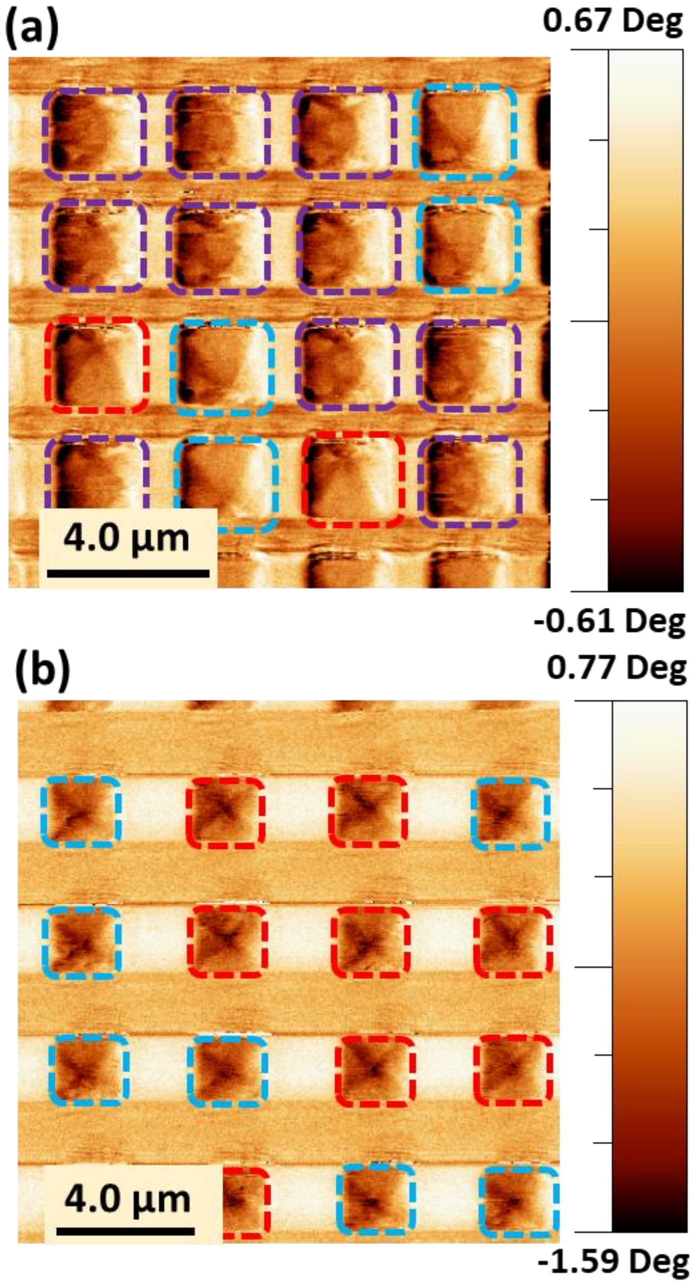

Figure 5.5: MFM images of 4 x 4 portion for (a) high MS array (b) low MS array at field of 3 mT along the positive x-direction. Squares with red, blue and purple dashes represent CCW, CW chiralities and the double vortex state, respectively. The colour bar represents phase shift. Note that for the 0 mT case, a maximum residual field of magnitude 1.2 mT is present due to remanence in the magnet poles.

5.5 Plain squares in high MS regime

5.5.1 Field-driven motion

Here the same MFM process as in Chapter 4 was used (see Section 4.4.1) to study the magnetisation process within square element arrays. To start, 3 x 3 sections of the high MS array and low MS array were selected randomly from the sample. However, to conduct more in-depth research, specific states were selected.

Figures 5.6 illustrate MFM images for squares in the high MS array when an in-plane field was applied in the positive x-direction. When applied along the positive x-axis, the vortex core moves to either the lower or higher quarter of the square as shown in Figure 5.6(b). Additionally, the in-plane field generates domain wall movement and creates magnetic surface ‘charges’ at the edges. At a field magnitude of 1 mT, the ratio of chirality preference favouring CCW over CW is 5:4. Additional field increments such as those shown in Figure 5.6(c) cause the formation of a double vortex state which then becomes the dominant state. Images obtained over larger area (see Fig. 5.5a) confirms these results. Further field increments result in core annihilation at around 7 mT (Fig. 5.6e) and opposing contrast can be seen at horizontal extremities of the squares, indicating that saturation is approaching. Reduction of the field shows core re-nucleation at 5 mT (see Fig. 5.6f) and yields either a single vortex state or double vortex state [171]. Both non-uniform states significantly reduce the average square magnetisation [26]. Once re-nucleation has occurred, the amount of vortex displacement is determined by a balance between the Zeeman and magnetostatic energy (see Figs. 5.6g, h). Whilst the double vortex state is dominant at 5 mT, in order to reduce the magnetostatic energy, a further reduction in field reduces the magnetisation along the field direction, and associated edge charges, allowing again for the single vortex state to again form. At 3 mT, the single vortex state becomes dominant, now with a chirality distribution ratio of 5:2 (CCW: CW) and now only 2 double vortex states (see Fig. 5.6h). In Figure 5.6(i), at a field of zero the CCW chirality now dominates further with a distribution ratio of 6:3 (CCW: CW).

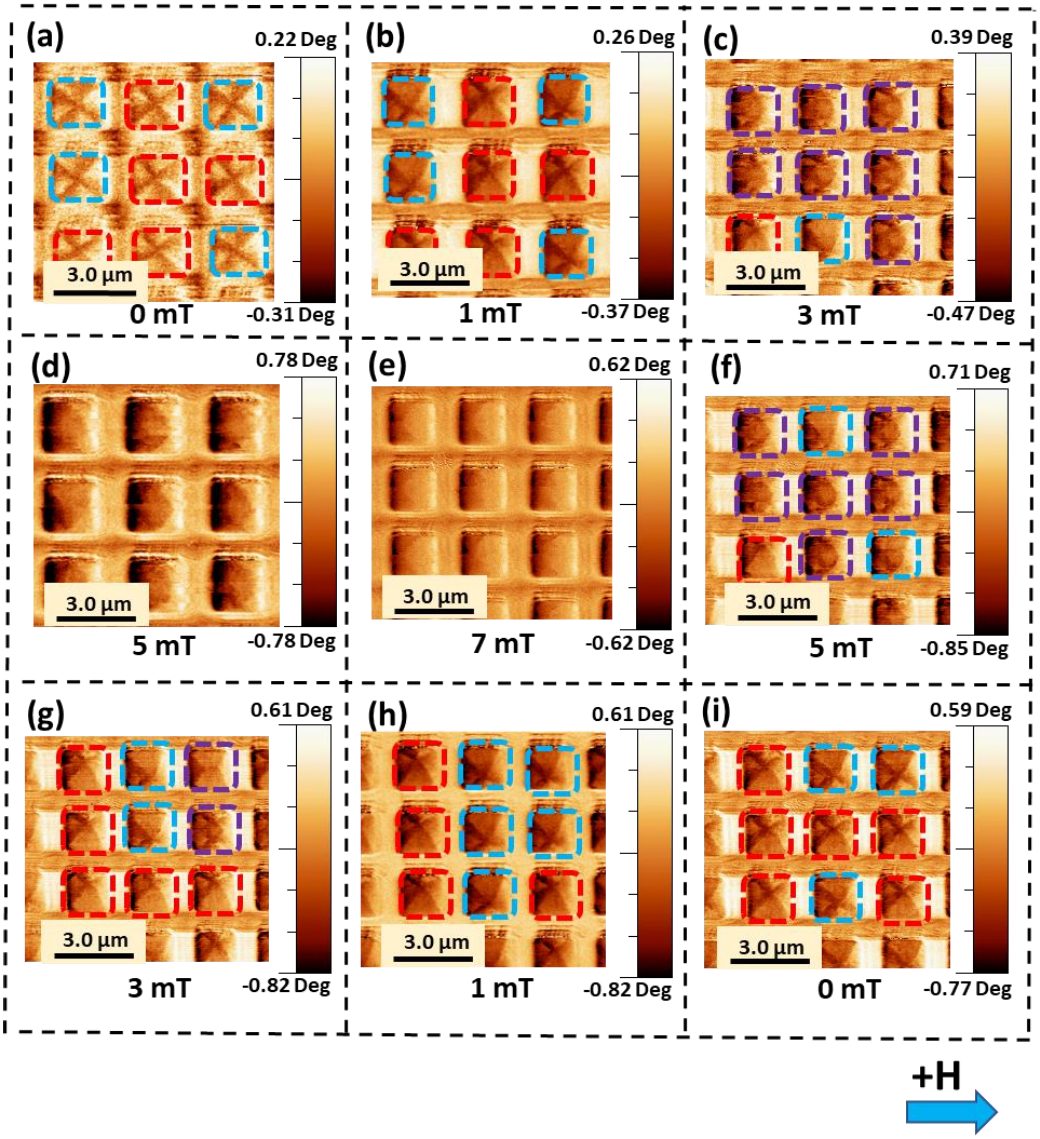

Figure 5.6: MFM images of 3 x 3 plain squares within the high MS array at (a) zero field and (b-h) under the application of an in-plane field H in the +x direction and (i) return to remanence, obtained at 2 mT steps up to +7 mT, Squares with red, blue and purple dashes represent CCW, CW and double vortex state, respectively. The colour bar represents phase shift. Note that for the 0 mT case, a maximum residual field of magnitude 1.2 mT is present due to remanence in the magnet poles.

It is interesting to note that the chirality of two squares switched, even at a low field of 1 mT, far away from the re-nucleation field. This dynamic phenomenon, which we name spontaneous reorganisation of chirality, has not been observed in the literature. One can see that the flipping of these two squares, reduces further the local magnetostatic energy for that part of the array. This has not been seen in the literature and the research group are investigating this further.

We now take a more detailed look at squares that magnetise via wall movement with vortex core translation and those that magnetise via the production of a double vortex state (see Figs. 5.7 and 5.8). In Fig 5.7, the core simply translates on the upsweep and then re-nucleates from the upper quarter via a single vortex state after emerging from saturation (g), as previously seen in the literature [71, 171, 172].

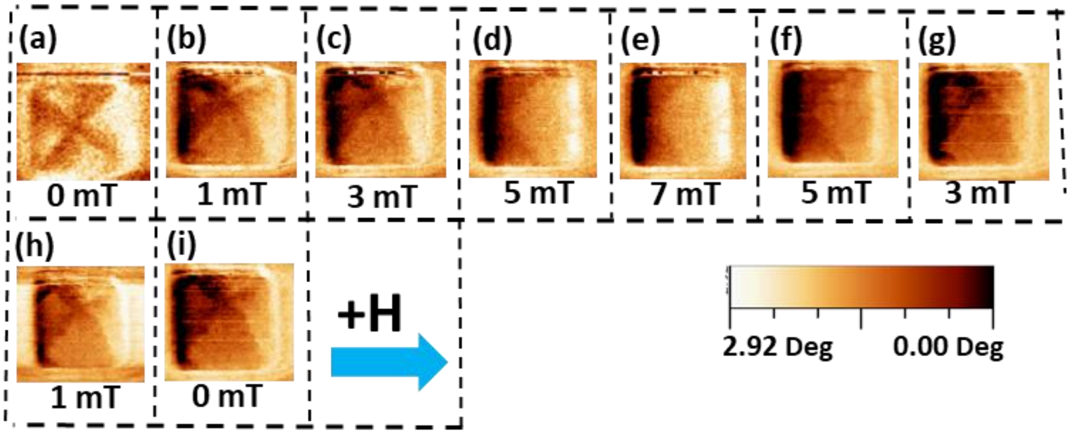

Figure 5.7: MFM images of single square in the high MS array under the application of an in-plane field H in the +x direction (see blue arrow). The colour bar represents phase shift. Note that for the 0 mT case, a maximum residual field of magnitude 1.2 mT is present due to remanence in the magnet poles.

In Fig. 5.8, a double vortex state is generated upon the up sweep (c) and then at re-nucleation (g). This observation has also been confirmed in previous work [173] which suggests it is the lowest energy state, in particular reducing the magnetostatic energy of the array. However, this state is only seen as a static state in the literature and not in re-nucleation but it is very interesting and the research group will be exploring this further. Overall, two magnetisation mechanisms are observed, which occur via either a single vortex state or a double vortex state. These magnetisation mechanisms were found to be random.

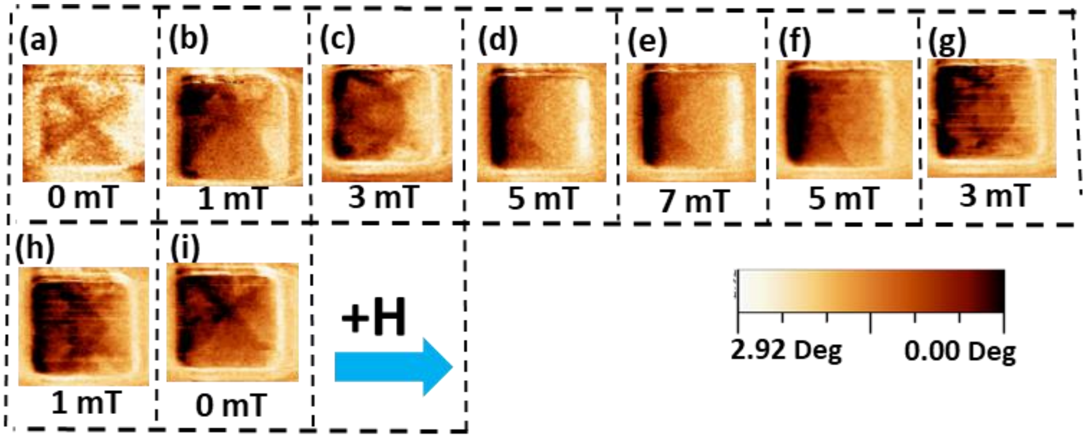

Figure 5.8: MFM images of single square in the high MS array at under the application of an in-plane field H in the +x direction (see blue arrow). The colour bar represents phase shift. Note that for the 0 mT case, a maximum residual field of magnitude 1.2 mT is present due to remanence in the magnet poles.

A further experiment was carried out on a 3 x 3 sample of the high MS array to determine how core displacement and magnetisation mechanism was affected by the direction of the field. Here it was anticipated that the selection of a different symmetry axis may preselect one of the magnetisation mechanisms. At remanence, the ratio of chirality preference favouring CCW over CW is 5:4. It is interesting to note that the chirality of two squares switched, even at a low field of 1 mT, far away from the re-nucleation field. This dynamic phenomenon, which we name spontaneous reorganisation of chirality, has not been observed in the literature. One can see that the flipping of these two squares, reduces further the local magnetostatic energy for that part of the array. This has not been seen in the literature and the research group are investigating this further. When a positive field is applied diagonally, as shown in Figure 5.9, the vortex core starts to displace either to the upper or lower corners (see Fig. 5.9, b). Further field increment result in core almost entirely displaces to the upper corner of the squares (see Fig. 5.9, c). This chirality preference is consistent with what been observed in the literature [174]. As seen in Figure 5.9(e), additional field increases lead to core annihilation at a field strength of approximately 7 mT. Figure 5.9(g) demonstrates that following a further field reduction, core re-nucleation occurs at 5 mT and the core displaces back to the centre of the square (see Fig. 5.9i).

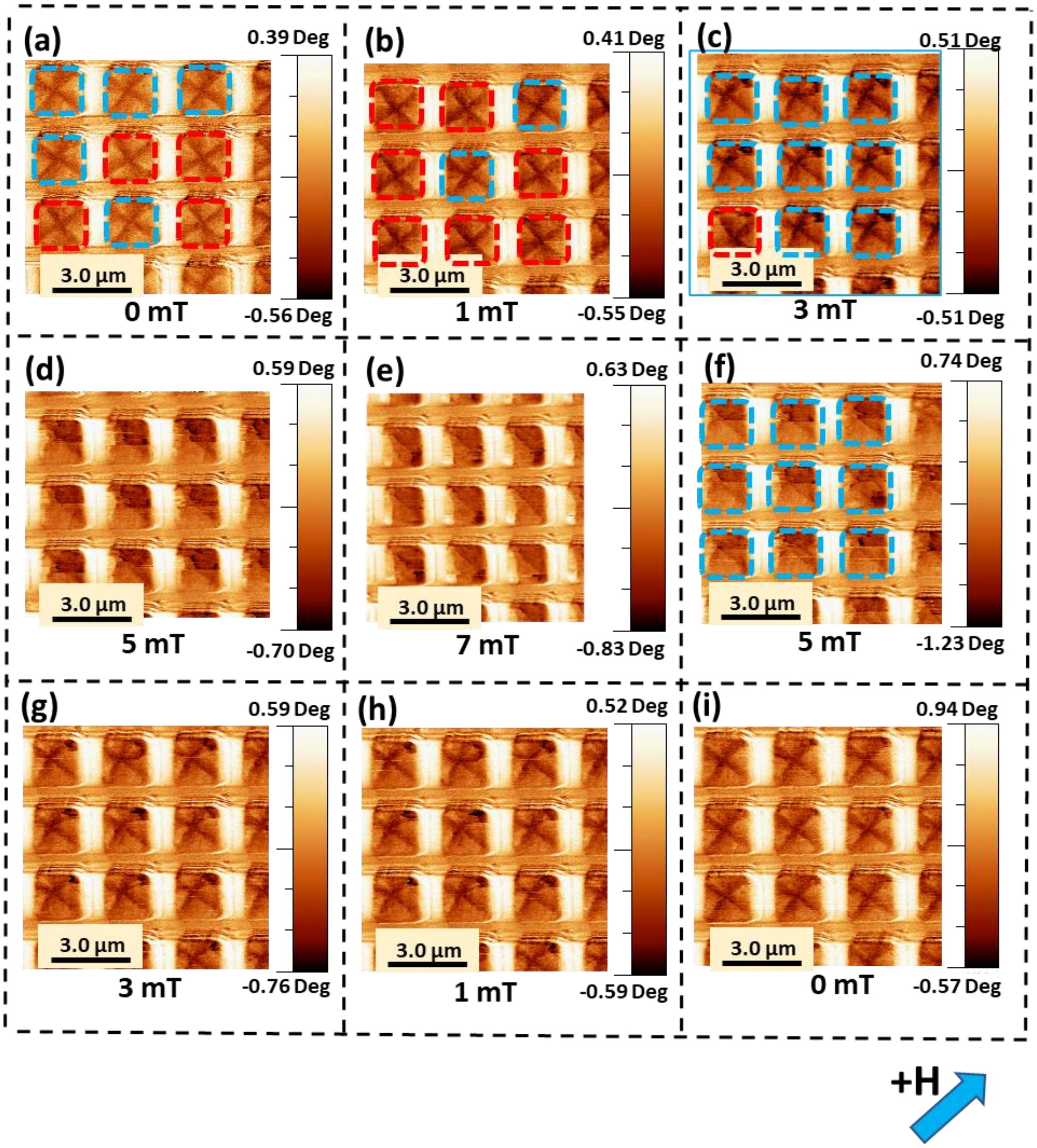

Figure 5.9: MFM images of 3 x 3 plain square in the high MS array at (a) zero field and (b-h) under the application of a diagonal field H in the (1,1) direction (see arrow) and (i) return to remanence, obtained at 20 mT steps up to +70 mT. Squares with red and blue dashes represent CCW, CW vortex state, respectively. The colour bar represents phase shift. Note that for the 0 mT case, a maximum residual field of magnitude 1.2 mT is present due to remanence in the magnet poles.

In this case, it has been shown that applying a field along diagonal maintains a mechanism whereby the system magnetises via core translation and maintained in a single vortex state, with no evidence of intermediatory double vortex states. This is likely to be due to the magnetisation direction that is possible in the double vortex state, which favours magnetisation to lay along edges. With field along edges, the Zeeman energy in the double vortex state remains low. However, for field applied along the diagonal, the Zeeman energy is high for each of the seven domains (see Fig. 5.10), making it unfavourable[175].

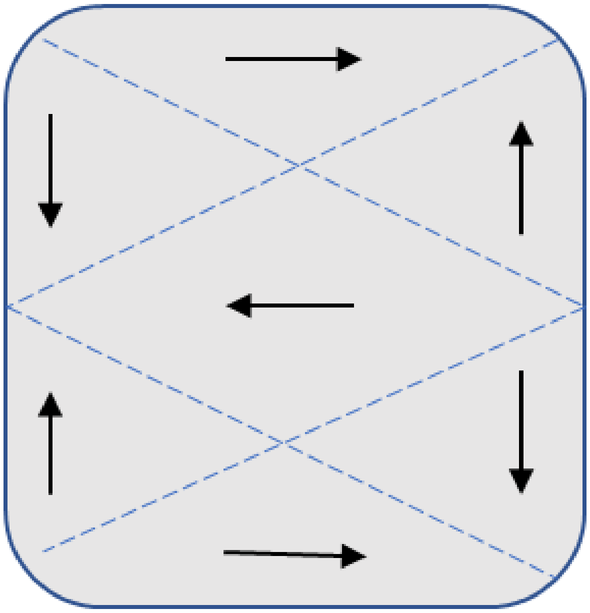

Figure 5.10: Schematic of the seven-domain pattern.

5.5.2 Micromagnetic simulations of high MS array

To better understand the magnetisation process, micromagnetic simulations of the high MS array were performed. The simulations were run using standard parameters in accordance with the details in Chapter 4 (see Section 4.4.2). Figures 5.11 illustrates the resultant magnetisation configuration and simulated MFM images, respectively. Micromagnetic simulations begin with an applied field of zero and then the field is applied in-plane in the x-direction (shown by the arrow), progressively increasing from 0 to 70 mT in 20 mT steps before reverting to zero. At remanence a vortex state is clearly seen with a core in the square centre, Landau pattern domains and the four 90° walls that divide them (see Fig. 5.11a).

Applying a field result in vortex core motion to the upper quarter of the square (see Figs. 5.11b, c) which is associated with the domain wall motion. At a field of 70 mT, the squares approach saturation and are close to a single domain state (see Fig. 5.11e). Reduction of the field shows that a single vortex state (C-state) is responsible for the re-nucleation of the vortex, as seen in Figure 5.10(f). As the field is further reduced the vortex core relaxes back to the centre of the square (see Fig. 5.11i). Overall, the simulations are consistent with what has been observed in the literature [19].

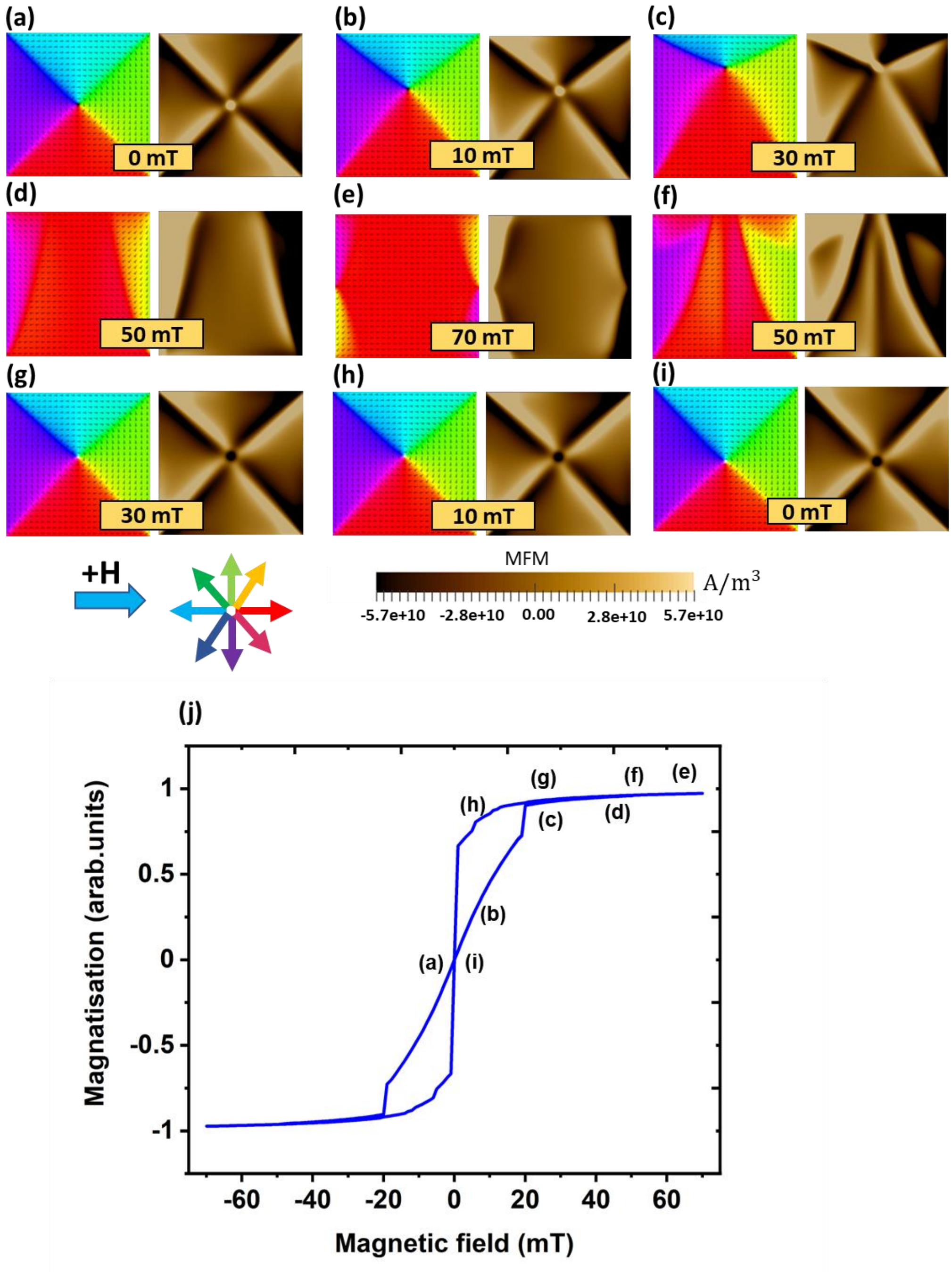

Figure 5.11: Simulated spin configuration and the corresponding MFM for high MS array at (a) zero field and (b-h) under the application of an in-plane field H in the +x direction (see arrow) and (i) return to remanence. Different colours represent the direction of magnetisation with respect to the applied field, as depicted in the colour wheel. (j) Simulated hysteresis loop, with labels corresponding to the configurations (a-i).

Figure 5.11(j) shows a simulated hysteresis loop for a square with a side length of 2 μm that matches previous work [71]. A symmetric Landau vortex state ise seen at remanence (a). When the field strength is increased, the vortex core moves to the upper quarter of the square (b-d), increasing the magnetisation. Subsequently, the core annihilates, and the magnetisation distribution eventually approaches uniformity at point (e). A sudden increase in the magnetisation in the field direction causes a distinctive step to appear in the hysteresis loop during the process of vortex annihilation (between points c and d). After reaching saturation, reducing the field causes the magnetisation configuration to change into a single vortex state and there is a reduction in magnetisation at (f) which is followed by a compression of the domain magnetised in the direction of the applied field, characterised by a jump at (g). At extremely low fields, the system is characterised by an irreversible jump (h) from vortex nucleation at one of the square sides and translation to the vortex centre state (i).

Overall, there is good agreement between the experimental and simulated MFM results. Both exhibit perfect Landau-flux-closure confirmation at remanence and showed magnetisation processes of vortex core displacement, annihilation and re-nucleation via a single vortex or a double vortex state which is also consistent with those seen in literature [19, 173]. The characteristic fields for experimental and simulated results are shown in table 5.1.

	Annihilation field (mT)	Re-nucleation field (mT)
Experiment	7	5
Simulation	70	50

Table 5.1: A summary of experimental and simulated annihilation and re-nucleation fields for high MS array.

5.6 Plain squares in low MS regime

5.6.1 Field-driven motion

MFM experiments were performed on a second sample where the lattice spacing was raised to the negligible MS regime (low MS). Figure 5.12(a) illustrates the remanent state (as-deposited state) in which all squares demonstrate the usual flux closure domain with 90° domain walls and a central vortex. In general, the same types of features are seen as in the high MS array, including typical core displacement, domain wall motion (see Figs. 5.12b, c), and approximately 5:4 chirality distribution ratios (CCW: CW). The core annihilated by 7 mT, as shown in Figure 5.12(d, e), and re-nucleated at 3 mT, as shown in Figure 5.12(g). This lower re-nucleation field value than the high MS array (see table 5.2) is due to the effect of the magnetostatic interaction in the magnetisation process has also been seen on plain disk arrays in the previous chapter. We note that all squares in this low MS regime show a relaxation back to zero field via a single vortex state, indicating that the double vortex state is intimately related to the magnetostatic field distribution provided by closely packed squares.

	Annihilation field (mT)	Re-nucleation field (mT)
High MS array	7	5
Low MS array	7	3

Table 5.2: A summary of experimental annihilation and re-nucleation fields for both the high MS and low MS array.

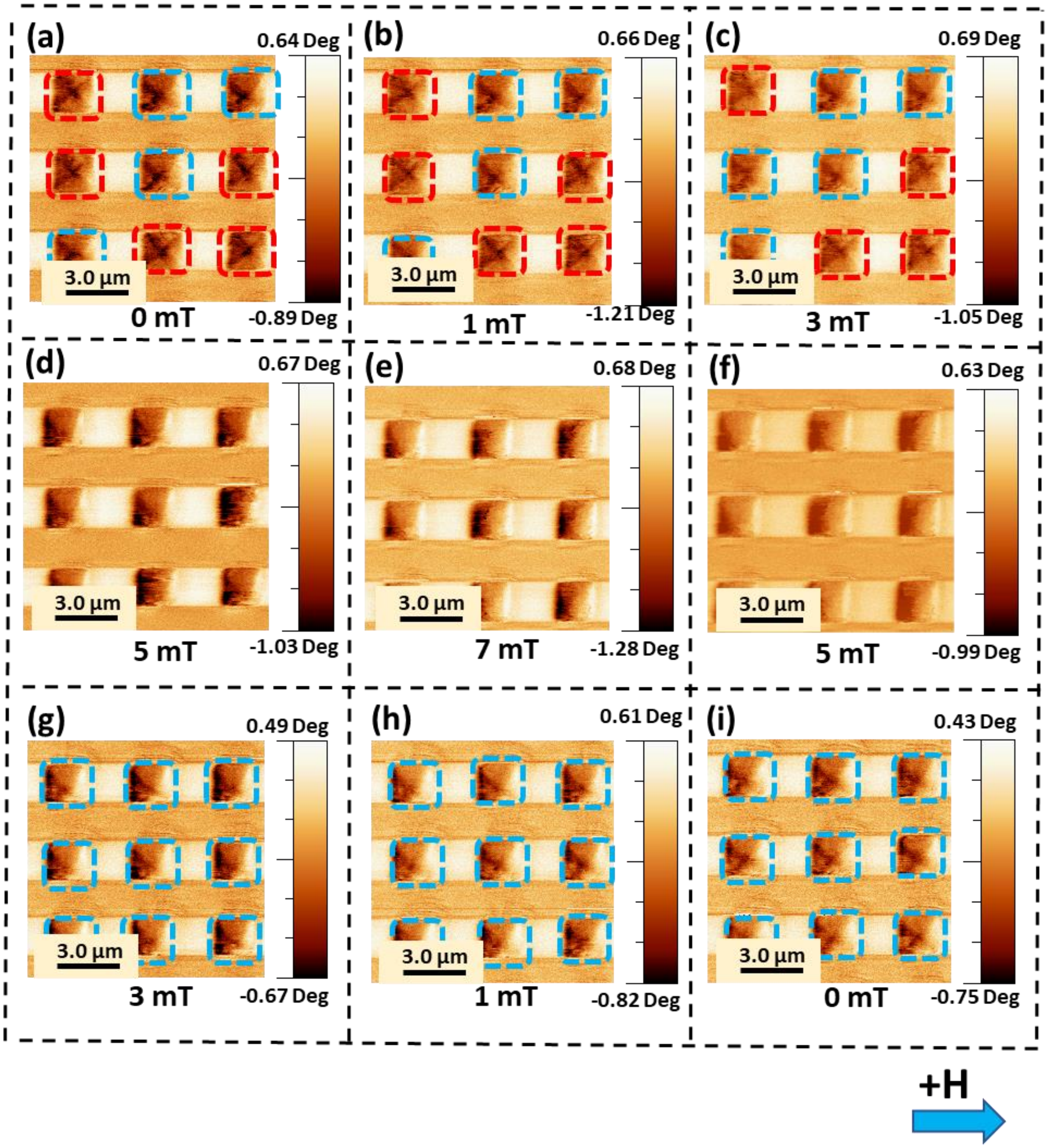

Figure 5.12: MFM images of 3 x 3 area within the low MS array at (a) zero field and (b-h) under the application of an in-plane field H in the +x direction and (i) after returning to remanence, obtained at 2 mT steps up to +7 mT. Squares with red and blue outlines represent CCW and CW respectively. The colour bar represents phase shift. Note that for the 0 mT case, a maximum residual field of magnitude 1.2 mT is present due to remanence in the magnet poles.

5.6.2 Micromagnetic simulations of low MS regime

The simulations for a low MS array are shown in Figure 5.13.

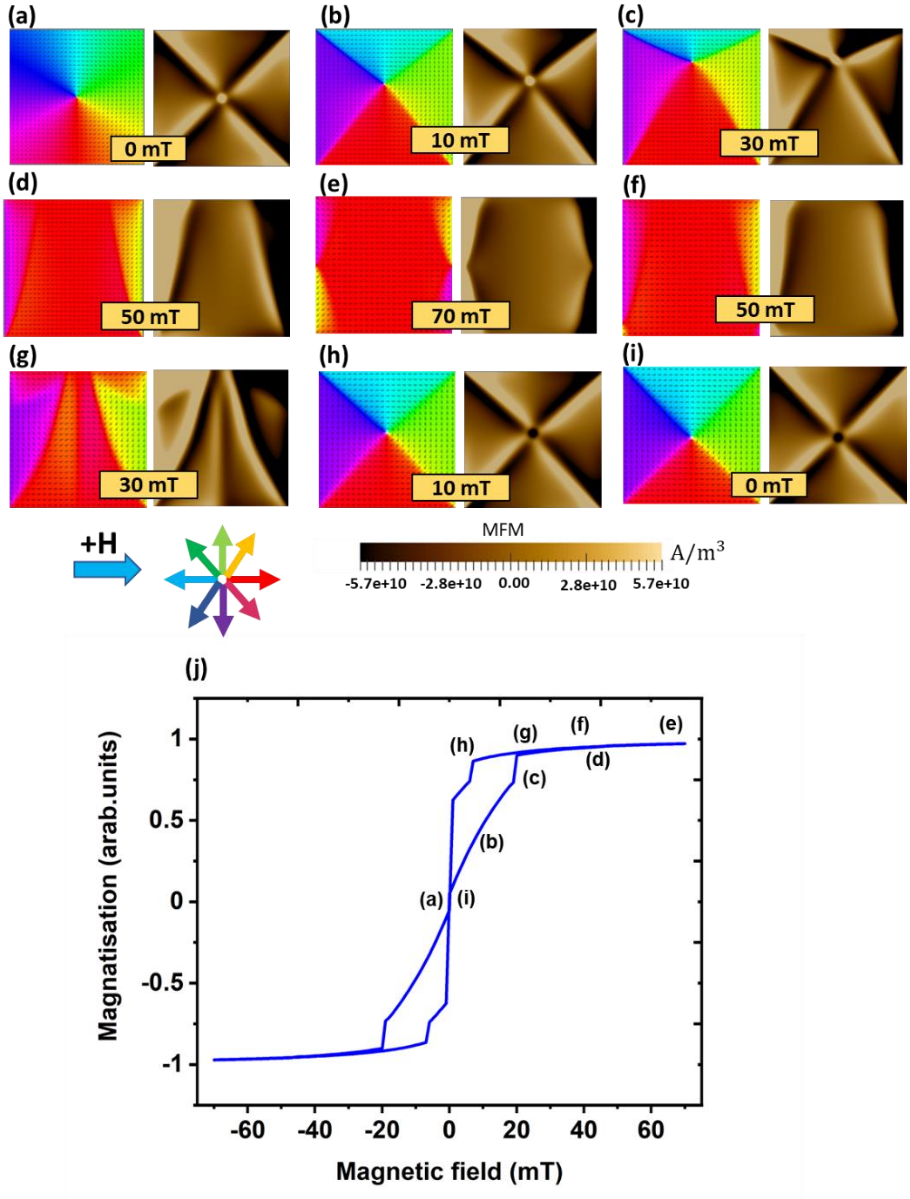

Figure 5.13: Simulated spin configuration and the corresponding MFM for low MS array at (a) zero field and (b-h) under the application of an in-plane field H in the +x direction and (i) return to remanence. Different colours represent the direction of magnetisation with respect to the applied field, as depicted in the colour wheel. (j) Simulated hysteresis loop, with labels corresponding to the configurations (a-i).

These simulations are shown in a manner comparable to the previous simulations and the middle square was selected for reasons of symmetry. In general, a behaviour that is comparable to that of the high MS array is observed with the exception of the re-nucleation field which has a lower value of 30 mT (see Fig. 5.13g), consistent with experiments.

Figure 5.13(j) depicts the simulated hysteresis loop generated by the simulation. It is clear that the shape of the loop as well as the re-nucleation and annihilation fields are different from that observed in the high MS system. As shown in Figure 5.13, there is a difference in the characteristic fields for vortex re-nucleation at point (g, h) in high and low MS arrays. It is believed that the higher demagnetising field magnitude, which is attributable to neighbouring squares, is the cause of the enhanced field for the interacting array. This is in accordance with what has been observed in the literature [171]. It has previously been noted that the annihilation and re-nucleation fields in soft magnetic elements are affected by the symmetry of the stray field caused by neighbouring elements. Also, the difference in the loop shape is directly related to the extent of magnetostatic interactions between the neighbouring elements. The interaction field experienced by a single square in this array is the summation of the interaction fields produced from the neighbouring elements.

Comparing both high and low MS arrays, the findings of the experiment and the simulation, mostly coincide with one another. Both shows a Landau-flux-closure structure where the four 90° domain walls meet in the centre, forming the vortex. Four triangular domains are separated by the 90° domain walls aligned along the diagonals of the square. In addition, the low MS array demonstrated a lower re-nucleation field in comparison to the high MS array because of the function that magnetostatic interaction plays in the process of magnetisation at small inter-square distances. In the same manner as the disk array, the square high MS array shows a stronger stray field (H_s) interaction, which is induced by magnetic moments of adjacent squares. Considering applying a field in x-direction, in the saturation state the stray field prompts the magnetic moment of adjacent squares to align in the same direction. Accordingly, the annihilation and re-nucleation field increase in high MS array due to stronger stray field interaction. Interaction effects here can be understood with a dipole–dipole model, which assumes that the total magnetic field acting on each square is the sum of the applied field and a dipolar field arising from the neighbouring particle. We note that this depends upon the complex field distribution generated by surrounding squares which have components due to horizonal adjacent disks and vertically adjacent disks, as discussed in the previous chapter.

5.7 High MS squares array with 3D defect

5.7.1 Morphological characterisation

It has previously been shown in chapter 4 that a 3D defect can be produced using TPL and it clearly effects the spin texture for disk systems. We now attempt to realise a more significant defect, which has an independent spin texture to see how this perturbs the state and switching of the square. We focus upon a hemispherical defect since this can be produced simply with the TPL point spread function. The study focuses on an array of $Ni_{81}Fe_{19}$ squares with length of 2 μm and a thickness of 40 nm and is located in the high MS array. In this case, the decision was taken to examine the coupled regime for this sample in order to determine whether or not the collective interactions that are driven by magnetostatics can be controlled by large 3D perturbations. The defect has the shape of a hemisphere with a diameter of 600 nm and height 240 nm. The defect position was chosen by carrying out a suite of micromagnetic simulations whereby the defect offset was varied in 50 nm steps until significant pinning of the core was observed (see Fig. 5.14).

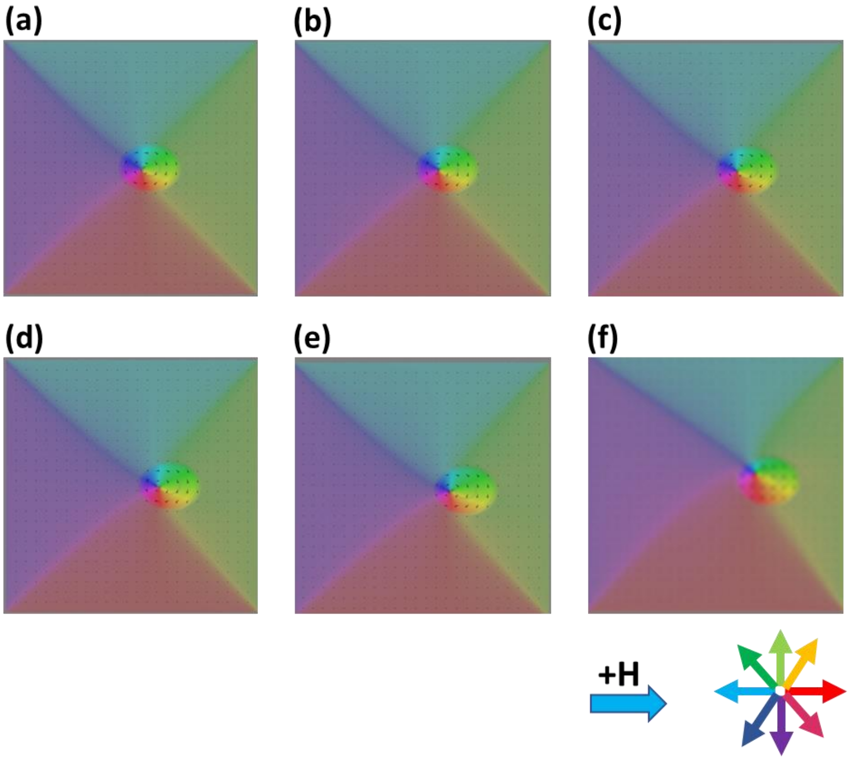

Figure 5.14: Micromagnetic simulation of varying defect positions (a) 50 nm, (b) 100 nm, (c) 150 nm, (d) 200 nm, (e) 250 nm and (f) 300 nm after a saturation along positive field direction and brought back to remanence.

The final design placed the defect at an offset of 300 nm from the square centre (see Figure 5.15).

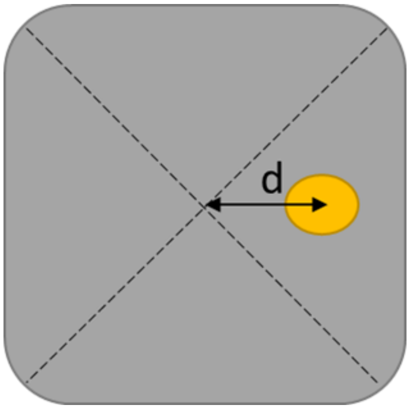

Figure 5.15: Design of a $Ni_{81}Fe_{19}$ square with a hemispherical defect. The distance (d) between the square and hemispherical defect centre is 300nm.

Figure 5.16(a) depicts a top-view SEM image of the defect array. The structures adhere to the design criteria because they have a side length of 2 µm. A tilted SEM image at 45˚ was also produced which provides an initial perspective of the defect and a better understanding of the 3D geometry (see Fig. 5.16b).

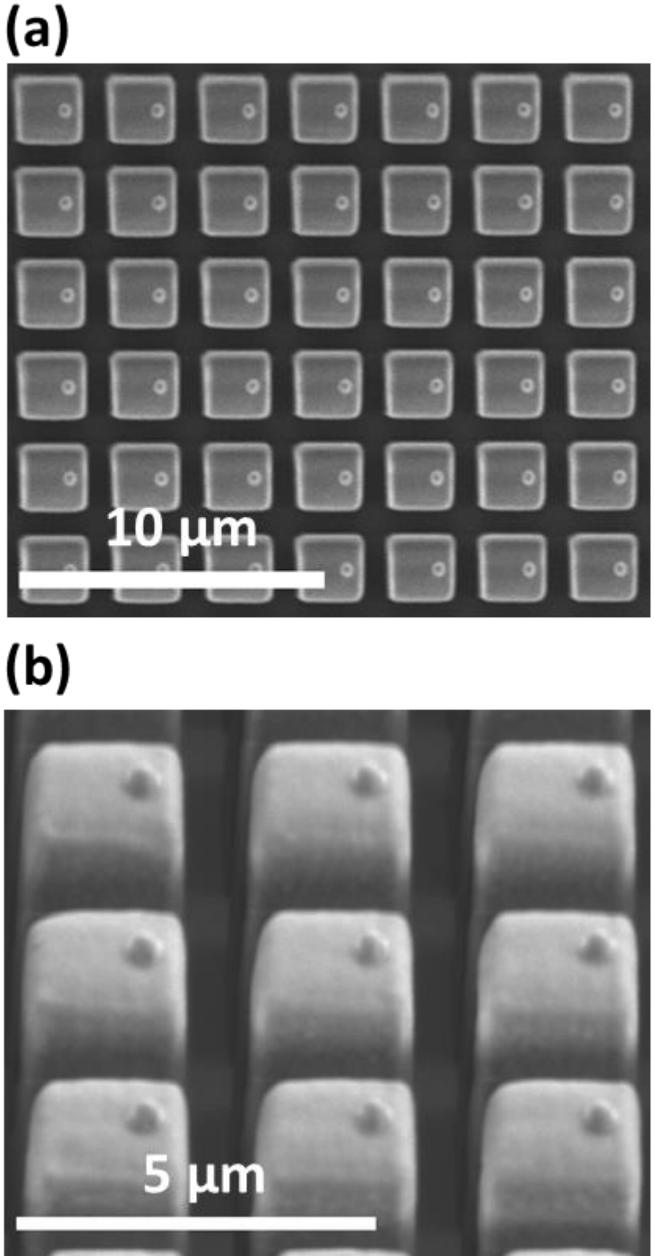

Figure 5.16: SEM images of square array with hemispherical defect from (a) a top-down view as well as at (b) a 45° tilt with respect to the substrate plane.

Figure 5.17(a) presents an AFM image of the array with defect. Fig 5.17(b) presents a line profile across a representative square which shows an abrupt increase in height close to the defect. A study of areas of the squares that are located far from the defect reveals that these regions have a smooth surface with limited roughness of approximately 6.2 ± 0.08 nm. Figure 5.17(c) presents a close-up of the AFM image of the defect which makes the 3D topography of the defect more evident and enables the geometry of the defect to be considered. Additionally, the defect geometry reflects the ellipsoidal point spread function. A slight elongation is likely due to weak optical aberration (see Fig. 5.17d).

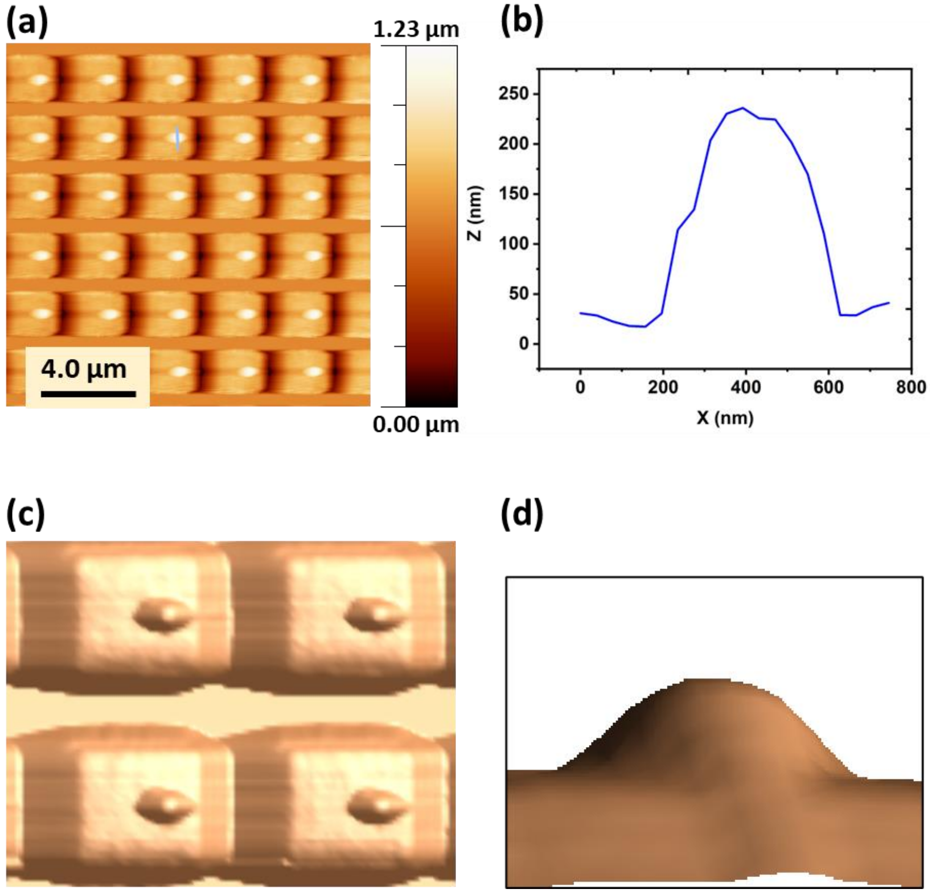

Figure 5.17: (a) AFM image of squares array with hemispherical defect in high MS regime, (b) line profile across square showing the defect, (c, d) 3D view.

The MFM image of the defect array in its as-deposited state is depicted in Figure 5.18. Both counter-clockwise (represented by the red dashed square) and clockwise (represented by the blue dashed square) chiralities can be seen. The pinning of the core above or below yields a CCW or CW chirality, respectively as shown in figure 5.19. The two distinct pinning positions and their relationship to a given chirality can be understood as followed. The position of the defect means it is only possible to have one continuous diagonal wall, either going from top-left to bottom-right or top-right to bottom left. The presence of both walls simultaneously, since this produces an additional small domain adjacent to the defect, which would be unfavourable with respect to magnetostatic energy. As shown schematically in Fig 5.19, a single diagonal wall from bottom-left to top-right, means the lower-right domain has a continuous magnetisation transition from pointing right to upwards (Green arrows). An upwards magnetisation is most magnetostatically favourable at the interface with the left-side of the defect, due to the left domain pointing downwards. Overall, this forces the pinning position to be higher. The contrast of the domain walls is vertically offset which suggests that the central core location has been changed compared to the plain high MS array at remanence. A chirality preference is also observed with the CCW being dominant direction over the whole array with a distribution ratio of 16:4. Here it appears the asymmetry in the caused by defect is sufficient to produce the preferential chirality. This is in contrast to the standard high MS array which showed almost 1:1 as-deposited.

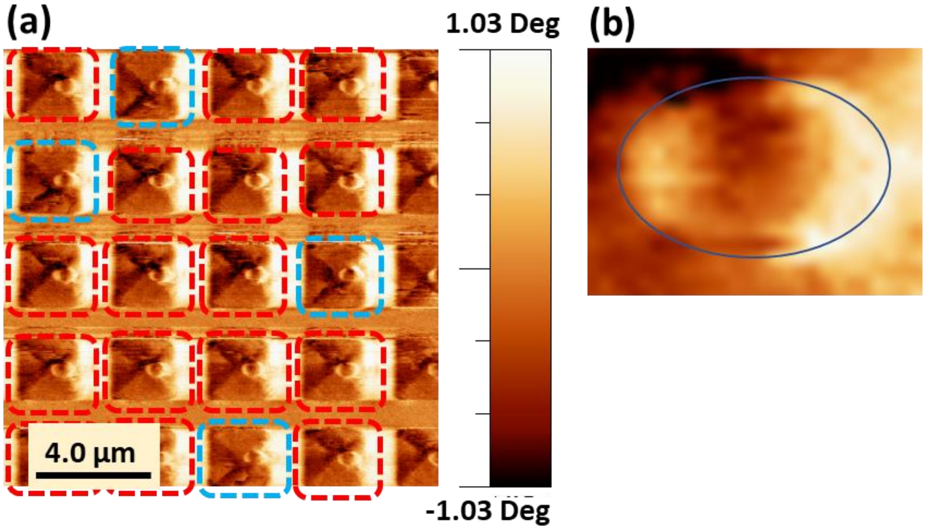

Figure 5.18: MFM images of (a) 4 x 4 array within the high MS regime and with hemispherical defects, in the as deposited state, (b) Zoomed contrast of the defect (squares with red and blue dashes represent CCW and CW, respectively). The colour bar represents phase shift.

In a 90˚ domain wall configuration, the introduction of such an out-of-plane curvature causes the wall to curl around the defect contour, since traversing over the defect would produce a significantly higher demagnetisation energy. The defect itself also has distinct contrast at its centre and appears to have contrast on either side (see Fig. 5.18b). According to the phase diagram of equilibrium states for soft magnetic hemispherical structures [176], the used geometrical parameters correspond to a vortex ground state. In these smaller hemispherical systems, the vortex core contrast is found to occupy a large fraction of the surface, as seen in our experimental data [15]. Its unfavourable for both domain walls to form since this yields a high energy domain close to the defect. Instead of a domain wall there is a smoother magnetisation transition within the single domain. As shown in figure 5.19

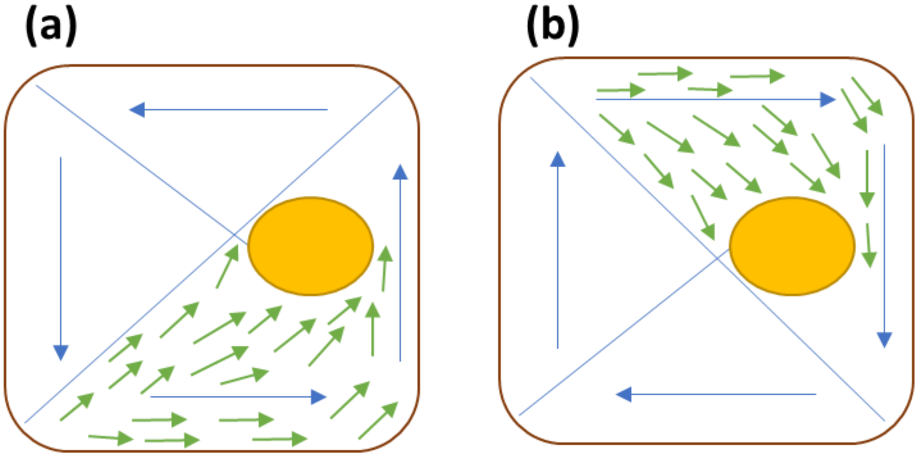

Figure 5.19: A sketch of the (a) CCW chirality linked to the core pinned up at the defect and (b) CW chirality linked to the core pinned down at the defect.

5.7.2 Field-driven motion

Figure 5.20 depicts MFM images of a 3 × 3 area of defect array under an in-plane field application. As seen in Figure 5.20(b), the introduction of a magnetic field causes the centre of the vortex to displace either to the upper or lower quarter of the square, depending on the chirality of the system: core pinned on above the defect are pushed upwards with field and core pinned below the defect are pushed downwards in the field (see Fig. 5.20b). The configuration is more like the pristine square on the left side, which results in more significant exchange and anisotropy energy densities. Additional field increments cause the formation of a double vortex state which eventually becomes the predominate state (see Fig. 5.20c). Core annihilation occurs at approximately 5 mT showing a single domain state (see Fig. 5.20d). Then, as the magnetic field reduces, re-nucleation of the field takes place at 3 mT (see Fig. 5.20e) through double vortex state and single vortex. These lower field values compared to the high MS standard is likely due to less area available for vortex displacement. This is similar to a phenomenon seen in asymmetric disks [177].

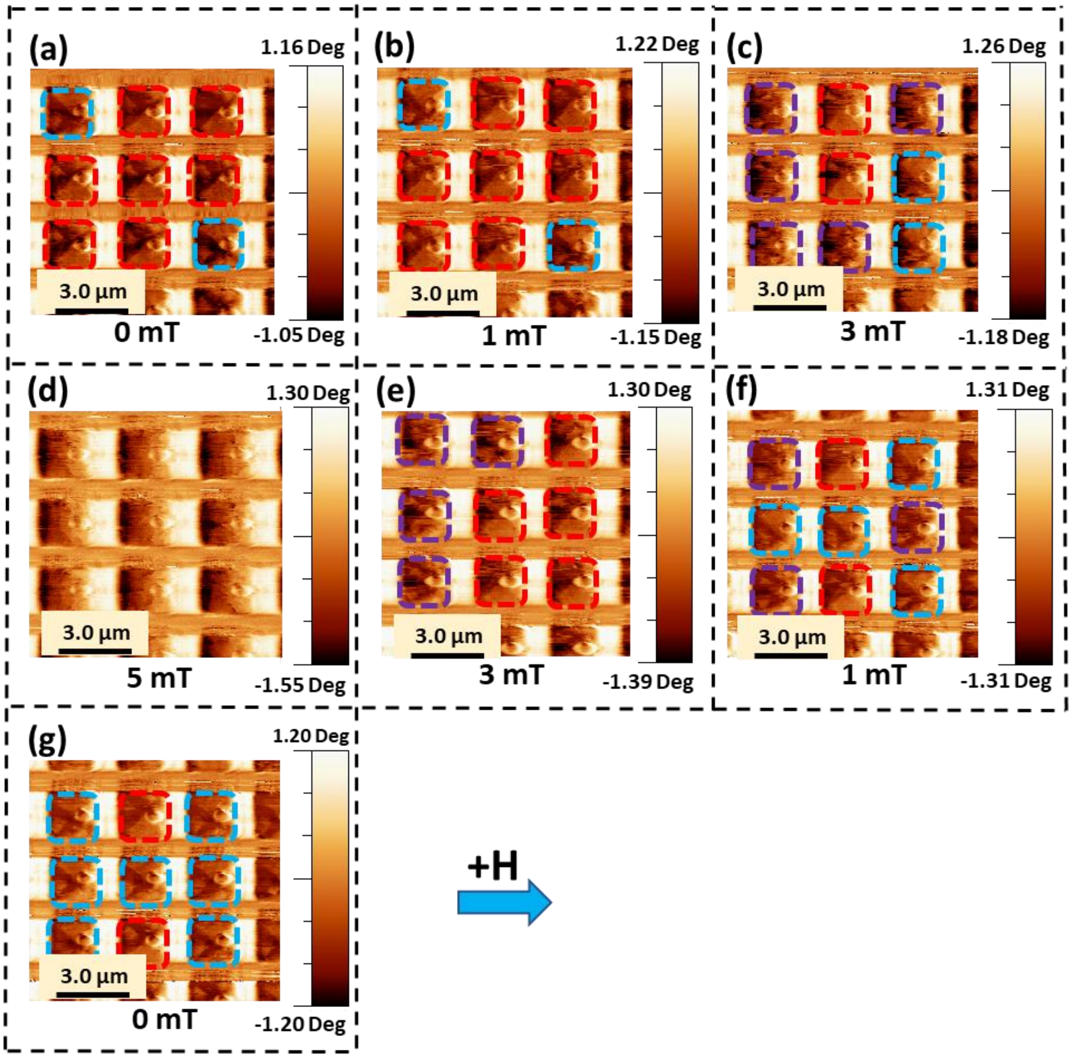

Figure 5.20: MFM images of 3 x 3 defect squares for high MS array at (a, g) zero field and (b-f) under the application of an in-plane field H in the + x direction and (g) after returning to remanence, obtained at 2 mT steps. Squares with red, blue and purple dashes represent CCW, CW and double vortex state, respectively. The colour bar represents phase shift. Note that for the 0 mT case, a maximum residual field of magnitude 1.2 mT is present due to remanence in the magnet poles.

In addition, When the field is decreased further, the single vortex state, starts to predominate over the double vortex state with a chirality distribution ratio of 6:3 (see Fig. 5.20f). After reducing the field back down to zero (see Fig. 5.20g), it was discovered that the CW chirality predominated with a distribution ratio of 6:3 (CW: CCW), as would be anticipated for a high MS array.

A symmetrical pattern of behaviour emerges whenever a field is applied in the negative x-direction. The vortex core is displaced to the upper or lower quarter of the square and the chirality distribution ratio between CCW and CW was 6:3 (see Figs. 5.21b, c). As shown in Figure 5.21(d), saturation was reached by 5 mT with the bright and dark bands at the borders of the square exhibiting opposite contrast from the positive field sweep. Re-nucleation occurs by 3 mT (see Fig. 5.21e). However, at this stage it is difficult to differentiate the chirality because the domain wall is shifting towards the defect side (the square right side) which causes it to overlap with the defect contrast. After further field reduction, the chirality distribution became considerably clearer with a ratio similar to 7:1:1 (CW: CCW: double vortex state) (see Fig. 5.21f). After coming from negative saturation, the coupling effect is clear because CCW chirality dominates (see Fig. 5.21g). Figure 5.22 and Figure 5.23 provides an illustration of an example of the two distinct states that are shown in Figure 5.20 which gives a better analysis of re-nucleation states.

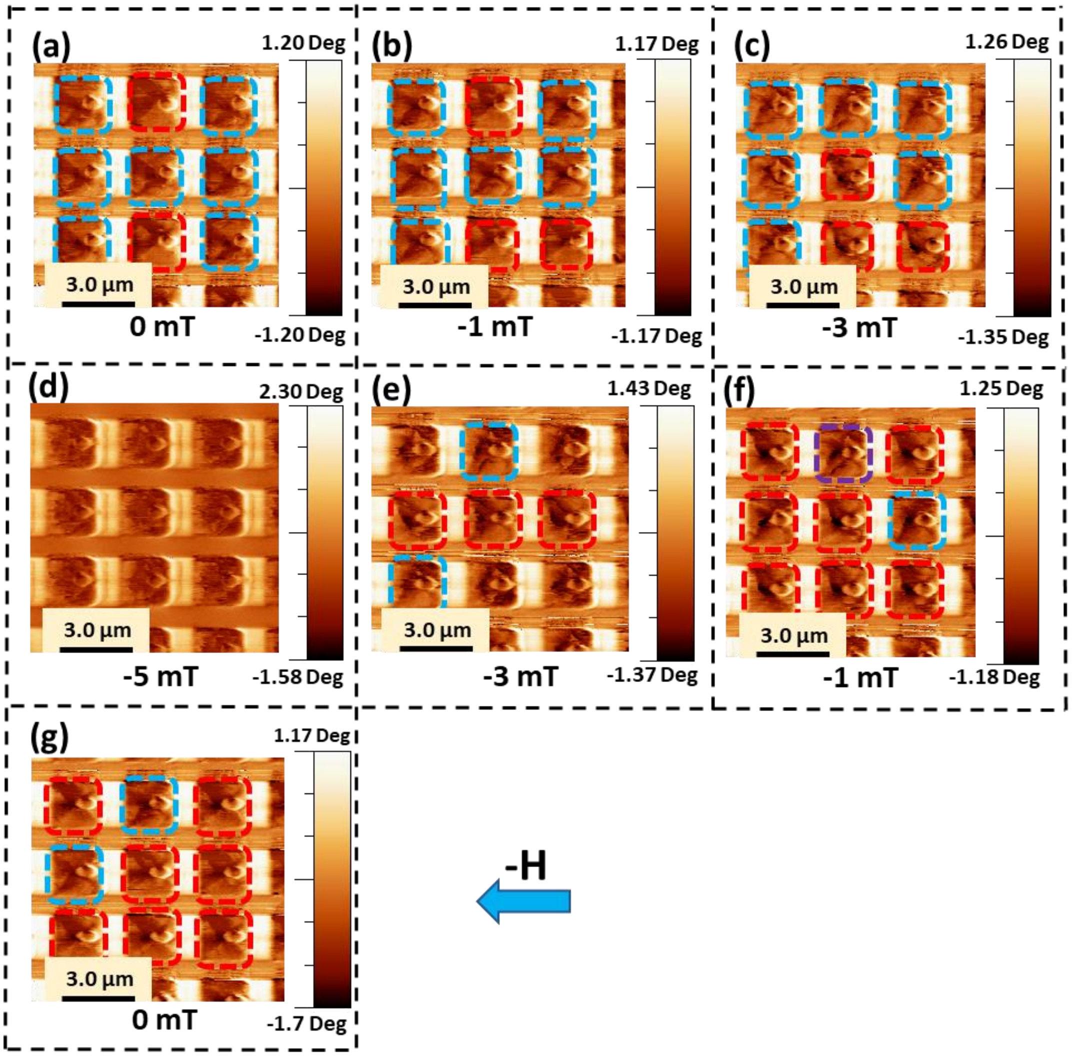

Figure 5.21: MFM images of 3 x 3 square array within high MS regime at (a, g) zero field and (b-f) under the application of an in-plane field H in the - x direction and (g) after returning to remanence, obtained at 2 mT steps. Squares with red, blue and purple dashes represent CCW, CW and double vortex state, respectively. The colour bar represents phase shift. Note that for the 0 mT case, a maximum residual field of magnitude 1.2 mT is present due to remanence in the magnet poles.

Figure 5.22 and Figure 5.23 displays the MFM images for the switching mechanism for two different squares in the defect array showing two different re-nucleation states. In the square with core pinned above the defect, application of a field in the positive field direction and with a CCW chirality yields a subtle translation upwards around the defect contour until annihilation reached (see Fig.5.22b-d). Figure 5.22(e) shows the core re-nucleates through a double vortex state before relaxing into the same configuration seen previously at remanence.

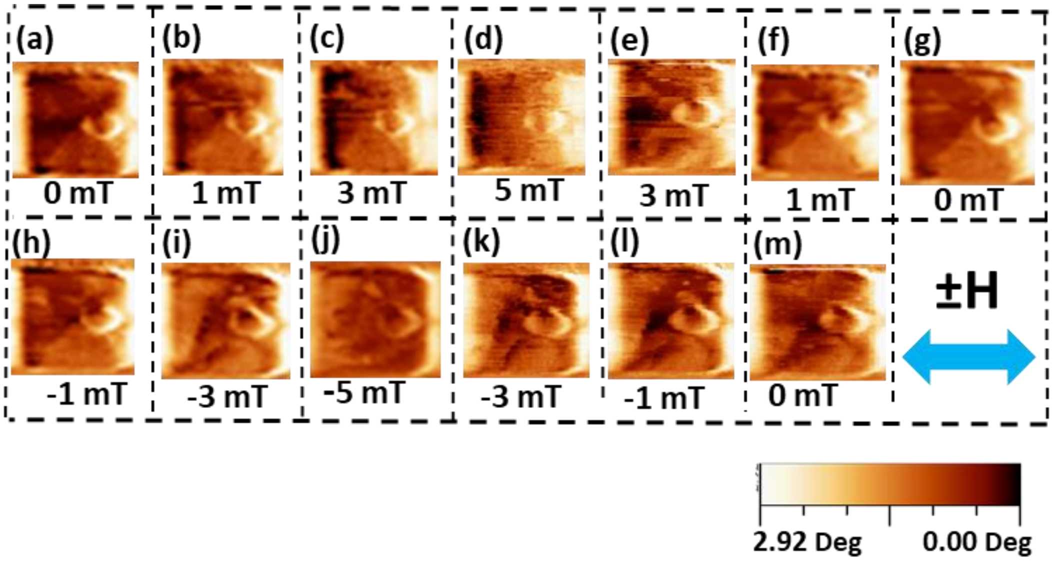

Figure 5.22: MFM images of square in high MS array, with core located above defect at (a, g, m) zero field and (b-l) under the application of an in-plane field H in the ± x direction (see blue arrow). Note that for the 0 mT case, a maximum residual field of magnitude 1.2 mT is present due to remanence in the magnet poles.

In the case of the core being pinned below the defect, application of a field in the positive field direction and with a CW chirality yields a subtle translation downwards around the defect contour until annihilation reached (see Fig. 5.23b-d). Figure 5.23(e), the vortex core re-nucleates through the single vortex state and relaxes back into the same state as seen at remanence (core below the defect). Subsequent application of a negative field then shows the wall boundary being pushed upwards around the defect (Fig 5.23h), before forming a complex double vortex state as seen in Fig. 5.23i. Further increments to the field yield an approach to saturation, with wall contrast no longer observable (Fig. 5.23j). Now reducing the field to -3 mT as shown in Fig 5.23k, shows a new state not seen previously, which shows symmetry above and below the defect. This is new state appears to show two walls on the left side of the defect merging to form the pinning site adjacent to the defect as seen in Fig 5.23l.

Higher resolution magnetic imaging, such as scanning transmission x-ray microscopy is required to confirm the exact micromagnetic state seen in 5.23k.

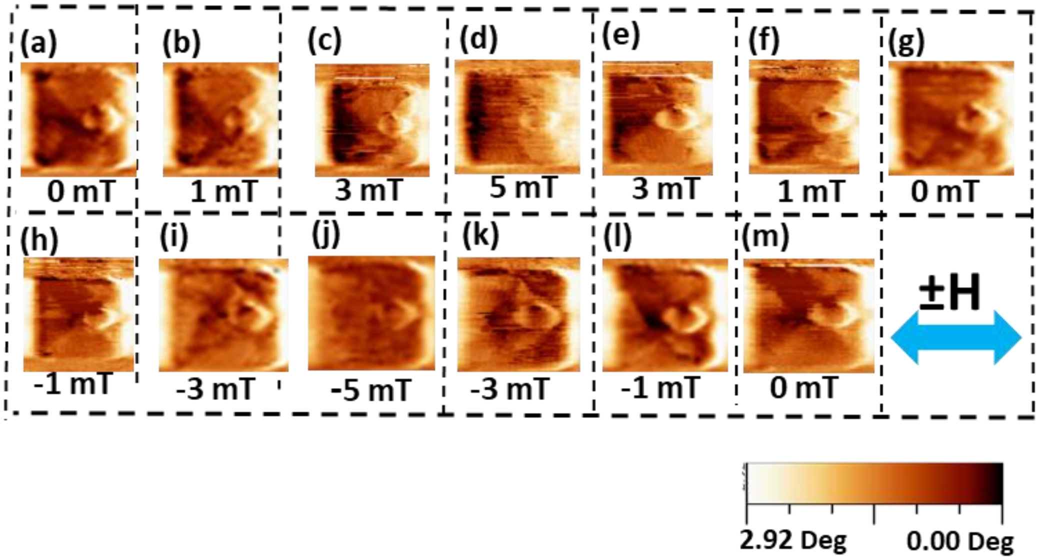

Figure 5.23: MFM images of square in high MS array, with core located below defect at (a, g, m) zero field and (b-l) under the application of an in-plane field H in the ± x direction (see blue arrow). Note that for the 0 mT case, a maximum residual field of magnitude 1.2 mT is present due to remanence in the magnet poles.

5.7.3 Micromagnetic simulation of high MS square arrays with 3D defect.

In order to provide insight into the expected behaviour from the array with defects, idealised simulations were performed. The defect was assumed to be of hemispherical geometry with a diameter of 600 nm and height 240 nm, as shown in Fig. 5.24 which is showing the shell geometry.

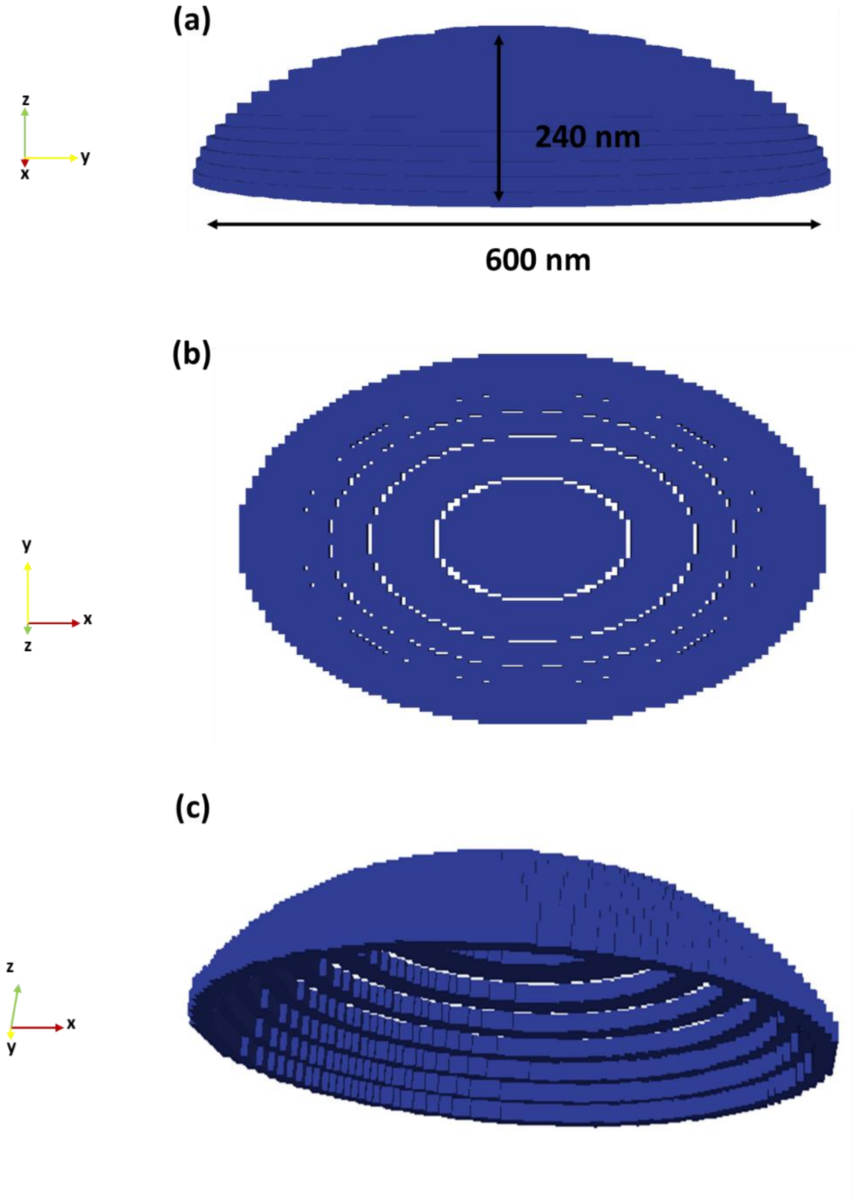

Figure 5.24: Simulated hemispherical defect geometry of 600 nm diameter and 240 nm height. The three panels showing the defect from different angles (a) side view, (b) top view and (c) tilted down view.

Simulations were run with a 3 x 3 array as previously. The behaviour of the central square was then analysed in positive and negative field directions as depicted in Fig. 5.25. Initial relaxation in the absence of a field, for the virgin magnetisation branch yielded a conventional vortex with no offset. After a first magnetisation cycle at remanence, the core and the domain wall are vertically offset which suggests that the central core location has been changed compared to the standard high MS array. Close examination of Fig. 5.25(a) actually indicates the core is pinned on the hemispherical defect. This remanent simulation agrees qualitatively with the experimental results in Fig. 5.20(a). When applying a field in the positive x-direction the core initially remains pinned (Fig. 5.25b) and eventually depins at 30 mT (Fig. 5.25c). It then displaces upwards passing away from the defect until it annihilates by 50 mT (see Fig. 5.25d). Reducing the field to 30 mT, as shown in Fig. 5.25(e) hints at re-nucleation of the core, from the lower edge. We also note the double vortex behaviour. This complex spin texture makes the comparison between the simulation and the experiment MFM contrast much more complex. Further field reduction Fig. 5.25(f) shows a double vortex state, with various walls pinned around the defect. When the field is back to zero, the vortex core does not return to the centre instead it is located below the defect, yielding a significant net magnetisation.

When applying a magnetic field in the opposite direction (negative x-direction), the core must move farther in the opposite direction since the defect is not centred. In Figs. 5.25(h, i) the core displaces downwards until it annihilates by 50 mT Fig. 5.25(j). As the field strength is decreased to 30 mT, the beginnings of double vortex can be seen forming (Fig. 5.25k). The complex spin texture even remains present at 10 mT (see Fig. 5.25l).

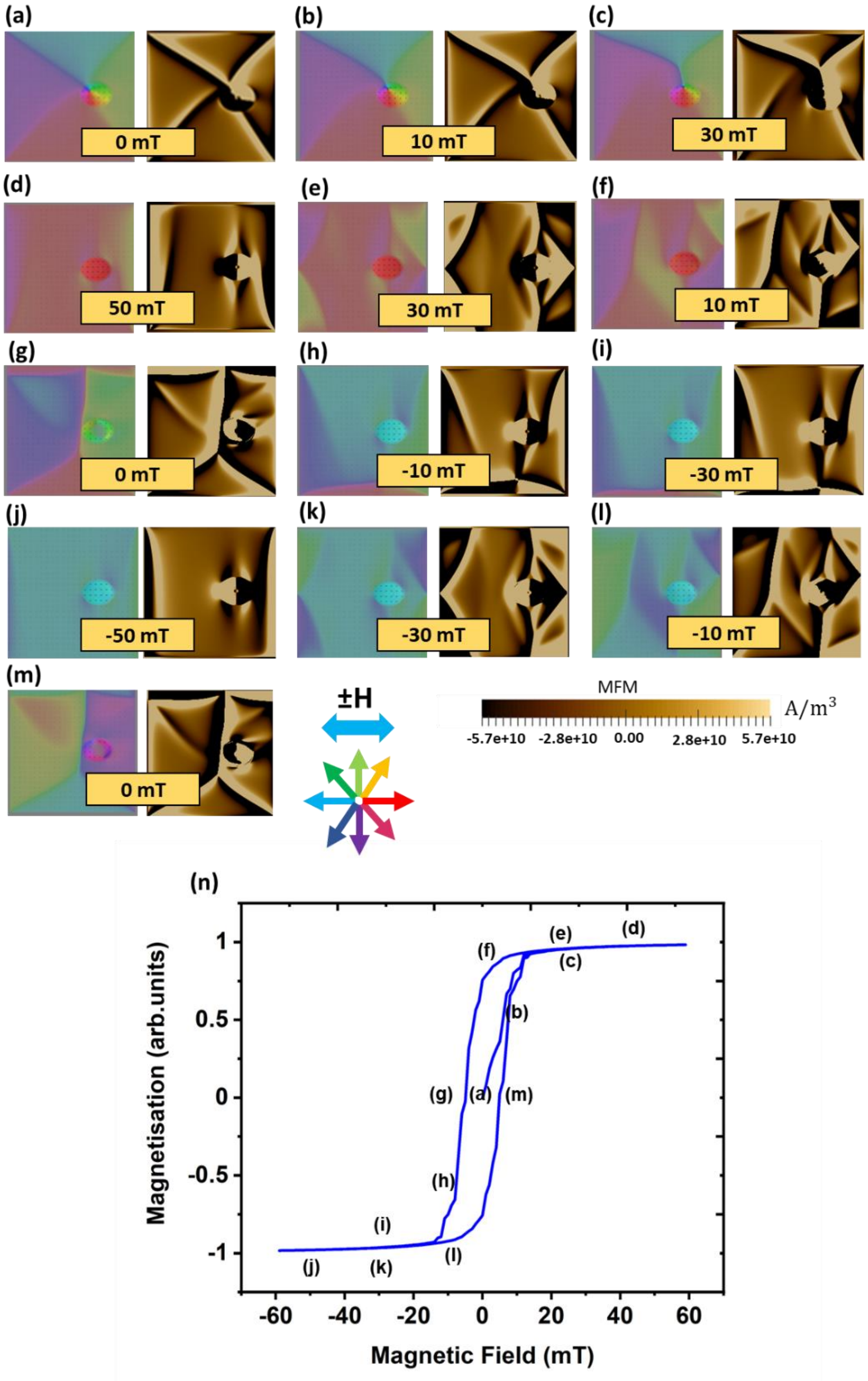

Figure 5.25: Simulated spin configuration and the corresponding MFM for high MS defect array at (a) zero field and (b-m) under the application of an in-plane field H in the ±x direction (see arrow). Different colours represent the direction of magnetisation with respect to the applied field, as depicted in the colour wheel. (n) Simulated hysteresis loop, with labels corresponding to the configurations (a-m).

Figure 5.25(n) reveals the simulated hysteresis loop for the defect array. Here, the loop is differing from the standard high MS sample. The initial magnetisation is close to zero as reflected by the four-domain vortex geometry seen in 5.25a. Application of a positive field yields a number of abrupt step features (b), as the vortex core depins from the defect and yielding saturation (c). Reduction of the field to zero, yields a high remanence of ~0.8, consistent with 5.25g. Here, it seems that a state with three walls that avoid crossing through the defect is more energetically favourable than the conventional vortex state. Application of the field in the negative shows a more abrupt transition, than in the virgin up-sweep since the mode of reversal is now domain wall motion (g). As the walls, are pushed against the lower boundary of the element a change in gradient in the loop is seen (h), likely due to the increase in magnetostatic energy. Reduction of the field to zero again yields a state with finite remanence and comparable to that seen in Fig 5.25g. It is interesting to note the difference between the original state that is relaxed in the absence of an applied field (Fig 5.25a) and the states obtained at remanence after saturation (Figs 5.25g and 5.25m). We believe that this is due to the energy landscape during the switching process versus, a simple relaxation in the absence of an applied field from randomised magnetisation. Whilst the initial relaxation appears to find a perturbed vortex as the energy minimum, we note that the 50 mT step shown in Fig 5.25d makes it more favourable for the 90 degree wall at the left boundary to propagate back towards the centre as the field is reduced, producing the seen flux closure pattern.

The previous experimental and simulated observations shows that the defect perturbed the remanent state and magnetisation process of the squares also significantly altering the values of the vortex nucleation and annihilation fields see table 5.3). In experiment, the vortex core in the plain square begins to re-nucleate at a field value equal to 5 mT but in the case of the defect square, the core starts to re-nucleate at a field value equal to 3 mT (see Fig. 5.6f and Fig. 5.21e). The lower field values than the high MS plain array are attributed to the asymmetric spin texture formed due to the defect which leads to a reduced distance for vortex displacement. However, this is only true for a given field direction. Application of a positive field direction pushed the core upwards from the defect wall. Application of reverse field leads to the core being pushed around the defect.

	Annihilation field (mT)	Re-nucleation field (mT)
Plain high MS	7	5
Defect high MS	5	3

Table 5.3: A summary of experimental annihilation and re-nucleation fields for plain and defect high MS array.

Since the static state obtained can often depend upon the initial magnetisation prior to relaxation, two initial conditions were tried. For example, in one set of conditions a state can be close to a local energy minima, providing a false ground state. For this reason, we investigated a state whereby the spin configuration was placed into a vortex state, figure 5.26(a), and a second simulation whereby the initial spin configuration was placed into a randomised configuration, figure 5.26(b). Overall, this provides an idea of what states are possible with different initial conditions. Figure 5.26(a), which was run with the vortex state initial condition, shows the core pinned on the left edge of the defect. Here the defect itself also is in a vortex state, with the same chirality (CCW) as larger square vortex as can be seen from Fig. 5.26(a, e). Here, it appears that a single core is shared between the larger square and the small defect. In contrast, using a randomised state initial condition always yielded a core located in the middle of the square Fig. 5.26(b). The defect, which appears to also be in a vortex state, is seen to have an independent core located on the right-hand edge. It is intriguing that the defect magnetisation shows a perturbed vortex state. We note that the literature suggests hemispherical systems of this size [176] do adopt a vortex configuration. The stray field from the underlying domain will have a strong vertical component, which means depending on the chirality, the defect core will be offset to the right or left, determining the two states.

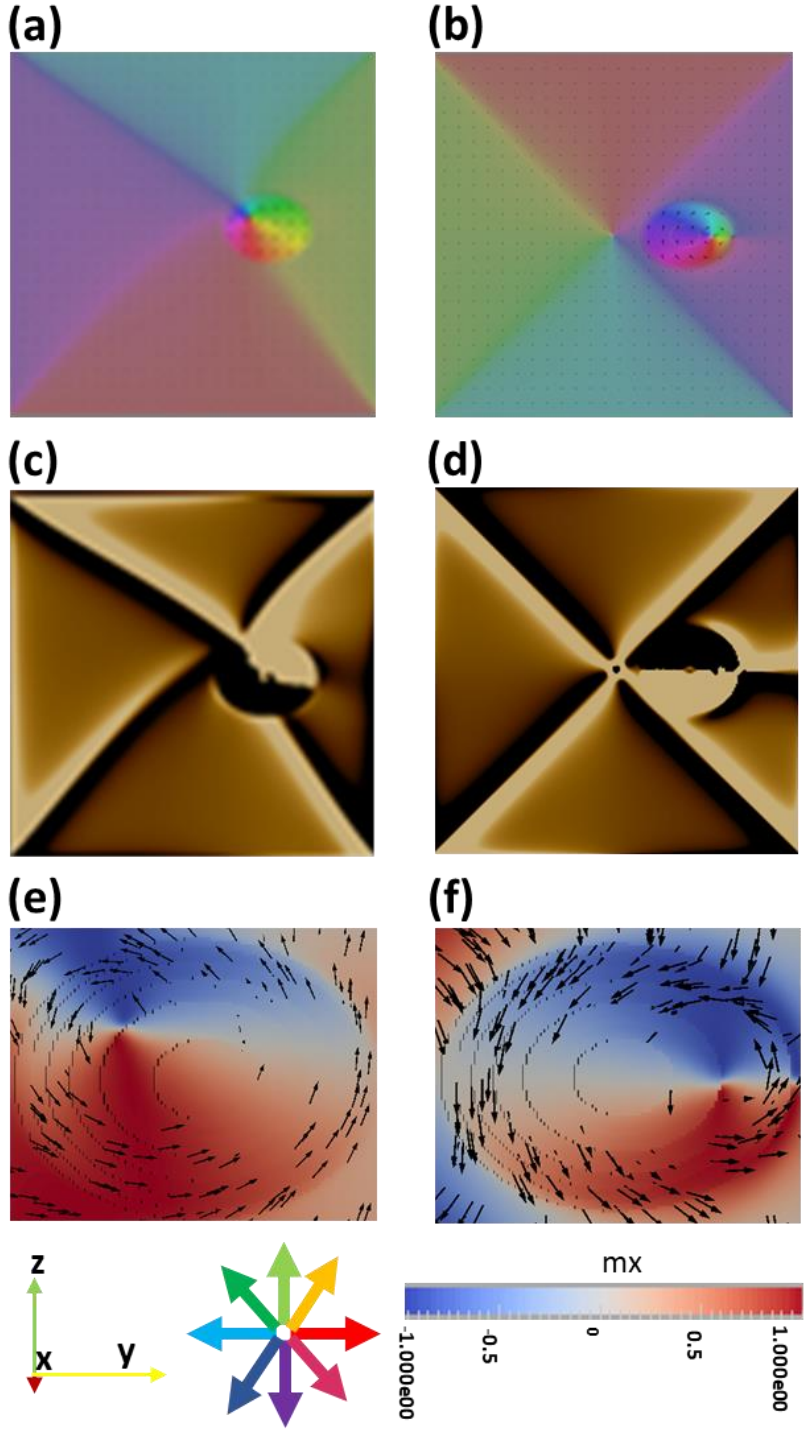

Figure 5.26: Simulated spin configuration and the corresponding MFM for simulations that had two initial conditions (a,c) vortex and (b,d) randomised spin texture. Note images shown here are for post-relaxation. Both show a vortex state with opposite chirality. (e, f) Top view of the defect spin configuration in both cases.

Discussion

The presence of a double vortex state during the field-driven magnetisation reversal is an interesting observation for samples in the coupled regime. Such states have been reported before, but mainly at remanence as a static configuration [19]. Here, using spin-polarised SEM the magnetic configuration of square arrays (640nm length with a thickness of 40nm) were studied. At remanence, a pattern characteristic of typical Landau contrast could be seen. It was apparent that the CW state was the most common, whereas the CCW state and a double vortex state occur less frequently.

An additional noteworthy study was conducted [175], in which the authors examined the field-induced transitions among different flux-closure states in an array of squares with side 5 μm with a thickness of 50 nm. The researchers employed scanning magnetoresistance microscopy (SMRM) to capture visual representations of magnetic domain structures under varying magnetic fields. Using SMRM, they imaged the behaviour of magnetic domain structures at different fields. Some squares exhibited a transition from a single vortex state to a double vortex state, during the field cycling process and also remain at remanence. A further study [178] investigated the remanent configuration and spin-wave dynamics of squares which varied in size between 1 – 4 μm and with varying separation. It was found that the lattice spacing drastically changed the remanent state populations. For low lattice spacings, a seven-configuration, double vortex state was observed in 90% of the squares, whereas in higher lattice spacing systems equal populations of single vortex and double vortex states were observed. Overall, the results suggest that even in these flux closure states, inter-element magnetostatic fields can strongly influence the observed configuration.

In this thesis, the observation that the transition between flux-closure states occurs with minimal alteration in the external field suggests that the energy barriers separating these distinct states are relatively low. Consequently, introducing a double vortex state, which serves as the lowest energy state and replaces the single vortex state, helps to reduce the magnetostatic energy of the array. The fact that micromagnetic simulations have not captured the double-vortex state seen in experiment is interesting and suggests that subtle differences in simulated and experimental geometry may be responsible. For example, the square systems as produced by TPL have finite surface roughness not seen in the simulations. Such subtleties have previously been used to explain the observation of double vortex states in squares [11]. Some early analytical models on similar ring-like systems on the micron scale have also explored the impact of roughness. Vaz et al. derive energy expressions for uniform and vortex states and study the impact of roughness [179]. The results suggest the roughness contribution to the magnetostatic energy is relatively large in the vortex state and this raises the energy when compared to the uniform state, for which roughness has less impact. The overall result was to decrease the stability of the vortex state when compared to the uniform state. This study suggests that the overall phase diagram can be impacted by simple roughness. We note that this has the most pronounced effects when studying vortex textures close the phase boundary. Overall, though the study is upon a ring system it provides some credibility to the idea that simple roughness is sufficient to dictate the state, particularly when considering a number of states separated by small energy barriers (ie. single and double vortex state).

A more recent study [180] has utilised more sophisticated micromagnetics developed in-house that was able to directly study the impact of roughness upon square elements with length 500 nm and thickness 50 nm. The out-of-plane moments arising due to local roughness was found to interact with the core with both exchange and magnetostatic interactions being important. The impact of this was to break the symmetry with respect to up and down core directions. Intriguingly, it was found that even a small amount of roughness (~10 nm) was sufficient to break the degeneracy between up and down polarity. We note that a key observation in this thesis has been a consistent core direction across an entire array. As stated previously, this is likely to be due to a small remanent field during the deposition process. Though roughness in single disks appear to break the degeneracy of up- and down- core states, it is unlikely to yield a net preferential core direction across many disks in an array due to the randomness of local roughness. Another explanation is the finite resolution of TPL, which yields slight rounding of corners in experimental structures. Such rounding will change the magnitude of the magnetostatic field experienced by adjacent elements. Overall, a further study is required to embed realistic experimental subtleties into the simulations. Such simulations are computationally expensive and the group are considering the use of the university supercomputer.

The defect within the square geometry studied in this thesis exhibited distinct, central MFM contrast. According to the phase diagram of equilibrium states for soft magnetic hemispherical structures [95, 176, 181], the thinnest samples yield an onion state (< 20 nm), whereas a vortex state is present for thicker films. As a result, the geometrical parameters applied in our work for the defect correspond to a vortex ground state. In these similar hemispherical systems, the vortex core contrast is found to occupy a large fraction of the surface, matching the contrast observed in our experimental data [182].

Conclusion

The findings that were presented in this chapter show that TPL can be used again to realise different 2D spin textures and once again has the ability to place more significant 3D defects than in the previous chapter upon the surface. In this study, we looked at the magnetic properties of square systems in a Landau flux closure state. The research focused on three primary systems: plain squares with low and high MS coupling arrays and squares with hemispherical defects in the high MS coupled array. In each individual instance, MFM was performed both at remanence and when an external field was present in order to assess the spin texture.

In the plain arrays, both high and low MS arrays, the findings of the experiment and the simulation coincide with one another. Both shows a Landau-flux-closure structure where the four 90° domain walls meet in the centre, forming the vortex. Four triangular domains are separated by the 90° domain walls aligned along the diagonals of the square. At remanence, the high MS and low MS arrays exhibited equal chirality distribution. When the field was applied, the array with a high MS exhibited a preference in the chirality distribution, whereas the array with a low MS displayed an equal chirality distribution. In addition, the low MS array demonstrated a lower re-nucleation field in comparison to the high MS array because of the function that magnetostatic interaction plays in the process of magnetisation at small inter-square distances.

In the case of the defect array, both experimental and simulation fundings shows that the core of the vortex and the domain wall can be shown to be offset due to the defect position. Furthermore, the findings indicate that the perturbed geometry induces lower annihilation and re-nucleation field values than the high MS plain array.

6. Chapter 6

Magnetisation response within 3D micron sized magnetic pyramids array

6.1 Introduction

According to what was addressed in section 2.14, most theoretical and empirical research has concentrated on the investigation of simple geometries, such as square or circular elements. This is mostly attributable to the myriad of practical challenges that come into play as geometries get more complex. On the other hand, the demands of magnetic applications are pushing length scales further and deeper into the sub-micron region. The shape has a significant impact on how things behave magnetically at these sizes and a variety of different 3D forms have been examined both experimentally and theoretically. In addition to this, it was stated that the 3D geometry of samples can support more stable magnetic states than ٢D equivalent, and as a result, is suitable for multi-bit information storage [183]. Most research has been done on nanoscale particles and clusters or thin films with a lithographically imposed pattern. On the other hand, relatively little research has been done on 3D elemental structures, whose dimensions are similar to the key characteristic physical length scales, such as the size of ferromagnetic domains and the width of domain walls.

The enhanced complexities in spin textures [184], the curvature-induced effective Dzyaloshinskii-Moriya interaction [185], and frustration in three dimensions [186] all point to the technological and scientific investigation of three-dimensional magnetic nanostructures as a promising new area of study that promises to provide intriguing novel physical phenomena. One may also predict that such systems will have a significant potential for innovative applications in magnetic sensor and information processing techniques, particularly in terms of better energy efficiency, increased processing speed, expanded functionality, and shrinking of future spintronic devices.

The main objective of this chapter is to present and discuss the efforts which have been made toward fabricating and characterising a 3D array of pyramid structures using a combination of TPL and thermal evaporation. This is a preliminary look at both the simulation of the phase diagram as well as the extent to which such structures can be fabricated using TPL. AS discussed previously, in TPL one is limited by the voxel size and in pyramids this will yield a rounding of corners. As a result, focus here is on micron-scale structures similar to the length scale used for both squares and disks earlier in this thesis. Future studies by another student in the group will explore smaller structures using a shorter wavelength TPL laser.

The arrays were imaged using SEM yielding an average pyramid length of 2 ± 0.08 μm and a height of 5 ± 0.03 μm, close to the design. AFM was used to understand the underlying topography of the pyramid samples. The root mean square (RMS) roughness of arrays is 8.7 ± 0.6 nm. Samples were constructed in regimes of high magnetostatic (MS) coupling with a lattice spacing of 0 μm, and pyramid edges touching. The spin texture was imaged using magnetic force microscopy (MFM) which shows a complex multi-domain state.

6.2 Magnetic configuration in pyramid structures

Figure 6.1 shows an investigation of how pyramid edge length (20-400 nm) and thicknesses (5-100 nm) impacts the magnetic configuration performed using micromagnetic simulations in the literature [103].

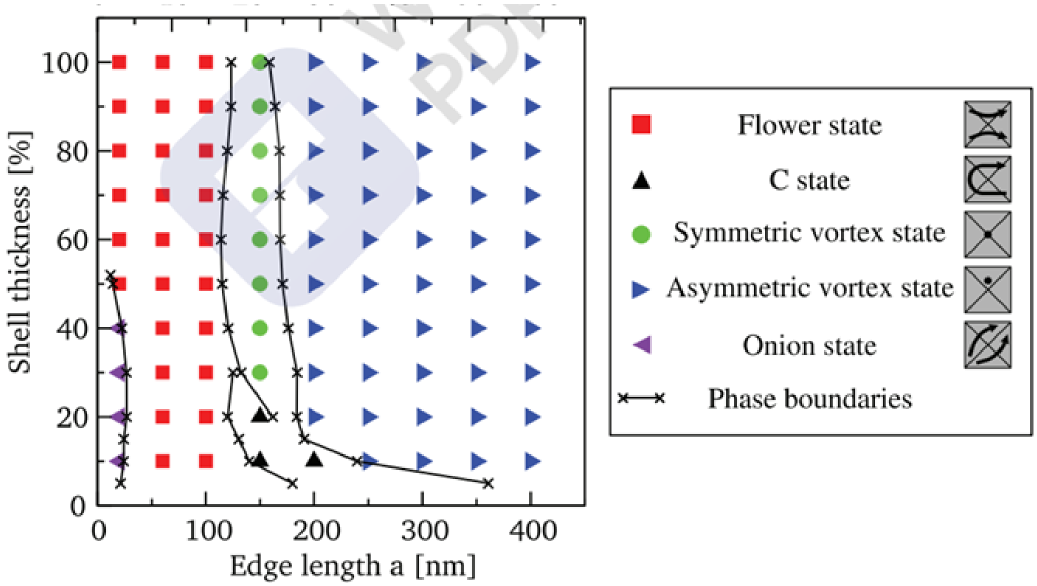

Figure 6.1: Phase diagram showing the ground states for different pyramidal structures as a function of the edge length and the shell thickness [103].

For systems with greater thickness and edge length, vortex states were found [103, 105]. This is made up of an in-plane magnetization component that curls around a tiny out-of-plane vortex core and a small out-of-plane vortex core. Two distinct vortex states were detected, a symmetric vortex and an asymmetric vortex. The symmetric vortex, is the 3D equivalent of that seen in our previously studied squares and consists of a circulating spin texture with an in-plane component and core at the central region. The z-component of the magnetization varies at neighboring faces as the rotation process occurs. In general, a wider core diameter is found than in planar systems, due to favourable magnetostatics allowing the magnetisation to sit perpendicular to the substrate plane. The asymmetrical vortex state, has the center of the vortex lying on one of the pyramid's four (outside) sides and is generally seen for greater thicknesses and lengths. The remanent magnetization of an asymmetric vortex state includes two components: one along the basal plane, where more "magnetic moments" point to the right than the left, and one along the axis of rotation, where the core of the vortex is more strongly magnetized than the rest of the state. For lower thicknesses and lengths, the reduced magnetostatic energy allows the formation of states with greater net magnetisation at remenance. This includes the flower state, the C state and the onion state.

The onion state refers to a single-domain condition in which the mean magnetization is aligned along the diagonal of the basal plane. Starting in the lower left and progressing to the upper right, the magnetization attempts to conform to the shape of the surface by pointing upwards in the lower left and downwards in the upper right. A flower state is the name given to the second single state. It has the normal tilting in the corner region, which creates a flower's appearance. Interestingly, the spatially averaged magnetization, which is oriented with either the x-axis or the y-axis, grows as the shell thickness rises. This happens because of the potential for surface charges to be generated on the pyramidal shell's base plane. The surface area of the latter increases proportionately with the shell's increase in thickness. Therefore, the increased force exerted by the basal plane results in a usually improved magnetization alignment along the x (or y) axis for thick shells. Lastly, is the C state. The latter term originates from the form of the flux lines, which resembles the letter C after being turned via a 90°clockwise direction. Compared to a flower state, a C state has a greater degree of flux closure, resulting in a reduction in the magnetostatic energy. This comes at the cost of a greater exchange of energy being required. The so-called S state is similar to the C state; it derives its name from the form of the flux lines, which resemble the shape of the letter S. This state is equivalent to the C state. When comparing the S state to the flower and the C state, we find that its mean magnetization is displaced from the flower and the basal plane towards a diagonal.

It is interesting to investigate what lies beyond the phase space observed previously, with TPL being used to produce such structures by design. To gain some initial insight into this, a micromagnetic simulation was performed whereby the pyramid size was set to 1500 nm, and film thickness 40 nm as shown in Fig. 6.2. It can be seen that a multi-domain configuration is present, though a large part of this is a dominant vortex structure that covers the majority of the area. Corners appear to favour the formation of additional 90° walls, yielding smaller vortex structures at the edges. Despite, multi-domain contrast being present, we proceed to fabrication to see the extent to which MFM can be used to determine contrast in true 3D structures. This initial work will pave the way for a further student, studying smaller structures in the vortex regime.

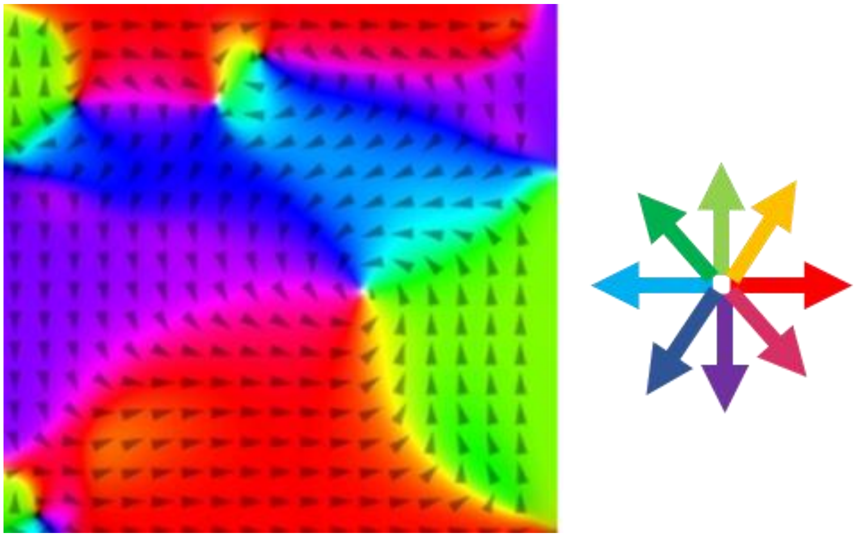

Figure 6.2: Simulated spin configuration for pyramid of 1500 nm edge length, height 5 μm and thickness 40 nm. Different colours represent the direction of magnetisation with respect to the applied field, as depicted in the colour wheel.

6.3 Morphological characterisation of 3D pyramidical arrays

Different process parameters were used to fabricate the structures, and the optimum writing circumstances were selected (see section 4.3.1). Figure 6.3(a) displays a 45° tilted SEM image of an array sub-section, which reveals that they adhere to particular design parameters with a pyramid side length of 2 μm and height of 5 μm. This proves that they were designed successfully. Because of the ellipsoidal voxel that was used in the TPL stage of manufacturing, the evaluated structures have a rounded corner in their geometry, these impacts both corners of the pyramid and the apex, as seen in the SEM.

Figures 6.3(b) shows an atomic force microscopy image of the pyramid array. The AFM line profile is displayed in Figure 6.3(c), showing the expected slope and height of 1 µm. Figure 6.3(d) illustrates a 3D rendering of the array. The topography reveals a rougher surface than seen previously at approximately 8.7 ± 0.6 nm. Further optimisation of hatching and slicing should reduce this roughness.

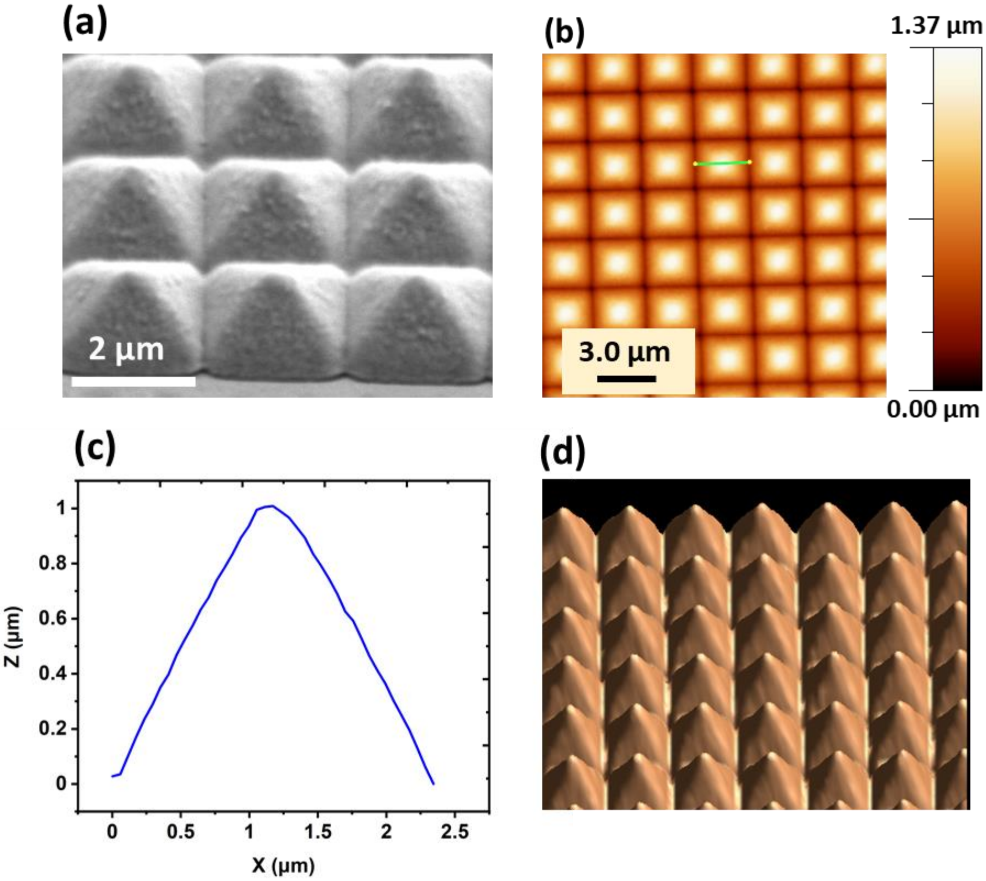

Figure 6.3: (a) SEM image for a pyramid array from a 45° tilt with respect to the substrate plane, (b) AFM image of pyramid array, (c) plot of line profile of one pyramid and (d) 3D view.

6.4 Initial ordering of pyramid arrays

Figure 6.4 illustrates MFM images of a pyramid array taken without the application of an external magnetic field (as deposited state). The result does not seem to be consistent with any of the phases predicted, and we were slightly surprised to see such ordered structure as-deposited given smaller micromagnetic simulations indicated a multi-domain state. In general, contrast is most clearly seen at pyramid edges, with intense contrast also seen at the apex. Furthermore, it can also be seen that the left side of the pyramid exhibits more negative contrast than the right side, suggesting at least a partially magnetised state.

Determining the magnetisation profile due to the MFM contrast is difficult since systems of this size cannot be simulated due to memory constraints upon our MuMax3 server. However, the contrast observed can be used to sketch out a possible configuration.

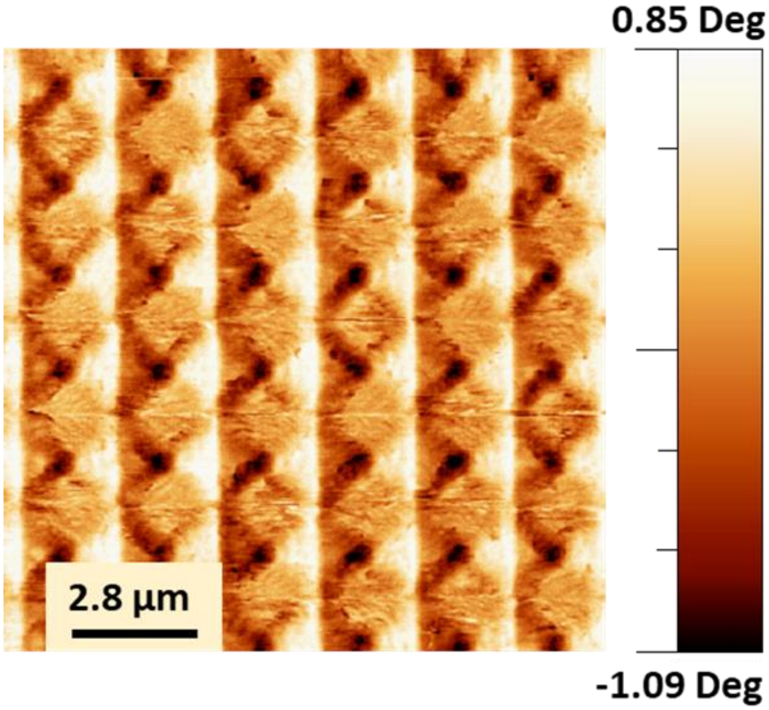

Figure 6.4: MFM image of a 6 x 6 portion of the pyramids array in the as-deposited state and in the absence of an applied field.

A diagram of the contrast and possible magnetisation profile is shown in Fig. 6.5, as inferred from MFM contrast. We emphasise that this is an estimation of the magnetisation profile. Two walls on the left edges, at the interface between faces A/D and D/C, exhibit dark bands, suggesting opposing magnetisation. This coupled with the bright contrast on the right face (B) suggests faces A, B and C all have a strong component of magnetisation pointing in the negative x-direction. Faces A and C are uniformly magnetised along their respective face edges, whereas face B has a strong diverging magnetisation with strong perpendicular component. Since face B and D both have component pointing inwards, this yields strong contrast at the apex as seen in the MFM.

Moving forward, there are plans to run simulations upon larger GPU clusters upon the Cardiff supercomputer in order to compare with the magnetic structure seen in images.

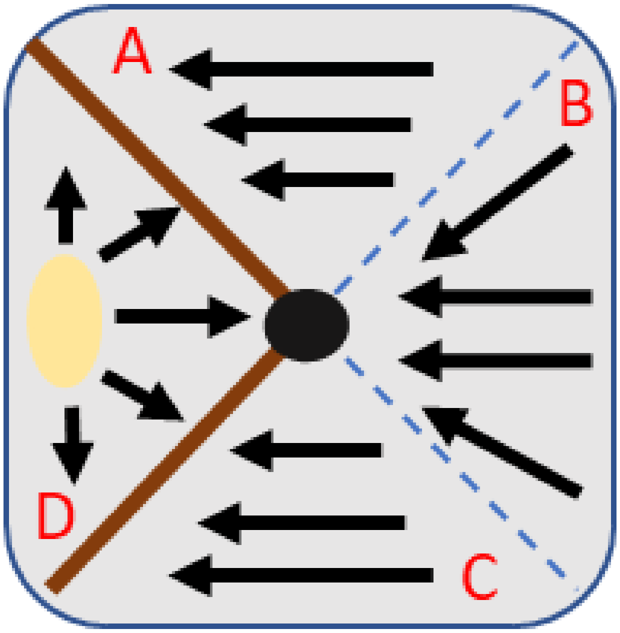

Figure 6.5: Sketch of magnetisation configuration, based upon MFM contrast.

Discussion

The aim of this study was to determine if TPL was able to realise magnetic pyramids which have the states documented in the literature. With regards to TPL voxel size, this preliminary study focused on larger structures of approximately 2 μm and, therefore, because we have a larger system, the state observed is multi-domain (see Figure 6.5).

Pyramidal patterns in micro or nano scales have previously been considered by two-step dual-bath electrodeposition [104] and by the combination of dry and wet etching processes [106]. A limitation of the two-step dual-bath electrodeposition technique is its inclination towards non-conformal growth on surfaces that are not planar. Growing a single element using a template which controls the growth does not present a problem in this case. However, in the case of an array, electrons tend to accumulate in the irregularities on the surface. Consequently, further deposition occurs at these specific points, thereby exacerbating the problem by increasing the roughness of the surface, as observed in the referenced study [104]. During etching processes, 3D structures may suffer geometric distortion due to non-uniformities in the process thereby changing their physical characteristics. Furthermore, concerns regarding the feasibility of generating specific shapes and the limited control over their arrangement are evident [106]. Unfortunately, neither of these two methods will provide the required control over geometry as TPL does. In order to move forward with this investigation, a TPL technique is required but with smaller voxel size. Previous work, has demonstrated that a 405nm diode laser can be implemented into a TPL setup and be used to realise sub-100nm feature size [187]. Our group has now implemented a similar scheme in Cardiff which allows the voxel to come down to 80 nm. Overall, we expect that this should allow the realisation of 400 nm x 400 nm pyramids which should have stable vortex configurations.

Conclusion

A preliminary investigation has been carried out upon ferromagnetic pyramid structures in order to pave the way for a future student. The published phase diagram has been found and it has been noted that with a conventional 780 nm TPL write, rounding would make much of the simulated states unobtainable. Micromagnetic simulations of larger structures upon a length scale of 1500 nm, indicated a multidomain state, with dominant vortex. A preliminary fabrication was carried out to determine the extent to which pyramid structures can be reproduced and magnetic contrast measured using MFM. Complex contrast was measured, that does not match any of the previously observed states. Further micromagnetic simulations are required to confirm the magnetisation state observed.

7. Chapter 7

Conclusion

The research that carried out in this thesis had a total of three primary goals that can be summed up as follows: Firstly, there was an aim to determine the potential of TPL to construct well-known spin textures seen in 2D magnetic elements. Secondly, was to investigate the opportunities presented by the in-house magnetic microscopy methods to characterise any structures that have been produced. Finally, the potential to place 3D defects upon structures and study the extent to which they impact the pristine spin textures.

Fabrication methods in 3D nanomagnetism have reported promising findings over the last several years (discussed in detail in chapter 2). However, they have had difficulty establishing themselves as the leading candidate to provide a path towards a variety of next-generation technologies. The focus has been on demonstrating the enormous potential and adaptability offered by TPL, intending to prove that this method needs to be regarded as a strong fabrication method in the field of 3D nanomagnetism. One of the primary advantages of TPL is that it can used with a wide variety of secondary methods to produce a wide variety of magnetic nanostructures. The process of thermal evaporation was selected as the second method used in this investigation at an early stage. Since thermal evaporation has been extensively used for decades to produce ultra-high purity magnetic films with very little setup time and a high degree of reproducibility, this was partly selected because it is simple. In addition, it was anticipated that this method would be the one most similar to earlier instances of 2D elements, given that they are also often created by a line-of-sight deposition after a lithographic procedure.

Initially, planar $Ni_{81}Fe_{19}$ magnetic islands were manufactured directly on a glass substrate. This made it possible to calibrate the thickness of the deposition using AFM, and it demonstrated that specific domain patterns, driven by shape anisotropy, can be directly viewed in structures 40 nm thick using MFM. When measuring 2D surfaces, scanning probe methods are commonly utilised. Here it was demonstrated that with atomic force microscopy (AFM) it was still possible to track the varying topography (approximately 1.5 μm) carefully and reconstruct magnetic contrast. Following the optimisation of AFM feedback settings, the MFM showed the remanent domain pattern of practically every structure. At the lowest aspect ratios, flux-closure domain patterns were seen, but single-domain states were detected at aspect ratios greater than approximately 4. Overall, proof-of-principle has been shown that this method could produce magnetic elements above the substrate with spin textures reproducing those seen in the literature.

The focus then shifted to fabricating a micron-sized disks and squares in high MS and low MS arrays, respectively. Since the elements are 5 microns above the substrate, the stray field from $Ni_{81}Fe_{19}$ on the sheet film is insignificant. Then arrays of disks/squares within the high MS regime were produced with a 3D hemispherical defect upon the surface after which a preliminary study was carried out on 3D pyramids.

In chapter 4 the focus was on $Ni_{81}Fe_{19}$ disk structures with a diameter of approximately 2 μm with high magnetostatic (MS) coupling (lattice spacing of 2 μm) and low MS coupling (lattice spacing of 3 μm). When examined at remanence, both samples showed sharp contrast in the disk centre consistent with a vortex state configuration. When an in-plane magnetic field was applied, typical characteristics of a vortex reversal were observed. These characteristics included the translation of the vortex core in a direction transverse to the field, the annihilation of the core, re-nucleation, and relaxation back to the centre. After completing this significant step in the process, an in-depth comparison between the high MS array and the low MS array was conducted. The low MS array demonstrated equal chirality distributions, in contrast to the high MS array, which had a remanent state nearly entirely composed of a single chirality. According to the experimental findings, the magnetostatic interaction plays a significant part in the magnetisation process for ferromagnetic micron disk arrays with close interdisk distances. In addition, it has been discovered that the enhanced magnetostatic interaction increases both the vortex annihilation and the re-nucleation fields. Since it was shown that it is possible to create well-known spin textures, an array of disks within the high MS regime were manufactured with a 3D hemispherical defect on the surface. It was discovered that this perturbation had a considerable impact on the remanent state and the magnetisation reversal. Compared to plain disks in high MS arrays. In particular, the vortex annihilation and re-nucleation fields were far lower when compared to the unperturbed system.

In chapter 5, the focus is on micron-sized magnetic square elements, arranged into lattices. The structures had side length of 2 μm and were again fabricated in high (lattice spacing of 2 μm) and low MS regimes (lattice spacing of 3 μm). The square configuration has a vortex core in the middle and consists of four domains that are separated by walls that are 90^0. Presence of the 90^0 walls made MFM interpretation more straightforward.

The typical vortex translation resulting from wall movement and annihilation was produced when an in-plane magnetic field was applied. Following the reduction of the external field, the core re-nucleated, and its location within the structure could be quickly determined by observing the movement of the domain wall. In the as-deposited state, both the high MS array and the low MS array exhibited a remanent state with an equal chirality distribution. The application of a saturating field and subsequent imaging demonstrated a chirality preference in the high MS array, while the low MS array demonstrated an equal chirality distribution. After proving that it was feasible to duplicate spin configurations described in the scientific literature, arrays of squares inside the high MS array were created with a 3D hemispherical defect on the surface, with a diameter of 600 nm. This defect was placed on the surface of the squares. It was found that this perturbation had a significant effect on both the remanent state and the magnetisation process. It was discovered that the domain walls at the remanent state are offset, and the core seems pinned to the defect. The subsequent application of a field demonstrated the well-known processes of vortex annihilation and re-nucleation. However, these phenomena were seen in lower fields than in the plain sample. The chirality of the vortices in these perturbed structures were found to be intertwined with the pinning location of the walls, with respect to the defect.

In chapter 6 a preliminary look at both experiment and simulation of a three-dimensional pyramid array was accomplished with an optimal base edge length of 2 μm, heights of 5 μm, and a thickness of 40 nm which shows a complex multi-domain state.

8. References

1. Yamamoto, K. and H. Kurebayashi, *Anatomy of spin–orbit torques.* Nature Nanotechnology, 2017. **12**(10): p. 941-942.
2. McCray, W.P., *How spintronics went from the lab to the iPod.* Nature Nanotechnology, 2009. **4**(1): p. 2-4.
3. Makarov, D., et al., *Shapeable magnetoelectronics.* Applied Physics Reviews, 2016. **3**(1): p. 011101.
4. Freitas, L.A.L., J.G.N. Rahmeier, and O.P.V. Neto, *Shape Engineering for Custom Nanomagnetic Logic Circuits in NMLSim 2.0.* IEEE Design & Test, 2021. **38**(4): p. 85-93.
5. Faure, B., et al., *2D to 3D crossover of the magnetic properties in ordered arrays of iron oxide nanocrystals.* Nanoscale, 2013. **5**(3): p. 953-960.
6. Sun, H., et al., *Self-organized honeycomb structures of Mn12 single-molecule magnets.* The Journal of Physical Chemistry B, 2009. **113**(44): p. 14674-14680.
7. Stamps, R.L., et al., *The 2014 magnetism roadmap.* Journal of Physics D: Applied Physics, 2014. **47**(33): p. 333001.
8. Ladak, S., A. Fernández-Pacheco, and P. Fischer, *Science and technology of 3D magnetic nanostructures.* APL Materials, 2022. **10**(12).
9. Donnelly, C., et al., *Complex free-space magnetic field textures induced by three-dimensional magnetic nanostructures.* Nature Nanotechnology, 2022. **17**(2): p. 136-142.
10. Jafari, S., et al., *Biomedical Applications of TiO2 Nanostructures: Recent Advances.* International Journal of Nanomedicine, 2020. **15**: p. 3447-3470.
11. Sulciute, A., et al., *ZnO Nanostructures Application in Electrochemistry: Influence of Morphology.* The Journal of Physical Chemistry C, 2021. **125**(2): p. 1472-1482.
12. Azzerboni, B., et al., *Magnetic nanostructures in modern technology: Spintronics, Magnetic MEMS and Recording*. 2007: Springer.
13. Akbarzadeh, A., M. Samiei, and S. Davaran, *Magnetic nanoparticles: preparation, physical properties, and applications in biomedicine.* Nanoscale research letters, 2012. **7**(1): p. 1-13.
14. Yan, J., S.C. Bae, and S. Granick, *Colloidal superstructures programmed into magnetic Janus particles.* Advanced Materials, 2015. **27**(5): p. 874-879.
15. Aharoni, A., *Introduction to the Theory of Ferromagnetism*. Vol. 109. 2000: Clarendon Press.
16. Cowburn, R., *Property variation with shape in magnetic nanoelements.* Journal of Physics D: Applied Physics, 2000. **33**(1): p. R1.
17. Cowburn, R.P., et al., *Single-domain circular nanomagnets.* Physical Review Letters, 1999. **83**(5): p. 1042-1045.
18. Pulwey, R., et al., *Switching behavior of vortex structures in nanodisks.* IEEE Transactions on Magnetics, 2001. **37**(4): p. 2076-2078.
19. Konoto, M., et al., *Formation and control of magnetic vortex chirality in patterned micromagnet arrays.* Journal of Applied Physics, 2008. **103**(2): p. 023904.
20. Streubel, R., et al., *Magnetism in curved geometries.* Journal of Physics D: Applied Physics, 2016. **49**(36): p. 363001.
21. Raabe, J., et al., *Magnetization pattern of ferromagnetic nanodisks.* Journal of Applied Physics, 2000. **88**(7): p. 4437-4439.
22. Gregurec, D., et al., *Magnetic Vortex Nanodiscs Enable Remote Magnetomechanical Neural Stimulation.* ACS Nano, 2020. **14**(7): p. 8036-8045.
23. Martínez-Pérez, M.J., et al., *Magnetic vortex nucleation and annihilation in bi-stable ultra-small ferromagnetic particles.* Nanoscale, 2020. **12**(4): p. 2587-2595.

24. Ehrmann, A. and T. Blachowicz, *Vortex and double-vortex nucleation during magnetization reversal in Fe nanodots of different dimensions.* Journal of Magnetism and Magnetic Materials, 2019. **475**: p. 727-733.
25. Novosad, V., et al., *Effect of interdot magnetostatic interaction on magnetization reversal in circular dot arrays.* Physical Review B, 2002. **65**(6): p. 060402.
26. Novosad, V., et al., *Shape effect on magnetization reversal in chains of interacting ferromagnetic elements.* Applied Physics Letters, 2003. **82**(21): p. 3716-3718.
27. Vogel, A., et al., *Influence of Dipolar Interaction on Vortex Dynamics in Arrays of Ferromagnetic Disks.* Physical Review Letters, 2010. **105**(3): p. 037201.
28. Almeida, T.P., et al., *Off-axis electron holography for the direct visualization of perpendicular shape anisotropy in nanoscale 3D magnetic random-access-memory devices.* APL Materials, 2022. **10**(6).
29. Prokaznikov, A.V., V.A. Paporkov, and V.A. Chirikov, *Controlling the Position of a Magnetic Vortex on a Nanostructured Surface in Magnetic Memory Elements.* Russian Microelectronics, 2022. **51**(1): p. 1-15.
30. Huong Giang, D.T., et al., *Magnetoelectric Vortex Magnetic Field Sensors Based on the Metglas/PZT Laminates.* Sensors (Basel), 2020. **20**(10).
31. Yu, T., Z. Luo, and G.E. Bauer, *Chirality as generalized spin–orbit interaction in spintronics.* Physics Reports, 2023. **1009**: p. 1-115.
32. Dobrovolskiy, O., et al., *Ultra-fast vortex motion in a direct-write Nb-C superconductor.* Nature communications, 2020. **11**(1): p. 3291.
33. Galeano-Villar, B.M., et al., *Core-shell Fe@ FexOy nanoring system: A versatile platform for biomedical applications.* Materials & Design, 2022. **213**: p. 110303.
34. Coffey, W.T. and Y.P. Kalmykov, *Thermal fluctuations of magnetic nanoparticles: Fifty years after Brown.* Journal of Applied Physics, 2012. **112**(12): p. 121301.
35. Stebliy, M.E., et al., *3-D architectural approach for manipulation of the micromagnetic configuration in nanodisks.* IEEE transactions on magnetics, 2012. **48**(11): p. 4406-4408.
36. Krishnan, K.M., *Fundamentals and Applications of Magnetic Materials*. 2016, Oxford University Press.
37. O'Handley, R.C., *Modern Magnetic Materials: Principles and Applications*. 2000.
38. O'Handley, R.C., *Modern magnetic materials:Principles and Applications*. 2000, Nwe York John Wiley. (pp.274-275).
39. Yu, R.R., *Magnetic vortices in ferromagnetic nanodots.* Журнал Сибирского федерального университета. Математика и физика, 2015. **8**(3): p. 327-339.
40. Arora, A., *Optical and electric field control of magnetism*. 2018, Universität Potsdam.
41. Landau, L. and E. Lifshitz, *3 - On the theory of the dispersion of magnetic permeability in ferromagnetic bodies Reprinted from Physikalische Zeitschrift der Sowjetunion 8, Part 2, 153, 1935*, in *Perspectives in Theoretical Physics*, L.P. Pitaevski, Editor. 1992, Pergamon: Amsterdam. p. 51-65.
42. Ramakanth, W.N.a.A., *Quantum Theory of Magnetism.* Springer, 2009.
43. Kikuchi, R., *On the Minimum of Magnetization Reversal Time.* Journal of Applied Physics, 1956. **27**(11): p. 1352-1357.
44. Guerra, Y., R. Peña-Garcia, and E. Padrón-Hernández, *Remanence State and Coercivity in 1-D Chain of Polycrystalline Hollow Cobalt Nanospheres.* IEEE Transactions on Magnetics, 2019. **55**(4): p. 1-5.
45. Gilbert, T.L., *A Lagrangian formulation of the gyromagnetic equation of the magnetization field.* Phys. Rev., 1955. **100**: p. 1243.
46. Mallinson, J., *On damped gyromagnetic precession.* IEEE Transactions on Magnetics, 1987. **23**(4): p. 2003-2004.
47. Chen, X., et al., *Advances in Nonlinear Optics*. 2015. 1-370.
48. Baldacchini, T., *Three-dimensional microfabrication using two-photon polymerization*. 2016, Oxford: Elsevier.

49. Nishiyama, H. and Y. Hirata, *Femtosecond Laser Nonlinear Lithography*, in *Lithography*, M. Wang, Editor. 2010, InTech: Rijeka. p. Ch. 04.
50. Pollino, J.M., et al., *Cross-linked and functionalized 'universal polymer backbones' via simple, rapid, and orthogonal multi-site self-assembly.* Tetrahedron, 2004. **60**(34): p. 7205-7215.
51. Wu, S., J. Serbin, and M. Gu, *Two-photon polymerisation for three-dimensional micro-fabrication.* Journal of Photochemistry and Photobiology A: Chemistry, 2006. **181**(1): p. 1-11.
52. Zieger, M.M., *Designing Functional 2D and 3D Structures: From Ultrathin Coatings to Laser Lithography*. 2019, Karlsruher Institut für Technologie (KIT).
53. Zhou, X., Y. Hou, and J. Lin, *A review on the processing accuracy of two-photon polymerization.* AIP Advances, 2015. **5**(3): p. 030701.
54. Miramond, C., et al., *Permalloy cylindrical submicron size dot arrays.* Journal of Magnetism and Magnetic Materials, 1997. **165**(1): p. 500-503.
55. Shinjo, T., et al., *Magnetic Vortex Core Observation in Circular Dots of Permalloy.* Science, 2000. **289**(5481): p. 930-932.
56. Ha, J.K., R. Hertel, and J. Kirschner, *Micromagnetic study of magnetic configurations in submicron permalloy disks.* Physical Review B, 2003. **67**(22): p. 224432.
57. Guslienko, K.Y., *Magnetic vortex state stability, reversal and dynamics in restricted geometries.* J Nanosci Nanotechnol, 2008. **8**(6): p. 2745-60.
58. Leroux, N., *Artificial neural networks with radio-frequency spintronic nano-devices*. 2022, Université Paris-Saclay.
59. Martins, L., et al., *Non-volatile artificial synapse based on a vortex nano-oscillator.* Scientific Reports, 2021. **11**(1): p. 16094.
60. Bohlens, S., et al., *Current controlled random-access memory based on magnetic vortex handedness.* Applied Physics Letters, 2008. **93**(14): p. 142508.
61. Cowburn, R.P., A.O. Adeyeye, and M.E. Welland, *Controlling magnetic ordering in coupled nanomagnet arrays.* New Journal of Physics, 1999. **1**: p. 16-16.
62. Xiaobin, Z., et al., *Direct observation of magnetostatic coupling of chain arrays of magnetic disks.* IEEE Transactions on Magnetics, 2003. **39**(5): p. 2744-2746.
63. Urbánek, M., et al., *Dynamics and efficiency of magnetic vortex circulation reversal.* Physical Review B, 2015. **91**(9): p. 094415.
64. Pokhil, T., D. Song, and J. Nowak, *Spin vortex states and hysteretic properties of submicron size NiFe elements.* Journal of Applied Physics, 2000. **87**(9): p. 6319-6321.
65. Vaňatka, M., et al., *Magnetic vortex nucleation modes in static magnetic fields.* AIP Advances, 2017. **7**(10): p. 105103.
66. Yakata, S., et al., *Chirality control of magnetic vortex in a square Py dot using current-induced Oersted field.* Applied Physics Letters, 2011. **99**(24): p. 242507.
67. Okuno, T., et al., *MFM study of magnetic vortex cores in circular permalloy dots: behavior in external field.* Journal of Magnetism and Magnetic Materials, 2002. **240**(1): p. 1-6.
68. Schneider, M., H. Hoffmann, and J. Zweck, *Lorentz microscopy of circular ferromagnetic permalloy nanodisks.* Applied Physics Letters, 2000. **77**(18): p. 2909-2911.
69. Kim, J., *Patterned Arrays of Magnetic Nanostructures.* Park, 2009.
70. García, J.M., et al., *Quantitative interpretation of magnetic force microscopy images from soft patterned elements.* Applied Physics Letters, 2001. **79**(5): p. 656-658.
71. Coïsson, M., et al., *Local field loop measurements by magnetic force microscopy.* Journal of Physics D: Applied Physics, 2014. **47**(32): p. 325003.
72. Schneider, M., H. Hoffmann, and J. Zweck, *Magnetic switching of single vortex permalloy elements.* Applied Physics Letters, 2001. **79**(19): p. 3113-3115.

73. Schneider, M., et al., *Stability of magnetic vortices in flat submicron permalloy cylinders.* Journal of Applied Physics, 2002. **92**(3): p. 1466-1472.
74. Tonomura, A., et al., *Direct Observation of Fine Structure of Magnetic Domain Walls by Electron Holography.* Physical Review Letters, 1980. **44**(21): p. 1430-1433.
75. Lai, M.-F. and C.-N. Liao, *Size dependence of C and S states in circular and square Permalloy dots.* Journal of Applied Physics, 2008. **103**(7): p. 07E737.
76. Zhao, G., F. Morvan, and X. Wan, *Micromagnetic calculation for exchange-coupled nanocomposite permanent magnets.* Reviews in Nanoscience and Nanotechnology, 2014. **3**(4): p. 227-258.
77. Zhu, M., et al., *Vortex state formation and stability in single and double layer nanorings and nanodisks.* Journal of Applied Physics, 2013. **113**(17): p. 17B905.
78. Mehrnia, M., et al., *Observation of Defect-Assisted Magnetic Vortex Core Reversal at Ultralow Critical Velocity.* Physical Review Applied, 2021. **16**(3): p. 034049.
79. Breitenstein, L., et al., *Stray field of a Landau magnetization pattern.* Journal of Applied Physics, 2008. **104**(8): p. 083909.
80. Jaafar, M., et al., *Control of the chirality and polarity of magnetic vortices in triangular nanodots.* Physical Review B, 2010. **81**(5): p. 054439.
81. Agramunt-Puig, S., et al., *Controlling vortex chirality and polarity by geometry in magnetic nanodots.* Applied Physics Letters, 2014. **104**(1): p. 012407.
82. Im, M.-Y., et al., *Simultaneous control of magnetic topologies for reconfigurable vortex arrays.* NPG Asia Materials, 2017. **9**(2): p. e348-e348.
83. Natali, M., et al., *Correlated vortex chiralities in interacting permalloy dot patterns.* Journal of Applied Physics, 2004. **96**(8): p. 4334-4341.
84. Usov, N. and S. Peschany, *Magnetization curling in a fine cylindrical particle.* Journal of Magnetism and Magnetic Materials, 1993. **118**(3): p. L290-L294.
85. Rahm, M., et al., *Vortex pinning at individual defects in magnetic nanodisks.* Journal of Applied Physics, 2003. **93**(10): p. 7429-7431.
86. Uhlig, T., et al., *Shifting and Pinning of a Magnetic Vortex Core in a Permalloy Dot by a Magnetic Field.* Physical Review Letters, 2005. **95**(23): p. 237205.
87. Compton, R.L. and P.A. Crowell, *Dynamics of a Pinned Magnetic Vortex.* Physical Review Letters, 2006. **97**(13): p. 137202.
88. Apolonio, F.A., et al., *A model for structural defects in nanomagnets.* Journal of Applied Physics, 2009. **106**(8): p. 084320.
89. Toscano, D., et al., *Magnetic vortex behavior and its dynamics in nanomagnets in the presence of impurities.* Physics Procedia, 2012. **28**: p. 99-104.
90. Stebliy, M.E., et al., *High-frequency switching of magnetic bistability in an asymmetric double disk nanostructure.* Applied Physics Letters, 2014. **104**(11): p. 112405.
91. Stebliy, M.E., et al., *Vortex manipulation and chirality control in asymmetric bilayer nanomagnets.* Journal of Applied Physics, 2015. **117**(17): p. 17A317.
92. Toscano, D., et al., *Dynamics of the vortex core in magnetic nanodisks with a ring of magnetic impurities.* Applied Physics Letters, 2012. **101**(25): p. 252402.
93. Ding, J., et al., *Spin Vortex Resonance in Non-planar Ferromagnetic Dots.* Scientific Reports, 2016. **6**: p. 25196.
94. Schmidt, O.G. and K. Eberl, *Thin solid films roll up into nanotubes.* Nature, 2001. **410**(6825): p. 168-168.
95. Streubel, R., et al., *Equilibrium magnetic states in individual hemispherical permalloy caps.* Applied Physics Letters, 2012. **101**(13).
96. Liakakos, N., et al., *Solution Epitaxial Growth of Cobalt Nanowires on Crystalline Substrates for Data Storage Densities beyond 1 Tbit/in2.* Nano Letters, 2014. **14**(6): p. 3481-3486.

97. May, A., et al., *Realisation of a frustrated 3D magnetic nanowire lattice.* Communications Physics, 2019. **2**(1): p. 13.
98. Crossland, E.J., et al., *Control of gyroid forming block copolymer templates: effects of an electric field and surface topography.* Soft Matter, 2010. **6**(3): p. 670-676.
99. Llandro, J., et al., *Visualizing Magnetic Structure in 3D Nanoscale Ni–Fe Gyroid Networks.* Nano Letters, 2020. **20**(5): p. 3642-3650.
100. Keller, L., et al., *Direct-write of free-form building blocks for artificial magnetic 3D lattices.* Scientific Reports, 2018. **8**(1): p. 1-13.
101. Zhang, X., et al., *Design, fabrication, and mechanics of 3D micro-/nanolattices.* Small, 2020. **16**(15): p. 1902842.
102. Askey, J., et al., *Use of two-photon lithography with a negative resist and processing to realise cylindrical magnetic nanowires.* Nanomaterials, 2020. **10**(3): p. 429.
103. Knittel, A., et al., *Micromagnetic studies of three-dimensional pyramidal shell structures.* New Journal of Physics, 2010. **12**(11): p. 113048.
104. Nasirpouri, F., et al., *Three-dimensional ferromagnetic architectures with multiple metastable states.* Applied Physics Letters, 2011. **98**(22): p. 222506.
105. Knittel, A., et al., *Effect of rounded corners on the magnetic properties of pyramidal-shaped shell structures.* Journal of Applied Physics, 2012. **111**(7): p. 07D127.
106. Irmikimov, A., et al., *Atomically Architected Silicon Pyramid Single-Crystalline Structure Supporting Epitaxial Material Growth and Characteristic Magnetism.* Crystal Growth & Design, 2021. **21**(2): p. 946-953.
107. Abitan, H., H. Bohr, and P. Buchhave, *Correction to the Beer-Lambert-Bouguer law for optical absorption.* Applied Optics, 2008. **47**(29): p. 5354-5357.
108. Heo, Y.J., S. Iwanaga, and S. Takeuchi, *A nanochannel fabrication technique by two-photon direct laser writing.* Proceedings of the IEEE International Conference on Micro Electro Mechanical Systems (MEMS), 2012: p. 997-1000.
109. GmbH, N., *Photonic Professional (GT)User Manual.* 2017.
110. Serbin, J., A. Ovsianikov, and B. Chichkov, *Fabrication of woodpile structures by two-photon polymerization and investigation of their optical properties.* Optics Express, 2004. **12**(21): p. 5221-5228.
111. Mattox, D.M., *Chapter 6 - Vacuum Evaporation and Vacuum Deposition*, in *Handbook of Physical Vapor Deposition (PVD) Processing (Second Edition)*, D.M. Mattox, Editor. 2010, William Andrew Publishing: Boston. p. 195-235.
112. Pulker, H.K., *Film Deposition Methods*, in *Optical Interference Coatings*, N. Kaiser and H.K. Pulker, Editors. 2003, Springer Berlin Heidelberg: Berlin, Heidelberg. p. 131-153.
113. Lutišan, J. and J. Cvengroš, *Mean free path of molecules on molecular distillation.* The Chemical Engineering Journal and the Biochemical Engineering Journal, 1995. **56**(2): p. 39-50.
114. Stokes, D., *Principles and practice of variable pressure/environmental scanning electron microscopy (VP-ESEM)*, ed. S. Royal Microscopical and L. Microscopical Society of. 2008, Chichester, U.K.: Chichester, U.K. : Wiley.
115. Binnig, G., C.F. Quate, and C. Gerber, *Atomic Force Microscope.* Physical Review Letters, 1986. **56**(9): p. 930-933.
116. Giessibl, F.J., *Advances in atomic force microscopy.* Reviews of Modern Physics, 2003. **75**(3): p. 949-983.
117. Casuso, I., et al., *Contact-mode high-resolution high-speed atomic force microscopy movies of the purple membrane.* Biophys J, 2009. **97**(5): p. 1354-61.
118. Jalili, N. and K. Laxminarayana, *A review of atomic force microscopy imaging systems: application to molecular metrology and biological sciences.* Mechatronics, 2004. **14**(8): p. 907-945.
119. *Tapping mode*. 2022; Available from: https://parksystems.com/cn/AFM_gallery/AFM_gallery_view.php?id=91&word=Nano.

120. Borase, R.P., et al., *A review of PID control, tuning methods and applications.* International Journal of Dynamics and Control, 2021. **9**(2): p. 818-827.
121. Instruments, V., *Dimension 3100 Manual.* 2004.
122. Passeri, D., et al., *Magnetic force microscopy: quantitative issues in biomaterials.* Biomatter, 2014. **4**: p. e29507.
123. Abelmann, L., A. van den Bos, and C. Lodder, *Magnetic Force Microscopy — Towards Higher Resolution*, in *Magnetic Microscopy of Nanostructures*, H. Hopster and H.P. Oepen, Editors. 2005, Springer Berlin Heidelberg: Berlin, Heidelberg. p. 253-283.
124. Schwarz, A. and R. Wiesendanger, *Magnetic sensitive force microscopy.* Nano Today, 2008. **3**(1-2): p. 28-39.
125. Ferri, F., M. Pereira-da-Silva, and E. Marega, *Magnetic Force Microscopy: Basic Principles and Applications*. 2012.
126. Hans Fangohr, T.F., Matteo Franchin, Giuliano Bordignon, Jacek Generowicz, Andreas Knittel, Michael Walter, Maximilian Albert, *NMAG User Manual (v0.2).* 2012.
127. Bar, L. and N. Sochen, *Strong Solutions for PDE-Based Tomography by Unsupervised Learning.* SIAM Journal on Imaging Sciences, 2021. **14**(1): p. 128-155.
128. Vansteenkiste, A., et al., *The design and verification of MuMax3.* AIP Advances, 2014. **4**(10): p. 107133.
129. Fangohr, H., et al., *NMAG User Manual (0.2.1)*. 2012.
130. Fernandez-Roldan, J., *Micromagnetism of cylindrical nanowires with compositional and geometric modulations*. 2019.
131. Abo, G.S., et al., *Definition of Magnetic Exchange Length.* IEEE Transactions on Magnetics, 2013. **49**(8): p. 4937-4939.
132. Fischbacher, T., et al., *A Systematic Approach to Multiphysics Extensions of Finite-Element-Based Micromagnetic Simulations: Nmag.* IEEE Transactions on Magnetics, 2007. **43**(6): p. 2896-2898.
133. Takada, K., H.-B. Sun, and S. Kawata, *Improved spatial resolution and surface roughness in photopolymerization-based laser nanowriting.* Applied Physics Letters, 2005. **86**(7): p. 071122.
134. Gomez, R.D., et al., *Domain configurations of nanostructured Permalloy elements.* Journal of Applied Physics, 1999. **85**(8): p. 6163-6165.
135. Rave, W. and A. Hubert, *Magnetic ground state of a thin-film element.* IEEE Transactions on Magnetics, 2000. **36**(6): p. 3886-3899.
136. Liou, S.H., et al., *Magnetic domain patterns of rectangular and elliptic arrays of small permalloy elements.* Journal of Magnetism and Magnetic Materials, 2001. **226-230**: p. 1270-1272.
137. Wiese, N., et al., *On the scaling behaviour of cross-tie domain wall structures in patterned NiFe elements.* EPL, 2007. **80**: p. 57003.
138. Felton, S., et al., *Domain configuration of permalloy ellipses in a rotating magnetic field.* Journal of Physics D: Applied Physics, 2006. **39**(4): p. 610-614.
139. Chao, C.-T., et al., *Study of inter-dot coupling in nano-patterned permalloy dots array.* Journal of Physics: Conference Series, 2011. **266**: p. 012005.
140. Moreira, C.D., et al., *Decreasing the size limit for a stable magnetic vortex in modified permalloy nanodiscs.* Journal of Magnetism and Magnetic Materials, 2017. **443**: p. 252-260.
141. Xiao, Z.G. and C. Menon, *Counting grasping action using force myography: an exploratory study with healthy individuals.* JMIR Rehabilitation and Assistive technologies, 2017. **4**(1): p. e6901.
142. Passeri, D., et al., *Magnetic force microscopy: Quantitative issues in biomaterials.* Biomatter, 2014. **4**(1): p. e29507.
143. Natali, M., et al., *Configurational anisotropy in square lattices of interacting cobalt dots.* Journal of Applied Physics, 2002. **91**(10): p. 7041-7043.
144. Guslienko, K.Y., et al., *Magnetization reversal due to vortex nucleation, displacement, and annihilation in submicron ferromagnetic dot arrays.* Physical Review B, 2001. **65**(2): p. 024414.

145. Guslienko, K.Y., *Magnetic anisotropy in two-dimensional dot arrays induced by magnetostatic interdot coupling.* Physics Letters A, 2001. **278**(5): p. 293-298.
146. Yang, J.H., et al., *Exchange bias of Co/CoO multilayers deposited on nanosphere array.* Applied Physics A, 2012. **108**(2): p. 363-368.
147. Rahm, M., et al., *Vortex nucleation in submicrometer ferromagnetic disks.* Applied Physics Letters, 2003. **82**(23): p. 4110-4112.
148. Sahoo, S., et al., *Observation of Coherent Spin Waves in a Three-Dimensional Artificial Spin Ice Structure.* Nano Letters, 2021. **21**(11): p. 4629-4635.
149. Wurft, T., et al., *Evolution of magnetic vortex formation in micron-sized disks.* Applied Physics Letters, 2019. **115**(13): p. 132407.
150. Vargas, N., et al., *Asymmetric magnetic dots: A way to control magnetic properties.* Journal of Applied Physics, 2011. **109**(7).
151. Shima, H., et al., *Magnetization reversal in magnetostatically coupled dot arrays.* Journal of applied physics, 2002. **91**(10): p. 6952-6954.
152. Mironov, V.L., et al., *MFM probe control of magnetic vortex chirality in elliptical Co nanoparticles.* Journal of Magnetism and Magnetic Materials, 2007. **312**(1): p. 153-157.
153. El-Mezeini, A.M., T.J. Flack, and M.E. Welland, *Control of magnetic vortex chirality and polarization in indented and notched nanomagnetic disks.* Materials Research Express, 2014. **1**(4): p. 046109.
154. Stebliy, M.E., et al., *Manipulation of magnetic vortex parameters in disk-on-disk nanostructures with various geometry.* Beilstein journal of nanotechnology, 2015. **6**: p. 697-703.
155. Zvezdin, K. and E. Ekomasov, *Spin currents and nonlinear dynamics of vortex spin torque nano-oscillators.* Physics of Metals and Metallography, 2022. **123**(3): p. 201-219.
156. Sravani, M., P.K. Mishra, and S. Bhuktare, *Injection locking of spin torque nano oscillators using surface acoustic waves.* Journal of Magnetism and Magnetic Materials, 2022. **564**: p. 170048.
157. Jiang, S., et al., *Field-free high-frequency exchange-spring spin-torque nano-oscillators.* Nano Letters, 2023. **23**(4): p. 1159-1166.
158. Cambel, V. and G. Karapetrov, *Control of vortex chirality and polarity in magnetic nanodots with broken rotational symmetry.* Physical Review B, 2011. **84**(1): p. 014424.
159. Liu, Y. and A. Du, *Vortex core switching by coherent excitation controlled by defect in nanodisk.* Journal of Applied Physics, 2010. **107**(1): p. 013906.
160. Okazaki, S., *Resolution limits of optical lithography.* Journal of Vacuum Science & Technology B: Microelectronics and Nanometer Structures Processing, Measurement, and Phenomena, 1991. **9**(6): p. 2829-2833.
161. Gates, B.D., et al., *New approaches to nanofabrication: molding, printing, and other techniques.* Chemical reviews, 2005. **105**(4): p. 1171-1196.
162. Chao, C.-T., et al. *Study of inter-dot coupling in nano-patterned permalloy dots array*. in *Journal of Physics: Conference Series*. 2011. IOP Publishing.
163. Schnauber, P., et al., *Using low-contrast negative-tone PMMA at cryogenic temperatures for 3D electron beam lithography.* Nanotechnology, 2016. **27**(19): p. 195301.
164. Stebliy, M.E., et al., *Vortex manipulation and chirality control in asymmetric bilayer nanomagnets.* Journal of Applied Physics, 2015. **117**(17).
165. Dietrich, C., et al., *Influence of perpendicular magnetic fields on the domain structure of permalloy microstructures grown on thin membranes.* Physical review. B, 2008. **77**(17).
166. Kim, P.D., et al., *Collective motion of magnetization in two-dimensional arrays of square elements.* The European Physical Journal B, 2018. **91**(5): p. 90.
167. García-Martín, J., et al., *Imaging magnetic vortices by magnetic force microscopy: experiments and modelling.* Journal of Physics D: Applied Physics, 2004. **37**(7): p. 965.

168. Gubbiotti, G., et al., *Normal mode splitting in interacting arrays of cylindrical permalloy dots.* Journal of Applied Physics, 2006. **99**(8): p. 08C701.
169. Vogel, A., et al., *Signal transfer in a chain of stray-field coupled ferromagnetic squares.* Applied Physics Letters, 2011. **99**(4): p. 042506.
170. Fernandez, A. and C.J. Cerjan, *Nucleation and annihilation of magnetic vortices in submicron-scale Co dots.* Journal of Applied Physics, 2000. **87**(3): p. 1395-1401.
171. Coïsson, M., et al., *Magnetic vortex chirality determination via local hysteresis loops measurements with magnetic force microscopy.* Scientific Reports, 2016. **6**(1): p. 29904.
172. Gomez, R.D., et al., *Domain wall motion in micron-sized permalloy elements.* Journal of Applied Physics, 1999. **85**(8): p. 4598-4600.
173. Liou, S., et al., *Magnetic domain patterns of rectangular and elliptic arrays of small permalloy elements.* Journal of magnetism and magnetic materials, 2001. **226**: p. 1270-1272.
174. Díaz, J., et al., *Chiral asymmetry detected in a 2D array of permalloy square nanomagnets using circularly polarized x-ray resonant magnetic scattering.* Nanotechnology, 2019. **31**(2): p. 025702.
175. Mazumdar, D. and G. Xiao, *Scanning magnetoresistive microscopy study of quasi-static magnetic switching in mesoscopic square dots: observation of field-driven transition between flux-closure states.* IEEE transactions on magnetics, 2005. **41**(7): p. 2226-2229.
176. Sloika, M.I., et al., *Curvature induced chirality symmetry breaking in vortex core switching phenomena.* Applied Physics Letters, 2014. **104**(25): p. 252403.
177. Wu, K.-M., et al., *Influence of asymmetry on vortex nucleation and annihilation in submicroscaled permalloy disk array.* Applied Physics Letters, 2008. **92**(26): p. 262507.
178. Gubbiotti, G., et al., *Finite size effects in patterned magnetic permalloy films.* Journal of Applied Physics, 2000. **87**(9): p. 5633-5635.
179. Vaz, C., et al., *Energetics of magnetic ring and disk elements: Uniform versus vortex state.* Phys. Rev. B, 2006. **73**.
180. Vansteenkiste, A., et al., *Chiral symmetry breaking of magnetic vortices by sample roughness.* New Journal of Physics, 2009. **11**(6): p. 063006.
181. SHEKA, D.D., et al., *EQUILIBRIUM STATES OF SOFT MAGNETIC HEMISPHERICAL SHELL.* SPIN, 2013. **03**(03): p. 1340003.
182. Streubel, R., et al., *Magnetic vortices on closely packed spherically curved surfaces.* Physical Review B, 2012. **85**(17): p. 174429.
183. Zhou, Y. and F. Zeng, *2D compressive sensing and multi-feature fusion for effective 3D shape retrieval.* Information Sciences, 2017. **409-410**: p. 101-120.
184. Shishkin, I.S., et al., *Nonlinear geometric scaling of coercivity in a three-dimensional nanoscale analog of spin ice.* Physical Review B, 2016. **94**(6): p. 064424.
185. Pylypovskyi, O.V., et al., *Rashba torque driven domain wall motion in magnetic helices.* Scientific Reports, 2016. **6**(1): p. 1-11.
186. May, A., *Realising 3D artificial spin-ice systems using two-photon lithography and line-of-sight deposition*. 2020, Cardiff University.
187. Mueller, P., M. Thiel, and M. Wegener, *3D direct laser writing using a 405 nm diode laser.* Opt Lett, 2014. **39**(24): p. 6847-50.